Site U1404[1]

R.D. Norris, P.A. Wilson, P. Blum, A. Fehr, C. Agnini, A. Bornemann, S. Boulila, P.R. Bown, C. Cournede, O. Friedrich, A.K. Ghosh, C.J. Hollis, P.M. Hull, K. Jo, C.K. Junium, M. Kaneko, D. Liebrand, P.C. Lippert, Z. Liu, H. Matsui, K. Moriya, H. Nishi, B.N. Opdyke, D. Penman, B. Romans, H.D. Scher, P. Sexton, H. Takagi, S.K. Turner, J.H. Whiteside, T. Yamaguchi, and Y. Yamamoto[2]

Chapter contents

[1] Norris, R.D., Wilson, P.A., Blum, P., Fehr, A., Agnini, C., Bornemann, A., Boulila, S., Bown, P.R., Cournede, C., Friedrich, O., Ghosh, A.K., Hollis, C.J., Hull, P.M., Jo, K., Junium, C.K., Kaneko, M., Liebrand, D., Lippert, P.C., Liu, Z., Matsui, H., Moriya, K., Nishi, H., Opdyke, B.N., Penman, D., Romans, B., Scher, H.D., Sexton, P., Takagi, H., Turner, S.K., Whiteside, J.H., Yamaguchi, T., and Yamamoto, Y., 2014. Site U1404. *In* Norris, R.D., Wilson, P.A., Blum, P., and the Expedition 342 Scientists, *Proc. IODP,* 342: College Station, TX (Integrated Ocean Drilling Program). doi:10.2204/iodp.proc.342.105.2014
[2] **Expedition 342 Scientists' addresses.**

Background and objectives

Integrated Ocean Drilling Program (IODP) Site U1404 (proposed Site JA-13A; 40°0.80′N, 51°48.60′W; 4710 m water depth) (Fig. **F1**) is the second deepest water site drilled on J-Anomaly Ridge. This site was positioned to capture a record of predominantly calcareous sediment 251 m shallower than the largely sub–carbonate compensation depth (CCD) record at Site U1403. Site U1404 is located to reconstruct the CCD history in the deepest expanded record of the plastered drift at the foot of J-Anomaly Ridge. We expect to obtain a record of shoaling excursions of the CCD during the Paleogene. The drift was expected to be composed of Paleogene pelagic sediment. Drilling at Site U1403 encountered ~150 m of upper to lower Eocene sediment with an average sedimentation rate of ~1.4 cm/k.y. above lower Eocene chert. Consequently, the ~500 m thick sediment package at Site U1404 is expected to have an average sedimentation rate of ~4.7 cm/k.y.

The principal objective at Site U1404 was to obtain an expanded sequence of drift deposits just above the Eocene CCD. The Paleogene sediment package at Site U1404 is about the same thickness as other shallow sites on J-Anomaly Ridge. Hence, the stratigraphy at Site U1404 should be broadly representative of expanded Paleogene records on the Newfoundland ridges depth transect. Site U1404 should also be a sensitive recorder of large-amplitude CCD shoaling and deepening events including those not quite large enough to have triggered changes in calcium carbonate accumulation at Site U1403.

We expected Site U1404 to be a sensitive recorder of greenhouse gas–driven shoaling of the CCD. The common occurrence of "clay beds" associated with hyperthermal events at shallow and mid-depth Paleogene sites is a reflection of periods when the CCD shoaled well above its average position (Ridgwell, 2007; Sexton et al., 2011; Zachos et al., 2005; Bohaty et al., 2009). Such CCD shoaling events are expected to result from abrupt increases in oceanic and atmospheric inventories of greenhouse gases at the onset of hyperthermal events. It is presently unclear how much oceanic carbonate chemistry changed associated with any of the Paleogene hyperthermals because no depth transects that capture the full magnitude of CCD excursions have been studied (Zachos et al., 2005). Large climate transients such as the Paleocene/Eocene Thermal Maximum (PETM) are hypothesized to have been triggered by large, rapid changes in greenhouse gas concentra-

doi:10.2204/iodp.proc.342.105.2014

tions in the exogenic carbon cycle. Yet, huge uncertainty remains over the size of the carbon release involved, even for the best studied of these events, the PETM (estimates range from ~1200 to >4300 GT carbon, depending upon assumptions of the carbon source, the magnitude of the temperature anomaly, and the magnitude of the CCD excursion involved). Constraints are even poorer for smaller amplitude hyperthermals such as the "ELMO" and "X" events (Lourens et al., 2005), the numerous middle Eocene events described by Sexton et al. (2011), and the Middle Eocene Climate Optimum (MECO; Bohaty et al., 2009). A set of drill holes that capture the position of the CCD to within a few hundred meters should provide a tight constraint on the size of the CCD excursion for a wide range of hyperthermal events.

Carbonate preservation is hypothesized to improve in the aftermath of hyperthermals in response to rebalancing oceanic bicarbonate inventories as a consequence of elevated weathering of seafloor carbonate and terrestrial silicate weathering during greenhouse gas–fueled hyperthermal events (Dickens et al., 1997; Zachos et al., 2005; Leon-Rodriguez, 2010). We expected to see improved carbonate preservation associated with "overshoots" of ocean alkalinity associated with the late stages of hyperthermal events. CCD deepening events involving similar overshoot dynamics are also hypothesized to be associated with the Cenozoic initiation of large ice sheets on Antarctica across the Eocene–Oligocene Transition (EOT) and also perhaps with their subsequent expansion across the Oligocene–Miocene transition (Coxall et al., 2005; Zachos and Kump, 2005; Holbourn et al., 2005; Merico et al., 2008). New long-term records of Cenozoic CCD in the equatorial Pacific Ocean also indicate major transient CCD deepening events during the middle Eocene (Lyle et al., 2002; Pälike et al., 2012).

Large-amplitude CCD deepening events should be evident at Site U1404, both through increased abundances of carbonate and improved carbonate microfossil preservation. Our goal was to recover a sequence that is a record of sedimentation at Site U1404 from ~100 to 150 m above the local long-term average CCD for the Paleogene as reconstructed by Tucholke and Vogt (1979) so that deepening events can be well documented using modern coring and stratigraphic techniques.

Seismic stratigraphy shows that the Paleogene sediment package downdip of Site U1404 thins considerably between a modern depth of 4800 and 4900 meters below sea level (mbsl) (Fig. **F2**), corresponding to paleodepths at 50 Ma of ~4600 mbsl using the subsidence reconstruction of Tucholke and Vogt (1979) (see Fig. **F2** in the "Expedition 342 summary" chapter [Norris et al., 2014a]). In that reconstruction, the contemporaneous North Atlantic CCD is positioned at a paleodepth of ~4400–4300 mbsl and prominent CCD deepening is indicated below 5500 mbsl in the latest Cretaceous and early Paleocene. These CCD reconstructions, together with our drilling results from Site U1403, suggest that the CCD in the North Atlantic Ocean during the early Eocene was much deeper (by ~1.5 km) than in the contemporaneous equatorial Pacific Ocean (Pälike et al., 2012). We interpret the thinning of the Paleogene sediment package as an indication of the average position of the CCD in the early to late Eocene.

The acoustic expression of the sequence drilled at Site U1404 comprises an ~80 m thick surficial, reflector-rich unit overlying a highly expanded (~400 m thick) Paleogene drift sediment package that shows almost no internal reflections, suggesting that the sediment pile has a fairly uniform composition (Figs. **F2, F3**). In detail, the upper half of the drift sequence at Site U1404 is virtually seismically transparent, whereas the lower half has a fuzzy acoustic expression but no well-developed internal reflections. Drilling at Site U1403 suggests that the fuzzy acoustic unit is of early Eocene age and has a higher carbonate and biogenic opal content than the overlying transparent upper Eocene and middle Eocene package. Therefore, we expect to find that this sequence also has a higher carbonate and siliceous sediment content than the overlying unit. The lack of distinct internal reflections within these two acoustic units suggests that they do not contain major unconformities or major changes in sediment composition. This uniformity has a number of possible explanations. One possibility is that CCD fluctuations were either too brief or too modest in amplitude to give rise to fluctuations in carbonate content prominent enough to exhibit a notable acoustic expression. Alternative explanations are that the entire drift package accumulated rapidly during an interval of relative CCD stasis or during an interval of CCD variability that took place at depths too shallow or too deep to influence this site.

In addition to its utility for CCD reconstructions, Site U1404 will also be used to understand the history of deepwater currents. Most deep ocean drill sites are located at mid-ocean depths when we account for thermal subsidence. Hence, Site U1404, at a paleodepth of ~4300 mbsl at 50 Ma, is one of the few to recover a representative sequence of carbonate sediment deposited under true deep water. Furthermore, the site is well placed to record the history of deep water formed in the far North Atlantic, or even the Arctic, because the Deep Western Boundary

Current is constrained to flow directly over or around the Newfoundland Ridges by geostrophic flow and the shape of the ocean basin. As the deep end of the J-Anomaly depth transect, the site should record the chemistry and flow history of abyssal waters in the Paleogene.

Finally, Site U1404 may preserve records of late Eocene impacts. We provisionally identified a late Eocene impact deposit at Site U1403 in sediment corresponding to Chron C16, a horizon that could correlate with the impact blanket from the Chesapeake Impact structure. Assuming that there is no hiatus between the impact layer and the middle and lower Eocene fossiliferous sediments at Site U1403, it seems likely that a similar but more expanded sequence of sediment exists at Site U1404.

Operations

All times are local ship time (Universal Time Coordinated – 2.5 h). See Table T1 for coring summary.

Hole U1404A summary

Latitude: 40°00.7997′N
Longitude: 51°48.5990′W
Water depth below sea level (m): 4742.3
Date started: 1030 h, 20 June 2012
Date finished: 2040 h, 22 June 2012
Time on hole (days): 3.2
Seafloor depth (m drilling depth below rig floor [DRF]): 4753.8
Seafloor depth estimation method: mudline core
Rig floor to sea level (m): 11.5
Penetration depth (m drilling depth below seafloor [DSF]): 308.8
Cored interval (m): 308.8
Recovered length (m): 281.02
Recovery (%): 91
Total cores (number): 36
Advanced piston corer (APC) cores (number): 32
Extended core barrel (XCB) cores (number): 4
Drilling system: 11⅞ inch APC/XCB bit with 136.00 m bottom-hole assembly (BHA)
Objective: core from seafloor to ~250 m DSF
Result: target exceeded; objectives achieved

Hole U1404B summary

Latitude: 40°00.7999′N
Longitude: 51°48.5856′W
Water depth below sea level (m): 4747.6
Date started: 2255 h, 22 June 2012
Date finished: 1310 h, 24 June 2012
Time on hole (days): 1.7
Seafloor depth (m DRF): 4759.1
Seafloor depth estimation method: mudline core
Rig floor to sea level (m): 11.5
Penetration depth (m DSF): 228.7
Cored interval (m): 228.7
Recovered length (m): 228.04
Recovery (%): 100
Total cores (number): 27
APC cores (number): 27
Drilling system: 11⅞ inch APC/XCB bit with 136.00 m BHA
Objective: core from seafloor to ~250 m DSF
Result: target and objectives achieved; problems with the core liners after achieving the main science objectives forced the abandonment Hole U1404B

Hole U1404C summary

Latitude: 40°00.7890′N
Longitude: 51°48.5857′W
Water depth below sea level (m): 4747.5
Date started: 1445 h, 24 June 2012
Date finished: 1945 h, 24 June 2012
Time on hole (days): 0.3
Seafloor depth (m DRF): 4759.1
Seafloor depth estimation method: Hole U1404B depth
Rig floor to sea level (m): 11.6
Penetration depth (m DSF): 44.5
Cored interval (m): 28.5
Recovered length (m): 28.98
Recovery (%): 102
Drilled interval (m): 16
Drilled interval (number): 1
Total cores (number): 3
APC cores (number): 3
Drilling system: 11⅞ inch APC/XCB bit with 136.00 m BHA
Objective: capture interval of science interest; deepen per direction
Result: target likely overshot because of variable seafloor depth

Description

The vessel arrived at Site U1404 after a 4.2 nmi transit from Site U1403 and stabilized over Site U1404 at 1455 h on 19 June 2012. The plan for this site called for drilling three holes to a depth of ~250 m DSF. After completion of Holes U1404A and U1404B to 308.8 and 228.7 m DSF, respectively, Hole U1404C was drilled to 16 m DSF and then cored to 44.5 m DSF in an attempt to recapture a zone hypothesized to contain gas hydrate. The total time spent at Site U1404 was 124.75 h (5.2 days). The XCB was deployed four times, and the APC was deployed 62 times. The XCB-cored interval was 37.8 m with a re-

covery of 23.05 m (61.0% recovery). The APC-cored interval was 528 m with a recovery of 515 m (97.5% recovery). The overall recovery for Site U1403 was 95.1%.

Hole U1404A coring

The drill bit was spaced out to 4715 m drilling depth below rig floor (DRF) for the first attempt at a mudline core. The calculated precision depth recorder (PDR) depth for the site was 4718.4 m DRF. A mistake in the pipe tally resulted in an APC wireline run to ~4705 m DRF. The depth of the bit was repeatedly lowered until mudline was established at 4753.8 m DRF (4742.3 mbsl), which was 35.4 m below the PDR depth. Hole U1404A was spudded at 1030 h on 20 June. Three possible explanations for the discrepancy between the PDR depth and the drill pipe depth were offered:

1. Strong currents were causing the drill pipe to bend in an S-shape,
2. The acoustic signal was significantly affected by thermal or current layering in the water column, or
3. Seafloor bedforms caused local seafloor depth to vary considerably.

The second explanation is supported by the poor quality of the acoustic signal received from the acoustic beacon on the seafloor.

Cores 342-U1404A-1H through 32H were recovered using nonmagnetic core barrels and the FlexIT core orientation tool. The liner of Core 4H shattered, presumably from hitting a manganese nodule. Nodules as long as 10 cm were recovered in Core 1H, and others, perhaps even larger ones, may have been washed into the bottom of the hole. In Core 22H, the formation began to firm up, and the first partial stroke was recorded. Cores 22H through 32H were partial strokes, and the hole was advanced by recovery. The XCB was deployed for Cores 33X through 36X to a final depth of 308.8 m DSF. The drill bit cleared the seafloor at 2040 h on 22 June, ending Hole U1404A. Overall core recovery for Hole U1404A was 281.02 m for the 308.8 m interval cored (91% recovery). The total time spent on Hole U1404A was 77.75 h.

Hole U1404B coring

The vessel was offset 20 m east. The bit was spaced out to 4752.0 m DRF in an attempt to recover ~7–8 m of the mudline core. Hole U1404B was spudded at 2255 h on 22 June, and a 2.48 m mudline core established the seafloor depth at 4759.1 m DRF (4747.6 mbsl). Cores 342-U1404B-1H through 27H were recovered to a depth of 228.7 m DSF using nonmagnetic core barrels and the FlexIT core orientation tool. The liner of Core 7H returned shattered and collapsed for unknown reasons. Cores 21H through 27H were partial strokes, and the hole was advanced by recovery. Eight core liners either collapsed or broke, and three of those had to be pumped out of the core barrel with a high-pressure pump. The bit cleared the seafloor at 1310 h on 24 June, ending Hole U1404B. A total of 27 piston cores were taken over a 228.7 m interval with a total recovery of 228.04 m (100% recovery). The total time spent on Hole U1404B was 40.5 h.

Hole U1404C coring

The vessel was offset 20 m south. Hole U1404C was spudded at 1445 h on 24 June and was drilled to a depth of 16 m DSF. The seafloor depth was assumed (perhaps incorrectly) to be the same as that for Hole U1404B (4759.1 m DRF; 4747.6 mbsl). Cores 342-U1404C-2H through 4H were recovered to a final depth of 44.5 m DSF. The total advance was 28.5 m, with 28.98 m of core recovered (102% recovery). The bit cleared the seafloor at 1945 h on 24 June, ending Hole U1404C. The drill floor was secured, and the vessel began moving to Site U1405 in dynamic positioning mode at a speed of 0.9 kt. The total time spent on Hole U1404C was 6.5 h.

Lithostratigraphy

The sedimentary progression recovered from Holes U1404A–U1404C reveals a diversity of deep-sea pelagic sediments of Pleistocene to middle Eocene age comprising four lithostratigraphic units (Figs. **F4, F5, F6, F7, F8;** Table **T2**). Unit I is ~2 m thick and composed of Pliocene–Pleistocene brown foraminiferal sandy clay and nannofossil ooze, with notable manganese nodules, transitioning downhole to Pliocene brown clay with silt. Unit II is green and greenish gray carbonate-poor Oligocene–Miocene clay that occurs in a nearly 200 m thick sequence and contains abundant diatoms, radiolarians, and sponge spicules. A dolomite cobble is present at the top of Unit II. Unit II is divided into an upper Subunit IIa (20 m thick) that is barren of microfossils and lower Subunit IIb (180 m thick) that contains abundant siliceous microfossils (diatoms, radiolarians, and sponge spicules) and comparably minor abundances of calcareous nannofossils. Unit III is a ~26 m interval of carbonate-rich nannofossil ooze alternating with clay-rich nannofossil ooze and clay that spans the lowermost Oligocene and uppermost Eocene. Unit IV is an ~75 m thick succession of clay and claystone with some intervals containing abundant radiolarians and/or calcareous nannofossils. Sand-sized lithoclasts are found in the >63 µm size fraction in

Site U1404 sediment, particularly in the Miocene and Oligocene sequences.

Lithostratigraphic units and boundaries are defined by changes in lithology (as identified by visual core description and smear slide observations), physical properties, color reflectance (L*, a*, and b*), and biogenic content (calcium carbonate and silica) (Fig. F4). The lithologic differences observed between units are primarily attributable to varying abundances of nannofossils, diatoms, radiolarians, and foraminifers (Figs. F6, F7, F8). Lithologic descriptions are based on sediments recovered from Hole U1404A and supplemented with observations from the two shorter Holes U1404B and U1404C.

Unit I

Interval: 342-U1404B-1H-1, 0 cm, to 1H-2, 83 cm
Depth: Hole U1404B = 0–2.33 meters below seafloor (mbsf)
Age: Pliocene to Pleistocene
Lithology: foraminiferal sand and nannofossil ooze

Unit I is a 2.33 m thick succession of sediment encountered only in Hole U1404B (Fig. F4). This thin lithostratigraphic unit was not recovered in Hole U1404A as a result of poor mudline core recovery (see **"Stratigraphic correlation"**). The sediment in Core 342-U1404B-1H is very pale brown (10YR 8/2) moderately bioturbated nannofossil ooze (Fig. F5B) with abundant sand-sized foraminifers in the uppermost 57 cm of Section 342-U1404B-1H-1 (Fig. F5A) and Mn nodules as large as 10 cm.

Unit II

Intervals: 342-U1404A-1H-1, 0 cm, to 23H-4, 120 cm; 342-U1404B-2H-1, 0 cm, to 24H-1, 136 cm; 342-U1404C-2H-1, 0 cm, to 4H-CC, 29 cm
Depths: Hole U1404A = 0.00–200.60 mbsf; Hole U1404B = 2.40–203.56 mbsf; Hole U1404C = 16.00–45.01 mbsf
Age: Oligocene to Miocene
Lithologies: clay, silty clay, biosiliceous clay, and biosiliceous clay with nannofossils

Unit II and its two subunits, IIa and IIb, comprise a 195–200 m thick succession of predominantly clay and biosiliceous clay with some intervals of biosiliceous clay with nannofossils (Figs. F4, F5). The top of the unit is defined by pale brown (10YR 6/3) clay and silty clay underlying the nannofossil-rich sediment of Unit I. The boundary between Subunits IIa and IIb is defined by the first downhole occurrence of biogenic sediment within Unit II (top of Section 342-U1404A-5H-1 [33.20 mbsf] and top of Section 342-U1404B-4H-3 [24.40 mbsf]). The base of Unit II is defined by the occurrence of nannofossil ooze at 200.60 mbsf in Hole U1404A and 203.56 mbsf in Hole U1404B. A large (7 cm long) dolomite clast interpreted as a glacial dropstone is present in the top of Core 342-U1404A-1H.

Subunit IIa

Intervals: 342-U1404A-1H-1, 0 cm, to 3H-CC, 11 cm; 342-U1404B-2H-1, 0 cm, to 4H-2, 150 cm
Depths: Hole U1404A = 0.00–22.32 mbsf; Hole U1404B = 2.40–24.40 mbsf
Age: Miocene
Lithologies: clay and silty clay; minor lithology includes clayey silt

Subunit IIa is a 17–20 m thick succession of pale brown (10YR 6/3), greenish gray (10GY 5/1), and pinkish gray (7.5YR 6/2) to dark greenish gray (10Y 4/1) clay to silty clay with slight to moderate bioturbation (Figs. F4, F5C). Clayey silt is present as a minor lithology, typically as thin (<3 cm) beds alternating with silty clay. Shipboard X-ray diffraction (XRD) analysis indicates distinctive peaks for quartz, illite, plagioclases, montmorillonite, and some chlorite. The presence of disseminated Mn oxides and discrete Mn nodules is variable throughout and, where highly concentrated, impart a dark greenish gray color to the sediment (10Y 4/1). Nodule-shaped patches of possibly authigenic glauconite are present in Sections 342-U1404A-3H-1 through 3H-3 (Fig. F9). Subunit IIa is barren of microfossils.

Subunit IIb

Intervals: 342-U1404A-5H-1, 0 cm, to 23H-4, 120 cm; 342-U1404B-4H-3, 0 cm, to 24H-1, 136 cm; 342-U1404C-2H-1, 0 cm, to 4H-CC, 29 cm
Depths: Hole U1404A = 33.20–200.60 mbsf; Hole U1404B = 24.40–203.56 mbsf; Hole U1404C = 16.00–45.01 mbsf
Age: Oligocene to Miocene
Lithologies: biosiliceous clay, biosiliceous ooze with clay, and biosiliceous clay with calcareous nannofossils

Subunit IIb is a ~170–180 m thick succession of moderately bioturbated, greenish gray (5GY 5/1) to dark greenish gray (5GY 4/1 and 10Y 4/1) biosiliceous clay or biosiliceous ooze with clay with intervals of biosiliceous clay with calcareous nannofossils (Figs. F4, F5C). Subunit IIb is differentiated from overlying Subunit IIa based on the presence of siliceous microfossils. Siliceous biogenic components include diatoms, radiolarians, sponge spicules, and silicoflagellates (Figs. F6, F7, F8). Shipboard XRD analyses for Subunit IIb yield similar results to those for Subunit IIa. Only kaolinite and calcite seem to be more common in Subunit IIb than Subunit IIa, although ka-

olinite is still relatively rare. In contrast, calcite is more common in Subunit IIb as a result of more common nannofossils. The clay also contains variable abundances of quartz, sulfides, oxides, biotite mica, feldspar, and heavy minerals in the clay to fine silt size range that were observed in smear slides. Color variations in Subunit IIb are largely centimeter- to decimeter-scale banding resulting from the bioturbation of Mn oxide layers. Color bands have minor differences in nannofossil abundance (Fig. F5C). Core 342-U1404A-11H contains small (millimeter sized) white blebs composed of highly angular silt-sized quartz grains with occasional mica or feldspar grains. Similar sandy patches, possibly ice-rafted debris (IRD), were also observed in Section 342-U1404B-21H-1 (Fig. F10). Coarse sand-sized clasts of quartz siltstone are present at Site U1411, where they produce blebs of quartz silt similar to those at Site U1404 upon dissolution of their calcite cement.

Unit III

Intervals: 342-U1404A-23H-4, 122 cm, to 26H-5, 0 cm; 342-U1404B-24H-1, 136 cm, to 27H-2, 100 cm
Depths: Hole U1404A = 200.62–226.50 mbsf; Hole U1404B = 203.56–225.11 mbsf
Age: late Eocene to Oligocene
Lithology: clayey/silty nannofossil ooze and nannofossil ooze

Unit III is 22–26 m thick and composed of brownish gray (2.5Y 6/2), gray (5Y 6/1), to light yellowish brown (2.5Y 6/3) moderately bioturbated nannofossil ooze and clayey nannofossil ooze alternating with clay (Figs. F4, F5, F6, F7, F8, F11). The color variation observed in Unit II corresponds well with qualitative smear slide analysis of carbonate content. Moreover, a distinguishing characteristic of this lithostratigraphic unit is the highest calcium carbonate content values (several data points >40 wt%) observed within any unit at Site U1404 (Figs. F4, F12; see also "Geochemistry"). These intervals of high calcium carbonate are associated with the EOT (Figs. F11, F12; see also "Eocene–Oligocene transition"). Section 342-U1404A-26H-1 contains a conspicuous ~40 cm thick greenish gray (5BG 5/1) silty layer within the background grayish brown (2.5Y 5/2) nannofossil ooze contained within Chron C17 (see "Paleomagnetism").

Unit IV

Intervals: 342-U1404A-26H-6, 0 cm, to 36X-1, 72 cm; 342-U1404B-27H-3, 0 cm, to 27H-CC, 62 cm
Depth: Hole U1404A = 226.50–299.82 mbsf; Hole U1404B = 225.11–228.75 mbsf
Age: middle to late Eocene
Lithology: clay/claystone and radiolarian clay

Unit IV is a 73 m thick succession of clay/claystone and radiolarian clay recovered primarily in Hole U1404A (Figs. F4, F5, F6, F7, F8). Only 3.64 m of this lithostratigraphic unit, the deepest and oldest lithostratigraphic unit drilled at Site U1404, was encountered in Hole U1404B at the base of Core 342-U1404B-27H. Unit IV contains variable abundances of radiolarians and/or calcareous nannofossils in some intervals (Fig. F7). Centimeter- to decimeter-scale color variation, from greenish gray (5GY 6/1 and 5GY 5/1) to dark greenish gray (5GY 4/1), occurs through most of the unit and is the result of differential bioturbation intensity and, in some cases, diagenesis. Cores 342-U1404A-33X through 36X were drilled with the XCB and, as a result, are significantly disturbed by biscuiting and fracturing.

Notable events

Carbonate content in Site U1404 sediment is generally very low, suggesting the site was positioned close to the CCD for much of its Cenozoic history. Increases in carbonate abundance may well reflect CCD deepening events in the Eocene and the EOT. For much of the Eocene–Miocene interval, the site is below the CCD, with discrete horizons indicating CCD deepening events in the lowermost Oligocene. At 195 mbsf in Hole U1404A, we observed a peak in the carbonate concentration, presumably reflecting deepening and overshoot of the CCD in the early Oligocene. Surprisingly, the record in the Eocene records a number of possible carbonate "events."

Eocene–Oligocene transition

The EOT was recovered in a rare carbonate-rich interval at Site U1404. The EOT was identified on the basis of biostratigraphic and magnetostratigraphic observations (see "Biostratigraphy" and "Paleomagnetism") and is characterized by a series of striking lithologic changes (Fig. F11). Oligocene and late Eocene sediment over- and underlying the EOT are moderately bioturbated, greenish gray (5GY 5/1) biosiliceous clay to radiolarian claystone typically containing <5 wt% calcium carbonate. In Hole U1404A, the EOT is overlain by 2.67 m of relatively unmottled (i.e., more completely bioturbated) greenish gray sediment overlain by the typical mottled greenish gray sediment of the early Oligocene. We are unable to comment on the presence or absence of the Eocene/Oligocene boundary in Hole U1404B because of extensive core disturbance (flow-in) in the lowermost four sections of Core 342-U1404B-23H.

The general interval associated with the EOT is identified as a lithostratigraphic unit (Unit III) on the basis of the unique lithology, including the presence of clayey nannofossil ooze to nannofossil ooze, light

brownish gray (2.5Y 6/2) to gray (5Y 6/1) sediment, and variable carbonate content (Fig. F4). The uppermost part of Unit III, a brown mottled and banded 0.14 m thick section in Hole U1404B, is not observed in Hole U1404A (Fig. F11). This mottled and banded section is followed by a 3.77–4.92 m thick carbonate-rich interval that is mottled in Hole U1404A and banded in Hole U1404B. Underlying this carbonate-rich interval is the Chron C13r/C13n boundary, the Eocene/Oligocene boundary, and a ~4 m thick interval that is brown with reddish mottles. This interval is followed in Hole U1404A by a second, short (0.275 m thick) carbonate-rich interval. This second carbonate-rich interval and the underlying light brown interval (2.125 m thick) are not observed in Hole U1404B (Fig. F11).

Carbonate concentrations reach their highest value (>50 wt%) in calcareous nannofossil Zone NP21 and Chron C13n and coincide with the lightest colored sediment recovered at Site U1404 (Figs. F11, F12). Color reflectance, magnetic susceptibility, and carbonate content are broadly correlated in Hole U1404A. Color reflectance data, particularly a* and b*, and magnetic susceptibility increase through the late Eocene (~207 to ~227 mbsf in Hole U1404A). Magnetic susceptibility, a*, and b* peak in the earliest Oligocene, followed by a peak in L* that correlates with the highest carbonate content (purple shading in Fig. F12). Calcium carbonate content increases through the late Eocene in a series of discrete intervals. All three data types (magnetic susceptibility, color reflectance, and calcium carbonate) drop to a sustained low in the early Oligocene. For instance, mean magnetic susceptibility values increase from 26 to 45 instrument units (IU) from ~207 to ~227 mbsf in Hole U1404A during the late Eocene ramp up and then decrease to 20 IU at ~198 mbsf.

Sand-sized lithic grains

Sand-sized (>63 µm) lithics were observed within two intervals at Site U1404. These lithics consist of quartz grains, which are mostly transparent but also pink and smoky varieties, as well as metamorphic rock fragments within the 63–150 µm sieve size fraction (Fig. F10). The quartz grain shape is often angular and occasionally shows conchoidal fractures. The first common occurrence of sand-sized lithic grains takes place in the lowermost Oligocene directly downhole from the change from carbonate-bearing brownish sediment to darker, grayish green clay in Section 342-U1404A-23H-4. An analysis of core catcher and section samples revealed that these grains are common constituents within the fine sand fraction uphole to the base of Core 342-U1404A-19H (172 mbsf) and are interpreted to be IRD. Larger particles, as large as coarse sand– or granule-sized grains, have also been observed but are comparatively rare (Figs. F10, F13). The sand-sized lithic grains occur in intervals 342-U1404A-18H-CC through 23H-3, 117–119 cm (163–199 mbsf), which can be stratigraphically correlated with the EOT. The abundance of sand-sized lithic grains in this deep-sea sediment is suggestive of IRD, supporting the existence of continental ice sheets in the northern hemisphere before 15 Ma, as previously proposed by Tripati et al. (2007) and Eldrett et al. (2008). Another explanation for the occurrence of the observed coarse siliciclastic sediment might be strongly enhanced bottom-current activity transporting fine sand material into the drift deposits. However, the well-developed angular habits of the grains argue for short transport typical for IRD. A second sand-sized lithic grain occurrence was reported from Section 342-U1404A-12H-5, with a composition and size comparable to the occurrence described above. This second interval may correspond to the Miocene Mi-1 glaciation.

Deepwater authigenic glauconite

Sediment in Subunit IIa includes nodular-shaped green accumulations that we interpreted as Mn nodules altering to glauconite/illite (Fig. F9). XRD data from Sample 342-U1404A-3H-1, 140–141 cm, indicate a concentration of glauconite/illite. Given the shape and distribution of this authigenic material, we speculate that the glauconite/illite lumps derived from the alteration of Mn nodules. To our knowledge, this style of deep-marine glauconite occurrence has not been reported in any detail in the geologic literature.

Biostratigraphy

Coring at Site U1404 recovered a 300 m thick sequence of Pleistocene to middle Eocene clay, with subordinate nannofossil ooze mainly in the Eocene/Oligocene boundary interval. The clay contains varying amounts of biosilica and nannofossils. Nannofossils and planktonic foraminifers are present in the uppermost brown foraminifer sandy clay and nannofossil ooze (Core 342-U1404B-1H; 0–2.46 mbsf) and indicate Quaternary to Pliocene ages (Zones NN21/NN20–NN15). We were unable to provide biostratigraphic ages for the interval between 4.70 and 40.61 mbsf because of the absence of siliceous or calcareous microfossils. Below 40.61 mbsf, first radiolarians and then radiolarians, nannofossils, and occasionally planktonic foraminifers provide biostratigraphic control indicating middle Miocene to middle Eocene-age sediments. Benthic foraminifers are generally rare and moderately to well pre-

served in lithostratigraphic Units I and II, whereas Subunit IIb contains well-preserved assemblages, including *Globobulimina pacifica,* indicative of suboxic conditions. Unit III contains abundant and relatively well preserved benthic foraminifers. Benthic foraminifers suggest a lower bathyal to abyssal paleodepth for this site (van Morkhoven et al., 1986).

An integrated calcareous and siliceous microfossil biozonation is shown in Figure **F14.** Nannofossil datum and zonal determinations agree well with the radiolarian biostratigraphy. An age-depth plot including biostratigraphic and paleomagnetic datums is shown in Figure **F15.** A summary of calcareous and siliceous microfossil abundances and preservation is given in Figure **F16.**

Calcareous nannofossils

Calcareous nannofossil biostratigraphy is based on analysis of core catcher samples and additional working section half samples from Holes U1404A and U1404B to refine datum levels, particularly at the Oligocene–Miocene and Eocene–Oligocene transitions. Depth positions and age estimates of biostratigraphic marker events are shown in Table **T3.** Calcareous nannofossil occurrence data are shown in Table **T4.** Note that the distribution chart is based on shipboard study only and is therefore biased toward age-diagnostic species.

At Site U1404, preservation of calcareous nannofossils varies from poor to moderate through the Miocene–Oligocene succession, and very poorly preserved dissolved assemblages are present in middle Eocene sediment. Calcareous nannofossil preservation is good in the carbonate-rich interval around the EOT (Fig. **F13**).

The uppermost interval from Sample 342-U1404B-1H-1, 40 cm, to 1H-CC (0.41–2.46 mbsf) contains abundant nannofossils indicative of Pliocene–Pleistocene Zones NN20–NN15, as indicated by the base of large *Gephyrocapsa* (Sample 342-U1404B-1H-1, 40 cm; 0.41 mbsf), top of *Discoaster tamalis* (Sample 1H-1, 135 cm; 1.36 mbsf), and top of *Reticulofenestra pseudoumbilicus* (Sample 1H-CC; 2.46 mbsf). The sediment is noncalcareous and barren of nannofossils from Sample 342-U1404B-1H-CC to 342-U1404A-6H-CC (2.46–49.36 mbsf).

The interval from Sample 342-U1404A-6H-CC to 14H-1, 43 cm (49.36–115.63 mbsf), contains rare to common calcareous nannofossils ascribed to lower Miocene Zone NN2 because of the common presence of *Triquetrorhabdulus carinatus* and the absence of *Dictyococcites bisectus*. The sporadic presence of *Discoaster druggii,* the base of which defines the base of Zone NN2, is seen from Sample 342-U1404A-10H-5, 115 cm, to 15H-6, 100 cm (87.86–133.03 mbsf), supporting the early Miocene age for this interval.

The Miocene/Oligocene boundary interval is carbonate poor, and nannofossils are generally poorly preserved and of low diversity or absent. Upper Oligocene Zone NP25 is identified by the top and base of *Sphenolithus ciperoensis* in Samples 342-U1404A-17H-CC (153.72 mbsf) and 21H-3, 93 cm (185.64 mbsf), respectively. A 9.0 m noncalcareous interval follows, lying above a richly nannofossiliferous Oligocene/Eocene boundary succession (from Sample 342-U1404A-21H-CC to 23H-4, 120 cm; 191.71–200.60 mbsf).

The highest lower Oligocene nannofossil assemblage lies immediately below a sharp boundary in Hole U1404A (200.63 mbsf), which may be a sheared contact drilling artifact (see **"Paleomagnetism"**). Nannofossils appear in a gradual succession of increasing downhole carbonate in Section 342-U1404B-24H-1. The assemblage contains the tops of *Coccolithus formosus, Isthmolithus recurvus,* and *Reticulofenestra umbilicus,* indicating the presence of a short hiatus (0.9 m.y.) or condensed section in the overlying barren interval. The top of *C. formosus* indicates the presence of Zone NP21, the nannofossil zone that spans the Eocene/Oligocene boundary. The intra–Zone NP21, top acme of *Clausicoccus subdistichus* event occurs in Sample 342-U1404A-23H-5, 60 cm (201.50 mbsf).

The highest upper Eocene datum event, the top of *Discoaster saipanensis,* occurs in Sample 342-U1404A-24H-3, 30 cm (207.61 mbsf), and marks the base of Zone NP21. The base of *I. recurvus* in Sample 342-U1404A-24H-6, 96 cm (212.76 mbsf), marks the base of Zone NP19–NP20. The occurrences of single specimens in several lower samples (downhole to Sample 342-U1404A-26H-1, 72 cm; 221.22 mbsf) may represent rare occurrences prior to the base common occurrence, which is the NP19 zonal boundary datum level.

The upper Eocene interval is characterized by carbonate-poor clay containing dissolved nannofossils; therefore, the datum levels reported should be treated with some caution. The interval from Sample 342-U1404A-26H-1, 72 cm, to 33X-CC (221.22–279.56 mbsf) is assigned to Zones NP17–NP18, which cannot be differentiated because of the absence of *Chiasmolithus oamaruensis* in the upper Eocene at Site U1404. The top of *Chiasmolithus grandis,* which lies slightly below the base of Zone NP18, occurs in Sample 342-U1404A-25H-CC (220.56 mbsf).

The base of *D. bisectus* has been consistently found in the upper part of Chron C18r, predating the MECO (Fornaciari et al., 2010). At Site U1404, *D. bisectus* is observed from Sample 342-U1404A-28H-CC

(244.03 mbsf) above an interval barren of calcareous nannofossils (Samples 342-U1404A-29H-1, 64 cm, to 30H-CC; 245.01–259.72 mbsf). This suggests that the MECO may lie within this carbonate-free interval.

The top of *Nannotetrina* spp. and presence of *R. umbilicus* in Sample 342-U1404A-34X-1, 56 cm (281.27 mbsf), indicates the presence of upper Zone NP16 in this lowermost nannofossiliferous sample. Calcareous nannofossils are not present from Sample 342-U1404A-34X-7, 60 cm, to 36X-1, 67 cm (289.83–299.80 mbsf).

Radiolarians

Radiolarian biostratigraphy is based on analysis of selected core catcher and working section half samples from Hole U1404A. No samples from Hole U1404B were examined. Radiolarians occur sporadically and are poorly preserved in the undated upper part of Hole U1404A. Radiolarians are abundant and well preserved through the lower Miocene and upper Oligocene but are absent from the Oligocene–Eocene transition. They are abundant and well preserved in the middle Eocene. Depth positions and age estimates of biostratigraphic marker events are shown in Table **T5,** and the radiolarian distribution is shown in Table **T6.** Note that the distribution chart is based on shipboard study and is biased toward age-diagnostic species. Some distinctive elements of Miocene and Eocene radiolarian assemblages are illustrated in Figure **F17.**

The uppermost interval, from Sample 342-U1404A-1H-CC to 4H-CC (4.7–22.36 mbsf), is barren or contains only rare and poorly preserved radiolarians.

Radiolarians are abundant and well preserved from Sample 342-U1404A-5H-CC to 19H-CC (40.59–172.77 mbsf) and are assigned to radiolarian Zones RN2–RP21, which span the Miocene–Oligocene transition. Lower Miocene Zone RN2 is identified by the co-occurrence of *Cyrtocapsella tetrapera* and *Stichocorys delmontensis* in Samples 342-U1404A-5H-CC to 11H-CC (40.59–96.24 mbsf), along with the absence of Zone RN3 index species *Stichocorys wolffii*. The top of *Dorcadospyris ateuchus* also occurs within this interval (Sample 342-U1404A-8H-CC; 71.30 mbsf), which is consistent with the Zone RP21–RN2 range reported by Sanfilippo et al. (1985). Samples from this zone contain abundant diatoms.

The interval between the base of *S. delmontensis* in Sample 342-U1404A-11H-CC (96.24 mbsf) and the bases of *C. tetrapera* and *Calocycletta virginis* in Sample 342-U1404A-14H-CC (124.87 mbsf) is assigned to Zone RP1. The base of *Eucyrtidium diaphanes* is recorded in Sample 342-U1404A-13H-CC (115.07 mbsf), although the species is known to range into underlying Zone RP22 at other locations and is a potential marker for the base of the Miocene (Kamikuri et al., 2012). Samples from this zone contain distinctive large orosphaerid radiolarians (Fig. **F17**). Diatoms are present but less common than in Zone RN2.

Lowermost Miocene–uppermost Oligocene Zone RP22 extends to the base of *Lychnocanoma elongata,* which is identified in Sample 342-U1404A-16H-CC (144.00 mbsf). Radiolarian biostratigraphy indicates that the Oligocene/Miocene boundary lies between Samples 342-U1404A-14H-CC and 16H-CC (124.87–144.00 mbsf). Upper Oligocene Zone RP21 extends to the base of *D. ateuchus* in Sample 342-U1404A-19H-CC (172.77 mbsf). The bases of *Artophormis gracilis, Didymocyrtis prismatica,* and *Theocyrtis annosa* occur within this zone in Hole U1404A. All three species have well-established first appearance datums in Zone RP20, which was not identified in Hole U1404A because of a barren interval (see below). Diatoms are generally rare in samples from Zones RP21 and RP22 but are abundant in Sample 342-U1404A-18H-CC (163.20 mbsf). Diatoms are rare to very rare in underlying Samples 342-U1404A-19H-CC to 36X-1, 67 cm (172.77–299.80 mbsf).

The interval from Sample 342-U1404A-20H-CC to 27H-CC (181.99–236.48 mbsf) contains the EOT but is barren of radiolarians. Rare radiolarians occur in Sample 342-U1404A-28H-CC, and below this level radiolarians are abundant and well preserved. Radiolarian assemblages from Samples 342-U1404A-29H-1, 52–53 cm, to 36X-1, 67 cm (244.63–299.80 mbsf), are assigned to middle Eocene radiolarian Zones RP16–RP14. Sample 342-U1404A-29H-1, 52–53 cm (244.63 mbsf), is assigned to Zone RP16 based on the presence of the zonal markers *Podocyrtis goetheana, Thyrsocyrtis bromia,* and *Thyrsocyrtis tetracantha*. Samples 342-U1404A-29H-CC to 32H-CC (253.05–270.64 mbsf) are correlated with Zone RP15 based on the faunal crossover from *Podocyrtis mitra* to *Podocyrtis chalara* in Sample 342-U1404A-32H-CC (270.64 mbsf). The tops of *Lophocyrtis biaurita* and *Phormocyrtis striata striata* occur within this zone. The lowermost sample examined (Sample 342-U1404A-36X-1, 67 cm; 299.80 mbsf) is correlated with Zone RP14 based on the presence of the zonal marker *P. mitra*.

Planktonic foraminifers

Core catchers and additional samples from working half sections were examined from Hole U1404A. Samples were, for the most part, barren of planktonic foraminifers except for intervals in the lower Miocene and Oligocene. Samples from the lower Miocene through Oligocene yielded rare to few planktonic foraminiferal specimens with moderate to very

good preservation. Planktonic foraminifers are of limited use in the development of biostratigraphy but provide some zonal assignments near the Oligocene/Miocene boundary. Depth positions and age estimates of identified biostratigraphic marker events are shown in Table T7. The stratigraphic distribution of planktonic foraminifers is shown in Table T8 and Figure F16. The sporadic occurrence of planktonic foraminifers at Site U1404 (4710 mbsl) is interpreted to be the result of calcite dissolution below or close to the CCD.

Sections 342-U1404A-8H-2 through 11H-2 (64.35–92.55 mbsf) contain reasonably diverse and well-preserved lower Miocene assemblages containing the marker species *Globoturborotalita angulisutularis, Globigerinoides altiapertura, Paragloborotalia kugleri,* and *Globoquadrina dehiscens,* indicating Zone M2–Subzone M1a. The base of *G. dehiscens* marks the Subzone M1a/M1b boundary (Sample 342-U1404A-10H-6, 115–117 cm; 89.36 mbsf). The top and base of *P. kugleri* occurs in Samples 342-U1404A-9H-3, 115–117 cm (75.36 mbsf), and 11H-2, 100–102 cm (92.54 mbsf), respectively.

Samples 342-U1404A-13H-CC to 21H-5, 129–130 cm (115.07–189.00 mbsf), contain sporadic, moderate to well-preserved planktonic foraminifers of late Oligocene age. However, differentiation of biozones in the upper Oligocene was hindered by the absence of key taxa.

Planktonic foraminifers are absent across the EOT and in the upper and middle Eocene from Samples 342-U1404A-21H-CC to 36H-CC (191.71–299.80 mbsf).

Benthic foraminifers

Benthic foraminifers were examined semiquantitatively in core catcher samples from Hole U1404A and from working section half samples of Cores 342-U1404A-1H to 16H. Additional working section half samples taken from Cores 342-U1404A-21H through 36X were examined for preservation and relative abundance of total benthic foraminifers and individual morphogroups. Benthic foraminifers at this site are rare (the "present" category) relative to total sediment particles >150 µm in the lower Miocene to Oligocene and abundant in the uppermost Eocene (the "dominant" category) (Fig. F16). The abundance of benthic foraminifers decreases from the upper Eocene to lower Eocene. Assemblages generally suggest a lower bathyal to abyssal paleodepth for this site (van Morkhoven et al., 1986). Preservation of foraminifer tests is generally moderate to good and very good in Cores 342-U1404A-7H through 16H (Figs. F16, F18). The occurrences of benthic foraminifers at this site are shown in Tables T9 and T10.

Samples 342-U1404A-1H-3, 73–75 cm, and 1H-CC predominantly contain agglutinated benthic foraminifers, such as *Bathysiphon* sp. and *Cyclammina* sp., most probably a result of dissolution below the CCD.

Benthic foraminifer occurrences are rare in Cores 342-U1404A-17H through 23H (153.72–204.53 mbsf). Cores 342-U1404A-8H through 13H (71.30–115.07 mbsf) yield slightly more diverse faunas, including *Bathysiphon* sp., *Dentalina* sp., *G. pacifica, Gyroidinoides* sp., and others. Among these species, *G. pacifica,* indicative of suboxic bottom water condition, is notably abundant (Fig. F18). Although carbonate content is very low, the preservation of *G. pacifica* and other constituents of the suboxic assemblage is very good. The occurrence of *G. pacifica* is accompanied by abundant centric diatoms and higher total organic carbon content, which implies high primary production rate at the sea surface. Enhanced organic matter transport to the seafloor may have contributed to the inferred bottom water suboxia.

The upper Eocene to lower Oligocene is characterized by alternation of barren samples and samples with abundant benthic foraminifers. Abundant benthic foraminifers occur in Samples 342-U1404A-23H-6, 51–53 cm, through 24H-1, 55–56 cm (202.92–204.86 mbsf); 24H-4, 55–56 cm, through 24H-CC (209.36–212.79 mbsf); and 26H-1, 50–51 cm, through 26H-2, 50–51 cm (221.01–222.51 mbsf), with barren intervals in between. Calcareous assemblages of these intervals are mainly characterized by *Anomalinoides* sp., *Cibicidoides* spp., *Dentalina* sp., *Nuttallides truempyi, Oridorsalis umbonatus,* and *Stilostomella lepidula* (Table T9). Fluctuations of benthic foraminifer abundances correspond to changes in carbonate content of the sediment and may indicate changes of the late Eocene to early Oligocene CCD.

Although lithostratigraphic Unit IV is predominantly barren of benthic foraminifers, Samples 342-U1404A-31H-CC (265.27 mbsf) and 32H-CC (270.64 mbsf) yield *Cibicidoides* spp. and *N. truempyi.*

Paleomagnetism

We completed a paleomagnetism study of APC and XCB cores from Holes U1404A–U1404C with the primary objective of establishing a magnetostratigraphy of the site to provide chronostratigraphic age control. The natural remanent magnetization (NRM) of each archive section half was measured at 2.5 cm intervals before and after demagnetization treatment in a peak alternating field (AF) of 20 mT. We processed the archive-half measurement data by removing measurements made within 7.5 cm of section

ends and from disturbed intervals described in the Laboratory Information Management System database. Cores 342-U1404A-1H through 23H and 342-U1404B-1H through 27H were azimuthally oriented using the FlexIT tool (Table T11); all other cores were not oriented.

We also took 198 discrete samples from working section halves to verify the archive-half measurement data and to measure the anisotropy of magnetic susceptibility (AMS) and bulk susceptibility of Site U1404 sediment. Discrete samples were collected and stored in 7 cm^3 plastic cubes and typically taken from the least disturbed region closest to the center of each section from Hole U1404A. One discrete sample was collected from Core 342-U1404B-24H. Most of the samples were first subjected to AMS measurements, including bulk susceptibility. Subsequently, NRMs before and after 20 mT AF demagnetization were measured. Twenty-six samples were selected for step-wise demagnetization at 10, 20, 30, 40, and 60 mT; demagnetization up to 80 mT was made in some cases. All discrete sample data are volume corrected to 7 cm^3.

Results

Downhole paleomagnetism data after 20 mT demagnetization are presented for Holes U1404A, U1404B, and U1404C in Figures F19, F20, and F21, respectively. Similar to paleomagnetism results from Site U1403 (see "Paleomagnetism" in the "Site U1403" chapter [Norris et al., 2014c]), archive-half measurement data from XCB cores are difficult to interpret because of biscuiting and substantial core disturbance. Therefore, for Site U1404 we chose to interpret only results obtained from APC cores. Also, cores from Hole U1404C span only a ~30 m interval in the upper 50 m of the recovered section and are not oriented; we do not discuss results from Hole U1404C any further.

We found the following main features in the paleomagnetism data at Site U1404:

- A long, persistent interval of low magnetic intensity and susceptibility from Cores 342-U1404A-3H through 21H (14.20–191.73 mbsf) and 342-U1404B-3H through 23H (12.48–198.6 mbsf);
- Inclination bias toward positive values; and
- ~180° alternations in declination direction in Cores 342-U1404A-22H through 32H and 342-U1404B-24H through 26H.

These magnetic characteristics are similar to those of sediments from Site U1403.

Low-intensity zones

Magnetic intensity lows are most frequently associated with green-gray sediment (see "Lithostratigraphy"). Magnetic susceptibility values are also very low within these same intervals (less than ~10^{-4} SI; Figs. F19, F20). These trends may indicate either a lower initial supply of paramagnetic and ferromagnetic minerals or diagenetic loss of these materials in these intervals. Many of these intervals are characterized by disseminated and layered pyrite, as well as glauconite (see "Lithostratigraphy"). Therefore, we favor the interpretation that the magnetic intensity lows are caused by reductive dissolution, which is common in oceanic sediment. Obtaining meaningful paleomagnetism signals from these horizons was often difficult.

Inclination bias

The inclination bias indicates that a substantial drilling overprint exists even with the use of nonmagnetic core barrels and cutting shoes and after 20 mT AF demagnetization. Similar to results from Site U1403, we observed only a few horizons which show –60° inclinations (expected for the ~40°N latitude of Site U1404) during reversed magnetozones. Because of this strong inclination biasing, we often cannot identify paleomagnetism polarity solely based on shipboard inclination data.

Declination trends

Oriented APC cores were recovered downhole to Core 342-U1404A-23H (204.37 mbsf) and for the entire recovered interval in Hole U1404B. We interpret intervals with declination values of ~0° (~180°) to indicate normal (reversed) magnetozones. A magnetozone with a primary normal polarity should not display inclinations less than ~40°, barring sedimentary inclination shallowing biases. Notably, intervals with ~180° declination almost always correspond to inclination values that are shallower than those in the intervals with declination of ~0° (e.g., ~205–210 mbsf; Fig. F20). Thus, the drilling overprint mainly obscured remanent inclination but not declination, similar to the paleomagnetism results from Site U1403.

Anomalous declination trends

Oriented paleomagnetism declinations from Core 342-U1404A-23H show a systematic offset from expected azimuths. Moreover, the magnitude of this offset increases downhole (Fig. F22A). These observations are best explained by "rifling," in which the

APC drilling assembly rotates as it is fired into the sediment. Rifling may explain the brittle shear features (P-bands and Reidel shears) observed near the unusually sharp lithostratigraphic contact at interval 342-U1404A-23H-4, 120–122 cm (Fig. F22B, F22C), and throughout Core 342-U1404A-23H. The amount of displacement, compaction, or both along this contact is unknown, but it is probably minor.

Comparison between pass-through and discrete sample data

AF demagnetization results for the discrete samples are summarized in Table T12. Of the 26 samples treated with peak AF demagnetization fields of 60 or 80 mT, 17 reveal relatively stable components of magnetization (e.g., Fig. F23A). These samples have remanent magnetizations that are high enough to be measured by the onboard JR-6A spinner superconducting rock magnetometer. The remaining samples usually displayed NRM intensities that decreased by an order of magnitude following AF demagnetization in 10 or 20 mT fields, with components above this treatment level characterized by poor direction stability (e.g., Fig. F23B). This behavior indicates that the combination of drilling overprint and low magnetic intensity described above has obscured the primary magnetic signal in these stratigraphic intervals. Nevertheless, these results are useful for verifying the 20 mT pass-through paleomagnetism data from the archive section halves. Magnetization intensity and declination are generally consistent between the discrete samples and the archive-half samples (Figs. F19, F20).

We note that inclinations measured in discrete samples are often more shallow than their counterpart values in the archive-half samples. Discrete samples were collected from the central part of the cores, which is generally least affected by mechanical and magnetic drilling overprint (Acton et al., 2002). Therefore, discrete samples are often considered to preserve the least-biased primary remanences. Moreover, discrete samples are not affected by signal smoothing, which is an inherent feature of pass-through measurements (Roberts, 2006; Xuan and Channell, 2009).

An exception to this trend is observed in the interval between 30.0 and 62.5 cm in Section 342-U1404B-24H-4 (~207.0–207.4 mbsf). In this interval, archive-half measurement data yielded ~90° inclination and ~0° declination even after 20 mT AF demagnetization, resulting in an apparent normal polarity magnetozone (Fig. F24). We collected a discrete sample from this interval to test the superconducting rock magnetometer results. AF demagnetization of the sample shows that the drilling overprint could not be removed even with a peak demagnetization field of 80 mT (Fig. F23C). The lower one-third of this interval has a reddish hue (Fig. F24), suggesting that it contains oxidized iron, such as hematite. We conclude that this interval contains high-coercivity iron oxides, which can easily acquire a remanence overprint but resist AF demagnetization treatments. Shore-based coercivity experiments can easily verify this interpretation. Because we interpret this interval as a drilling overprint, we exclude it from further analysis.

In summary, paleomagnetism data from archive section halves and discrete samples from oriented core intervals generally agree well and reveal a semicontinuous series of magnetozones from Sections 342-U1404A-23H-4 to 32H-3 (200.67–268.49 mbsf) and 342-U1404B-24H-1 to 26H-3 (203.07–218.49 mbsf). Downhole plots indicate that a discontinuous series of magnetozones is probably recorded higher in the recovered section in both Holes U1404A and U1404B, but shore-based studies are necessary to identify and fully characterize magnetozones in this low–magnetic intensity interval.

Magnetostratigraphy

Identification of magnetozones and correlation to the geomagnetic polarity timescale (GPTS) was straightforward for azimuthally oriented APC intervals in lithostratigraphic Units III and IV in Hole U1404B. Unoriented APC cores in Hole U1404A also yielded a distinct magnetostratigraphy. Our general strategy was to identify magnetozones first by using systematic changes in inclination, but more frequently by using declination reversals from oriented cores. Intervals with downward and northerly (~0°) magnetizations are assigned normal polarity, whereas intervals with low-to-upward and southerly (~180°) declinations indicate reversed polarity. This approach yields several normal and reversed magnetozones throughout Holes U1404A and U1404B (Fig. F25). In Hole U1404A, we identified magnetozones in Sections 342-U1404A-23H-4 through 32H-3 (~200.67–268.49 mbsf). In Hole U1404B, we identified magnetozones from Section 342-U1404B-24H-1 through 26H-4 (~203–220 mbsf).

By utilizing radiolarian and nannofossil biostratigraphic datums from Holes U1404A and U1404B (see "Biostratigraphy"), we can correlate these series of magnetozones to a nearly continuous earliest early Oligocene to late Eocene magnetostratigraphy. Correlation of magnetozones between Holes U1404A and U1404B is corroborated by lithostratigraphic horizons and physical property features (see "Strati-

graphic correlation"). Our correlation is presented in Table T13 and shown in Figures F19, F20, and F25.

In Hole U1404A, we identified the Chron C12r/C13n boundary (33.157 Ma) at ~200.67 mbsf. This correlation is based on the identification of nannofossil Zone NP21 at ~200.06 mbsf. The Chron C13r/C15n boundary (34.999 Ma) is located at ~206.42 mbsf in Section 342-U1404A-24H-2. This correlation, which is based on nannofossil Zone NP19/NP20, indicates that the Chron C13n–C13r transition is missing in the core gap between Cores 342-U1404A-23H and 24H, a gap that is consistent with stratigraphic correlation. The Chron C16n.1r/C16n.2n, C16n.2n/C16r, and C16r/C17n.1n boundaries are recorded in Core 342-U1404A-25H. This correlation is based on the identification of nannofossil Zone NP19/NP20 in the bottom of this core and requires a substantial core gap between Cores 342-U1404A-24H and 25H to explain the absence of the Chron C15n/C15r boundary in either of these cores. We identified the Chron C17n.1r/C17n.2n boundary at ~222.22 mbsf in Core 342-U1404A-26H based on nannofossil Zone NP19/NP20 and NP18 datums in the reversed polarity magnetozone at the top of this core. A distinctive blue lithostratigraphic horizon characterized by a large decrease in magnetic intensity and a possible normal polarity excursion occurs ~40 cm above this magnetozone boundary, serving as a strong tie point between Holes U1404A and U1404B.

We assigned the long normal magnetozone in Core 342-U1404A-27H and the top of Core 28H to Chron C18n.1n. This correlation requires that Chrons C17n.2r, C17n.3n, and C17r, representing ~0.522 Ma, are in the core gap between Cores 342-U1404A-26H and 27H. Two short reversed polarity intervals observed in the declination record in Core 342-U1404A-27H may correspond to cryptochrons, such as Chron C18n.1n-1. We refrain from correlating these declination anomalies to the GPTS until we can confirm the robustness of the paleomagnetic signal. These potential magnetozones are currently based on only 1 or 2 data points from pass-through shipboard measurements.

We correlate the normal-reversed-normal polarity signal in Core 342-U1404A-28H to the base of Chron C18n.1n, C18n.1r, and the top of C18n.2n. The boundary between Chrons C18n.2n and C18r occurs at ~248.89 mbsf in Core 342-U1404A-29H. The long, reversed magnetozone in Cores 342-U1404A-30H and 31H and the top of Core 32H is correlated to Chron C18r, which is consistent with Zone NP16 nannofossils found in Core 31H. The reversed-normal-reversed magnetostratigraphy observed in Core 342-U1404A-32H is correlated to the Chron C18r/C19n and C19n/C19r boundaries. We refrained from correlating magnetozones observed in XCB cores below Core 32H, but note that the pattern is consistent with Chrons C19r and C20n.

In Hole U1404B, we correlated our magnetostratigraphy to a nearly continuous series of earliest Oligocene to latest late Eocene chrons. We identified the Chron C12r/C13n and C13n/C13r boundaries in Core 342-U1404B-24H. Nannofossil Zones NP21 and NP19/NP20 indicate that the series of well-resolved magnetozones in Core 342-U1404B-25H are the bottom of Chrons C13r, C15n, C15r, C16n.1n, C16n.1r, and most of C16n.2n. The Chron C16n.1r/C16n.2n boundary (36.051 Ma) at ~212.96 mbsf in Section 342-U1404B-25H-3 provides a tie point to Core 342-U1404A-25H-1. We correlate the normal-reversed-normal magnetozonation observed in Hole U1404B to Chrons C17n.1n, C17n.1r, and C17n.2n, providing tie points to Core 342-U1404A-26H. Our correlations imply that Chron C16r is missing in the core gap between Cores 342-U1404B-25H and 26H.

Although distinct magnetozones are evident above these described intervals in lithostratigraphic Subunit IIb, we cannot correlate them to the GPTS at this time. The series is intermittent because of the low magnetization intensity of this reduced sediment and the sensitivity of shipboard magnetometers. In many intervals in Subunit IIb, a strong drilling-induced overprint has also obscured the primary magnetostratigraphy.

The magnetostratigraphic age model for Site U1404 allows for precise dating of carbonate accumulation events in lithostratigraphic Units III and IV (see "Lithostratigraphy") and precise identification of the Eocene/Oligocene boundary. The Eocene/Oligocene boundary (33.89 Ma) occurs just prior to the Chron C13n/C13r boundary (33.705 Ma). We identified this chron boundary at interval 342-U1404B-24H-3, 110–120 cm (206.30–206.40 mbsf) (Fig. F24). Site U1404 magnetostratigraphy verifies the low accumulation rates (<1 m/m.y.) across the Eocene/Oligocene boundary and the high accumulation rates (>13 m/m.y.) in the middle Eocene implied by the radiolarian and nannofossil biostratigraphy (Fig. F20). These results indicate that high sedimentation at Site U1404 persisted through the late middle Eocene, whereas downslope at Site U1403, clay accumulation waned in the early middle Eocene.

The distinctive gray-blue interval observed at Site U1403 in intervals 342-U1403A-6H-2, 80–120 cm, and 342-U1403B-6H-5, 50–90 cm, is found in intervals 342-U1404A-26H-1, 85–115 cm, and 342-U1404B-26H-3H, 110–150 cm, at Site U1404. Site U1404 magnetostratigraphy indicates that this interval was deposited during Chron C17n.1r (37.753–

37.872 Ma). This correlation suggests that we have misinterpreted a dissolution/overprint horizon in Holes U1403A and U1403B as magnetozones and that our Site U1403 magnetostratigraphy may need revision. Thus, this distinctive blue horizon probably is not the Chesapeake Bay Impact event during Chron C16n.1n (35.706–35.892 Ma) as previously considered and may instead be another, earlier impact event (Coccioni et al., 2009) or volcanic ash. Detailed shore-based geochemical and rock magnetic experiments should help clarify the origin of this distinctive stratigraphic horizon. We note, however, that Chron C16n.1n is represented in the Hole U1404B magnetostratigraphy in interval 342-U1404B-25H-3, 30.0–92.5 cm. This stratigraphic interval is characterized by a narrow horizon with the highest magnetic susceptibility values observed in all recovered sediment at Site U1404, in what is otherwise homogeneous reddish brown clay-rich nannofossil ooze (see **"Physical properties"**).

Magnetic susceptibility and anisotropy of magnetic susceptibility

Bulk magnetic susceptibility measured on 197 discrete samples is summarized in Table **T14.** Downhole variation in raw whole-round magnetic susceptibility (WRMS) and discrete sample magnetic susceptibility (DSMS) for Hole U1404A are shown in Figure **F19.** We multiplied the WRMS data, which are in instrument units, by a factor of 0.577×10^{-5} to convert to approximate SI volume susceptibilities (see **"Paleomagnetism"** in the "Methods" chapter [Norris et al., 2014b]). WRMS and DSMS data agree very well after this conversion, and we attribute small absolute differences to the fact that the conversion factor applied to the WRMS data is not constant downhole because of changes in core diameter and density; only discrete samples provide calibrated susceptibility values in SI units. Noise in the WRMS data is easily attributed to section edge-effects, core disturbance, or shear-pin fall-in, none of which have been trimmed from the raw WRMS data presented in Figure **F19.** Nevertheless, both magnetic susceptibility data sets show the same first- and second-order cyclic trends, as well as prominent steps, indicating that these trends are robust features of Site U1404 sediment.

AMS results for the discrete samples are also summarized in Table **T14** and shown in Figure **F26.** The eigenvalues associated with the maximum (τ_1), intermediate (τ_2), and minimum (τ_3) magnetic susceptibilities at Site U1404 show prominent downhole trends. Divergence between τ_1 and τ_3 increases from the top of Hole U1404A to the base of lithostratigraphic Subunit IIa (0–22.38 mbsf) (see **"Lithostratigraphy"**), indicating magnetic anisotropy increases with depth. This divergence increases substantially at the top of Subunit IIb (33.20 mbsf) and then gradually decreases to isotropic values with depth. τ_1 and τ_3 gradually diverge from the top of Unit III (200.60 mbsf) to the base of Unit IV (299.82 mbsf), with a noticeable increase in divergence beginning at 271.00 mbsf with the start of XCB core recovery. These eigenvalue trends have a close inverse correlation with bulk density and positive correlation with porosity (see **"Physical properties"**), counterintuitively suggesting that high magnetic anisotropy is related to low density (i.e., low compaction) and high interstitial water content in clay-rich Subunit IIa.

The inclination of the minimum eigenvector (V_3) is more variable in APC cores than it is in XCB cores, which is similar to AMS results from Site U1403. Moreover, V_3 shows the greatest variability in lithostratigraphic Subunit IIb. In contradistinction to results from Site U1403, the degree of anisotropy (P; τ_1/τ_3) is much higher in APC cores than in XCB cores, with a prominent peak in the upper part of Subunit IIb.

Collectively, AMS results suggest that magnetic anisotropy is largely controlled by lithology rather than coring method in APC-recovered intervals. Although subhorizontal oblate fabrics are evident in intervals recovered by XCB coring, they are most pronounced in the least lithified part of Subunit IIb.

Age-depth model and mass accumulation rates

Coring at Site U1404 recovered a 300 m thick sequence of Pleistocene to middle Eocene clay, with subordinate nannofossil ooze mainly in the Eocene/Oligocene boundary interval. Biostratigraphic and magnetostratigraphic datums from Hole U1404A (Table **T15**) were compiled to construct an age-depth model for this site (Fig. **F15**). A selected set of datums (Table **T16**) was used to calculate linear sedimentation rates (LSRs). Total mass accumulation rate (MAR), carbonate MAR (CAR), and noncarbonate MAR (nCAR) were calculated at 0.2 m.y. intervals using a preliminary shipboard splice rather than the sampling splice described in this volume (Table **T17;** Fig. **F27**).

Age-depth model

The main objective at Site U1404 was to recover an expanded record of upper Paleogene sediment. The expanded record recovered was somewhat younger than anticipated, comprising a 150 m thick sediment

section through the lower Miocene and upper Oligocene bounded by upper and lower condensed intervals of Pliocene–Miocene and lower Oligocene–upper Eocene sediment. The lowermost 200 m of the site is a relatively expanded middle Eocene succession.

The age-depth model is tied to Pliocene–middle Miocene nannofossil datums in the upper 60 mbsf. Through the lower Miocene and upper Oligocene, nannofossils are the primary datums, but planktonic foraminifers provide tie points at critical levels. Paleomagnetic datums are the primary age control in the lower Oligocene and Eocene and are well constrained by nannofossils and radiolarians.

Linear sedimentation and mass accumulation rates

Middle Eocene LSRs are 1.5 cm/k.y., dropping to 0.2–0.3 cm/k.y. from the upper middle Eocene to upper Oligocene. LSRs increase again in the upper Oligocene (1.5 cm/k.y.) and peak at 8 cm/k.y. in the lowermost Miocene, gradually decreasing to 0.3 cm/k.y. through the lower Miocene to lower Pliocene.

Carbonate contents at Site U1404 are <10 wt% in the middle Eocene; thus, most of the MAR is driven by nCAR (Fig. **F27**). However, the pulsed pattern of carbonate sedimentation significantly alters the square wave pattern of MAR imparted by the LSR. In the middle Eocene, an antithetical relationship is apparent between CAR and nCAR. A general increase in MAR is primarily due to three pulses in nCAR, whereas MAR minima correspond to three pulses in CAR.

In the upper Eocene and lower Oligocene, MAR is 0.2–0.3 g/cm^2/k.y. Pulses of higher carbonate content continue through the lowermost Oligocene and account for as much as 50% of MAR (Table **T17**). Above the lowermost Oligocene, noncarbonate components dominate mass accumulation, which peaks during the upper Oligocene (1.3 g/cm^2/k.y.) and lowermost Miocene (4.5 g/cm^2/k.y.).

Geochemistry

The geochemistry program during operations at Site U1404 included

- Hydrocarbon analysis on headspace gas samples,
- Analysis of interstitial water constituents (i.e., major and minor elements in whole-round and Rhizon samples), and
- Elemental geochemistry of carbon and nitrogen on solid sediment samples.

Headspace gas samples

As part of the routine environmental protection and safety monitoring program, evolved gases from 35 headspace gas samples were analyzed at a frequency of one sample per core in Hole U1404A (Table **T18**), usually from the bottom half of each core (i.e., Sections 4, 5, or 6). Methane concentrations are 1.75–28.8 ppmv. In the upper 212 mbsf, methane concentration reaches a maximum of 4.24 ppmv. Below 212 mbsf (Core 342-U1404A-25H), methane and ethane concentrations increase to ~28.8 and ~1.79 ppmv, respectively.

Interstitial water geochemistry

Interstitial water samples were typically taken at a frequency of one per core (Tables **T19, T20**) immediately after sectioning on the catwalk, although some cores were too disturbed or recovery was too low to allow a whole-round sample to be taken for analysis. Manual titrations of alkalinity, pH, and chlorinity were routinely performed on all samples from Hole U1404A. Ion chromatography analysis of interstitial water splits included Ca^{2+}, Cl^-, Mg^{2+}, K^+, Na^+, and SO_4^{2-} measurements using standard calibration and drift correction techniques. Routine inductively coupled plasma–atomic emission spectroscopy sample measurements included Fe, Mn, and Sr (Fig. **F28**).

Alkalinity and pH measurements show gradual increasing and decreasing trends, respectively, in the upper 230 mbsf of Hole U1404A, perhaps reflecting the decomposition of organic matter by the Mn oxide reduction pathway. Salinity, chloride, and sodium show little downhole change until 230 mbsf. pH and alkalinity, along with salinity, chloride, and sodium, all show marked inflections around 230 mbsf, corresponding to the ooze–claystone transition near the lithostratigraphic Unit III/IV boundary (see **"Lithostratigraphy"**) and may reflect carbonate recrystallization. The lowermost 75 m of Hole U1404A is very biscuited and fractured; thus, the interstitial fluid profiles below ~225 mbsf were possibly also influenced by drilling.

Sulfate concentrations show a modest and steady decline with increasing depth through Hole U1404A, whereas manganese concentrations rapidly and steadily increase downhole. Iron concentrations are low and variable. These profiles suggest sedimentary diagenesis driven by organic matter degradation. For example, the typical sequence of electron acceptor use is manganese, followed by iron, then sulfate. The modest downhole decrease in interstitial sulfate together with the low iron and high manganese argues for a sedimentary redox sequence that does not progress beyond manganese oxidation. Interstitial

fluid geochemistry is not driven to sulfate reduction because of low organic carbon contents (cf. Emerson and Hedges, 2003.) An unsampled deep zone of reduction leading to sulfate depletion possibly has resulted in downward diffusion of sulfate (e.g., Berner, 1980).

Calcium concentrations steadily increase with depth in Hole U1404A, whereas magnesium concentrations decline rapidly in the upper 100 m and then taper to a steady decline to the bottom of Hole U1404A. Strontium concentrations show a near-uniform profile downhole to the lithostratigraphic Unit III/IV boundary (230 mbsf) and then increase below the ooze–claystone transition). Anomalously low strontium concentrations occur between 50 and 70 mbsf. Whether these anomalies are related to variations in the interstitial fluid profiles or to issues occurring during the analysis of these samples is not known. Overall, however, the increase in strontium concentrations is similar to that seen at Site U1403, although the profile at Site U1404 is more linear. A concomitant change in Sr/Ca ratio does not occur below the Unit III/IV boundary, suggesting that carbonate recrystallization (cf. Baker et al., 1982) has a negligible effect on interstitial water calcium concentrations. It is more likely that either dolomite deposition, exchange reactions with the basaltic basement rocks (Gieskes and Lawrence, 1981), or secular variability in the calcium concentrations of seawater (Stanley and Hardie, 1998; Hardie, 1996) are responsible for the downhole increase in calcium concentrations and declining Sr/Ca ratio. Interstitial fluids show decreasing Mg/Ca ratios with depth, consistent with basaltic basement exchange, yet this change is largely driven by increased calcium concentrations rather than decreased magnesium concentrations. This argues for carbonate recrystallization as the dominant driver of interstitial fluid profiles. Potassium concentrations decrease from maximum values of 16 mM in Subunit IIb to minimum values of 6 mM at the bottom of Hole U1404A. Although there are some prominent inflections (e.g., 100 and 140 mbsf), these changes do not strictly correspond to lithostratigraphic unit boundaries) and may reflect continual sorption onto clay minerals (Arthur, 1979).

Collectively, the interstitial fluid chemical profiles may reflect a combination of secular variations in seawater chemistry as well as postdepositional modifications. The modifications include those associated with organic matter degradation, sorption/desorption of chemical components on the surfaces of clay minerals, and chemical exchange with minerals undergoing diagenetic reactions.

Testing for the presence of gas hydrates

Hole U1404C was drilled and sampled to test for the presence of gas hydrates, the occurrence of which was suggested by several peculiarities in Cores 342-U1404B-4H and 5H (e.g., the presence of effervescent sediment, expelled section caps indicating high pressure, bulging core liners, a drop in bulk density, and the presence of pyrite). After scanning the core on the catwalk with a thermal imaging device, headspace gas samples and 5 cm whole rounds for interstitial water samples were taken at a sampling interval of one per section (Table **T20**). After logging Cores 342-U1404C-2H through 4H on the Special Task Multisensor Logger (STMSL), Rhizon samples were taken at an interval of 50 cm through Hole U1404C. Methane concentrations (1.82–2.99 ppmv) were not above atmospheric levels, and no other hydrocarbon traces were detected.

In Hole U1404C, 28 interstitial water samples were taken from 5 cm whole rounds in Cores 342-U1404C-2H through 4H at a sampling frequency of one sample per section to test for the existence of methane hydrates. In addition to squeezing whole-round samples for interstitial water analysis, 54 Rhizon samples were taken at a resolution of 50 cm in Cores 342-U1404C-2H through 4H. Manual titrations for pH, alkalinity, and chlorinity were performed on Hole U1404C interstitial water whole-round samples (Fig. **F29**). Uniform profiles, particularly of chlorinity, show that pore fluid geochemistry was not influenced by a shallow deposit of methane hydrate. Based on the headspace analysis of gas compounds (see **"Headspace gas samples"**) and interstitial fluid data from whole-round samples, a decision was made to archive the high-resolution Rhizon samples from Hole U1404C without analyzing their chemical components onboard.

Sediment geochemistry

Sediment plugs (5 cm^3) for downhole analysis of sediment elemental geochemistry were taken from Cores 342-U1404A-1H through 36X at an average resolution of one sample per section adjacent to the moisture and density sample (Table **T21**). Carbonate contents are generally low (<5 wt%) in the upper 200 mbsf, with prominent increases to ~10 wt% around 60, 75, 95, and 170 mbsf (Fig. **F30**). High-resolution sampling (20–40 cm spacing) was carried out on targeted intervals in Cores 342-U1404A-23H through 36X in order to resolve carbonate fluctuations in lithologically distinct portions of Holes U1404A and U1404B. Between 200 and 300 mbsf in Hole U1404A, carbonate contents oscillate between 0 and

57 wt% in multiple pulses of three high $CaCO_3$ values at 200–206, 208–213, and 239–245 mbsf. These carbonate peak values range from 17 to 57 wt%, with a few less pronounced events with peaks of as much as 14 wt% at 213–226 mbsf. The maximum carbonate value is 57 wt% at 202.75 mbsf, within the Eocene/Oligocene boundary transition (Fig. F31), and 265–279 mbsf, with two less distinct events between 213 and 226 mbsf.

The deepest carbonate pulse seen in Hole U1404A is centered on Chron 19n in the magnetostratigraphy of Hole U1404A (Fig. F32; see "Paleomagnetism"). The stratigraphic position of this pulse of high carbonate content is consistent with the timing of carbonate accumulation Event 3 identified by Pälike et al. (2012) in equatorial Pacific sediment (Lyle et al., 2002). Based on this interpretation, the low-carbonate interval immediately above Chron C19n likely corresponds to the MECO (e.g., Bohaty et al., 2009), marked by high temperatures and deep-sea carbonate dissolution. The interpretation of the low–carbonate content interval between 244 and 260 mbsf as corresponding to the MECO is supported by identification of the calcareous nannofossil *D. bisectus* (first abundant disappearance at 40.36 Ma) in Section 342-U1404A-28H-CC, the uppermost extent of an interval barren of calcareous nannofossils (see "Biostratigraphy").

Total organic carbon (TOC) values in Hole U1404A increase from 0.1 to 0.4 wt% at the lithostratigraphic Subunit IIa/IIb boundary (see "Lithostratigraphy") (Table T21). TOC remains at 0.4 wt% until ~150 mbsf, where TOC begins to decline, reaching 0.15 wt% at 200 mbsf. These TOC values persist until the bottom of Hole U1404A. High TOC values in Subunit IIb correspond to the interval of green and greenish gray carbonate-poor Oligocene to Miocene clay characterized by a low magnetic signature.

Physical properties

We measured physical properties on whole-round sections, section halves, and discrete samples from section halves. Gamma ray attenuation (GRA) bulk density, magnetic susceptibility, *P*-wave velocity, and natural gamma radiation (NGR) measurements were made on the whole-round sections using the Whole-Round Multisensor Logger (WRMSL) and NGR Logger. Thermal conductivity measurements could not be performed at Site U1404 because of technical problems. Compressional wave velocity was also measured on section halves at a frequency of two in each section (at ~50 and 100 cm) using the *P*-wave caliper (PWC). For moisture and density (MAD) analyses, one discrete sample was collected in each section (typically at ~35 cm from the top of a section). The Section Half Multisensor Logger was used to measure spectral reflectance and magnetic susceptibility on archive section halves.

Magnetic susceptibility

Magnetic susceptibility averages 80 IU in lithostratigraphic Unit I, which is essentially composed of clay (Fig. F33; see "Lithostratigraphy"). From the top of Unit II (~2 mbsf) to ~45 mbsf, magnetic susceptibility decreases from ~90 to 2 IU with a major step downhole at ~12 mbsf in the transition from clay- to silty clay–rich sediment. Below this level, Unit II is characterized by very low magnetic susceptibility values (<30 IU) and a small increase downhole. The top of Unit III (~200 mbsf) is marked by an increase in magnetic susceptibility to 65 IU, which correlates with the increase in carbonate content (see "Geochemistry"). This increase is followed by a decrease to ~10 IU at ~206 mbsf (bottom of Core 342-U1404A-23H and top of Core 342-U1404B-24H). This decrease probably reflects the downhole transition from nannofossil ooze to nannofossil biosiliceous ooze with clay (see "Lithostratigraphy"). Magnetic susceptibility is more variable (6–60 IU) in Units III and IV but shows an overall downhole decrease to the bottom of both holes.

Density and porosity

Two methods were used to evaluate bulk density at Site U1404. The GRA method provided a bulk density estimate from whole-round sections. The MAD method applied to 199 discrete samples from Site U1404 provided a second, independent measure of bulk density as well as dry density, grain density, water content, and porosity. Changes in bulk density of discrete samples are consistent with those in GRA bulk density (Fig. F33), although GRA bulk density values are slightly higher than the MAD bulk densities, which is speculated to be a GRA calibration issue. From the top of Hole U1404B to ~25 mbsf, bulk density decreases from 1.7 to 1.2 g/cm^3. We infer the same trend in Hole U1404A across the recovery gap between 20 and 30 mbsf. Below, bulk density values increase downhole to 1.8 g/cm^3 at the bottom of lithostratigraphic Unit II at ~200 mbsf. In Hole U1404A at ~110 and ~190 mbsf, bulk density from MAD analyses on discrete samples does not follow GRA density values, which exhibit two small peaks. In Unit III and in the upper part of Unit IV, bulk density averages 1.75 g/cm^3, with a small drop to 1.65 g/cm^3 between 242 and 254 mbsf associated with a radiolarian clay layer (see "Lithostratigra-

phy"). Bulk density decreases at ~272 mbsf at the top of Core 342-U1404A-33X at the same depth that the coring method changed from APC to XCB.

Water content and porosity in Holes U1404A and U1404B gradually increase from 0 to 21.6 mbsf and then decrease downhole to minima at ~200 mbsf, with steep gradients in these parameters between 170 and 200 mbsf (Fig. F33). From 200 to 300 mbsf, these physical properties maintain near-constant values (40 wt% water content and 60 vol% porosity), except for two minor peaks below at ~250 and ~275 mbsf.

Grain density varies between 2.6 and 2.8 g/cm^3 throughout Hole U1404A. At the top of Unit II (6.21–8.80 mbsf) and in Unit III (213.25–227.90 mbsf), some values are <2.5 g/cm^3.

P-wave velocity

Compressional wave velocity from whole-round sections and section halves follow similar trends in the three holes and are consistent with one another (Fig. F34). However, PWC values are slightly lower than those obtained by the *P*-wave logger in the APC-cored interval. Overall, *P*-wave velocity increases downhole from top to bottom in Holes U1404A and U1404B. Between the top of the hole and 200 mbsf, the increase is gradual (from 1500 to 1600 m/s). At ~196 mbsf, near the top of Unit III, velocity increases with a notable step from 1560 to 1640 m/s. In Unit IV in Hole U1404A, *P*-wave velocity gradually increases and reaches 1670 m/s at 260 mbsf.

Natural gamma radiation

NGR shows large variations between 10 and 50 cps over the uppermost 50 mbsf (upper part of lithostratigraphic Unit II) (Fig. F34; see also "Lithostratigraphy"). For the remainder of Unit II, from 50 to ~200 mbsf, NGR increases gradually from low values of 15 cps and reaches 60 cps by 200 mbsf. Between 200 and 275 mbsf in Unit III and upper Unit IV, NGR values are ~40 cps with large fluctuations between 18 and 60 cps. Minima of ~20 cps are found at 205 mbsf in Holes U1404A and U1404B and correspond to low magnetic susceptibility values. Below 235 mbsf, values decrease to ~30 cps and fluctuate between 35 and 45 cps.

Color reflectance

Color reflectance a* and b* parameters follow similar trends to one another and reflect changes in lithology (Fig. F35). In lithostratigraphic Unit I and the upper part of Unit III, both a* and b* have high values (a* = 0–6, and b* = 5–15). a* and b* values drop abruptly at 12 mbsf and are nearly constant within Unit II between 12 and 200 mbsf. In Unit III, a* and b* increase sharply and then decrease downhole, with the maximum at 208 mbsf in Hole U1404A and at 206 mbsf in Hole U1404B. a* and b* maintain consistent values in Unit IV (a* = –3–0, and b* = 0–5). Lower a* and b* values in Units II and IV reflect green clay. The higher a* and b* values recorded in Units I and IV correspond to yellow, brown, and gray sediment (see "Lithostratigraphy"). Changes in color reflectance are consistent with changes observed in magnetic susceptibility and NGR (Fig. F34) and reflect the major lithologic characteristics of the sequence drilled at Site U1404.

L* corresponds to sediment brightness and follows pronounced lithologic changes (Fig. F35). High values for L* are seen in Unit I and the upper 10 m of Unit II. L* values drop to ~40 at ~12 mbsf in Hole U1404A and maintain this value to ~200 mbsf. At ~206 mbsf in Holes U1404A and U1404B (Unit III), L* reaches a maximum of 65.

All three color parameters show the largest variations in carbonate-bearing intervals of Units III and IV.

Stratigraphic correlation

Sampling splice

Achieving an accurate splice using shipboard data at Site U1404 was challenging because of weak signals in the physical property data throughout the upper ~200 m of the sediment column. In order to verify the splice across the EOT, we conducted postcruise X-ray fluorescence (XRF) core scanning of the archive halves of sections from ~162 to ~313 m core composite depth below seafloor (CCSF) using the Avaatech XRF core scanner at Texas A&M University (USA). The sampling splice is based primarily on Fe/Ca ratio. Our correlation yields a growth rate of 3%–4% (Fig. F36), which represents the average increase of the CCSF depth scale relative to each hole's mbsf depth scale. The affine table (Table T22) summarizes the individual offsets for each core drilled.

Correlation during drilling operations

We attempted real-time correlation between Holes U1404A, U1404B, and U1404C using magnetic susceptibility and GRA bulk density data collected at 2.5 cm resolution on the STMSL before allowing cores to equilibrate to room temperature; however, the quickly generated records were inadequate for guiding drilling operations because the magnetic susceptibility signal rarely exceeded the noise level. GRA bulk density data were difficult to interpret on a core-by-core basis for the majority of the drilled strata, perhaps as a result of core deformation during

the drilling process. Another possible explanation for the between-hole discrepancy in GRA density data is lateral variation in the drift deposits. Despite the difficulty in correlating features between individual cores, overall GRA density increases with depth. In combination with the top-core depths reported on the drill floor, this trend provided a rough estimate of the depth relationships between the three holes while drilling. Hole U1404A spans the thickest sediment column recovered at this site, with a maximum depth for the bottom of Core 342-U1404A-36X of 299.82 mbsf. Hole U1404B extended only to 228.75 mbsf because of difficulty with APC drilling. Hole U1404C was drilled to target a shallow low-density zone thought to indicate the presence of gas hydrates and ended after three cores at 45.01 mbsf.

Tides were insignificant (<0.8 m) while drilling and the sea state was calm, ensuring comparatively low ship heave, but strong bottom currents may have added a bend to the drill string. Drilling recovered mudlines in Holes U1404A and U1404B, but the physical properties of Cores 342-U1404A-1H and 342-U1404B-1H revealed no identifiable tie point. As a result, we were unable to determine the relative offset between Holes U1404A and U1404B based on the mudline cores. The first clear correlation occurred between Cores 342-U1404A-2H and 342-U1404B-2H, indicated by an abrupt drop in magnetic susceptibility. These data demonstrated that coring gaps were roughly aligned, so we directed drilling operations to pull-up prior to shooting Core 342-U1404B-4H. This was the only adjustment to drilling operations made for the next ~150 mbsf in Hole U1404B.

The overall downhole increase in GRA bulk density allowed us to estimate the offset between cores leading up to the EOT, thought to occur between Cores 342-U1404A-23H and 24H. To bridge this critical gap, we directed drilling operations to pull-up prior to shooting Core 342-U1404B-18H. On both occasions that we pulled up to shoot a short core (342-U1404B-4H and 18H), recovery exceeded the coring advance significantly (by 2.41 m and 3.04 m, respectively). The upper portions of these cores are highly disturbed. We interpreted the extra recovery as indicative of either fall-in at the top of the core and/or doubling of the recovered sediment, which can occur when piston coring soft sediments. We discarded data collected on all clearly disturbed intervals (Table **T22**).

Correlation and splice construction

For stratigraphic correlation and splice construction, we used physical property data (primarily color reflectance b*) from 0 to ~162 m CCSF (Fig. **F37**) and XRF core scanner Fe/Ca ratio measurements from ~162 to 313 m CCSF (Fig. **F38**). XRF Fe/Ca ratio data shows significantly clearer features than shipboard physical properties, which are generally ambiguous (see **"Physical properties"**). WRMSL magnetic susceptibly shows no significant signal (<20 IU) or variability from ~20 to 200 m CCSF. The WRMSL GRA bulk density estimates show informative overall trends, but features of individual cores are difficult to correlate. We infer that drilling disturbance and deformation had a strong overprint on the GRA density signal, especially at the tops and bottoms of cores. Many individual cores show a GRA density record with an inverted U shape, which is due to differential compression and stretching rather than sedimentary features. Paleomagnetic and biostratigraphic results (see **"Paleomagnetism"** and **"Biostratigraphy"**) aided the stratigraphic interpretation of the EOT interval between ~200 m and 230 m CCSF.

We defined Core 342-U1404A-1H as the anchor in our splice. We interpret the clear difference between mudline cores as evidence of local erosion/deposition of sediment over short distances on the seafloor as a result of strong bottom currents (see **"Lithostratigraphy"**). A number of appended cores exist in the upper ~30 m CCSF of the splice, and we regard all the offsets applied to cores in the upper ~162 m CCSF of the stratigraphic column as tentative because they are based on ambiguous shipboard physical properties.

We included one of the cores drilled in Hole U1404C in the splice, though we added a large (15.5 m) offset to Core 342-U1404C-2H from the nominal mbsf top depth. We are confident that this offset is justified because Core 342-U1404C-2H has the low GRA density, low magnetic susceptibility, and low NGR characteristics of Core 342-U1404B-4H and below. In addition, the clear uncertainty in the seafloor depth demonstrated by the operational difficulty in achieving mudline cores for Holes U1404A and U1404B means that the assignment of the seafloor depth for Hole U1404C was likely inaccurate, especially because we did not recover a mudline core.

Below the prominent change in physical properties between Cores 342-U1404A-2H and 3H and between Cores 342-U1404B-2H and 3H, most shipboard physical properties show weak signals between ~18 and 160 m CCSF. Moreover, some apparently prominent features occur in only one hole. For instance, Cores 342-U1404A-6H through 9H show relatively large amplitude changes in color reflectance b* that do not appear in the equivalent cores in Holes U1404B or U1404C (Fig. **F37**). In the splice table (Table **T23**) we labeled tie points as tentative if

1. They occur near the top or bottom ~50 cm of a core,
2. They are based on general trends rather than clearly correlative features, and
3. The tie yields a poor correlation in at least one of the available physical property data sets.

We have more confidence in the splice below ~160 m CCSF as a result of XRF core scanning measurements. As a result of these data sets, combined with supporting biostratigraphic and paleomagnetic evidence (see **"Biostratigraphy"** and **"Paleomagnetism"**) we are confident that Core 342-U1404B-24H bridges the gap between Cores 342-U1404A-23H and 24H, suggesting complete recovery across the Eocene/Oligocene boundary. Following Core 342-U1404A-24H, we appended Core 342-U1404B-26H.

References

Acton, G.D., Okada, M., Clement, B.M., Lund, S.P., and Williams, T., 2002. Paleomagnetic overprints in ocean sediment cores and their relationship to shear deformation caused by piston coring. *J. Geophys. Res.: Solid Earth,* 107(B4):2067–2081. **doi:10.1029/2001JB000518**

Arthur, M.A., 1979. Origin of Upper Cretaceous multicolored claystones of the Western Atlantic. *In* Tucholke, B.E., Vogt, P.R., et al., *Init. Repts. DSDP,* 43: Washington, DC (U.S. Govt. Printing Office), 417–420. **doi:10.2973/dsdp.proc.43.111.1979**

Baker, P.A., Gieskes, J.M., and Elderfield, H., 1982. Diagenesis of carbonates in deep-sea sediments: evidence from Sr/Ca ratios and interstitial dissolved Sr^{2+} data. *J. Sediment. Res.,* 52(1):71–82. **doi:10.1306/212F7EE1-2B24-11D7-8648000102C1865D**

Berner, R.A., 1980. *Early Diagenesis: A Theoretical Approach:* Princeton, NJ (Princeton Univ. Press).

Bohaty, S.M., Zachos, J.C., Florindo, F., and Delaney, M.L., 2009. Coupled greenhouse warming and deep-sea acidification in the middle Eocene. *Paleoceanography,* 24(2):PA2207. **doi:10.1029/2008PA001676**

Coccioni, R., Frontalini, F., and Spezzaferri, S., 2009. Late Eocene impact-induced climate and hydrological changes: evidence from the Massignano global stratotype section and point (central Italy). *Spec. Pap.—Geol. Soc. Am.,* 452:97–118. **doi:10.1130/2009.2452(07)**

Coxall, H.K., Wilson, P.A., Pälike, H., Lear, C.H., and Backman, J., 2005. Rapid stepwise onset of Antarctic glaciation and deeper calcite compensation in the Pacific Ocean. *Nature (London, U. K.),* 433(7021):53–57. **doi:10.1038/nature03135**

Dickens, G.R., Castillo, M.M., and Walker, J.C.G., 1997. A blast of gas in the latest Paleocene: simulating first-order effects of massive dissociation of oceanic methane hydrate. *Geology,* 25(3):259–262. **doi:10.1130/0091-7613(1997)025<0259:ABOGIT>2.3.CO;2**

Eldrett, J.S., Harding, I.C., Wilson, P.A., Butler, E., and Roberts, A.P., 2007. Continental ice in Greenland during the Eocene and Oligocene. *Nature (London, U. K.),* 446(7132):176–179. **doi:10.1038/nature05591**

Emerson, S., and Hedges, J.I., 1988. Processes controlling the organic carbon content of open ocean sediments. *Paleoceanography,* 3(5):621–634. **doi:10.1029/PA003i005p00621**

Fornaciari, E., Agnini, C., Catanzariti, R., Rio, D., Bolla, E.M., and Valvasoni, E., 2010. Mid-latitude calcareous nannofossil biostratigraphy and biochronology across the middle to late Eocene transition. *Stratigraphy,* 7(4):229–264. **http://www.micropress.org/micropen2/articles/1/7/94581_articles_article_file_1717.pdf**

Gieskes, J.M., and Lawrence, J.R., 1981. Alteration of volcanic matter in deep-sea sediments: evidence from the chemical composition of interstitial waters from deep sea drilling cores. *Geochim. Cosmochim. Acta,* 45(10):1687–1703. **doi:10.1016/0016-7037(81)90004-1**

Gradstein, F.M., Ogg, J.G., Schmitz, M.D., and Ogg, G.M. (Eds)., 2012. *The Geological Time Scale 2012:* Amsterdam (Elsevier).

Hardie, L.A., 1996, Secular variation in seawater chemistry: an explanation for the coupled secular variation in the mineralogies of marine limestones and potash evaporates over the past 600 m.y. *Geology,* 24(3):279–283. **doi:10.1130/0091-7613(1996)024<0279:SVISCA>2.3.CO;2**

Holbourn, A., Kuhnt, W., Schulz, M., and Erlenkeuser, H., 2005. Impacts of orbital forcing and atmospheric carbon dioxide on Miocene ice-sheet expansion. *Nature (London, U. K.),* 438(7067):483–487. **doi:10.1038/nature04123**

Kamikuri, S., Moore, T.C., Ogane, K., Suzuki, N., Pälike, H., and Nishi, H., 2012. Early Eocene to early Miocene radiolarian biostratigraphy for the low-latitude Pacific Ocean. *Stratigraphy,* 9(1):77–108. **http://www.micropress.org/micropen2/articles/1/7/27546_articles_article_file_1785.pdf**

Kirschvink, J.L., 1980. The least-squares line and plane and the analysis of palaeomagnetic data. *Geophys. J. R. Astron. Soc.,* 62(3):699–718. **doi:10.1111/j.1365-246X.1980.tb02601.x**

Leon-Rodriguez, L., and Dickens, G.R., 2010. Constraints on ocean acidification associated with rapid and massive carbon injections: the early Paleogene record at Ocean Drilling Program Site 1215, equatorial Pacific Ocean. *Palaeogeogr., Palaeoclimatol., Palaeoecol.,* 298(3–4):409–420. **doi:10.1016/j.palaeo.2010.10.029**

Lourens, L.J., Sluijs, A., Kroon, D., Zachos, J.C., Thomas, E., Röhl, U., Bowles, J., and Raffi, I., 2005. Astronomical pacing of late Palaeocene to early Eocene global warming events. *Nature (London, U. K.),* 435(7045):1083–1087. **doi:10.1038/nature03814**

Lyle, M., Wilson, P.A., Janecek, T.R., et al., 2002. *Proc. ODP, Init. Repts.,* 199: College Station, TX (Ocean Drilling Program). **doi:10.2973/odp.proc.ir.199.2002**

Merico, A., Tyrrell, T., and Wilson, P.A., 2008. Eocene/Oligocene ocean de-acidification linked to Antarctic glacia-

tion by sea-level fall. *Nature (London, U. K.),* 452(7190):979–982. **doi:10.1038/nature06853**

Norris, R.D., Wilson, P.A., Blum, P., Fehr, A., Agnini, C., Bornemann, A., Boulila, S., Bown, P.R., Cournede, C., Friedrich, O., Ghosh, A.K., Hollis, C.J., Hull, P.M., Jo, K., Junium, C.K., Kaneko, M., Liebrand, D., Lippert, P.C., Liu, Z., Matsui, H., Moriya, K., Nishi, H., Opdyke, B.N., Penman, D., Romans, B., Scher, H.D., Sexton, P., Takagi, H., Turner, S.K., Whiteside, J.H., Yamaguchi, T., and Yamamoto, Y., 2014a. Expedition 342 summary. *In* Norris, R.D., Wilson, P.A., Blum, P., and the Expedition 342 Scientists, *Proc. IODP,* 342: College Station, TX (Integrated Ocean Drilling Program). **doi:10.2204/iodp.proc.342.101.2014**

Norris, R.D., Wilson, P.A., Blum, P., Fehr, A., Agnini, C., Bornemann, A., Boulila, S., Bown, P.R., Cournede, C., Friedrich, O., Ghosh, A.K., Hollis, C.J., Hull, P.M., Jo, K., Junium, C.K., Kaneko, M., Liebrand, D., Lippert, P.C., Liu, Z., Matsui, H., Moriya, K., Nishi, H., Opdyke, B.N., Penman, D., Romans, B., Scher, H.D., Sexton, P., Takagi, H., Turner, S.K., Whiteside, J.H., Yamaguchi, T., and Yamamoto, Y., 2014b. Methods. *In* Norris, R.D., Wilson, P.A., Blum, P., and the Expedition 342 Scientists, *Proc. IODP,* 342: College Station, TX (Integrated Ocean Drilling Program). **doi:10.2204/iodp.proc.342.102.2014**

Norris, R.D., Wilson, P.A., Blum, P., Fehr, A., Agnini, C., Bornemann, A., Boulila, S., Bown, P.R., Cournede, C., Friedrich, O., Ghosh, A.K., Hollis, C.J., Hull, P.M., Jo, K., Junium, C.K., Kaneko, M., Liebrand, D., Lippert, P.C., Liu, Z., Matsui, H., Moriya, K., Nishi, H., Opdyke, B.N., Penman, D., Romans, B., Scher, H.D., Sexton, P., Takagi, H., Turner, S.K., Whiteside, J.H., Yamaguchi, T., and Yamamoto, Y., 2014c. Site U1403. *In* Norris, R.D., Wilson, P.A., Blum, P., and the Expedition 342 Scientists, *Proc. IODP,* 342: College Station, TX (Integrated Ocean Drilling Program). **doi:10.2204/iodp.proc.342.104.2014**

Pälike, H., Lyle, M.W., Nishi, H., Raffi, I., Ridgwell, A., Gamage, K., Klaus, A., Acton, G., Anderson, L., Backman, J., Baldauf, J., Beltran, C., Bohaty, S.M., Bown, P., Busch, W., Channell, J.E.T., Chun, C.O.J., Delaney, M., Dewangan, P., Dunkley Jones, T., Edgar, K.M., Evans, H., Fitch, P., Foster, G,L., Gussone, N., Hasegawa, H., Hathorne, E.C., Hayashi, H., Herrle, J.O., Holbourn, A., Hovan, S., Hyeong, K., Iijima, K., Ito, T., Kamikuri, S., Kimoto, K., Kuroda, J., Leon-Rodriguez, L., Malinverno, A., Moore, T.C., Jr., Murphy, B.H., Murphy, D.P., Nakamura, H., Ogane, K., Ohneiser, C., Richter, C., Robinson, R., Rohling, E.J., Romero, O., Sawada, K., Scher, H., Schneider, L., Sluijs, A., Takata, H., Tian, J., Tsujimoto, A., Wade, B.S., Westerhold, T., Wilkens, R., Williams, T., Wilson, P.A., Yamamoto, Y., Yamamoto, S., Yamazaki, T., and Zeebe, R.E., 2012. A Cenozoic record of the equatorial Pacific carbonate compensation depth. *Nature (London, U. K.),* 488(7409):609–614. **doi:10.1038/nature11360**

Ridgwell, A., 2007. Interpreting transient carbonate compensation depth changes by marine sediment core modeling. *Paleoceanography,* 22(4):PA4102. **doi:10.1029/2006PA001372**

Roberts, A.P., 2006. High-resolution magnetic analysis of sediment cores: strengths, limitations and strategies for maximizing the value of long-core magnetic data. *In* Sager, W.W., Acton, G.D., Clement, B.M., and Fuller, M. (Eds.), *ODP Contributions to Paleomagnetism*. Phys. Earth Planet. Int., 156(3–4):162–178. **doi:10.1016/j.pepi.2005.03.021**

Sanfilippo, A., Westberg-Smith, M.J., and Riedel, W.R., 1985. Cenozoic Radiolaria. *In* Bolli, H.M., Saunders, J.B., and Perch-Nielsen, K. (Eds.), *Plankton Stratigraphy* (Vol. 2): *Radiolaria, Diatoms, Silicoflagellates, Dinoflagellates, and Ichthyoliths:* Cambridge (Cambridge Univ. Press), 631–712.

Sexton, P.F., Norris, R.D., Wilson, P.A., Pälike, H., Westerhold, T., Röhl, U., Bolton, C.T., and Gibbs, S., 2011. Eocene global warming events driven by ventilation of oceanic dissolved organic carbon. *Nature (London, U. K.),* 471(7338):349–352. **doi:10.1038/nature09826**

Stanley, S.M., and Hardie, L.A., 1998. Secular oscillations in the carbonate mineralogy of reef-building and sediment-producing organisms driven by tectonically forced shifts in seawater chemistry. *Palaeogeogr., Palaeoclimatol., Palaeoecol.,* 144(1–2):3–19. **doi:10.1016/S0031-0182(98)00109-6**

Tripati, A.K., Eagle, R.A., Morton, A., Dowdeswell, J.A., Atkinson, K.L., Bahé, Y., Dawber, C.F., Khadun, E., Shaw, R.M.H., Shorttle, O., and Thanabalasundaram, L., 2008. Evidence for glaciation in the Northern Hemisphere back to 44 Ma from ice-rafted debris in the Greenland Sea. *Earth Planet. Sci. Lett.,* 265(1–2):112–122. **doi:10.1016/j.epsl.2007.09.045**

Tucholke, B.E., and Vogt, P.R., 1979. Western North Atlantic: sedimentary evolution and aspects of tectonic history. *In* Tucholke, B.E., Vogt, P.R., et al., *Init. Repts. DSDP,* 43: Washington, DC (U.S. Govt. Printing Office), 791–825. **doi:10.2973/dsdp.proc.43.140.1979**

van Morkhoven, F.P.C.M., Berggren, W.A., Edwards, A.S., and Oertli, H.J., 1986. Cenozoic cosmopolitan deep-water benthic roraminifera. *Bull. Cent. Rech. Explor.—Prod. Elf-Aquitaine,* 11.

Xuan, C., and Channell, J.E.T., 2009. UPmag: MATLAB software for viewing and processing U channel or other pass-through paleomagnetic data. *Geochem., Geophys., Geosyst.,* 10(10):Q10Y07. **doi:10.1029/2009GC002584**

Zachos, J.C., and Kump, L.R., 2005. Carbon cycle feedbacks and the initiation of Antarctic glaciation in the earliest Oligocene. *Global Planet. Change,* 47(1):51–66. **doi:10.1016/j.gloplacha.2005.01.001**

Zachos, J.C., Röhl, U., Schellenberg, S.A., Sluijs, A., Hodell, D.A., Kelly, D.C., Thomas, E., Nicolo, M., Raffi, I., Lourens, L.J., McCarren, H., and Kroon, D., 2005. Rapid acidification of the ocean during the Paleocene–Eocene Thermal Maximum. *Science,* 308(5728):1611–1615. **doi:10.1126/science.1109004**

Publication: 3 March 2014
MS 342-105

Figure F1. Bathymetry map of the southwestern end of J-Anomaly Ridge showing the location of Site U1404 (red star). Track lines are from a single-channel seismic survey conducted during the Knorr179-1 site survey. See Figures F2 and F3 for seismic profiles.

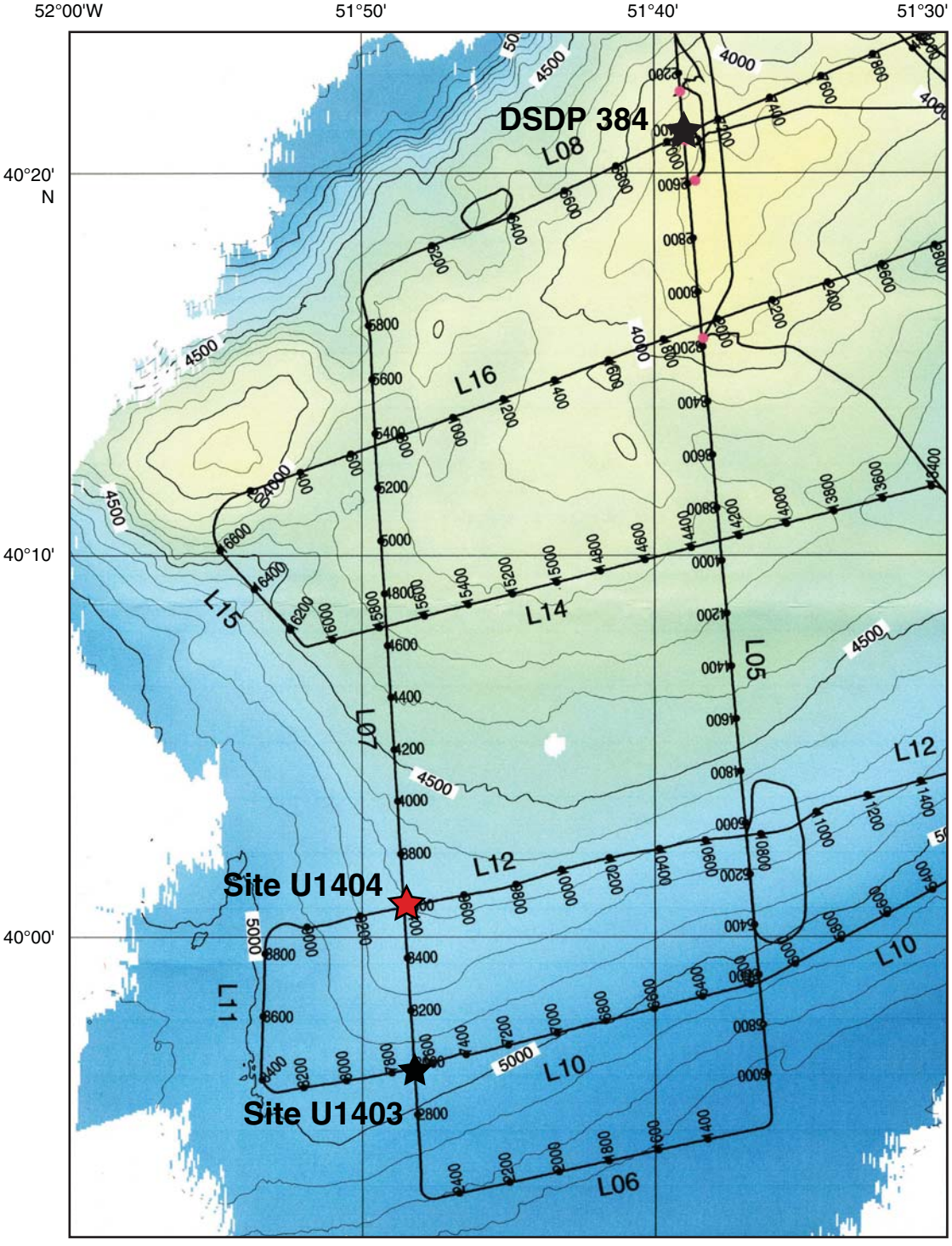

Figure F2. Single-channel seismic KNR179-1 Line 7 north–south dip line crossing Site U1404 (at shotpoint [SP] 3600). White bar represents approximate depth of penetration. Identified acoustic horizon is shown at the approximate location of the early/middle (e./m.) Eocene boundary. K/Pg = Cretaceous/Paleogene boundary.

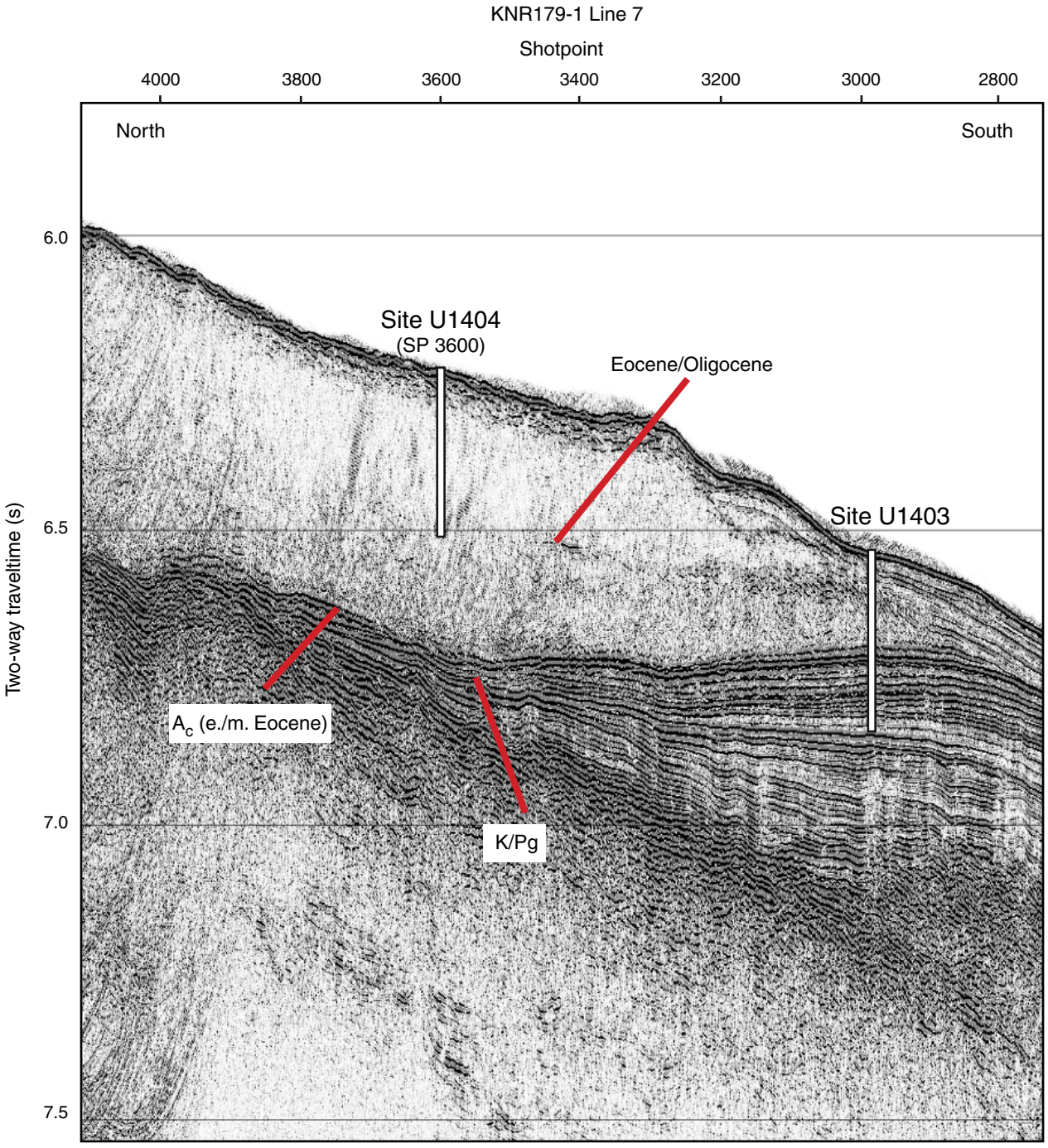

Figure F3. Single-channel seismic KNR179-1 Line 12 northeast–southwest strike line crossing Site U1404 (at shotpoint [SP] 9390). White bar represents approximate depth of penetration. Red line indicates the inferred position of the early/middle Eocene boundary.

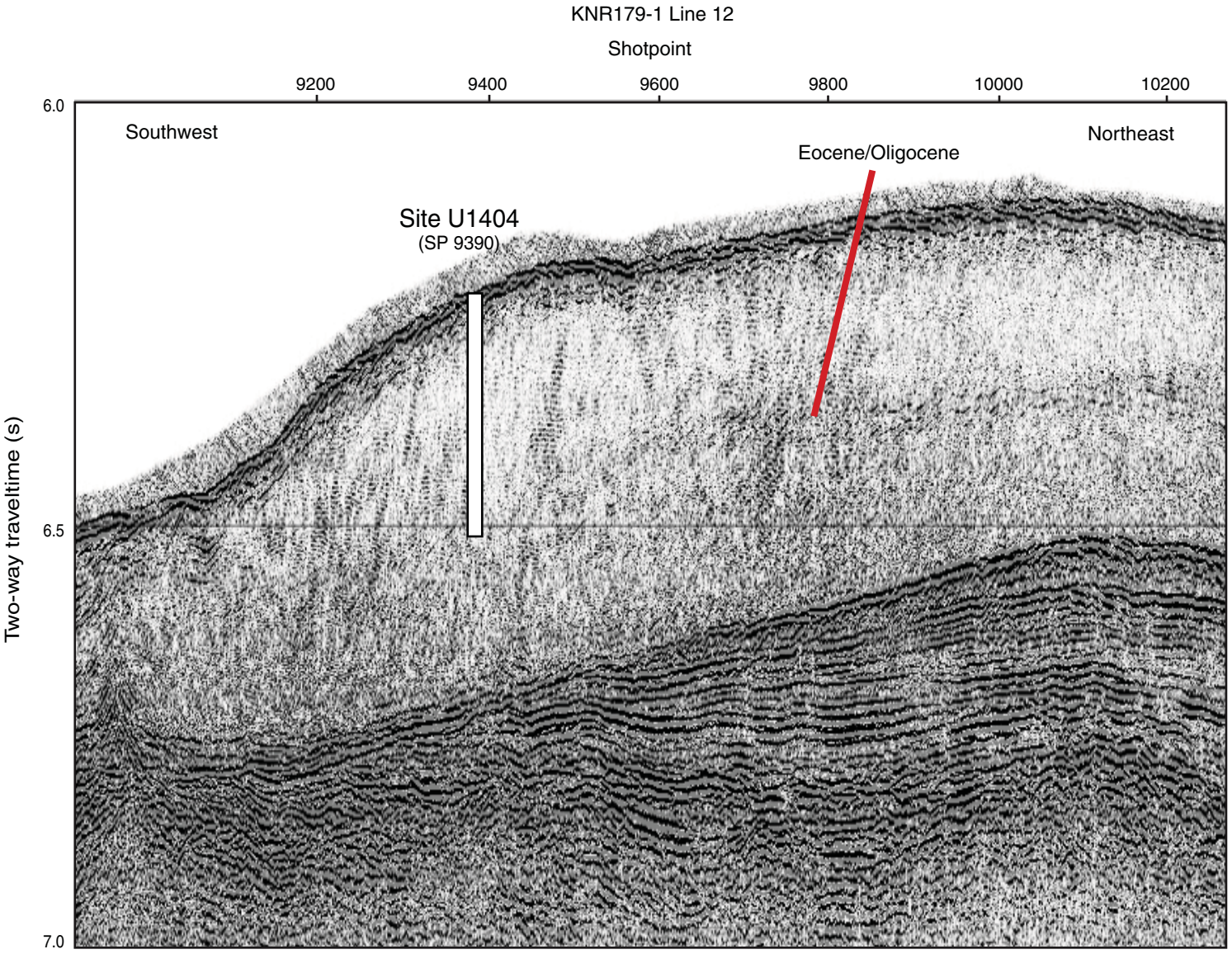

Figure F4. Lithostratigraphic summary, Site U1404.

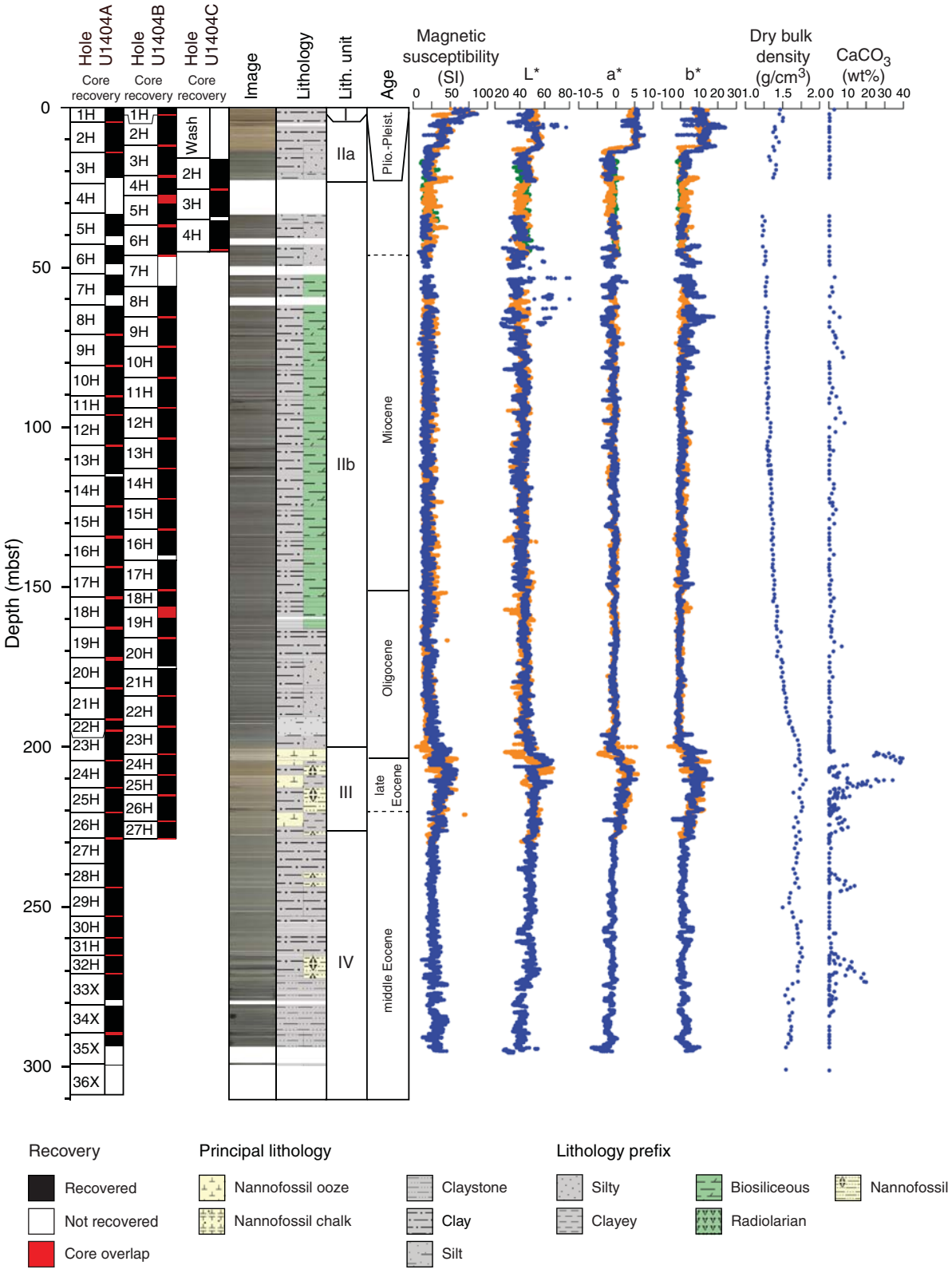

Figure F5. Line-scan images from most common lithologies, Site U1404. **A.** Pleistocene foraminiferal sand in nannofossil ooze, Unit I. **B.** Pliocene–Pleistocene nannofossil ooze, Unit I. **C.** Miocene biosiliceous clay and biosiliceous clay with nannofossils, Subunit IIb. Note the typical alternation between greenish gray and dark greenish gray. The latter color is associated with greater abundance of calcareous nannofossil. Clay in Subunit IIa has a similar macroscopic appearance. **D.** Latest Eocene clay with nannofossils, Unit III. **E.** Latest Eocene nannofossil ooze, Unit III. **F.** Eocene claystone, Unit IV.

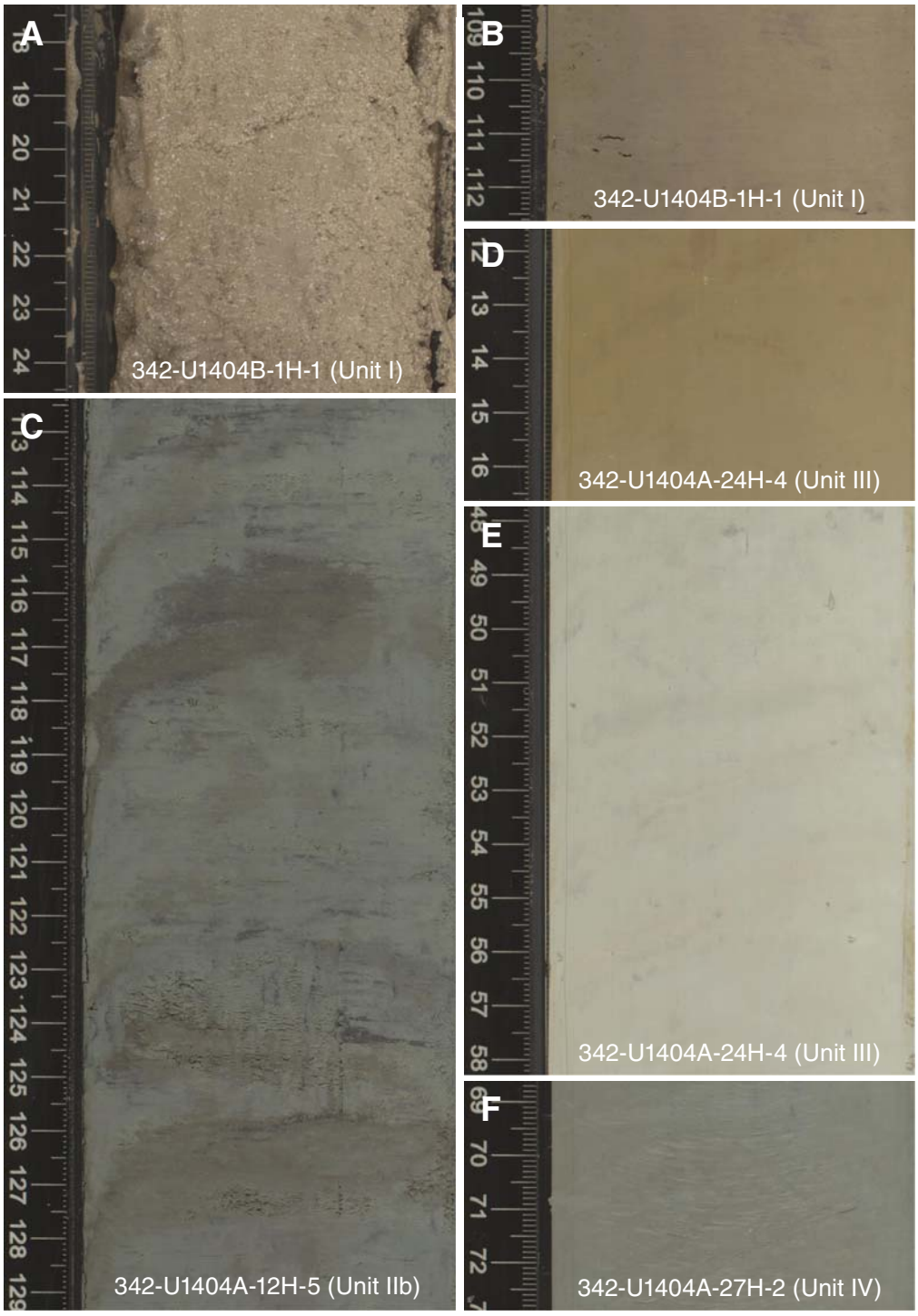

Figure F6. Photomicrographs of smear slides indicating the dominant lithologies of lithostratigraphic Units II–IV, Site U1404. **A.** Clay, Subunit IIa. **B.** Diatom ooze with nannofossils, Subunit IIb. **C.** Nannofossil ooze, Unit III. **D.** Nannofossil silty clay with radiolarians, Unit IV.

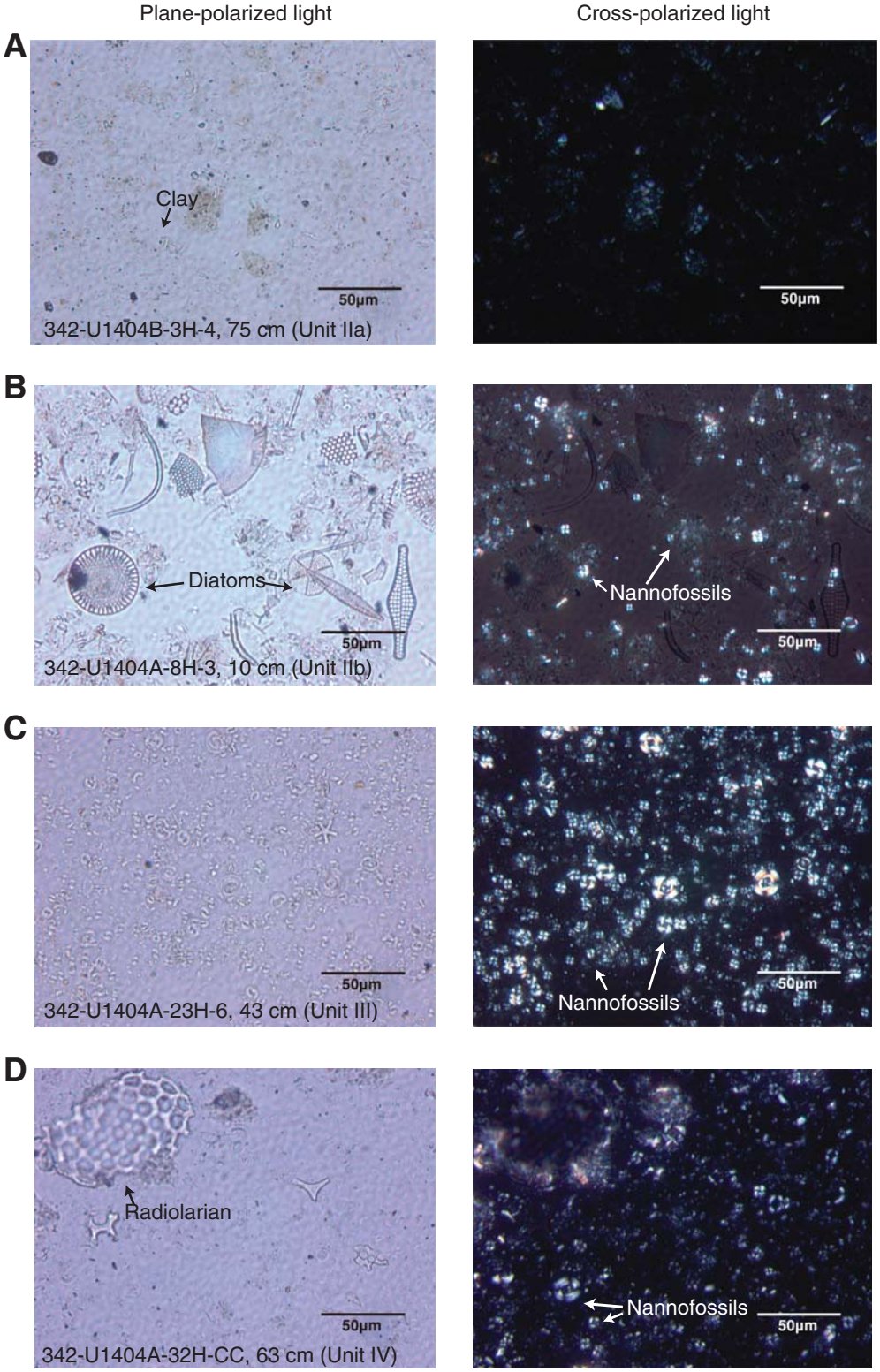

Figure F7. Plots of smear slide results of major biogenic and lithologic components and their relative abundance by depth, Hole U1404A. VA = very abundant, A = abundant, C = common, F = few, P = present.

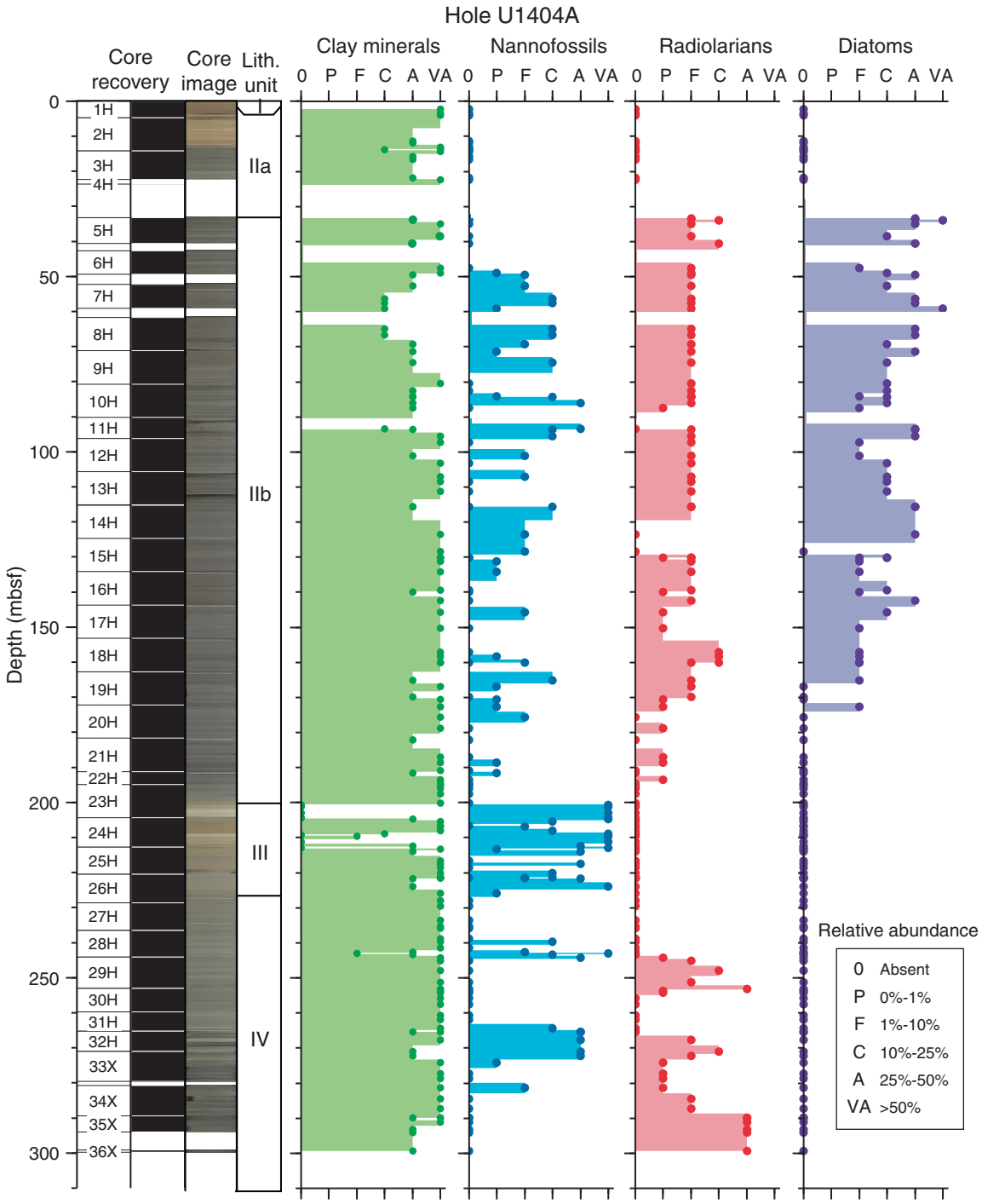

Figure F8. Plots of smear slide results of major biogenic and lithologic components and their relative abundance by depth, Hole U1404B. Note that the top of Hole U1404B has nannofossils, which are absent in Core 342-U1404A-1H, likely caused by the difference in mudline recovery. VA = very abundant, A = abundant, C = common, F = few, P = present.

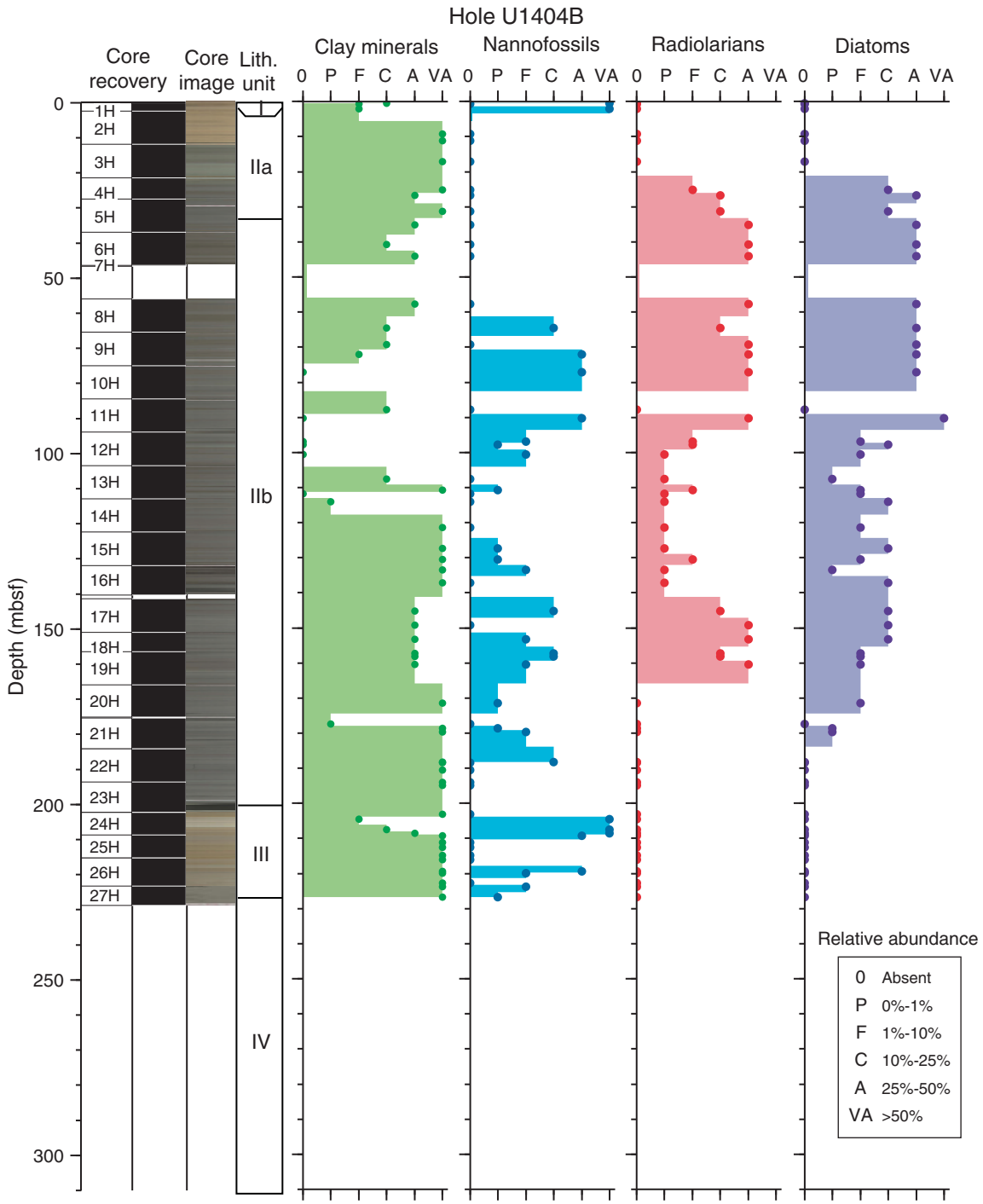

Figure F9. XRD spectrum of glauconitic nodule, as commonly observed in the upper cores of Site U1404. Data are from the center of the nodule shown in the inset. Glauconite belongs to the illite group and therefore shares several reflection peaks with illite. The distinction between glauconite and illite has been made by the lack of the 5 Å peak (17.7°2θ) for glauconite.

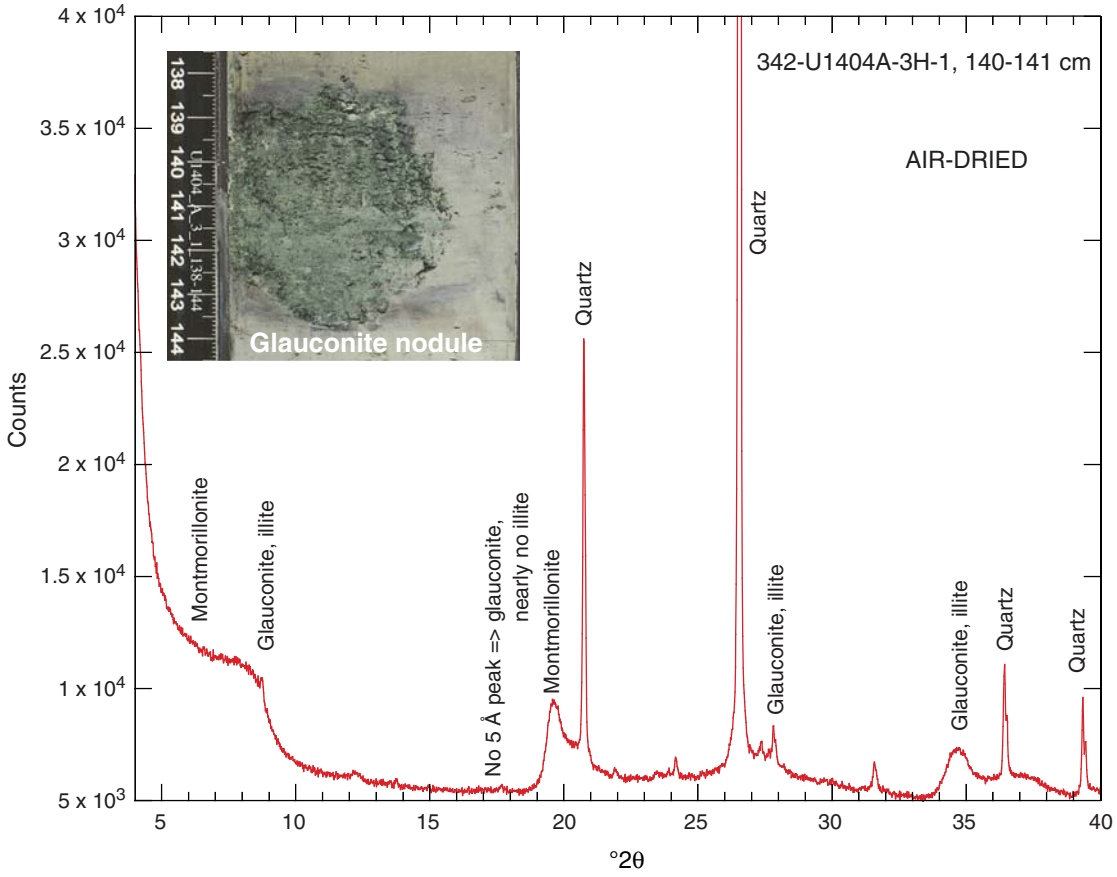

Figure F10. Photomicrographs of sand-sized lithic grains (possible ice-rafted debris), Hole U1404A. Scale bars = 100 µm. **A.** Overview of lithic grain types on a picking tray (63–150 µm sieve size fraction) showing large amounts of (angular) quartz grains and other mineral phases (Sample 342-U1404A-23H-3, 117–119 cm). **B.** Selection of sand-sized lithic grains (Sample 342-U1404A-20H-CC). **C.** Selection of sand-sized lithic grains (Sample 342-U1404A-22H-CC). Note the quartz grain in the lower right corner shows a conchoidal fracture. **D.** Two larger lithic grains of quartz (left) and rock fragment (right) (Sample 342-U1404A-19H-CC). **E.** Larger rock fragment with an unknown pinkish red mineral phase (Sample 342-U1404A-21H-CC).

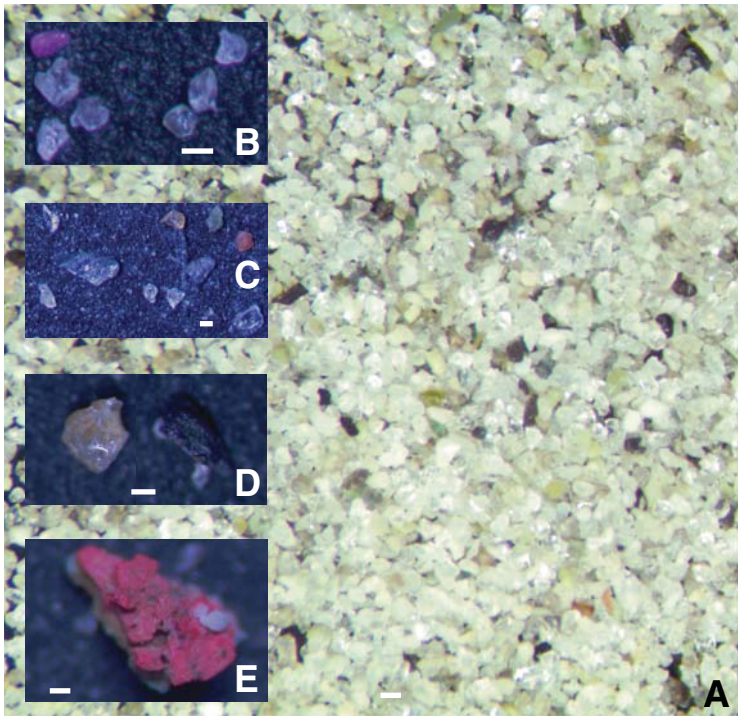

Figure F11. Diagram of proposed composite lithostratigraphy of the Eocene–Oligocene transition (EOT), Site U1404.

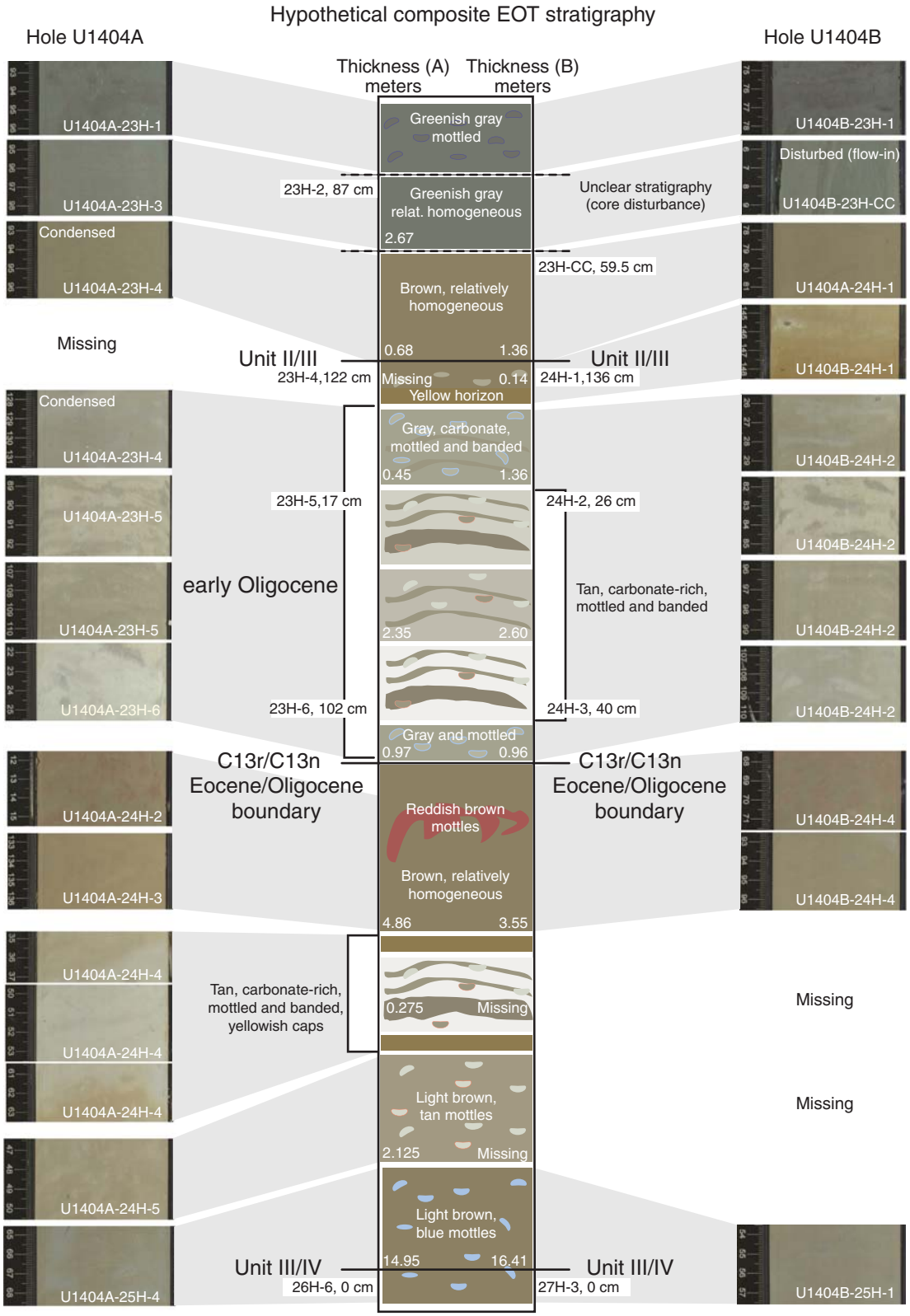

Figure F12. Plots of color reflectance, magnetic susceptibility, and carbonate content, Hole U1404A. A 15% weighted average of each series is shown to indicate long-term trends and to highlight the Eocene–Oligocene transition. Gray area represents high variations in color reflectance, magnetic susceptibility, and calcium carbonate, which match the Eocene–Oligocene transition (see text for discussion). Pink area may correspond to the Oi-1 glacial event according to sand-sized lithic grain data (see **"Sand-sized lithic grains"**).

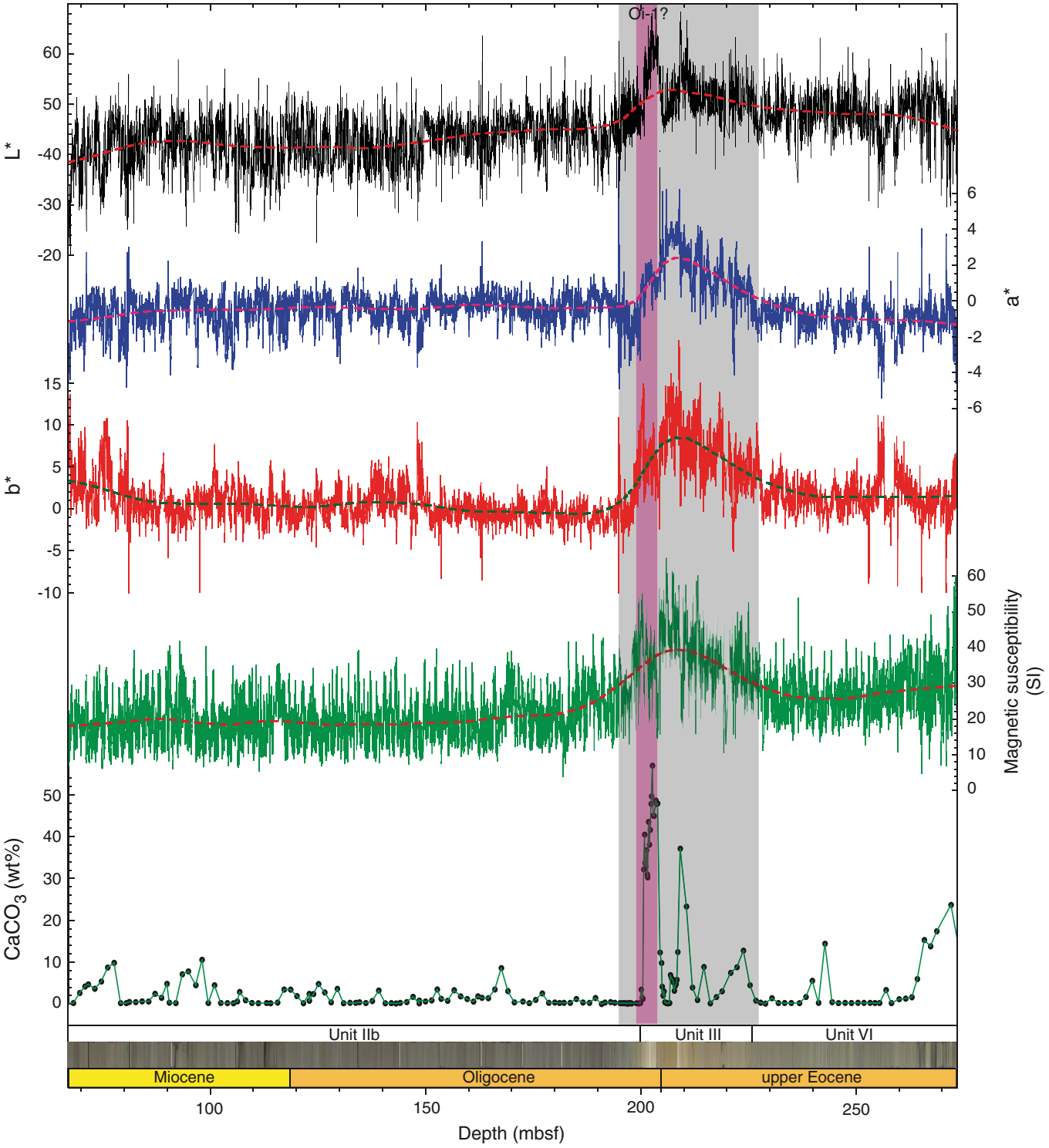

Figure F13. Close-up images of items of lithologic interest, Hole U1404A. **A.** Diagenetic sulfide halo after bioturbation or organic matter in middle Eocene claystone. **B.** Fish tooth with borings from middle Eocene claystone. **C.** Clast of poorly consolidated, poorly sorted, very fine quartz silty sandstone (possible ice-rafted debris). **D.** Lithic grain debris of very poorly consolidated, poorly sorted, very fine quartz silty sandstone from the late Eocene. Smaller clasts are typical of the style and size of most sand-sized lithic grains that are visible in split cores.

342-U1404A-33X-4A, 36-38 cm

342-U1404A-35X-2A, 84 cm

342-U1404A-19H-1A, 94-96 cm

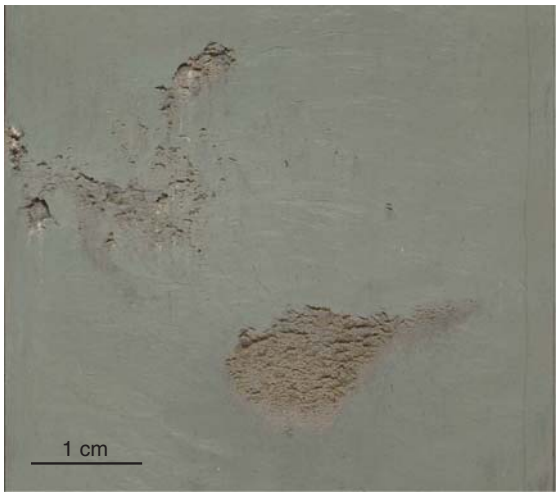

342-U1404A-30H-1A, 92-98 cm

Figure F14. Integrated calcareous and siliceous microfossil biozonation, Site U1404.

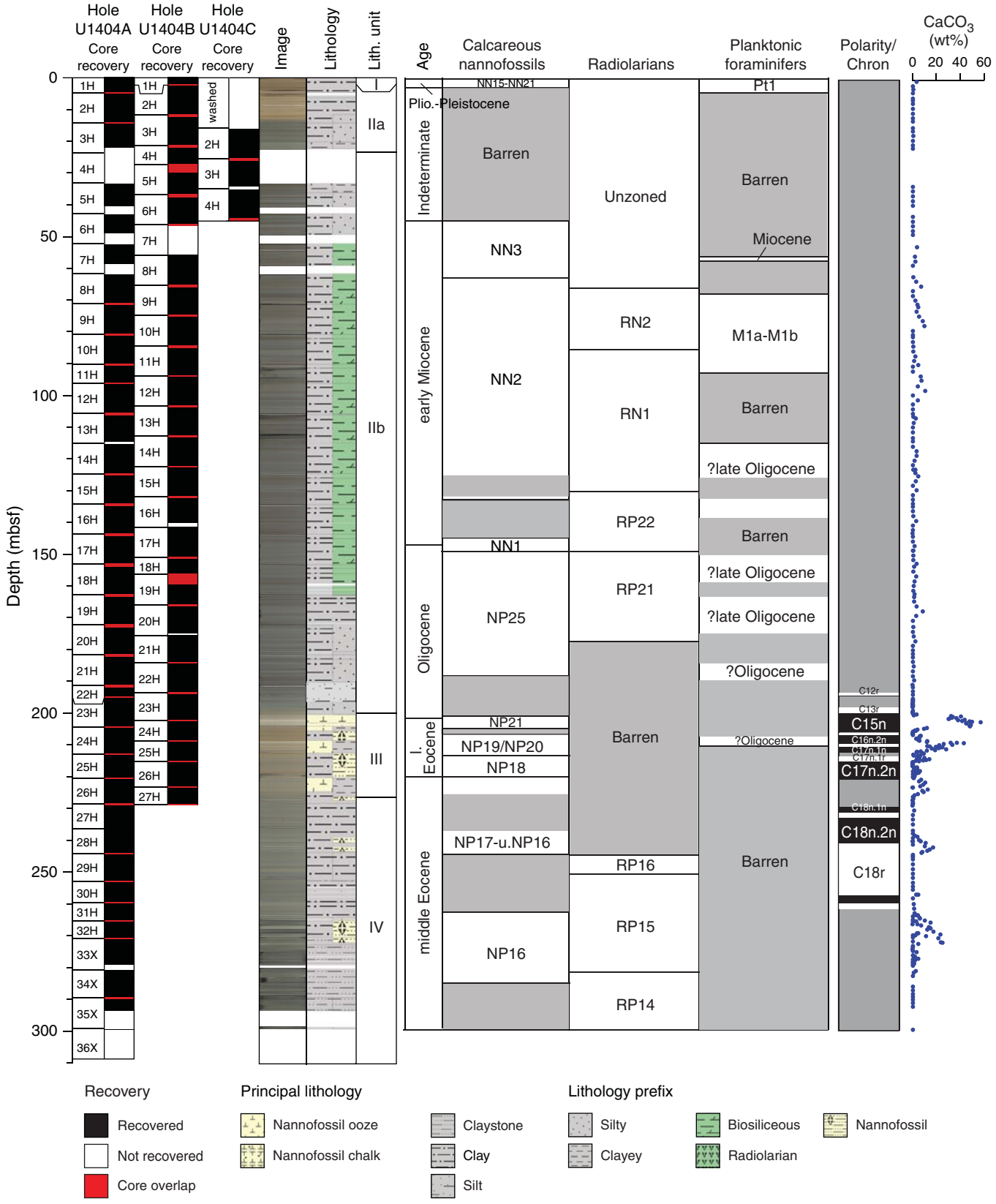

Figure F15. Plot of age-depth model for Hole U1404A showing biostratigraphic and magnetostratigraphic datums. Also shown are estimated linear sedimentation rates for line segments based on the key datums listed in Table **T16.**

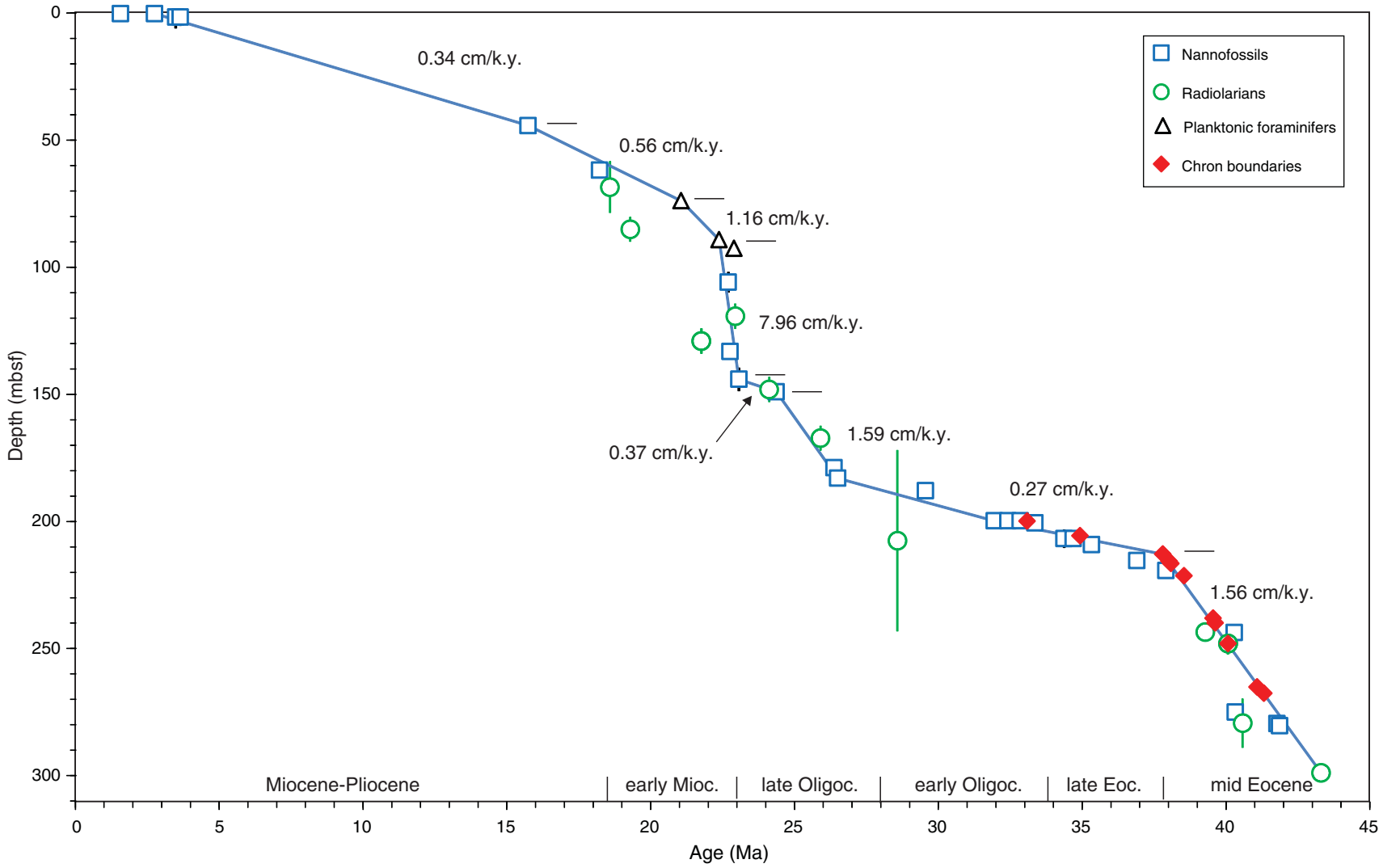

Figure F16. Plots of group abundance and preservation of calcareous and siliceous microfossils, Site U1404. Open and solid symbols represent Holes U1404A and U1404B, respectively. Note that abundance criteria are defined differently for each fossil group (see **"Biostratigraphy"** in the "Methods" chapter [Norris et al., 2014a]). Abundance: B = barren, P = present, R = rare, F = few, C = common, A = abundant, D = dominant. Preservation: P = poor, M = moderate, G = good, VG = very good.

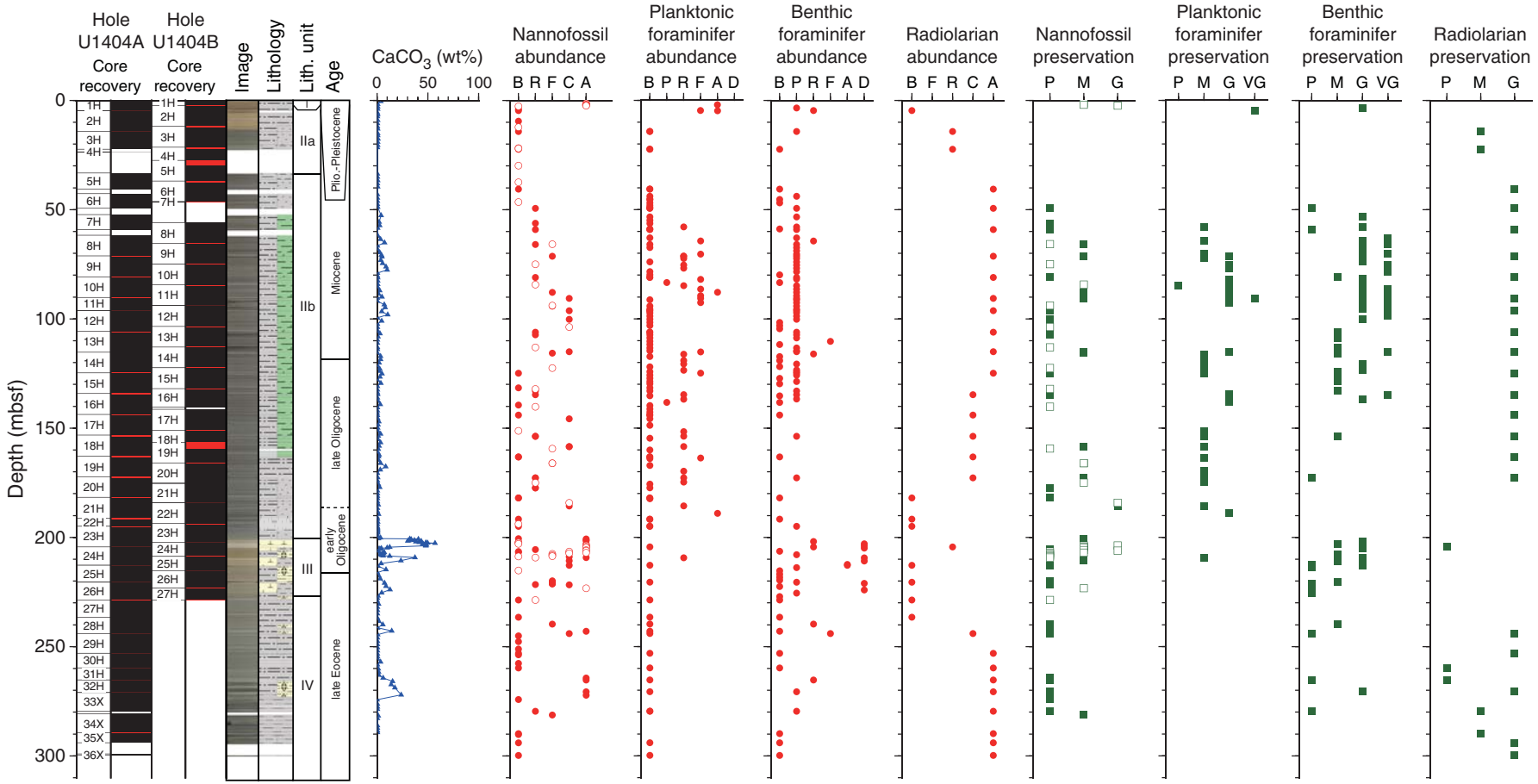

Figure F17. Photomicrographs of radiolarian assemblage examples, Site U1404. **A.** Large orosphaerid radiolarians common in Zone RN1. Inset is focused on background to show relative size of typical radiolarians (Sample 342-U1404A-12H-CC). **B.** Orosphaerid fragment as seen under transmitted light (Sample 342-U1404A-12H-CC). **C.** Typical lowermost Miocene radiolarian assemblage, Zone RP22. *Calocycletta robusta* is in the lower right corner, and *Dictyocoryne* sp. is in the upper center of the image (Sample 342-U1404A-16H-CC). **D.** Typical middle Eocene assemblage, Zone RP14 (Sample 342-U1404A-36X-CC).

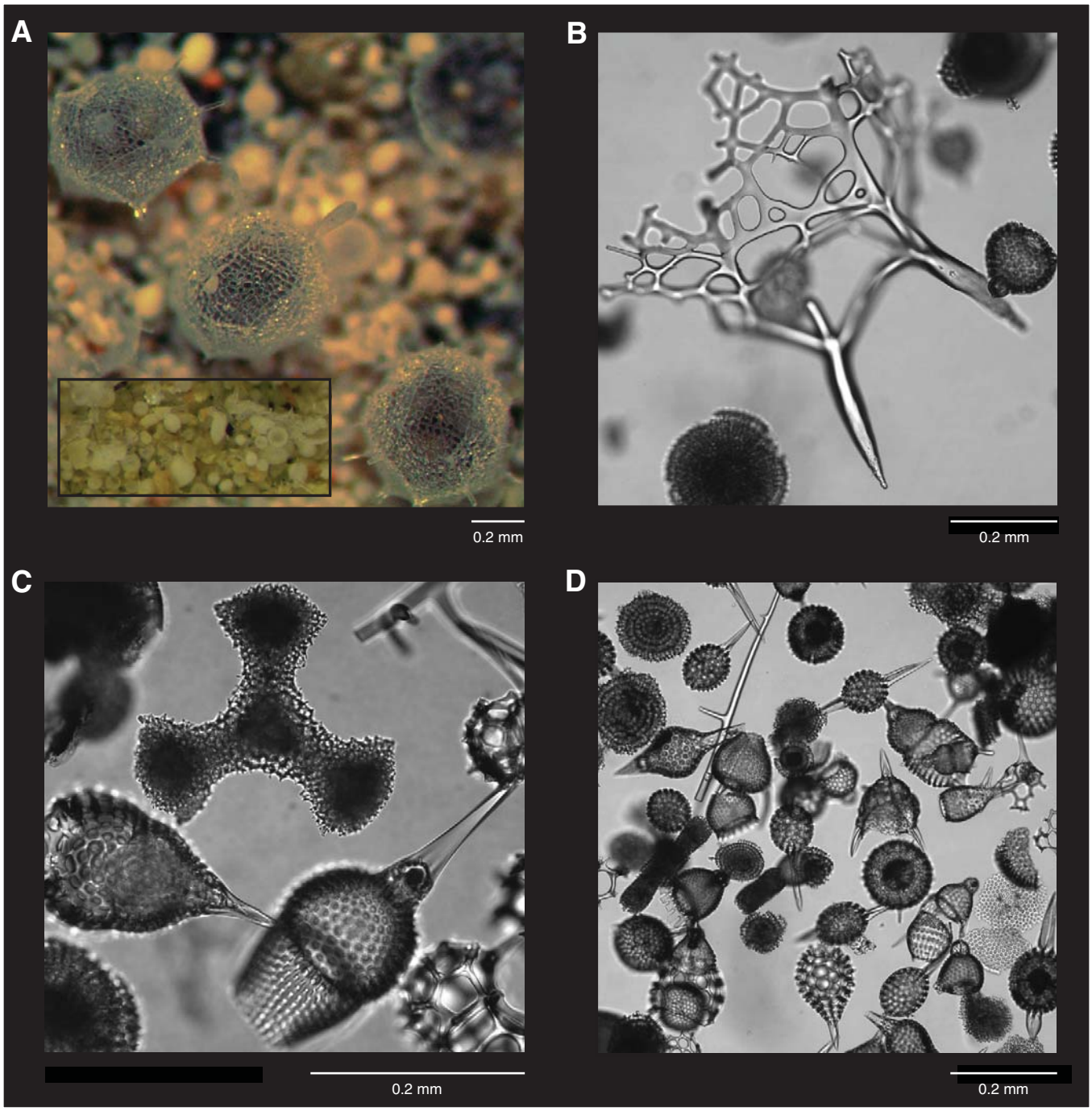

Figure F18. Plots of carbonate content (blue triangles), total organic carbon (black diamonds), group abundance and preservation of benthic foraminifers, and species abundance of *Globobulimina pacifica* (inset), Site U1404. Green and blue bars represent intervals of abundant large centric diatoms and orosphaerid radiolarians, respectively. Inset is a photomicrograph of *G. pacifica*. Abundance: B = barren, P = present, R = rare, F = few, C = common, A = abundant, and D = dominant. Preservation: P = poor, M = moderate, G = good, VG = very good.

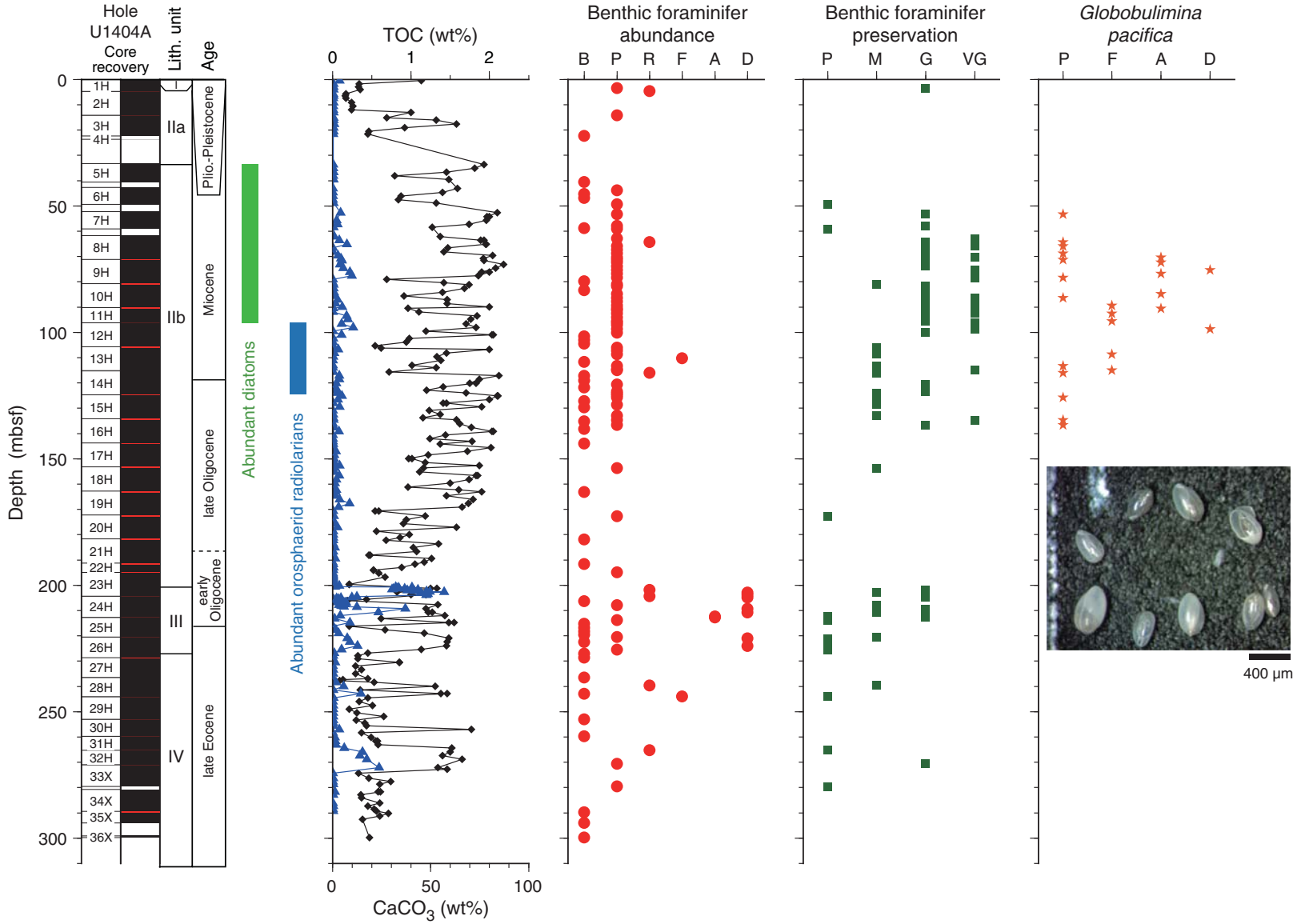

Figure F19. Plots of downhole variation of magnetic susceptibility and paleomagnetism data, Hole U1404A. Magnetization intensity, inclination, and declination are after 20 mT demagnetization. Only oriented advanced piston corer (APC) intervals show directions in geographic coordinates. Directions from all other intervals are shown in sample coordinates. For discrete sample data, if the samples were analyzed by principal component analysis (PCA; Kirschvink, 1980), then directions are shown according to PCA declination and inclination. Otherwise, directions following 20 mT demagnetization are shown. XCB = extended core barrel. Polarity: black = normal chron, white = reversed chron, gray = unidentified interval.

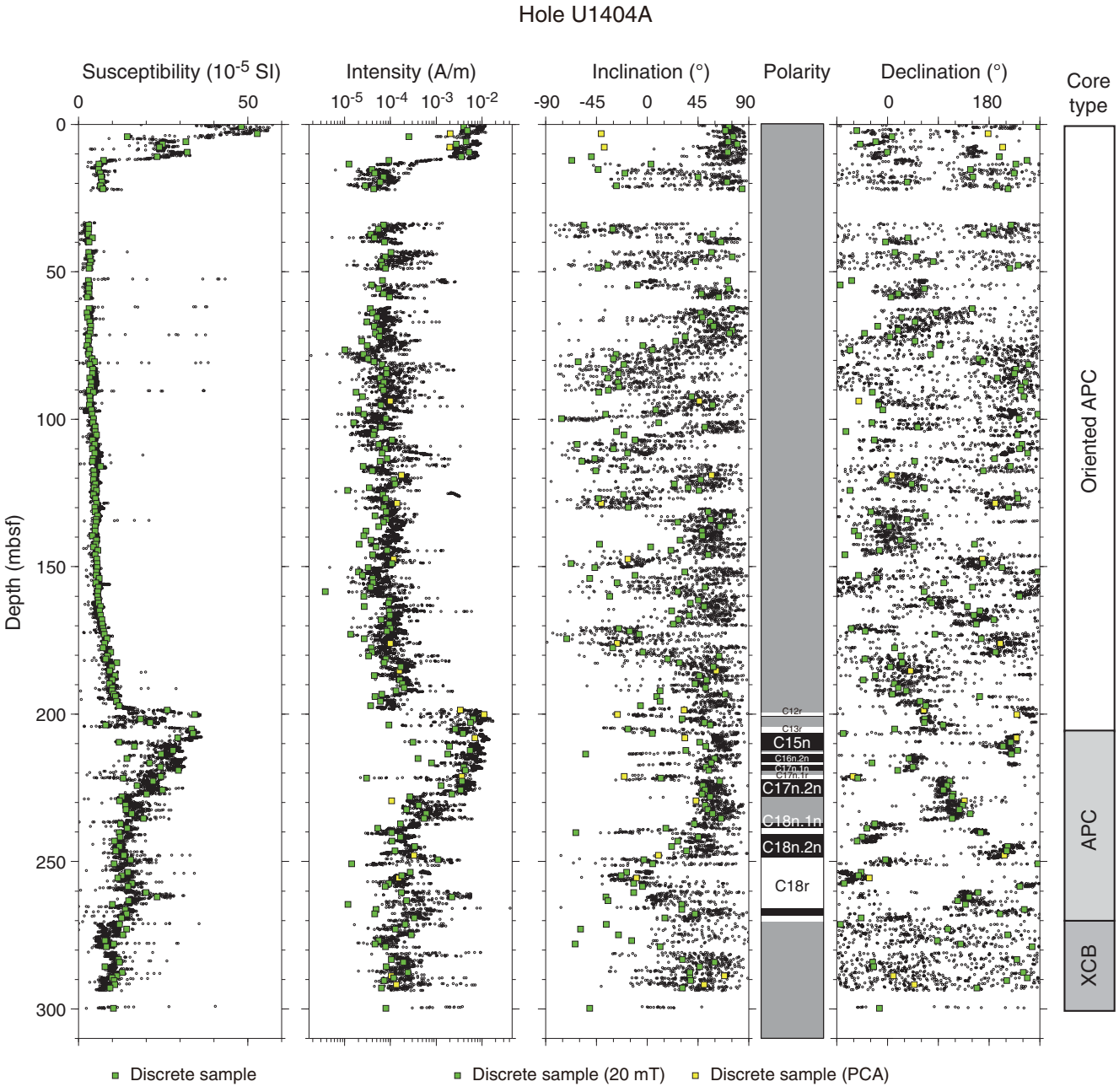

Figure F20. Plots of downhole variation of magnetic susceptibility and paleomagnetism data, Hole U1404B. Magnetization intensity, inclination, and declination are after 20 mT demagnetization. Directions are shown in geographic coordinates. APC = advanced piston corer. Polarity: black = normal chron, white = reversed chron, gray = unidentified interval.

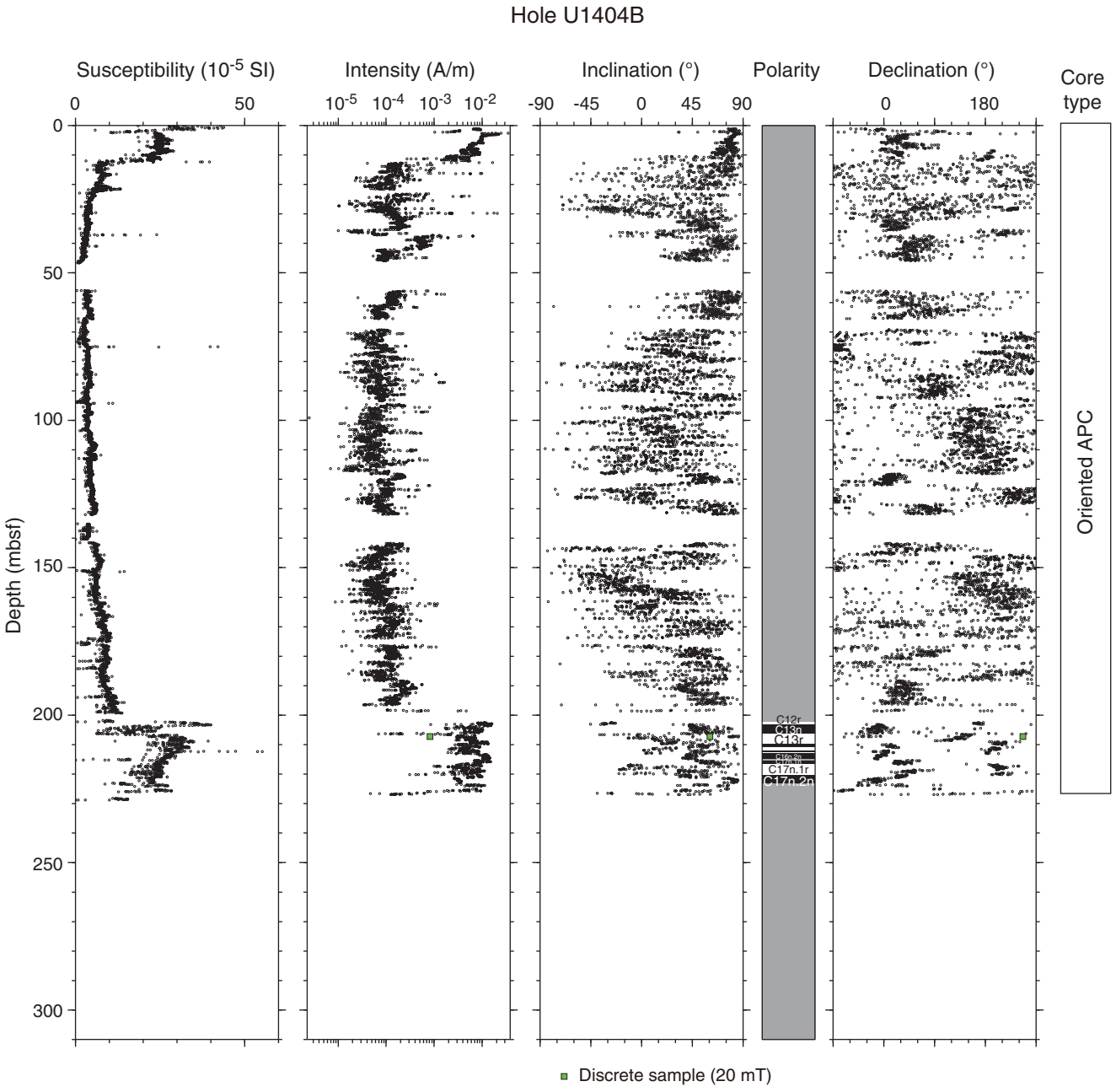

Figure F21. Plots of downhole variation of magnetic susceptibility and paleomagnetism data, Hole U1404C. Magnetization intensity, inclination, and declination are after 20 mT demagnetization. Directions are shown in sample coordinates. Polarity is unidentified. APC = advanced piston corer.

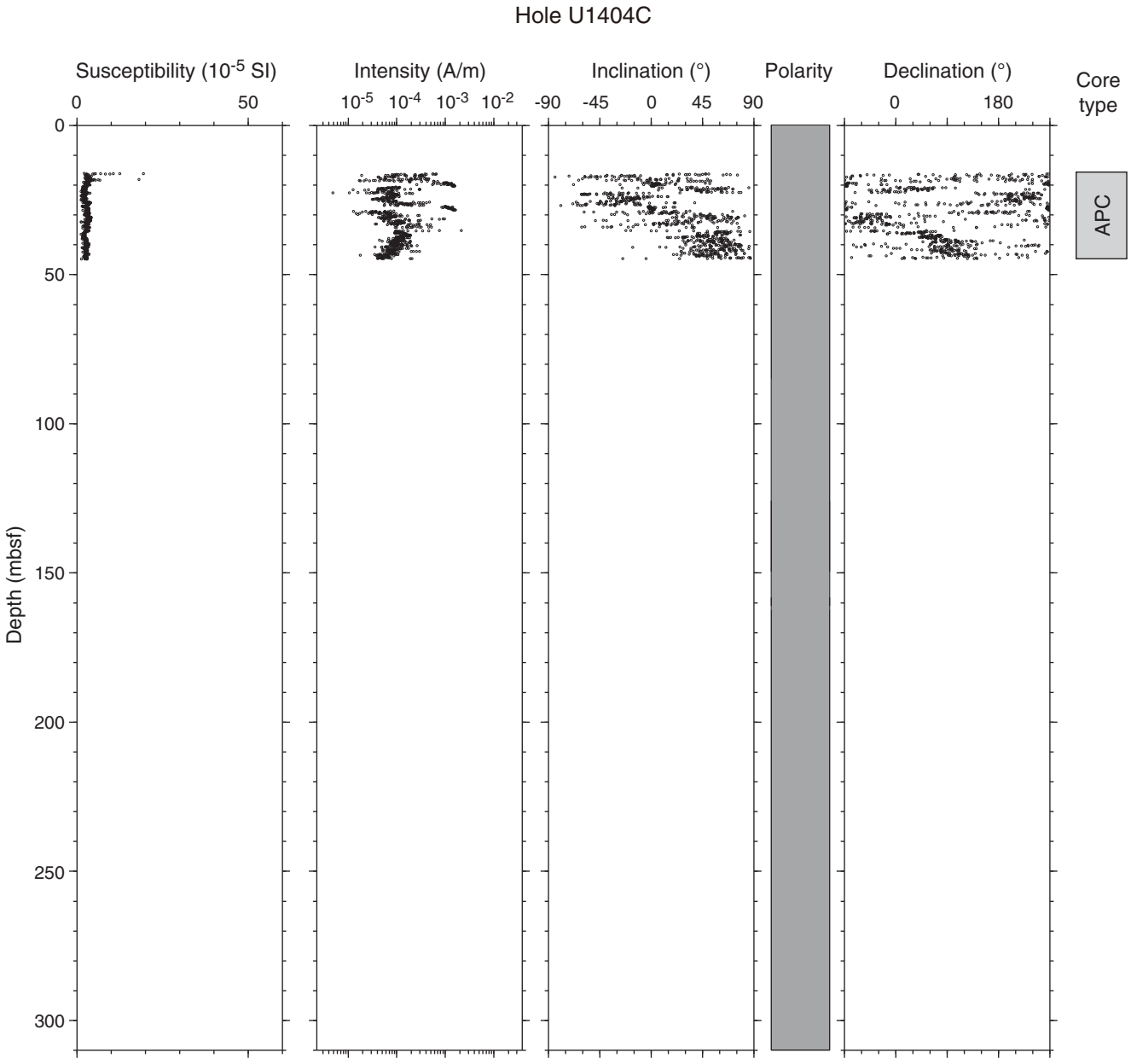

Figure F22. Plot and core images of paleomagnetism evidence for advanced piston corer "rifling," Hole U1404A. **A.** Declination trends measured in Core 342-U1404A-23H. Blue lines indicate expected directions for normal and reversed polarity declination in oriented cores. Thick red line emphasizes the downhole offset between expected and measured declination. **B, C.** Images of brittle shear fractures just above the sharp lithostratigraphic contact that are consistent with core deformation caused by a quickly rotating core barrel (interval 342-U1404A-23H-4, 117–122 cm).

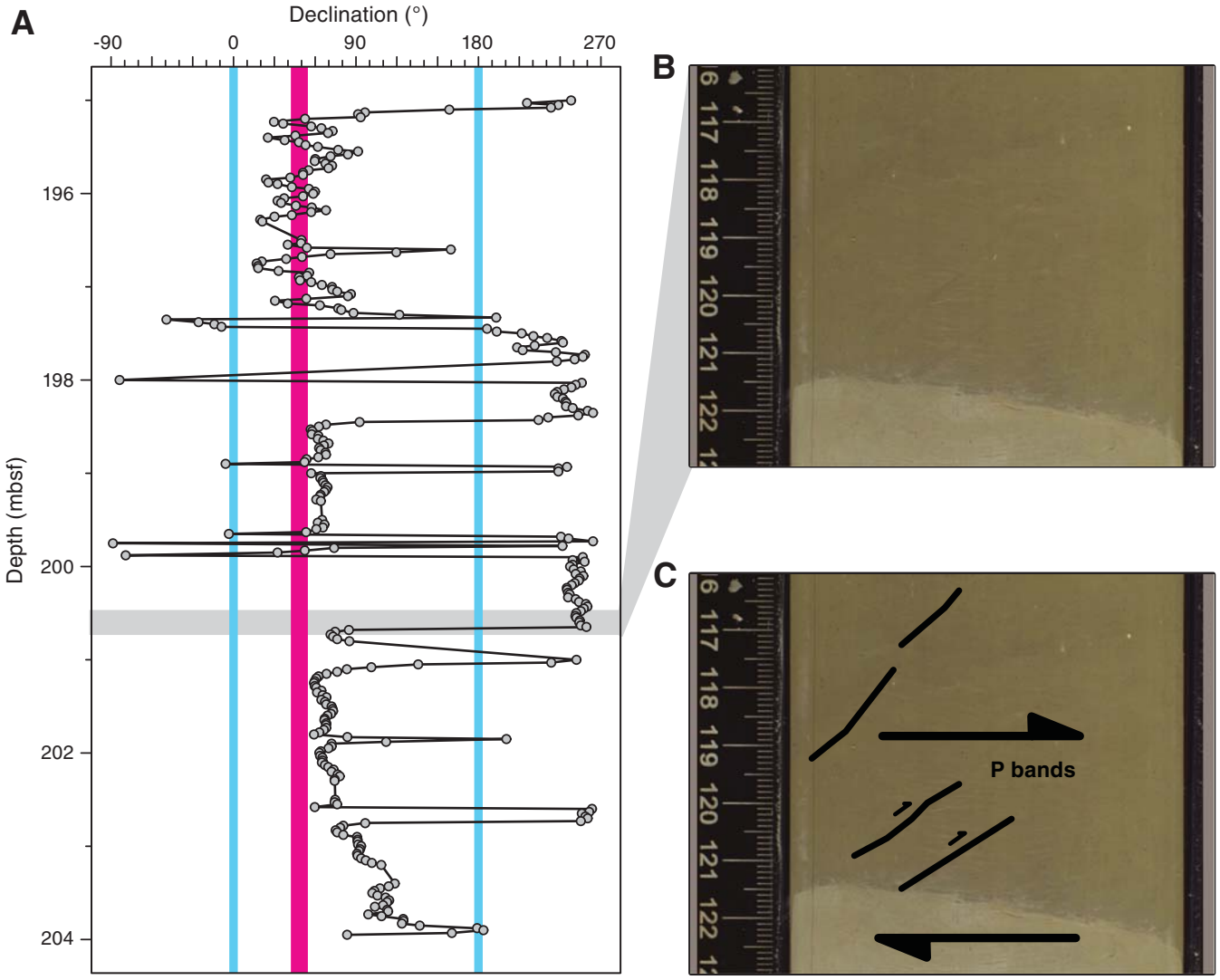

Figure F23. Plots of representative alternating field (AF) demagnetization results for discrete paleomagnetism samples, Site U1404. Upper plots show intensity variation with progressive demagnetization, and lower plots show vector endpoints of paleomagnetism directions on orthogonal vector diagrams (i.e., Zijderveld plots). Vector diagrams indicate that the sample in **A** records the well-resolved characteristic remanent magnetization (ChRM) direction, whereas the samples in **B** and **C** do not. Solid circles = horizontal projections, open circles = vertical projections, gray circles = data not used to calculate ChRM direction, black dashed line = ChRM direction. Inc = inclination, Dec = declination, MAD = maximum angle of deviation.

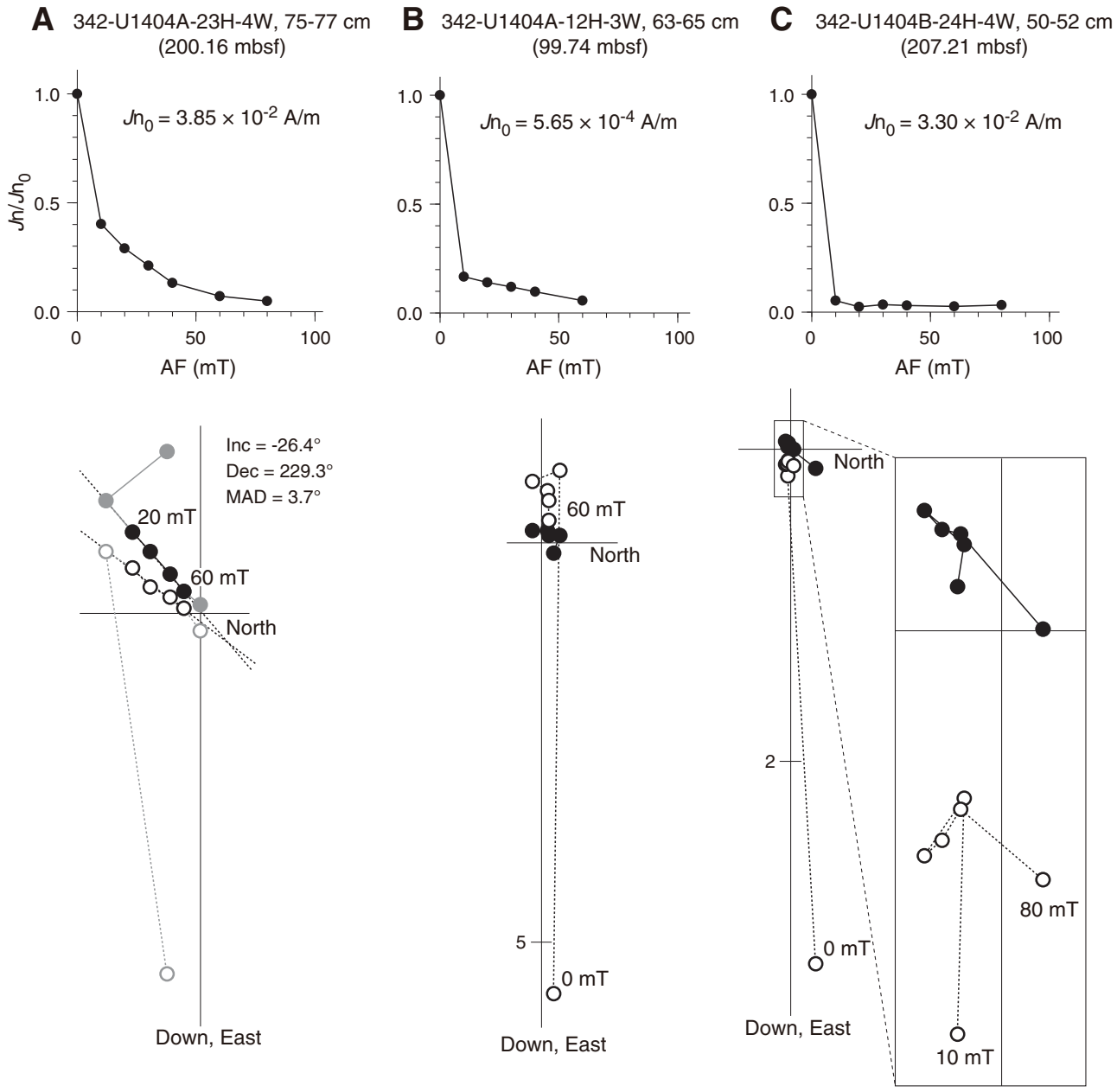

Figure F24. Plots of downhole variation of paleomagnetism data, Core 342-U1404B-24H. Blue lines indicate section breaks. Declination is after 20 mT demagnetization. Directions are shown in geographic coordinates. For discrete sample data, intensity and directions after 20 mT demagnetization are shown. Polarity: black = normal chron, white = reversed chron, gray = outlier caused by drilling overprint.

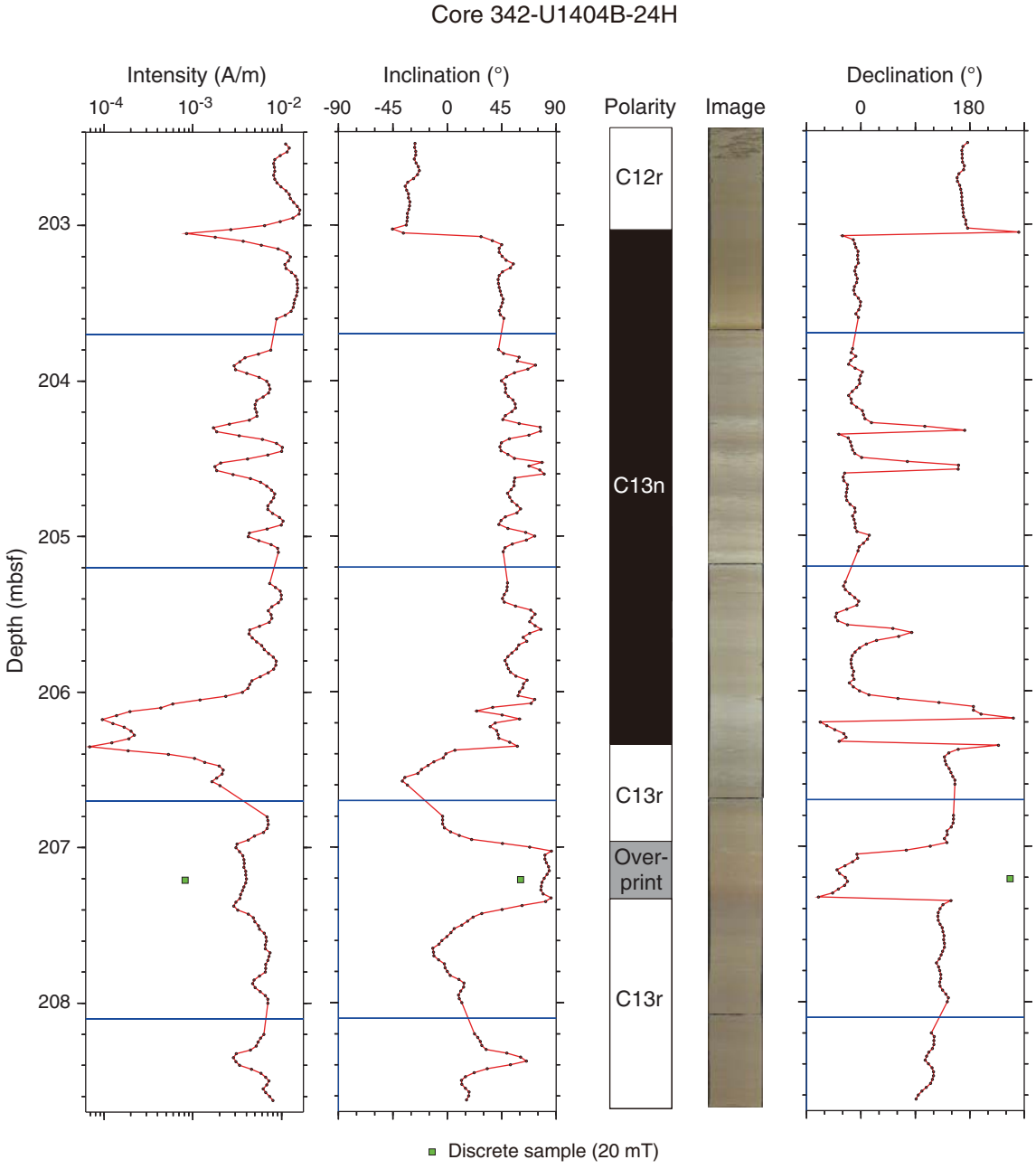

Figure F25. Illustration of magnetostratigraphy, Site U1404. Question marks above Chron C12r in Core 342-U1404A-23H indicate that the upper boundary of this chron was not confidently identified. Core recovery: black = recovered, red = overlap.

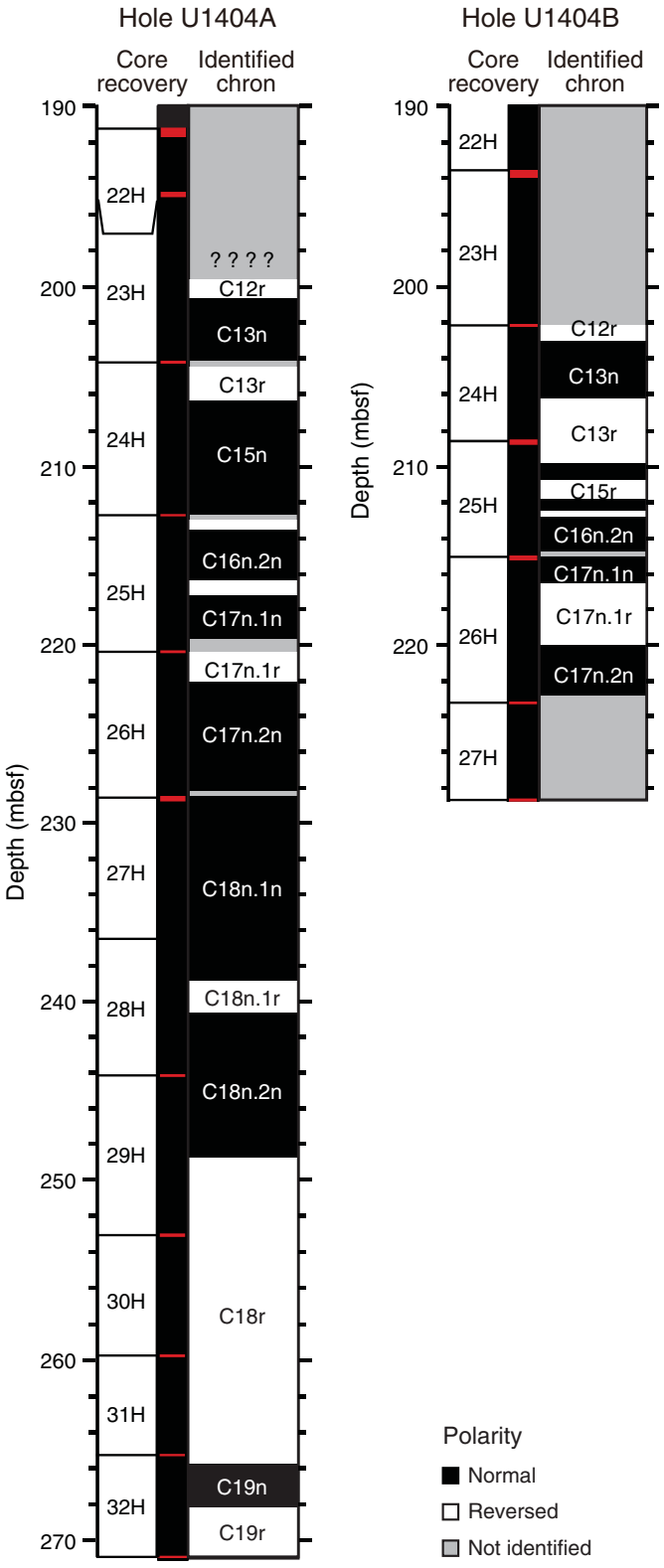

Figure F26. Plots of anisotropy of magnetic susceptibility, bulk density, and porosity vs. depth, Hole U1404A. Separation of eigenvalues is related to the shape and degree of magnetic fabric (see **"Paleomagnetism"** in the "Methods" chapter [Norris et al., 2014a]). For example, if τ_1 and τ_2 are close or indistinguishable but distinct from τ_3, then the bulk fabric is oblate. Bulk density and porosity are described in **"Physical properties"** and lithostratigraphic units in **"Lithostratigraphy."** Eigenvalues: τ_1 = maximum, τ_2 = intermediate, τ_3 = minimum. V_3 = minimum eigenvector, P = degree of anisotropy (τ_1/τ_3). APC = advanced piston corer, XCB = extended core barrel.

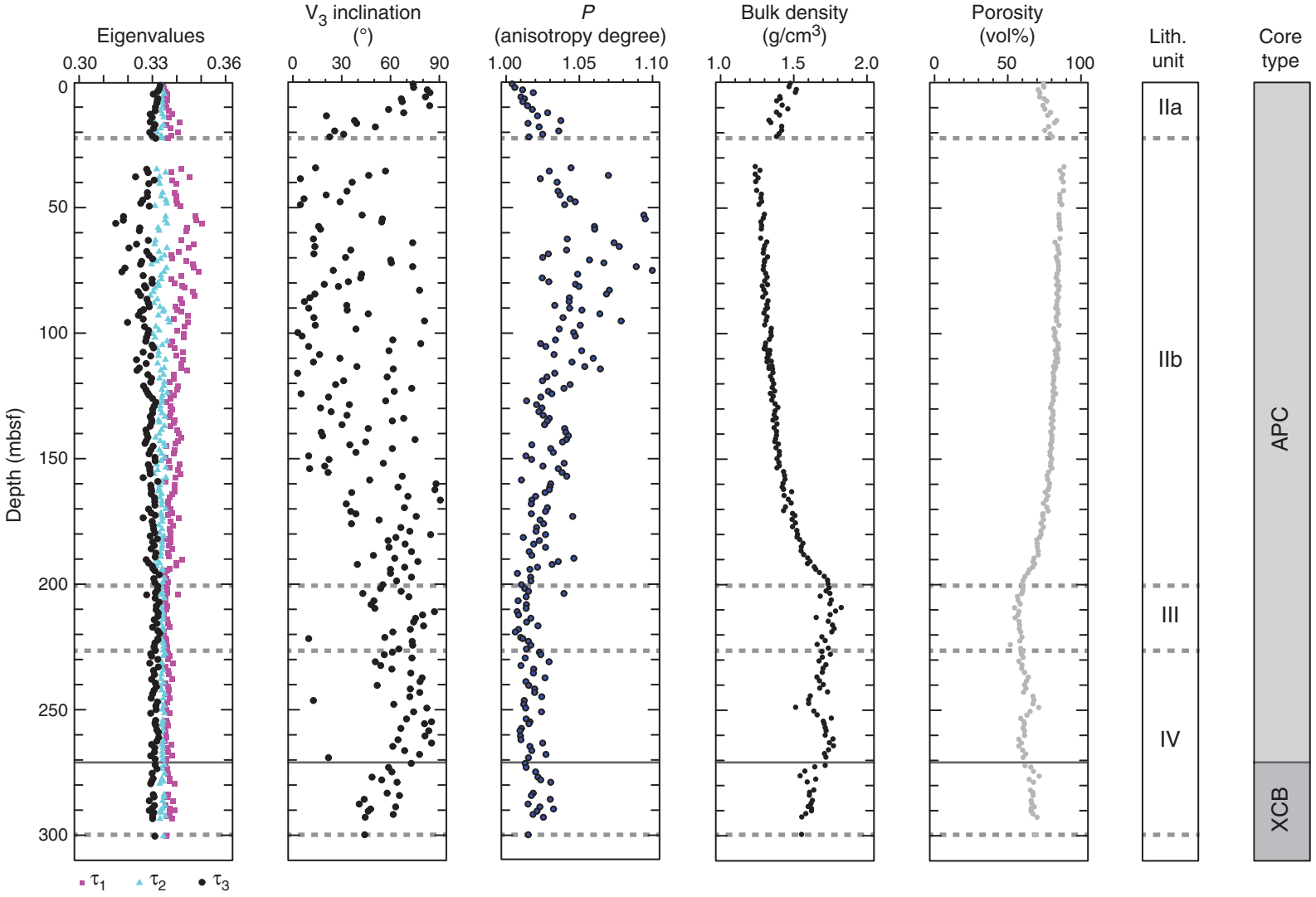

Figure F27. Plots of linear sedimentation rate (LSR), dry bulk density (DBD), carbonate content, and mass accumulation rate (MAR) at 200 k.y. time steps, Hole U1404A. Solid black diamonds show the inflection points in estimated LSR, DBD, and carbonate content. Geologic ages are shown on the GTS2012 timescale (Gradstein et al., 2012). CAR = carbonate mass accumulation rate, nCAR = noncarbonate mass accumulation rate.

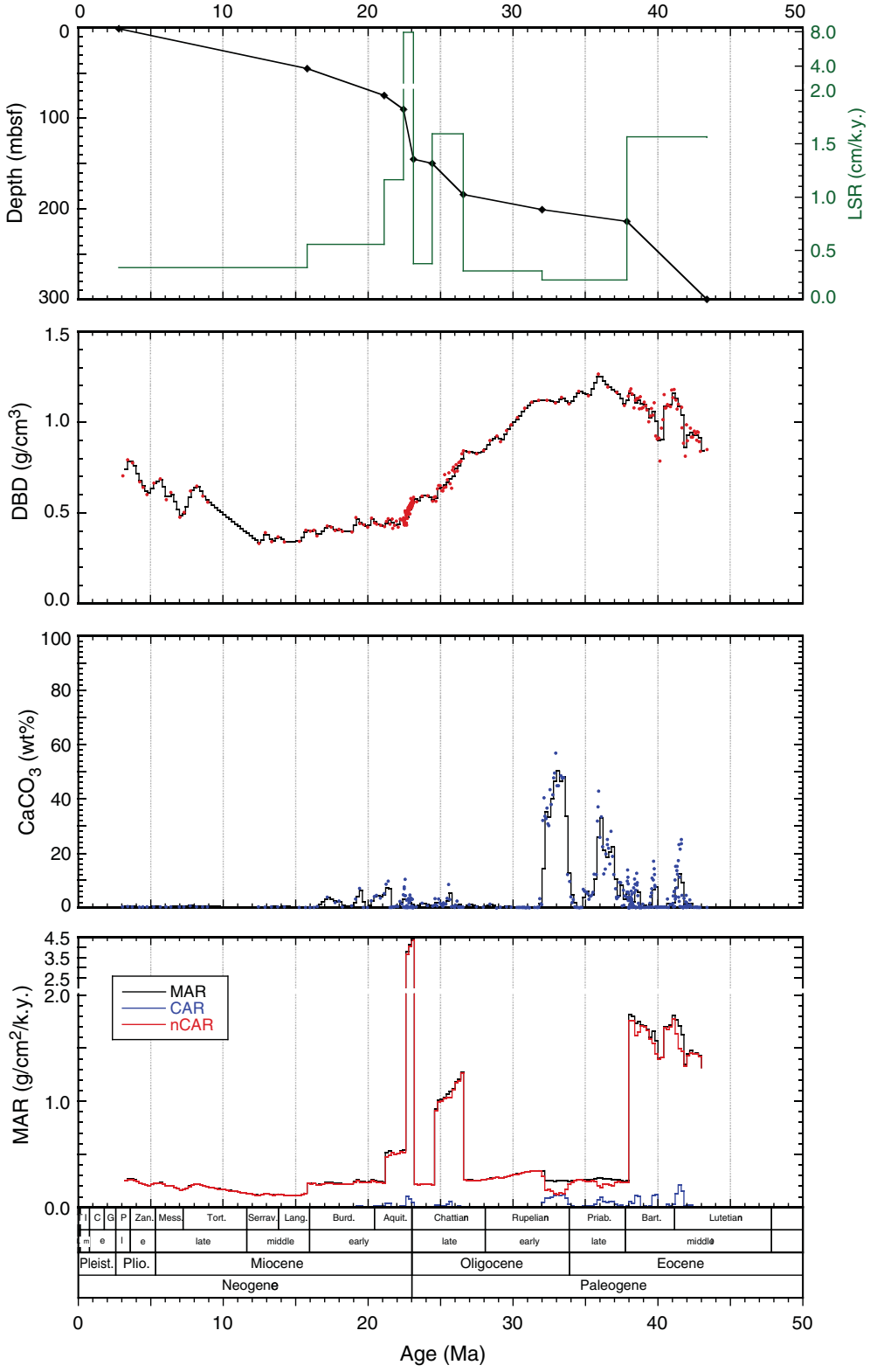

Figure F28. Plots of interstitial water constituent concentrations, Hole U1404A. IC = ion chromatography.

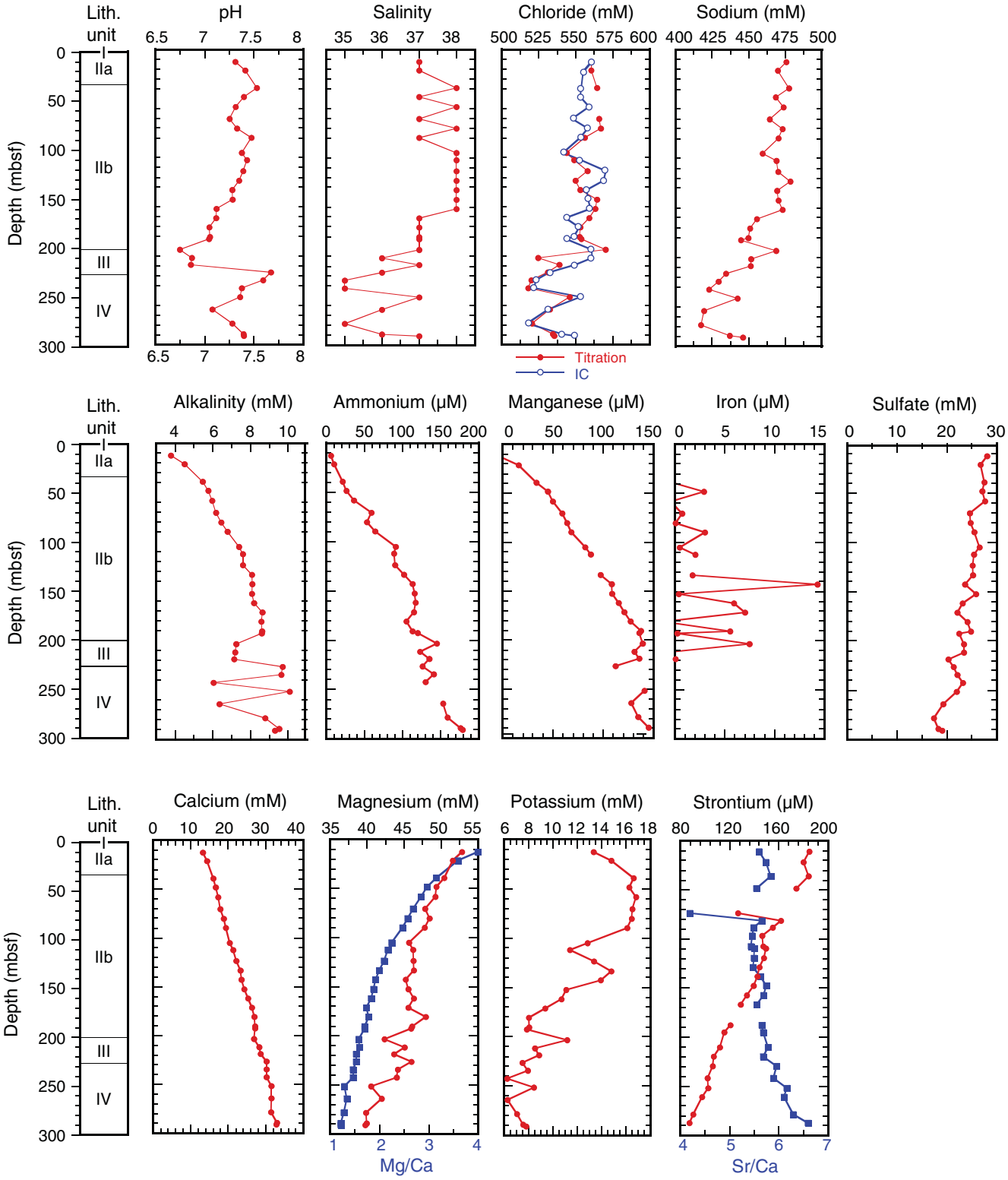

Figure F29. Plots of headspace sample (HS) methane content and interstitial water (IW) pH, chlorinity, and alkalinity, Hole U1404C. Core recovery: gray = washed interval, black = recovered, red = overlap.

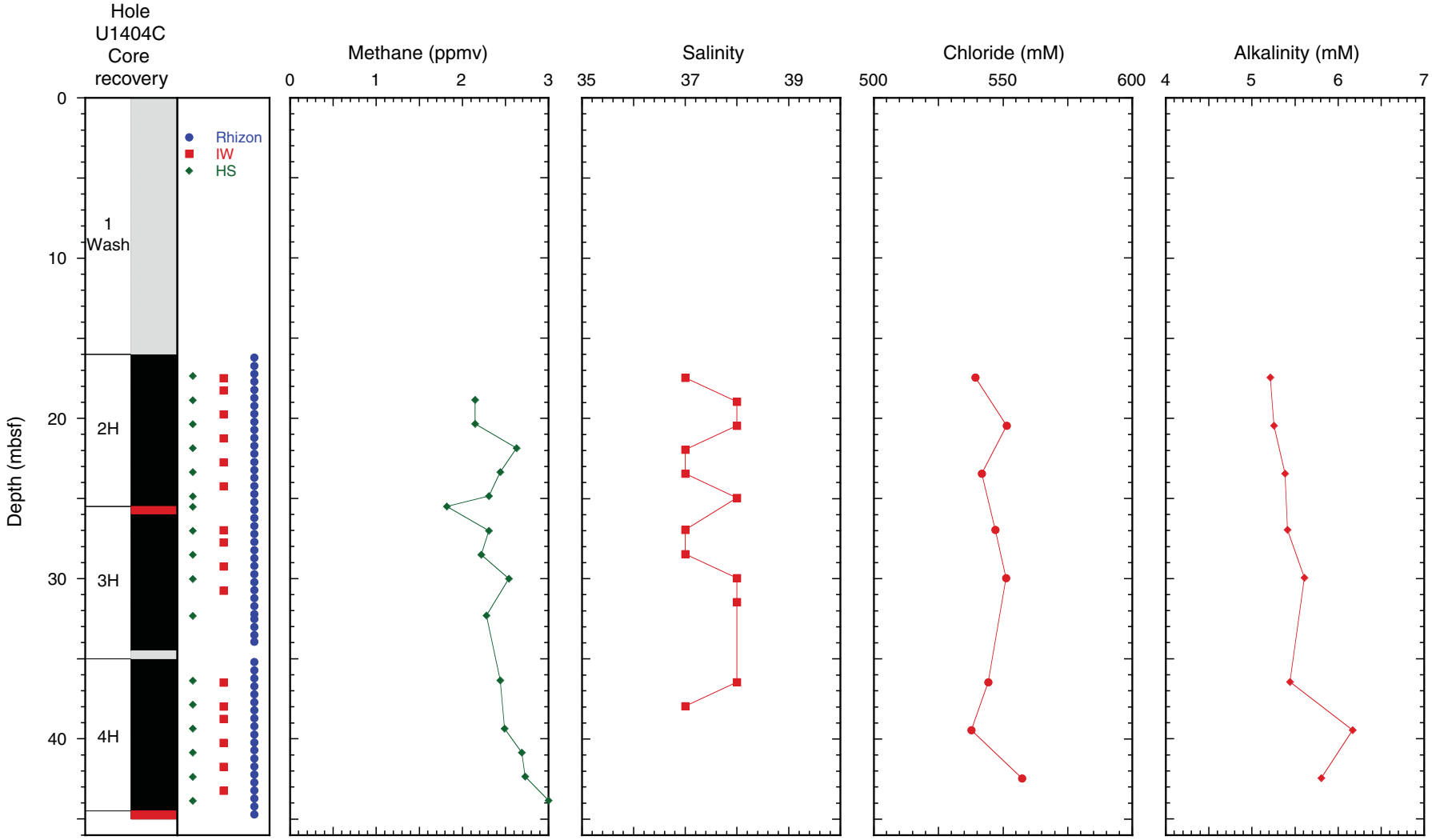

Figure F30. Plots of sedimentary carbon content, Hole U1404A. Core recovery: black = recovered, gray = not recover, red = overlap. TOC = total organic carbon.

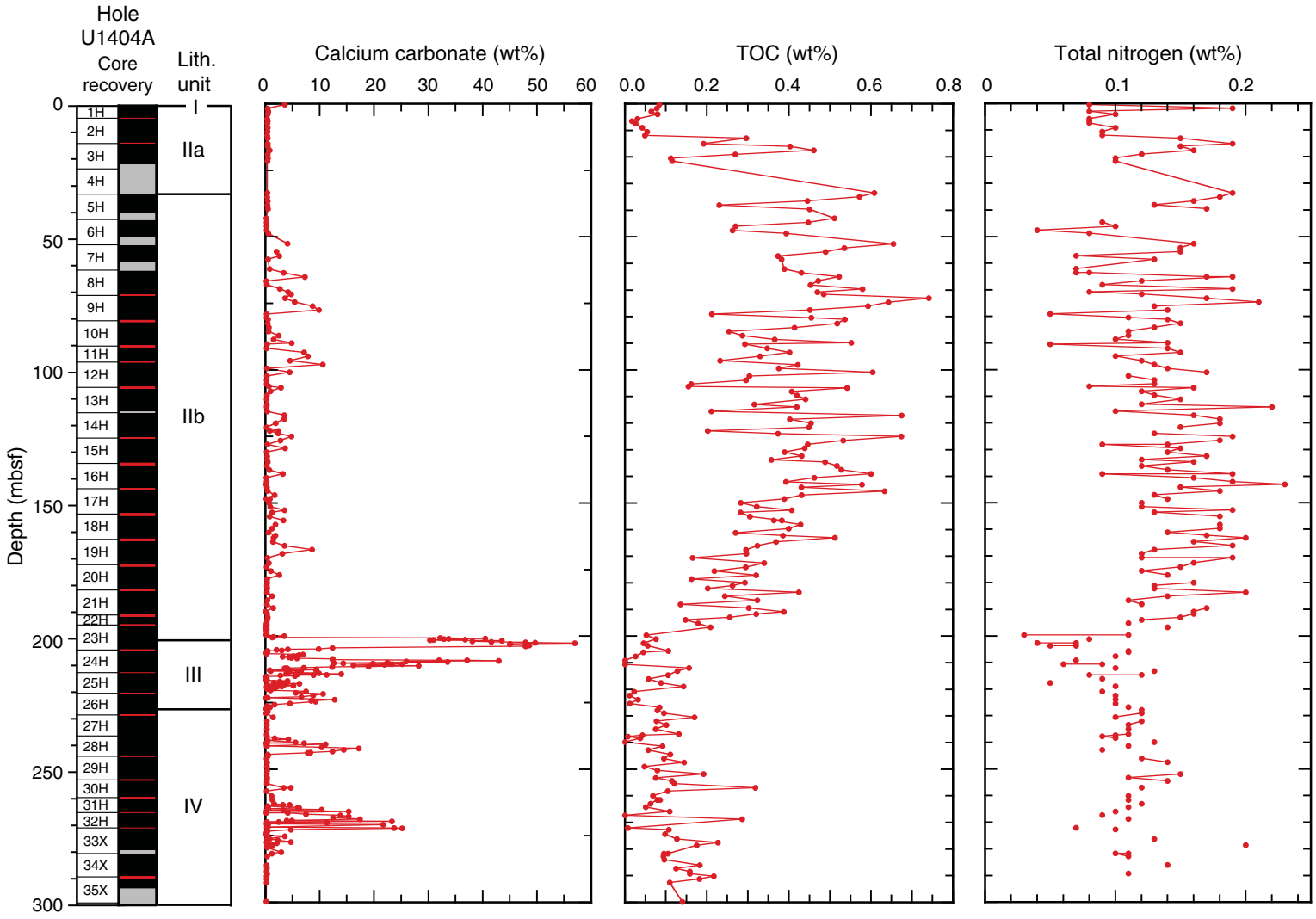

Figure F31. Core image and plot of carbonate data through the expanded uppermost Eocene to lowermost Oligocene sequence, Hole U1404A.

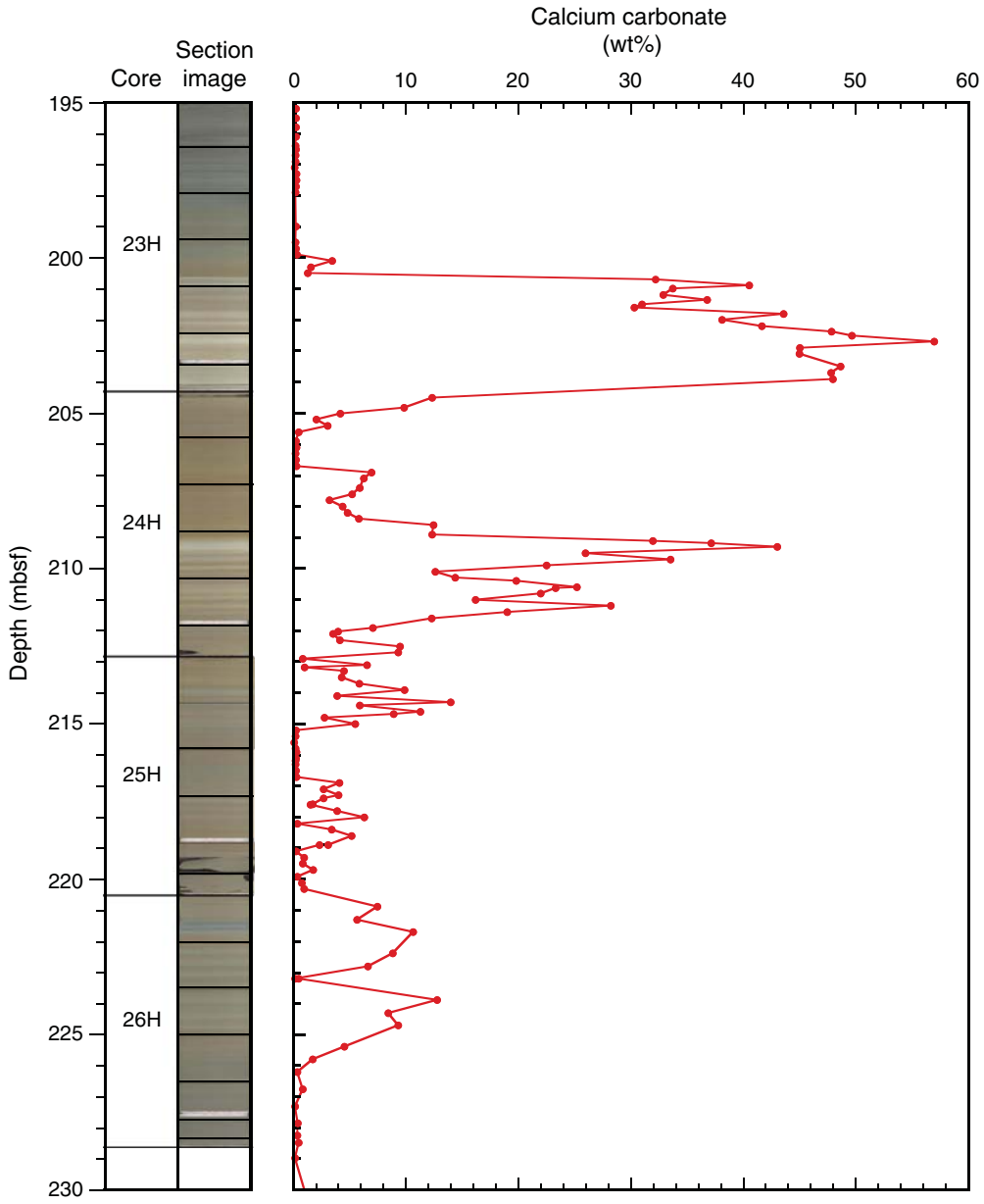

Figure F32. Core image and plot of carbonate data through the expanded Middle Eocene Climatic Optimum sequence, Hole U1404A. FAD = first abundant disappearance, CAE-3 = carbonate accumulation Event 3.

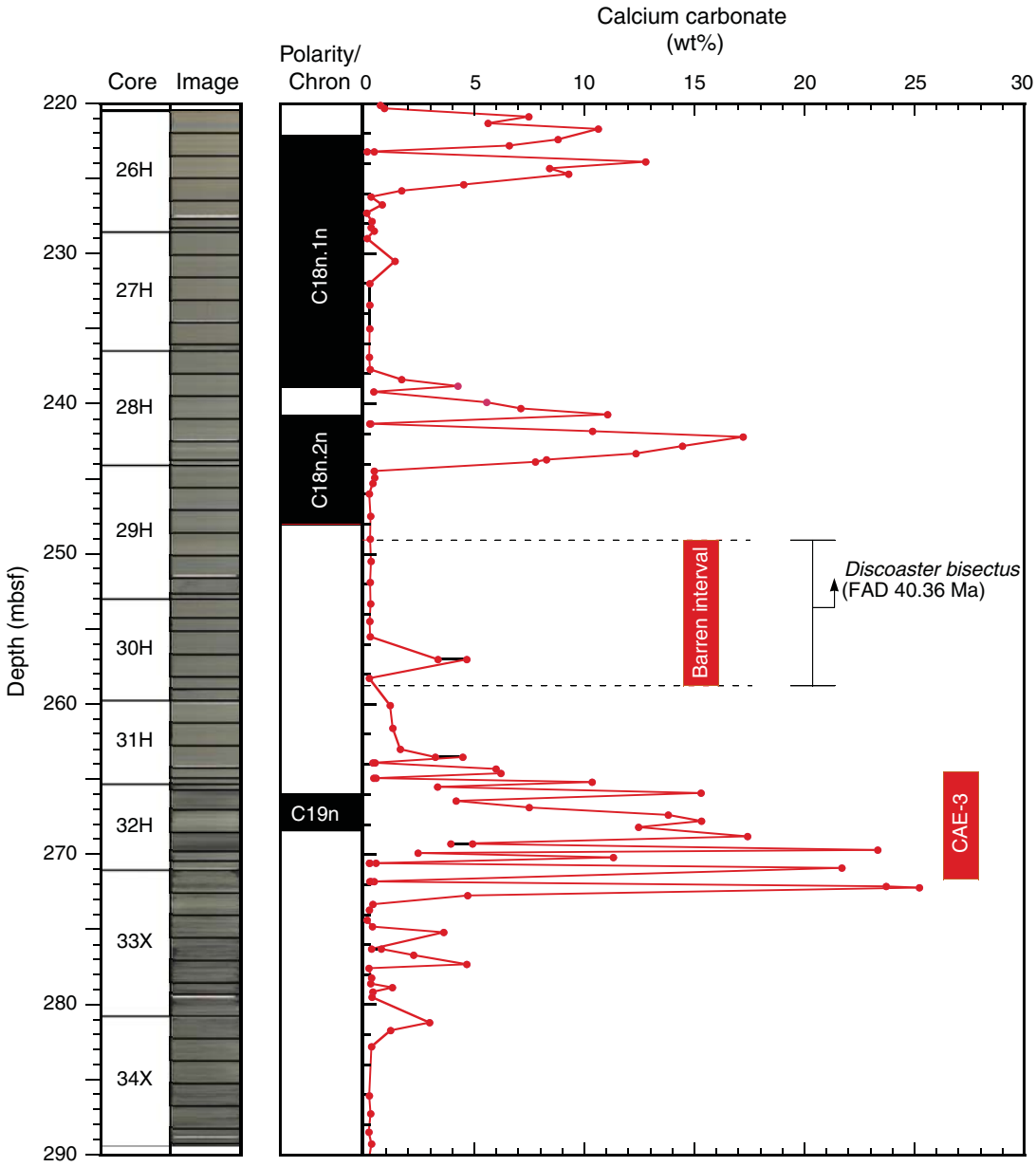

Figure F33. Plots of magnetic susceptibility (MS), bulk density (gray line = GRA density from Whole-Round Multisensor Logger, circles = moisture and density analysis from discrete samples), water content, porosity, and grain density, Site U1404. Green = data from Hole U1404C. Core recovery: black = recovered, white = not recovered, red = overlap. Horizontal gray lines indicate lithostratigraphic unit boundaries (see **"Lithostratigraphy"**). APC = advanced piston corer, XCB = extended core barrel.

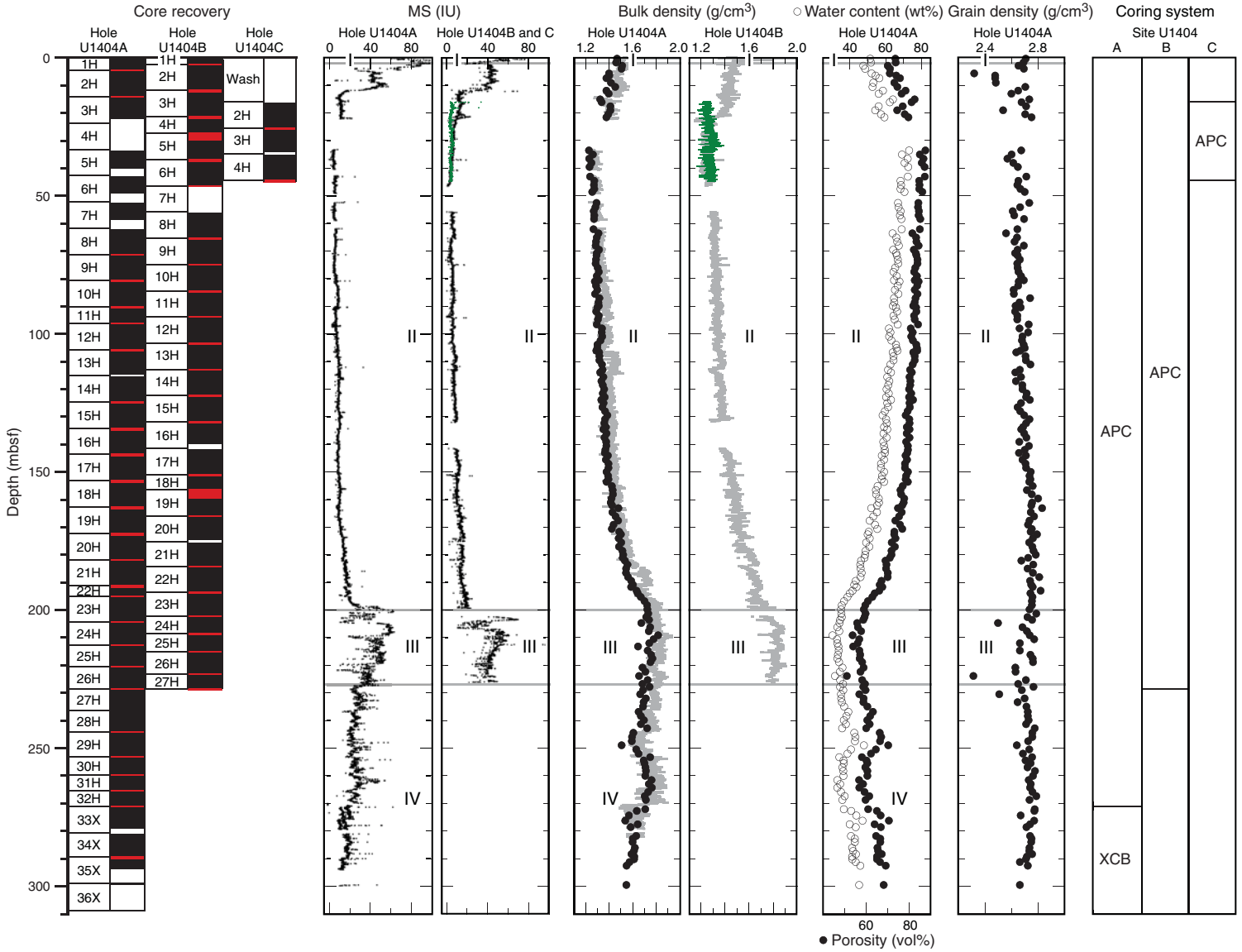

Figure F34. Plots of magnetic susceptibility (MS), *P*-wave velocity (gray line = *P*-wave logger data from whole-round sections, black circles = section-half caliper data, and natural gamma radiation (NGR), Site U1404. Green = data from Hole U1404C. Core recovery: black = recovered, white = not recovered, red = overlap. Horizontal gray lines indicate lithostratigraphic unit boundaries (see **"Lithostratigraphy"**). APC = advanced piston corer, XCB = extended core barrel.

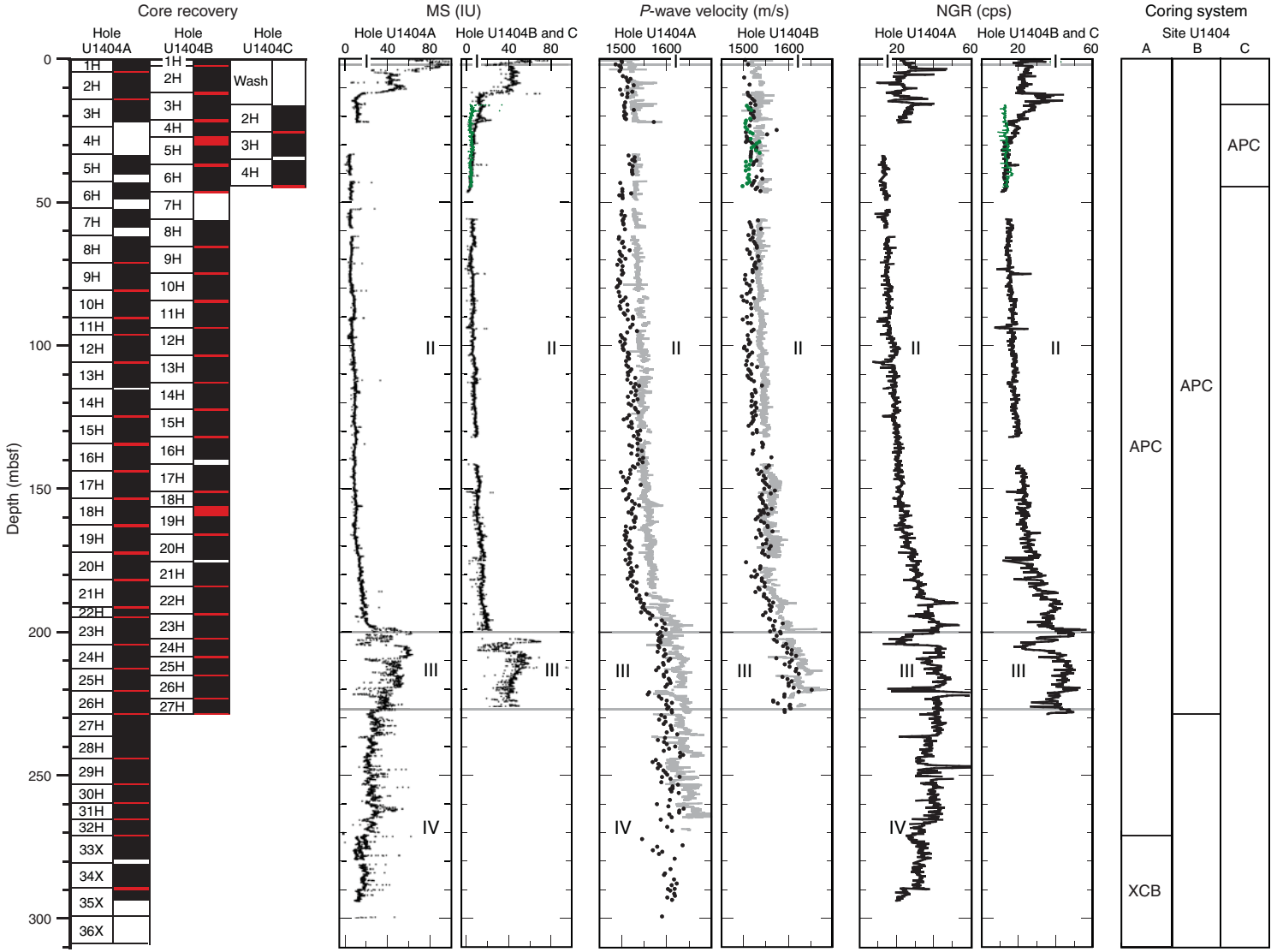

Figure F35. Plots of magnetic susceptibility (MS) and color reflectance, Site U1404. Green = data from Hole U1404C. Core recovery: black = recovered, white = not recovered, red = overlap. Horizontal gray lines indicate lithostratigraphic unit boundaries (see **"Lithostratigraphy"**). APC = advanced piston corer, XCB = extended core barrel.

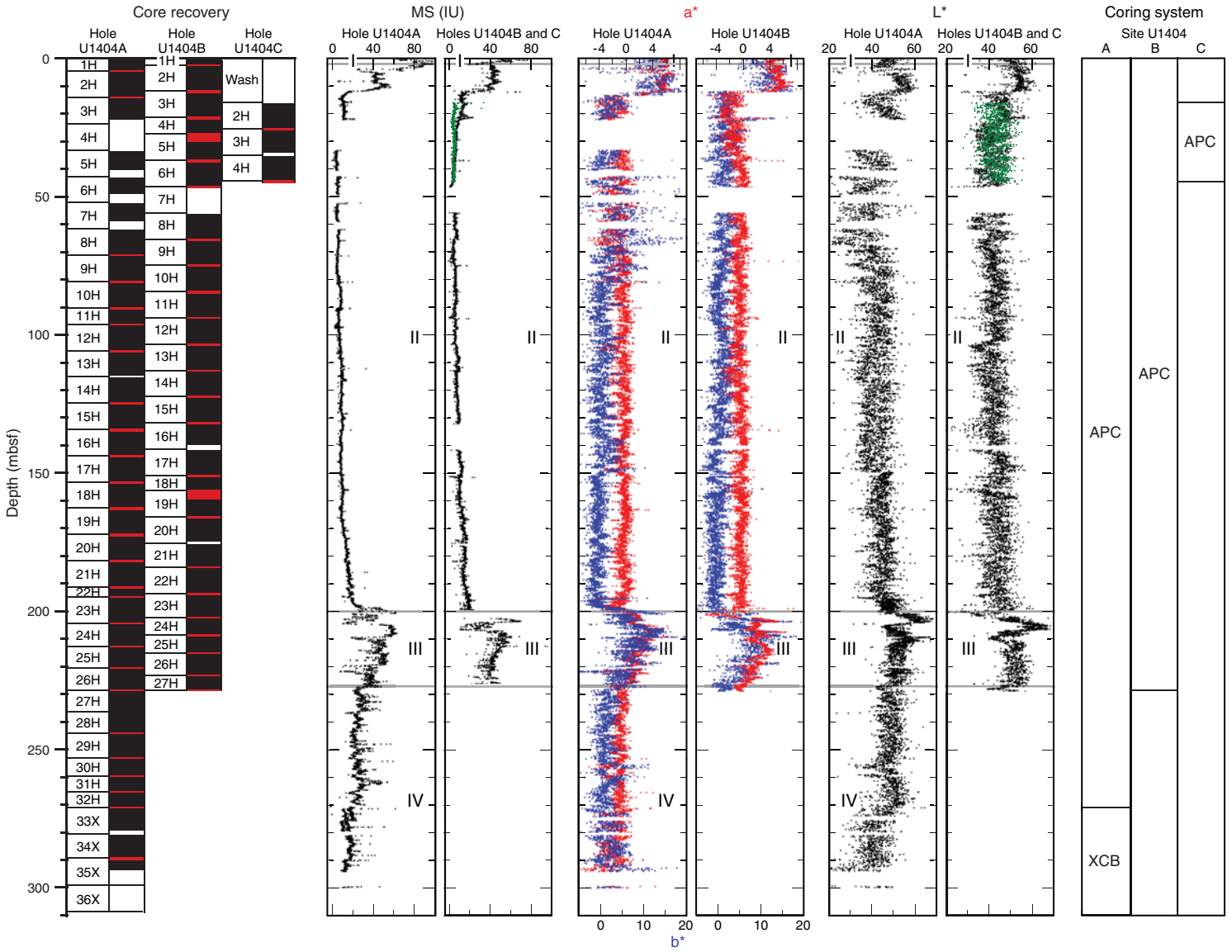

Figure F36. Plot of mbsf depth vs. CCSF depth for core tops, Site U1404. The growth factor is equal to the slope of the regression line.

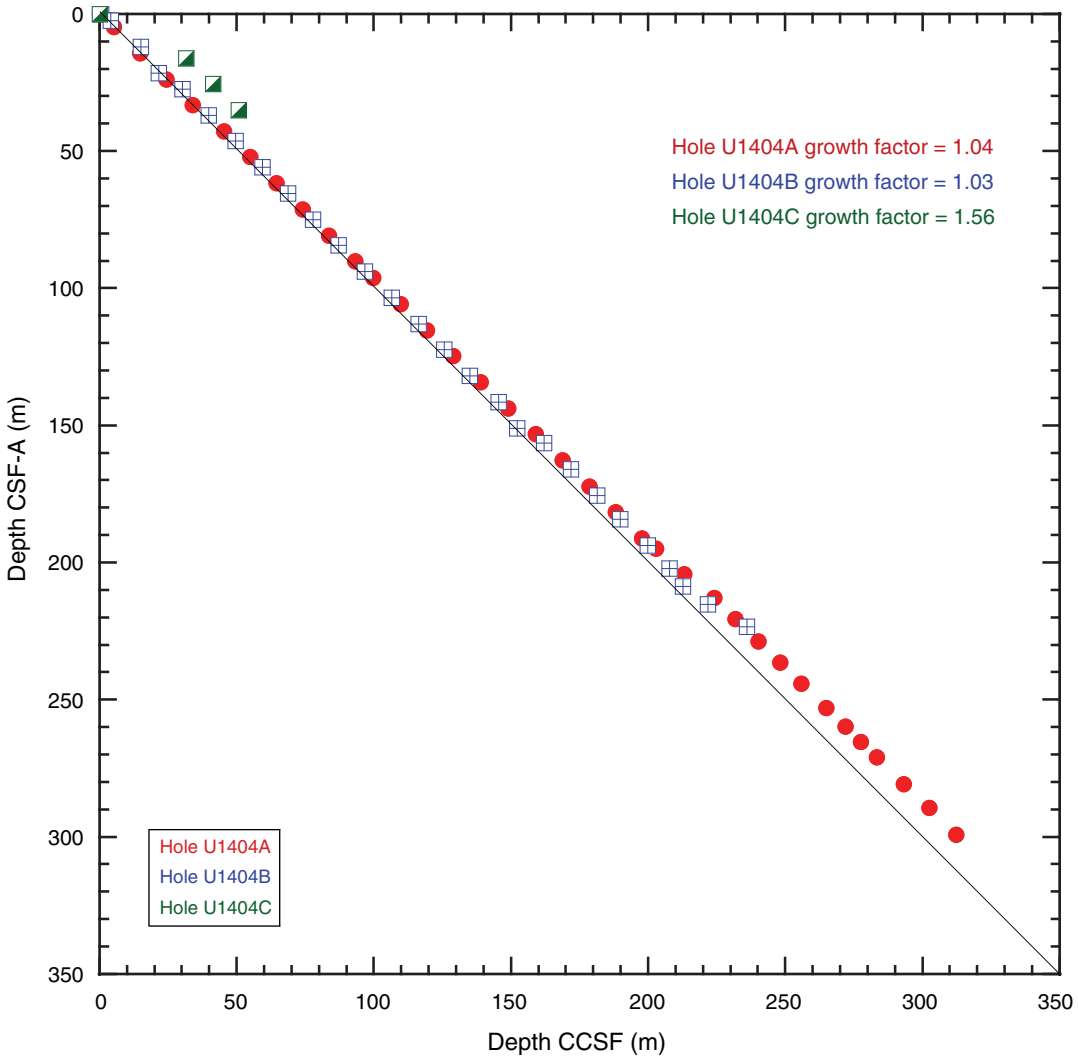

Figure F37. Plots of color reflectance data, Site U1404. Top panels show the spliced section for each interval of the splice. Bottom panels show all complete color reflectance b* records. Data from Holes U1404B and U1404C are offset by 20 and 40, respectively, to aid visualization. Open circles indicate core tops, excluding culled data from disturbed intervals. **A.** 0–50 m CCSF. (Continued on next six pages.)

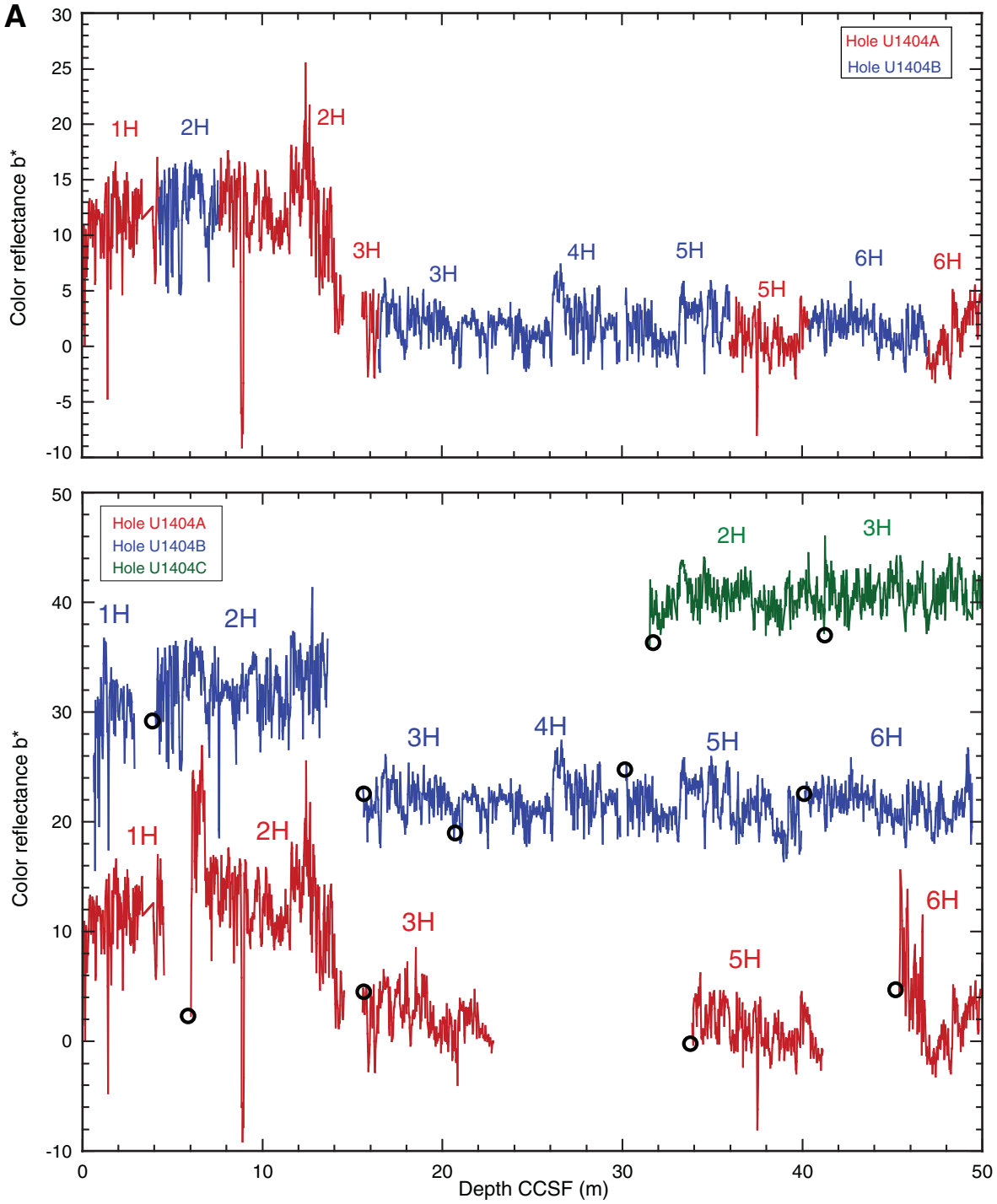

Figure F37 (continued). B. 50–100 m CCSF. (Continued on next page.)

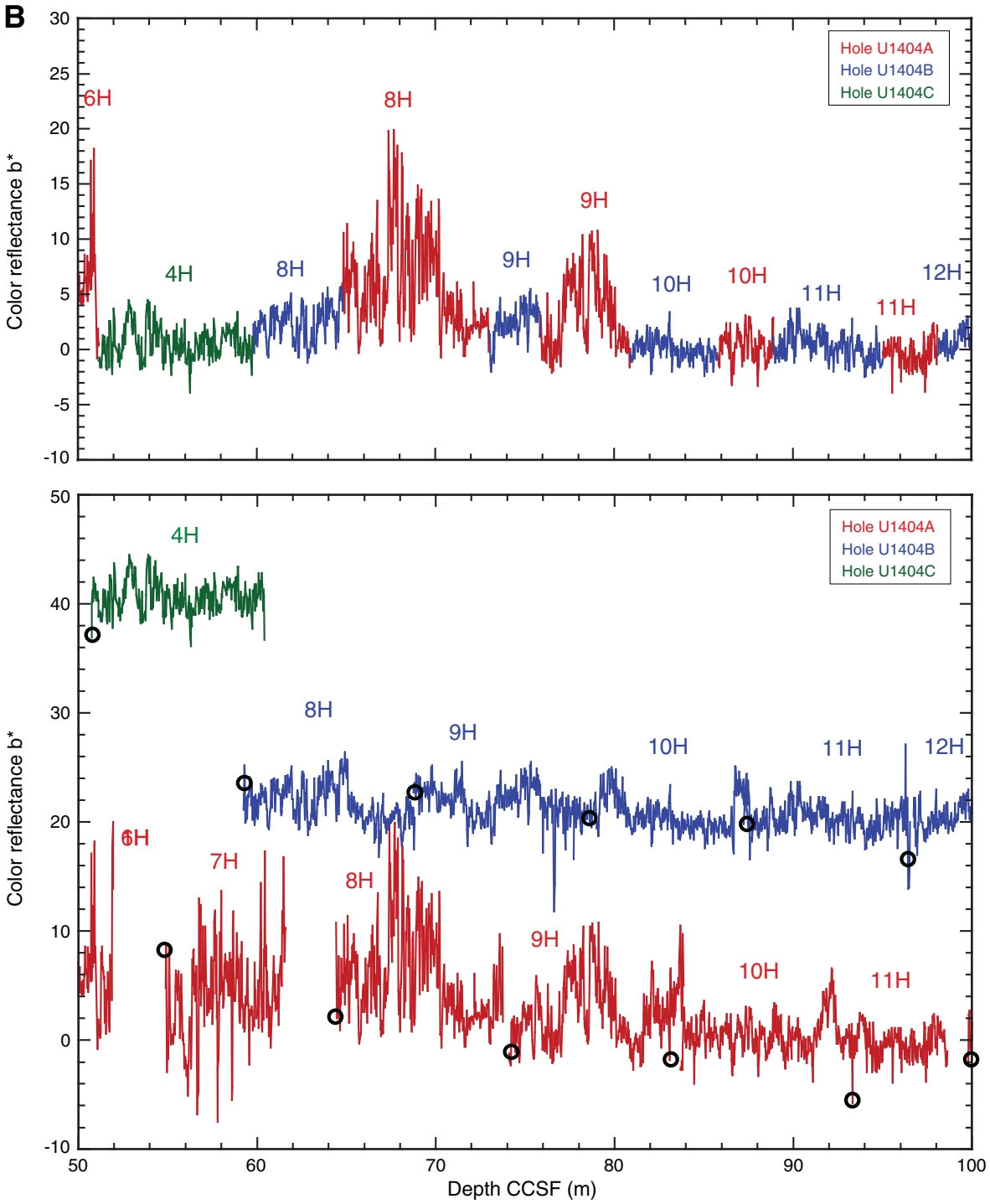

Figure F37 (continued). C. 100–150 m CCSF. (Continued on next page.)

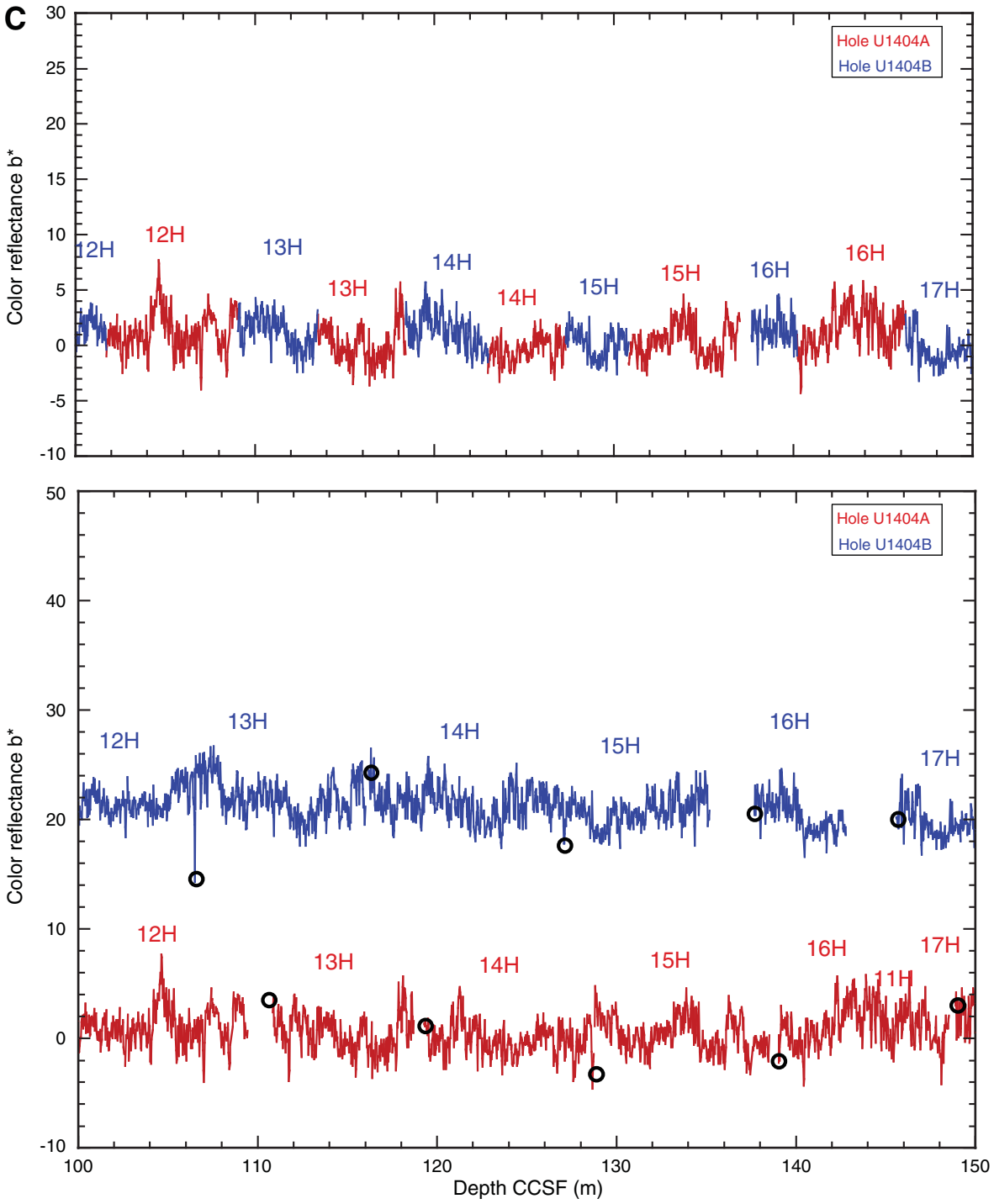

Figure F37 (continued). D. 150–200 m CCSF. (Continued on next page.)

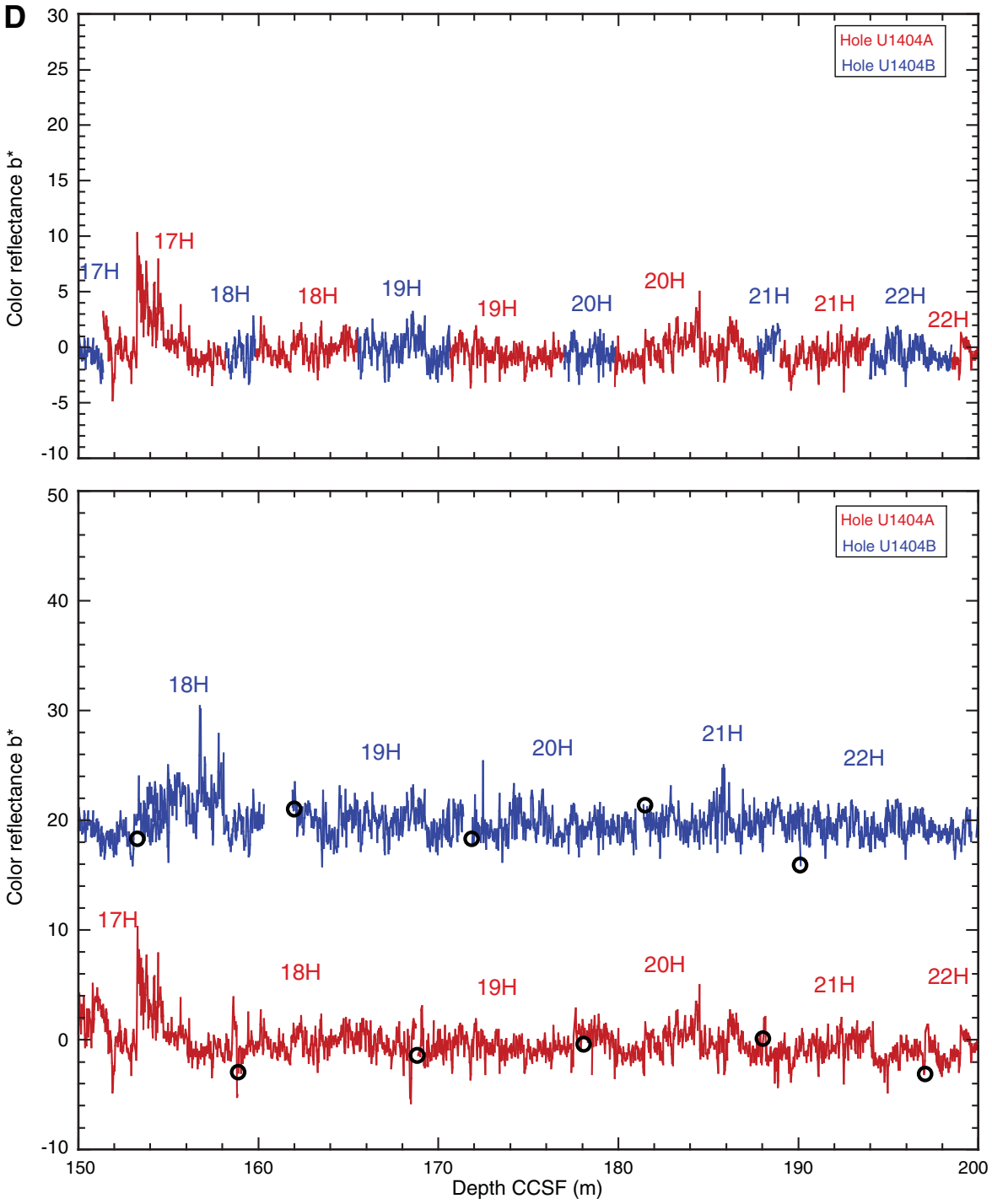

Figure F37 (continued). E. 200–250 m CCSF. (Continued on next page.)

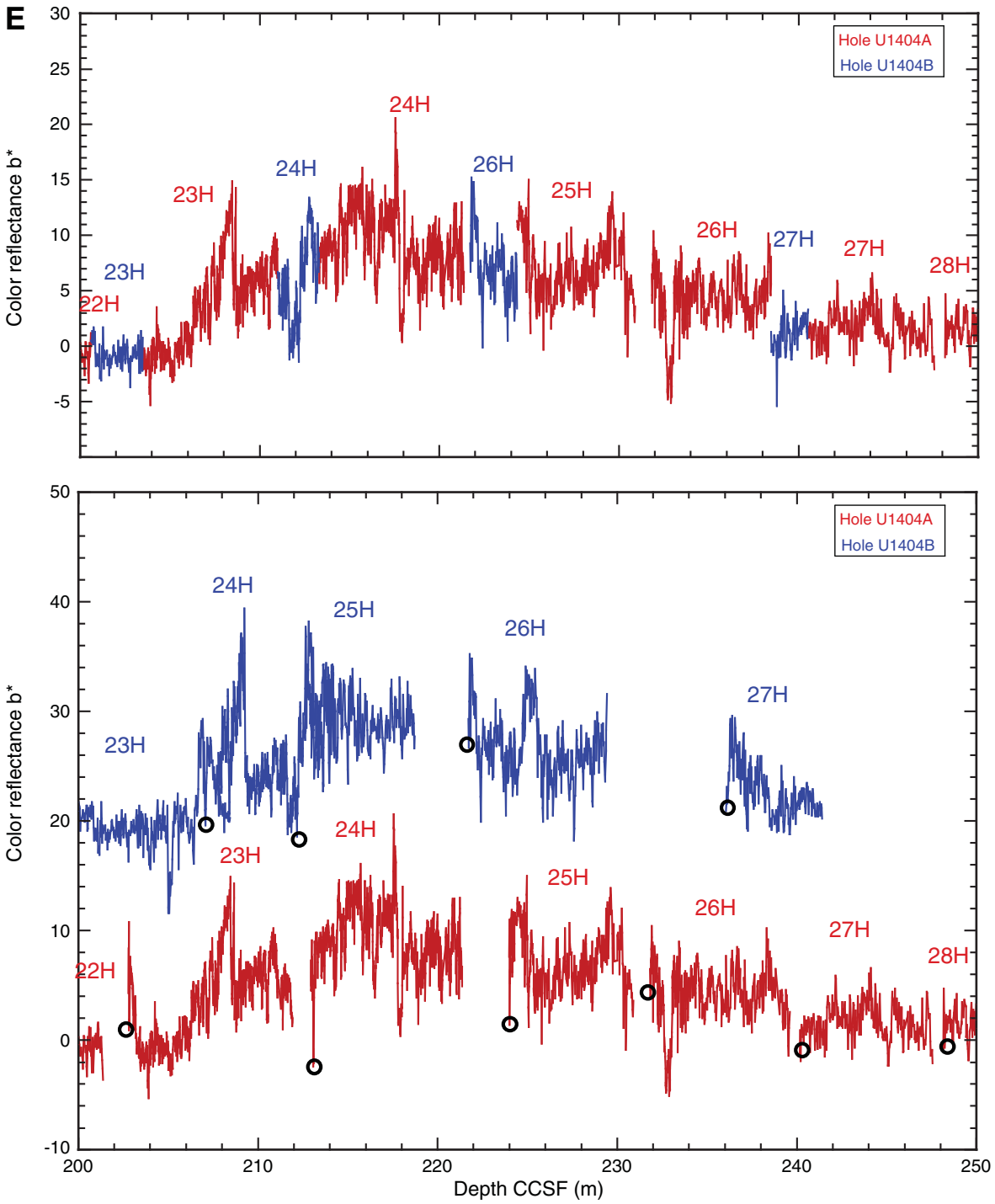

Figure F37 (continued). **F.** 250–300 m CCSF. **G.** 300–350 m CCSF.

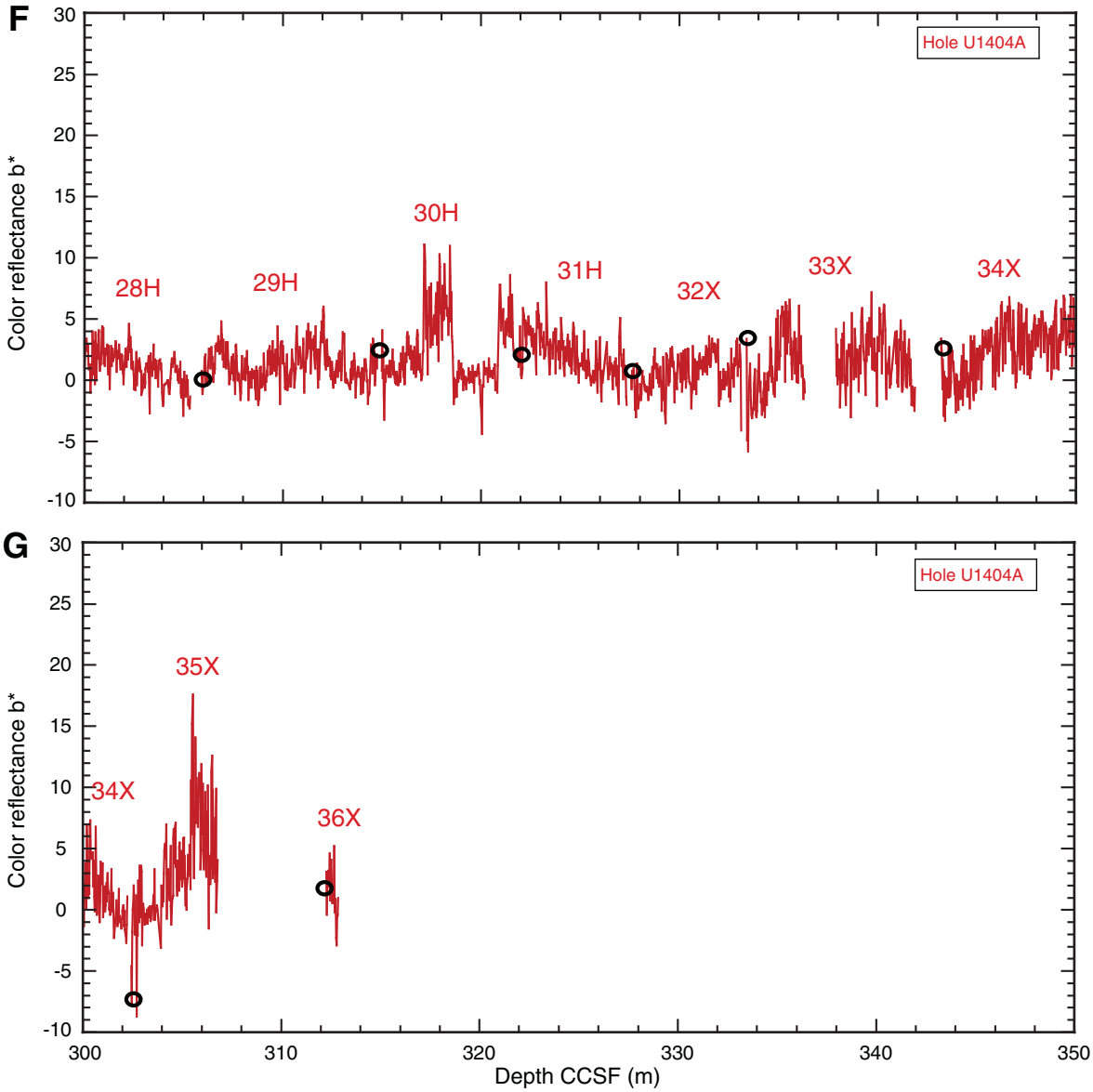

Figure F38. Plots of postcruise X-ray fluorescence Fe/Ca measurements, Site U1404. Top panels show the spliced section for each interval of the splice. Bottom panels show all complete Fe/Ca records. Data from Hole U1404B is offset by 20 to aid visualization. Open circles indicate core tops, excluding culled data from disturbed intervals. **A.** 150–200 m CCSF. (Continued on next page.)

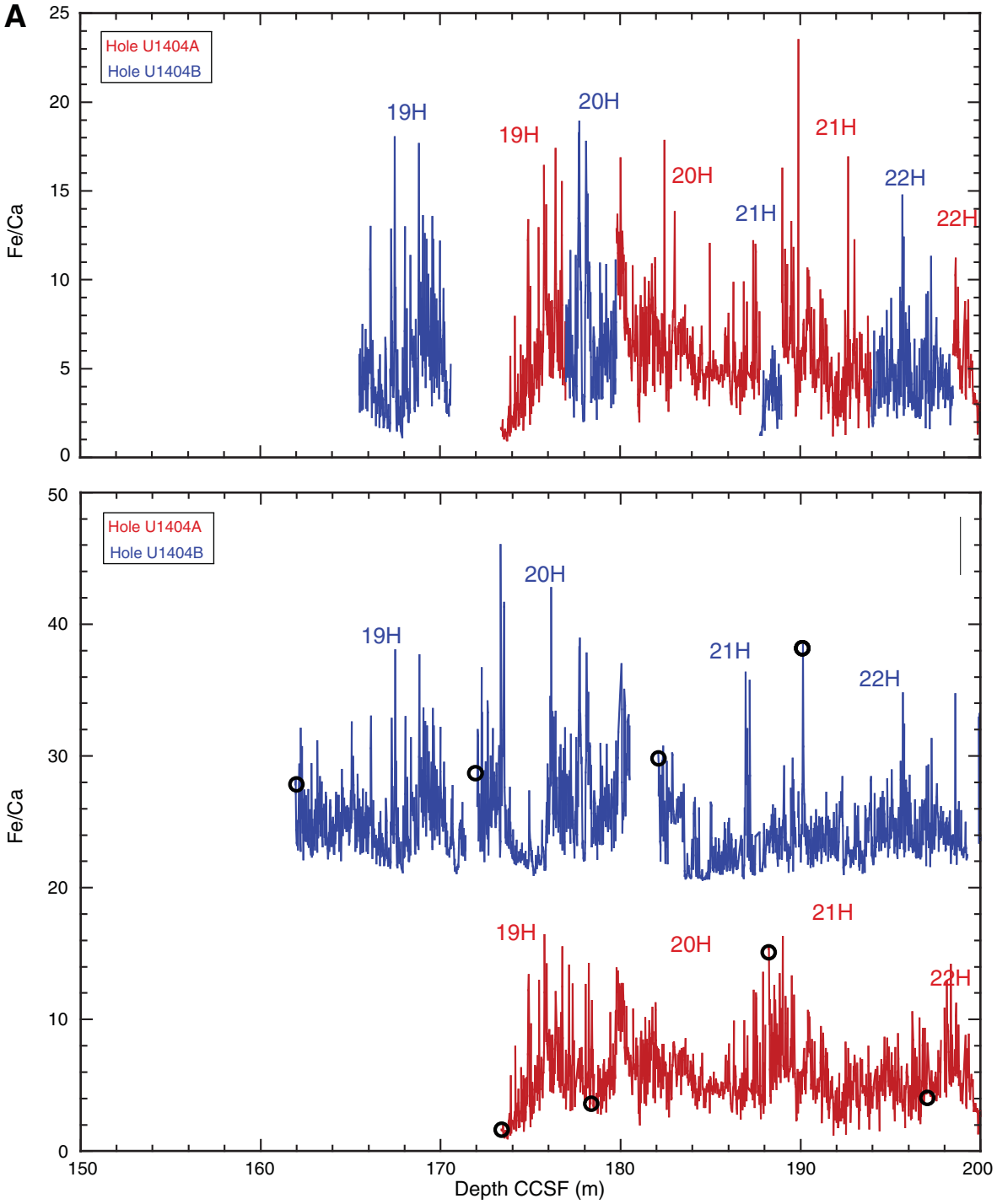

Figure F38 (continued). B. 200–250 m CCSF.

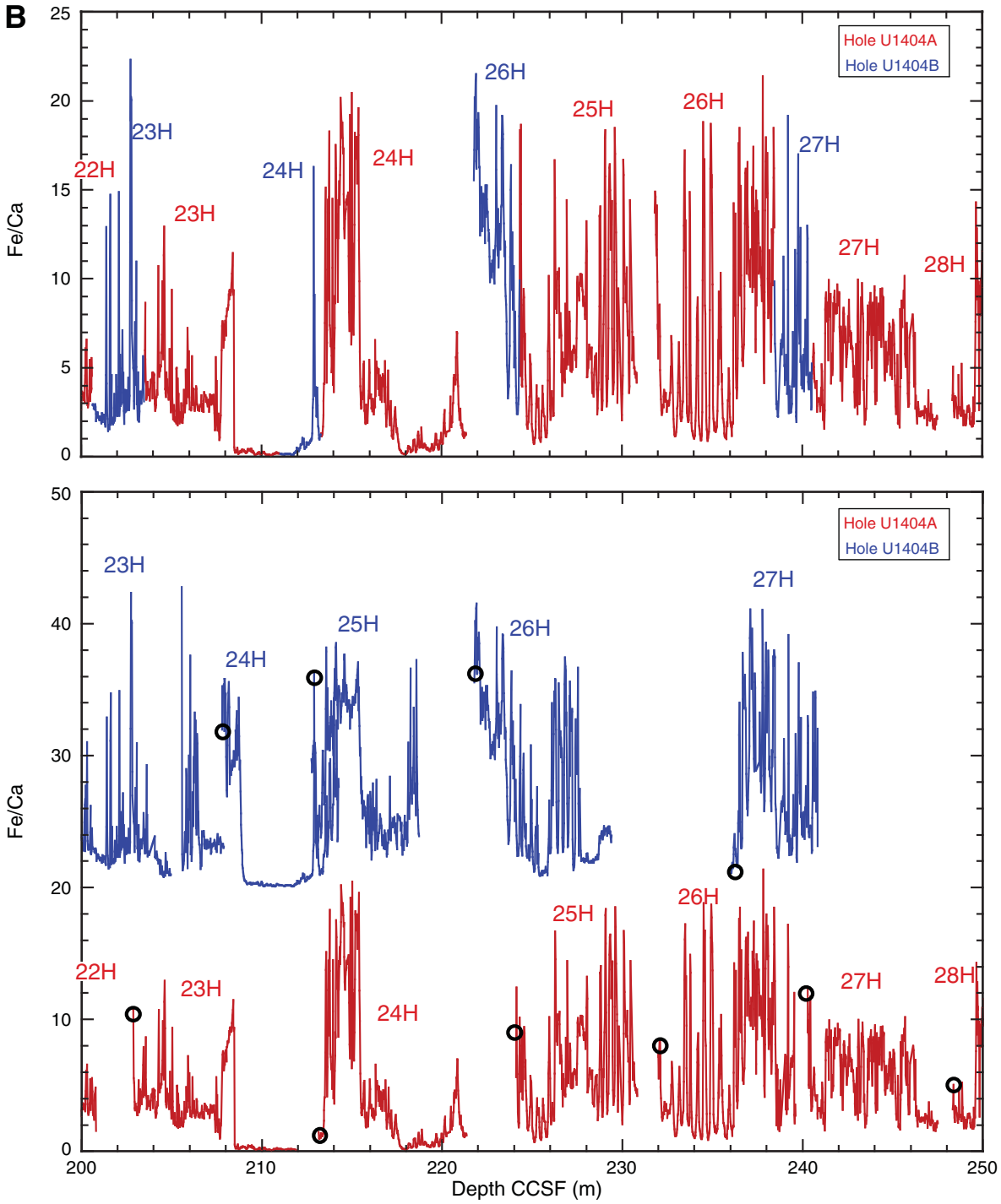

Table T1. Coring summary, Site U1404. (Continued on next page.)

Core	Date (2012)	Time UTC (h)	Depth DSF (m) Top of cored interval	Depth DSF (m) Bottom of cored interval	Interval cored (m)	Curated length (m)	Depth CSF-A (m) Top of core	Depth CSF-A (m) Bottom of core	Recovery (%)	Sections (*N*)
342-U1404A-										
1H	20 Jun	1320	0.0	4.7	4.7	4.72	0.00	4.72	100	5
2H	20 Jun	1450	4.7	14.2	9.5	9.53	4.70	14.23	100	8
3H	20 Jun	1605	14.2	23.7	9.5	8.18	14.20	22.38	86	7
4H	20 Jun	1715	23.7	33.2	9.5	0.00	23.70	23.70	0	0
5H	20 Jun	1845	33.2	42.7	9.5	7.41	33.20	40.61	78	6
6H	20 Jun	2000	42.7	52.2	9.5	6.68	42.70	49.38	70	6
7H	20 Jun	2130	52.2	61.7	9.5	6.93	52.20	59.13	73	6
8H	20 Jun	2245	61.7	71.2	9.5	9.60	61.70	71.30	101	8
9H	20 Jun	2350	71.2	80.7	9.5	9.88	71.20	81.08	104	8
10H	21 Jun	0105	80.7	90.2	9.5	9.89	80.70	90.59	104	8
11H	21 Jun	0210	90.2	96.2	6.0	6.06	90.20	96.26	101	5
12H	21 Jun	0545	96.2	105.7	9.5	9.88	96.20	106.08	104	8
13H	21 Jun	0655	105.7	115.2	9.5	9.40	105.70	115.10	99	8
14H	21 Jun	0825	115.2	124.7	9.5	9.69	115.20	124.89	102	8
15H	21 Jun	0945	124.7	134.2	9.5	10.03	124.70	134.73	106	8
16H	21 Jun	1125	134.2	143.7	9.5	9.82	134.20	144.02	103	8
17H	21 Jun	1240	143.7	153.2	9.5	10.04	143.70	153.74	106	8
18H	21 Jun	1350	153.2	162.7	9.5	10.02	153.20	163.22	105	8
19H	21 Jun	1500	162.7	172.2	9.5	10.09	162.70	172.79	106	8
20H	21 Jun	1615	172.2	181.7	9.5	9.81	172.20	182.01	103	8
21H	21 Jun	1735	181.7	191.2	9.5	10.03	181.70	191.73	106	8
22H	21 Jun	1850	191.2	194.9	3.7	3.78	191.20	194.98	102	4
23H	21 Jun	2100	194.9	204.3	9.4	9.47	194.90	204.37	101	8
24H	21 Jun	2300	204.3	212.8	8.5	8.51	204.30	212.81	100	6
25H	22 Jun	0015	212.8	220.5	7.7	7.73	212.80	220.53	100	6
26H	22 Jun	0200	220.5	228.6	8.1	8.21	220.50	228.71	101	7
27H	22 Jun	0310	228.6	236.5	7.9	7.90	228.60	236.50	100	6
28H	22 Jun	0440	236.5	244.1	7.6	7.63	236.50	244.13	100	6
29H	22 Jun	0555	244.1	253.0	8.9	8.98	244.10	253.08	101	7
30H	22 Jun	0715	253.0	259.7	6.7	6.75	253.00	259.75	101	6
31H	22 Jun	0900	259.7	265.3	5.6	5.61	259.70	265.31	100	5
32H	22 Jun	1035	265.3	271.0	5.7	5.71	265.30	271.01	100	6
33X	22 Jun	1430	271.0	280.7	9.7	8.58	271.00	279.58	88	7
34X	22 Jun	1630	280.7	289.4	8.7	9.15	280.70	289.85	105	7
35X	22 Jun	1910	289.4	299.1	9.7	4.60	289.40	294.00	47	4
36X	22 Jun	2130	299.1	308.8	9.7	0.72	299.10	299.82	7	1
				Totals:	308.8	281.02			92	233
342-U1404B-										
1H	23 Jun	0155	0.0	2.4	2.4	2.48	0.00	2.48	103	3
2H	23 Jun	0315	2.4	11.9	9.5	9.90	2.40	12.30	104	8
3H	23 Jun	0415	11.9	21.4	9.5	10.06	11.90	21.96	106	8
4H	23 Jun	0520	21.4	27.4	6.0	8.41	21.40	29.81	140	7
5H	23 Jun	0620	27.4	36.9	9.5	10.04	27.40	37.44	106	8
6H	23 Jun	0720	36.9	46.4	9.5	9.68	36.90	46.58	102	8
7H	23 Jun	0825	46.4	55.9	9.5	0.00	46.40	46.40	0	0
8H	23 Jun	0930	55.9	65.4	9.5	9.91	55.90	65.81	104	8
9H	23 Jun	1125	65.4	74.9	9.5	9.67	65.40	75.07	102	8
10H	23 Jun	1320	74.9	84.4	9.5	9.95	74.90	84.85	105	8
11H	23 Jun	1430	84.4	93.9	9.5	9.51	84.40	93.91	100	8
12H	23 Jun	1535	93.9	103.4	9.5	9.86	93.90	103.76	104	8
13H	23 Jun	1640	103.4	112.9	9.5	9.63	103.40	113.03	101	8
14H	23 Jun	1740	112.9	122.4	9.5	9.56	112.90	122.46	101	8
15H	23 Jun	1845	122.4	131.9	9.5	9.70	122.40	132.10	102	8
16H	23 Jun	1950	131.9	141.4	9.5	8.39	131.90	140.29	88	8
17H	23 Jun	2135	141.4	150.9	9.5	9.84	141.40	151.24	104	8
18H	23 Jun	2240	150.9	156.4	5.5	8.54	150.90	159.44	155	7
19H	23 Jun	2350	156.4	165.9	9.5	9.75	156.40	166.15	103	8
20H	24 Jun	0105	165.9	175.4	9.5	9.17	165.90	175.07	97	8
21H	24 Jun	0215	175.4	184.1	8.7	8.79	175.40	184.19	101	9
22H	24 Jun	0415	184.1	193.6	9.5	9.83	184.10	193.93	103	8
23H	24 Jun	0550	193.6	202.2	8.6	8.68	193.60	202.28	101	8
24H	24 Jun	0800	202.2	208.7	6.5	6.58	202.20	208.78	101	6

Table T1 (continued).

Core	Date (2012)	Time UTC (h)	Depth DSF (m) Top of cored interval	Depth DSF (m) Bottom of cored interval	Interval cored (m)	Curated length (m)	Depth CSF-A (m) Top of core	Depth CSF-A (m) Bottom of core	Recovery (%)	Sections (*N*)
25H	24 Jun	0915	208.7	215.2	6.5	6.53	208.70	215.23	100	6
26H	24 Jun	1035	215.2	223.3	8.1	8.13	215.20	223.33	100	7
27H	24 Jun	1200	223.3	228.7	5.4	5.45	223.30	228.75	101	6
				Totals:	228.7	228.04			101	195
342-U1404C-										
11	24 Jun	1735			****Drilled from 0.0 to 10.0 m DSF****					
2H	24 Jun	1930	16.0	25.5	9.5	9.96	16.00	25.96	105	8
3H	24 Jun	2040	25.5	35.0	9.5	9.01	25.50	34.51	95	8
4H	24 Jun	2140	35.0	44.5	9.5	10.01	35.00	45.01	105	8
				Totals:	44.5	28.98			76	24
				Site U1404 totals:	582.0	538.04			90	452

DSF = drilling depth below seafloor, CSF-A = core depth below seafloor, method A. H = advanced piston core, X = extended core barrel core, numeric core type = drilled interval.

Table T2. Lithostratigraphic unit intervals, Site U1404.

Lith. unit	Core, section, interval (cm) Top	Core, section, interval (cm) Bottom	Depth (mbsf) Top	Depth (mbsf) Bottom
	342-U1404A-	342-U1404A-		
I	Not recovered			
IIa	1H-1, 0	3H-CC, 11	0.00	22.32
IIb	5H-1, 0	23H-4, 120	33.20	200.60
III	23H-4, 122	26H-5, 0	200.62	226.50
IV	26H-6, 0	36X-1, 72*	226.50	299.82
	342-U1404B-	342-U1404B-		
I	1H-1, 0	1H-2, 83	0.00	2.33
IIa	2H-1, 0	4H-2, 150	2.40	24.40
IIb	4H-3, 0	24H-1, 136	24.40	203.56
III	24H-1, 136	27H-2, 100	203.56	225.11
IV	27H-3, 0	27H-CC, 62*	225.11	228.75
	342-U1404C-	342-U1404C-		
I	Drilled but not cored			
II	Drilled but not cored			
IIb	2H-1, 0	4H-CC, 29	16.00	45.01

* = end of hole.

Table T3. Calcareous nannofossil datums, Site U1404.

Hole, core, section, interval (cm)		Age	Zone	Marker species	Age (Ma)	Depth (mbsf)			
Top	Bottom					Top	Bottom	Mid-point	±
342-	342-								
		Pliocene–Pleistocene							
U1404B-1H-1, 40	U1404B-1H-1, 135			B *Gephyrocapsa* (>5.5 µm)	1.62	0.41	1.35	0.88	0.47
U1404B-1H-1, 40	U1404B-1H-1, 135			T *Discoaster tamalis*	2.80	0.41	1.35	0.88	0.47
U1404B-1H-2, 45	U1404B-1H-CC			T *Sphenolithus* spp.	3.54	1.96	2.46	2.205	0.25
U1404B-1H-2, 45	U1404B-1H-CC		NN16	T *Reticulofenestra pseudoumbilicus*	3.70	1.96	2.46	2.205	0.25
		Miocene							
U1404A-5H-CC*	U1404A-6H-CC			Tc *Discoaster deflandrei*	15.80	40.59	49.36	44.97	4.38
U1404A-7H-CC	U1404A-8H-3, 115		NN3	T *Triquetrorhabdulus carinatus*	18.28	59.11	65.86	62.48	3.38
U1404A-12H-CC	U1404A-13H-2, 100			B? *Sphenolithus disbelemnos*	22.76	106.06	107.23	106.64	0.59
U1404A-15H-6, 100	U1404A-15H-CC		NN2	B *Discoaster druggii*	22.82	133.03	134.71	133.87	0.84
U1404A-16H-CC*	U1404A-17H-2, 55			T *Dictyococcites bisectus* (>10 µm)	23.13	144.00	145.76	144.88	0.88
U1404A-17H-2, 55	U1404A-17H-CC		NN1	T *Sphenolithus ciperoensis*	24.43	145.76	153.72	149.74	3.98
		Oligocene							
U1404B-20H-CC	U1404B-21H-CC			T *Sphenolithus distentus*	26.44	175.05	184.17	179.61	4.56
U1404B-20H-CC	U1404A-21H-3, 93			Bc *Triquetrorhabdulus carinatus*	26.57	181.99	185.63	183.81	1.82
U1404A-21H-3, 93	U1404B-21H-CC*		NP24	B *Sphenolithus ciperoensis*	29.62	185.63	191.73	188.68	3.05
U1404A-23H-4, 120*	U1404A-23H-4, 123		NP23	T *Reticulofenestra umbilicus* (>14 µm)	32.02	200.60	200.63	200.62	0.02
U1404A-23H-4, 120*	U1404A-23H-4, 123			T *Isthmolithus recurvus*	32.49	200.60	200.63	200.62	0.02
U1404A-23H-4, 120*	U1404A-23H-4, 123		NP22	T *Coccolithus formosus*	32.92	200.60	200.63	200.62	0.02
U1404A-23H-5, 30	U1404A-23H-5, 60			Ta *Clausicoccus subdistichus*	33.43	201.20	201.50	201.35	0.15
		Eocene/Oligocene boundary			33.89				
		Eocene							
U1404A-24H-2, 90*	U1404A-24H-3, 30		NP21	T *Discoaster saipanensis*	34.44	206.71	207.61	207.61	0.45
U1404A-24H-2, 90*	U1404A-24H-3, 30			T *Discoaster barbadiensis*	34.76	206.71	207.61	207.61	0.45
U1404A-24H-4, 46	U1404A-24H-5, 30			T *Reticulofenestra reticulata*	35.40	209.26	210.61	209.93	0.67
U1404A-24H-6, 96 (CC)	U1404A-25H-1, 100		NP19/NP20	B *Isthmolithus recurvus*	36.97	212.76	213.80	213.28	0.52
U1404A-25H-5, 100	U1404A-25H-CC			T *Chiasmolithus grandis*	37.98	219.80	220.56	220.18	0.38
U1404A-28H-CC	U1404A-29H-1, 64*			B *Dictyococcites bisectus* (>10 µm)†	40.36	244.03	245.01	244.52	0.49
U1404A-33X-1, 120	U1404A-33X-CC		NP17	T *Chiasmolithus solitus*	40.40	272.21	279.56	275.88	3.67
U1404A-33X-CC	U1404A-34X-1, 56			T *Nannotetrina* spp.	41.85	279.56	281.27	280.41	0.86
U1404A-34X-1, 56	U1404A-34X-1, 56			B? *Reticulofenestra umbilicus* (>14 µm)	41.94	281.27	281.27	281.27	0.00
				T *Nannotetrina fulgens*	42.87				

* = barren sample. † = from Fornaciari et al. (2010). B = base, Bc = base common, T = top, Ta = top of acme, Tc = top common.

Table T4. Nannofossil distribution, Site U1404. This table is available in an **oversized format.**

Table T5. Radiolarian datums, Site U1404.

Core, section, interval (cm)		Age	Zone	Marker species	Age (Ma)	Depth (mbsf)			
Top	Bottom					Top	Bottom	Mid-point	±
342-U1404A-	342-U1404A-								
		Miocene							
7H-CC	8H-CC		Top RN2	T *Dorcadospyris ateuchis*	18.64	59.13	71.00	65.21	6.10
9H-CC	10H-CC		Base RN2	B *Stichocory delmontensis*	19.35	81.06	90.57	85.82	4.75
14H-CC	15H-CC		Base RN1	B *Calocycletta virginis*	21.82	124.87	134.71	129.79	4.92
14H-CC	15H-CC		Base RN1	B *Cyrtocapsella tetrapera*	21.82	124.87	134.71	129.79	4.92
		Oligocene							
13H-CC	14H-CC		Mid-RP22	B *Eucyrtidium diaphanes*	23.00	115.07	124.87	119.97	4.90
16H-CC	17H-CC		Base RP22	B *Lychnocanoma elongata*	24.18	144.00	153.72	148.86	4.86
18H-CC	19H-CC		Mid-RP21	B *Calocycletta robusta*	25.97	163.20	172.77	167.99	4.78
19H-CC	28H-CC		Base RP21	B *Dorcadospyris ateuchus*	28.64	172.77	244.03	208.40	35.63
		Eocene							
28H-CC	29H-1, 52–53		Low RP16	T *Sethochytris triconiscus*	39.35	244.03	244.63	244.33	0.30
29H-1, 52–53	29H-CC		Base RP16	B *Podocyrtis goetheana*	40.14	244.63	253.05	248.84	4.21
29H-1, 52–53	29H-CC		Top RP15	T *Lophocyrtis biaurita*	40.14	244.63	253.05	248.84	4.21
32H-CC	34X-7		Base RP15	X *Podocyrtis mitra – Podocyrtis chalara*	40.65	270.63	289.83	280.23	9.60
36X-CC			Base RP14	X *Podocyrtis sinuosa – Podocyrtis mitra*	43.38	299.80		299.80	

B = base, T = top, X = faunal turnover.

Table T6. Radiolarian distribution, Site U1404. (Continued on next two pages.)

Core, section, interval (cm)	Depth (mbsf)			Age (Ma)	Zone	Preservation	Abundance	Diatoms	*Amphisphaera coronata*	*Amphisphaera goruna*	*Anthocyrtidium mariae*	*Artophormis gracilis*	*Axoprunum bispiculum*	*Calocyclas bandyca*	*Calocyclas hispida*	*Calocycletta robusta*	*Calocycletta virginis*	*Calocycloma ampulla*	*Calocycloma castum*	*Clathrocyclas universa*	*Cryptocarpium ornatum*	*Cyrtocapsella cornuta*	*Cyrtocapsella tetrapera*	*Dictyoprora amphora*	*Dictyoprora mongolfieri*	*Didymocyrtis prismatica*	*Didymocyrtis tubaria*	*Didymocyrtis violina*	*Dorcadospyris ateuchus*	*Dorcadospyris forcipata*	*Dorcadospyris platyacantha*	*Eucyrtidium antiquum*	*Eucyrtidium cienkowksii*
	Bottom	Top	Mid-point																												
342-U1404A-																															
5H-CC	40.56	40.59	40.61	early Miocene	—	G	A	A				x	x				x				x								x		x	x
6H-CC	49.33	49.36	49.38	early Miocene	—	G	A	A			x	x	x			x	x				x	x	x			x	x					x
7H-CC	59.08	59.11	59.13	early Miocene	—	G	A	A			x	x									x					x	x	x				
8H-CC	71.29	71.30	71.30	early Miocene	RN2	G	A	A			x			x		x					x					x		x	x			
9H-CC	81.03	81.06	81.08	early Miocene	RN2	G	A	A			x	x									x	x	x			x	x					x
10H-CC	90.54	90.57	90.59	early Miocene	RN1	G	A	A			x	x										x	x					x	x			x
11H-CC	96.21	96.24	96.26	early Miocene	RN1	G	A	A				x														x	x	x	x			
12H-CC	106.03	106.06	106.08	early Miocene	RN1	G	A	F			x	x	x	x		x	x									x		x		x		
13H-CC	115.04	115.07	115.10	early Miocene	RN1	G	A	R	x			x	x			x	x						x			x	x		x			x
14H-CC	124.84	124.87	124.89	early Miocene	RN1	G	A	R	x		x		x			x	x						x			x		x	x			x
15H-CC	134.68	134.71	134.73	Miocene/Oligocene	RP22	G	C	F			x	x														x			x			x
16H-CC	143.97	144.00	144.02	Miocene/Oligocene	RP22	G	A	F			x	x	x			x							?			x	x		x			
17H-CC	153.69	153.72	153.74	late Oligocene	RP21	G	A	R	x			x				x										x			x			
18H-CC	163.17	163.20	163.22	late Oligocene	RP21	G	A	A			x	x	x			?																
19H-CC	172.74	172.77	172.79	late Oligocene	RP21	G	F	R																					x			
29H-1, 52–53	244.62	244.63	244.63	middle Eocene	RP16	G	A	R							x			x	x						x					x		
29H-CC	253.01	253.05	253.08	middle Eocene	RP15	G	A	R	x						x			x	x	x				x	x					x		
32H-CC	270.58	270.64	270.70	middle Eocene	RP15	G	A	R	x																x					x		
34X-7	289.80	289.83	289.85	middle Eocene	RP14	G	A	R	x	x								x		x				x	x					x		
36X-CC	299.77	299.80	299.82	middle Eocene	RP14	G	A	R	x				x		x			x	x	x				x	x					x		

Preservation: G = good, M = moderate, P = poor. Abundance: A = abundant, C = common, F = few, R = rare. — = not assigned. ? = undetermined. Rew = reworked. See **"Biostratigraphy"** in the "Methods" chapter (Norris et al., 2014b) for preservation and abundance definitions.

Table T6 (continued). (Continued on next page.)

Core, section, interval (cm)	Depth (mbsf)			Age (Ma)	Zone	Preservation	Abundance	Diatoms	*Eucyrtidium diaphanes*	*Eucyrtidium hexagonatum*	*Eucyrtidium spinosum*	*Eusyringium fistuligerum*	*Eusyringium lagena*	*Helioidiscus asteriscus*	*Lamprocyclas hannai*	*Lophocyrtis? biaurita*	*Lophocyrtis? galenum*	*Lophocyrtis aspera*	*Lophocyrtis jacchia*	*Lophocyrtis pegetrum*	*Lophocyrtis semipolita gr.*	*Lychnocanoma amphitrite*	*Lychnocanoma bellum*	*Lychnocanoma elongata*	*Lychnodictyum audax*	*Orosphaerid* spp.	*Periphaena decora*	*Periphaena heliasteriscus*	*Phormocyrtis alexandrae*	*Phormocyrtis ligulata*	*Phormocyrtis striata striata*	*Podocyrtis ampla*	*Podocyrtis chalara*
	Bottom	Top	Mid-point																											
342-U1404A-																														
5H-CC	40.56	40.59	40.61	early Miocene	—	G	A	A	x						x			x					x					x			
6H-CC	49.33	49.36	49.38	early Miocene	—	G	A	A	x						x								x					x			
7H-CC	59.08	59.11	59.13	early Miocene	—	G	A	A	x									x			x							x			
8H-CC	71.29	71.30	71.30	early Miocene	RN2	G	A	A	x						x			x			x										
9H-CC	81.03	81.06	81.08	early Miocene	RN2	G	A	A	x					x	x			x					x					x			
10H-CC	90.54	90.57	90.59	early Miocene	RN1	G	A	A	x	x								x					x								
11H-CC	96.21	96.24	96.26	early Miocene	RN1	G	A	A	x	x																		x			
12H-CC	106.03	106.06	106.08	early Miocene	RN1	G	A	F		x				x	x			x					x		x	x		x			
13H-CC	115.04	115.07	115.10	early Miocene	RN1	G	A	R	x	x		Rew			x		x	x		x			x	x	x			x			
14H-CC	124.84	124.87	124.89	early Miocene	RN1	G	A	R		x				x	x		x	x					x		x	x	x	x			
15H-CC	134.68	134.71	134.73	Miocene/Oligocene	RP22	G	C	F							x								x	x				x			
16H-CC	143.97	144.00	144.02	Miocene/Oligocene	RP22	G	A	F						x	x		x	x					x	x	x				x			
17H-CC	153.69	153.72	153.74	late Oligocene	RP21	G	A	R						x	x		x	x						x		?					
18H-CC	163.17	163.20	163.22	late Oligocene	RP21	G	A	A										?										x			
19H-CC	172.74	172.77	172.79	late Oligocene	RP21	G	F	R																							
29H-1, 52–53	244.62	244.63	244.63	middle Eocene	RP16	G	A	R			x	x							x			x					x				x
29H-CC	253.01	253.05	253.08	middle Eocene	RP15	G	A	R				x	?			x		?	x			x					x	x		x		x
32H-CC	270.58	270.64	270.70	middle Eocene	RP15	G	A	R				x	?			x					x	x					x			x		x
34X-7	289.80	289.83	289.85	middle Eocene	RP14	G	A	R				x	?									x						x		x	x	x
36X-CC	299.77	299.80	299.82	middle Eocene	RP14	G	A	R				x	?			x		?				x					x	x	x			

Table T6 (continued).

Core, section, interval (cm)	Depth (mbsf)			Age (Ma)	Zone	Preservation	Abundance	Diatoms	*Podocyrtis goetheana*	*Podocyrtis mitra*	*Podocyrtis papalis*	*Podocyrtis sinuosa*	*Podocyrtis trachodes*	*Pterocanium trilobum*	*Rhopalocanium ornatum*	*Saturnalis circularis*	*Sethochytris babylonis*	*Sethochytris chrysallis*	*Sethochytris triconiscus*	*Spongatractus pachystylus*	*Stichocorys delmontensis*	*Stichocorys subligata* gr.	*Theocorys redondoensis*	*Theocorys spongoconum*	*Theocotylissa ficus*	*Theocyrtis annosa*	*Tholospyris anthophora*	*Thyrsocyrtis bromia*	*Thyrsocyrtis lochites*	*Thyrsocyrtis rhizodon*	*Thyrsocyrtis tetracantha*	*Thyrsocyrtis triacantha*	*Zealithapium anoectum*	*Zealithapium mitra*
	Bottom	Top	Mid-point																													
342-U1404A-																																
5H-CC	40.56	40.59	40.61	early Miocene	—	G	A	A													x				x							
6H-CC	49.33	49.36	49.38	early Miocene	—	G	A	A								x					x			x	x							
7H-CC	59.08	59.11	59.13	early Miocene	—	G	A	A																			x						
8H-CC	71.29	71.30	71.30	early Miocene	RN2	G	A	A								x					x	x					x						
9H-CC	81.03	81.06	81.08	early Miocene	RN2	G	A	A													x						x						
10H-CC	90.54	90.57	90.59	early Miocene	RN1	G	A	A															x				x						
11H-CC	96.21	96.24	96.26	early Miocene	RN1	G	A	A														x	x				x						
12H-CC	106.03	106.06	106.08	early Miocene	RN1	G	A	F								x						x	x	x			x						
13H-CC	115.04	115.07	115.10	early Miocene	RN1	G	A	R															x				x			x			
14H-CC	124.84	124.87	124.89	early Miocene	RN1	G	A	R															x			x	x						
15H-CC	134.68	134.71	134.73	Miocene/Oligocene	RP22	G	C	F						x							?		x				x						
16H-CC	143.97	144.00	144.02	Miocene/Oligocene	RP22	G	A	F														x	x			x	x						
17H-CC	153.69	153.72	153.74	late Oligocene	RP21	G	A	R															x			x	x						
18H-CC	163.17	163.20	163.22	late Oligocene	RP21	G	A	A																			x						
19H-CC	172.74	172.77	172.79	late Oligocene	RP21	G	F	R																			x						
29H-1, 52–53	244.62	244.63	244.63	middle Eocene	RP16	G	A	R	x	x	x						x	x	x								x	x		x	x		x
29H-CC	253.01	253.05	253.08	middle Eocene	RP15	G	A	R		x	x		x		x		x	x	x	x					x		x						x
32H-CC	270.58	270.64	270.70	middle Eocene	RP15	G	A	R			x						x	x	x	x							x						
34X-7	289.80	289.83	289.85	middle Eocene	RP14	G	A	R		x	x				x		x	x		x							x			x	x		
36X-CC	299.77	299.80	299.82	middle Eocene	RP14	G	A	R		x	x	x					x			x					x		x			x			

Table T7. Planktonic foraminifer datums, Site U1404.

Core, section, interval (cm)		Age	Zone/ Subzone	Marker event	Age (Ma)	Depth (mbsf)			
Top	Bottom					Top	Bottom	Mid-point	±
342-U1404A-	342-U1404A-								
9H-2, 115–117	9H-3, 115–117	Miocene	M1b/M2	T *Paragloborotalia kugleri*	21.12	73.85	75.35	74.60	0.75
10H-6, 115–117	10H-CC	Miocene	M1a/M1b	B *Globoquadrina dehiscens*	22.44	89.35	90.54	89.95	0.60
11H-2, 100–102	11H-3, 100–102	Miocene	OE7/M1a	B *Paragloborotalia kugleri*	22.96	92.53	94.06	93.30	0.77

T = top, B = base.

Table T8. Planktonic foraminifer distribution, Site U1404. This table is available in an **oversized format.**

Table T9. Benthic foraminifer distribution, Site U1404. This table is available in an **oversized format.**

Table T10. Benthic foraminifer morphotype distribution, Site U1404.

Core, section, interval (cm)	Depth (mbsf)	Preservation	Abundance	Agglutinated	Elongated	Planispiral	Tapered	Trochospiral
342-U1404A-								
23H-5, 101–103	201.92	G	R	B	B	B	B	P
23H-6, 51–53	202.92	M	D	P	F	B	B	D
23H-7, 40–42	203.81	G	D	B	R	B	B	D
24H-1, 55–56	204.86	G	D	B	R	B	B	D
24H-2, 55–56	206.36	—	B					
24H-3, 55–56	207.86	M	P	B	P	B	B	B
24H-4, 55–56	209.36	G	D	P	F	B	B	D
24H-5, 55–56	210.86	M	D	B	R	B	B	D
24H-6, 55–56	212.36	P	A	B	F	B	B	F
25H-1, 100–101	213.81	P	P	B	P	B	B	P
25H-2, 100–101	215.31	—	B					
25H-3, 100–101	216.81	—	B					
25H-4, 100–101	218.31	—	B					
25H-5, 75–76	219.56	—	B					
26H-1, 50–51	221.01	P	D	B	R	B	B	A
26H-2, 50–51	222.51	—	B					
26H-3, 50–51	224.01	P	D	B	P	B	B	R
26H-4, 50–51	225.51	P	P	B	B	B	B	P
26H-5, 50–51	227.01	—	B					
28H-3, 15–16	239.66	M	R	B	P	B	B	R
28H-5, 45–46	242.96	—	B					

Preservation: G = good, M = moderate, P = poor. Abundance: D = dominant, A = abundant, F = few, R = rare, P = present, B = barren. — not assigned. See **"Biostratigraphy"** in the "Methods" chapter (Norris et al., 2014b) for preservation and abundance definitions.

Table T11. Core orientation data, Site U1404.

Hole U1404A		Hole U1404B	
Core	MTF (°)	Core	MTF (°)
342-U1404A-		342-U1404B-	
1H	239	1H	96
2H	270	2H	260
3H	205	3H	350
4H	141	4H	270
5H	39	5H	25
6H	257	6H	115
7H	332	7H	40
8H	335	8H	273
9H	130	9H	73
10H	240	10H	40
11H	335	11H	185
12H	307	12H	189
13H	294	13H	204
14H	44	14H	98
15H	265	15H	204
16H	211	16H	247
17H	311	17H	61
18H	165	18H	183
19H	286	19H	289
20H	100	20H	94
21H	24	21H	128
22H	200	22H	164
23H	126	23H	206
		24H	217
		25H	347
		26H	282
		27H	219

MTF = magnetic tool face orientation from geomagnetic north.

Table T12. Summary of AF demagnetization results for discrete samples, Holes U1404A and U1404B. (Continued on next two pages.)

Core, section, interval (cm)	Depth (mbsf)	Declination 20 mT or PCA (°)	Inclination 20 mT or PCA (°)	PCA MAD (°)	PCA range (mT)	NRM 20 mT (A/m)
342-U1404A-						
1H-1W, 72–74	0.73	268.3	72.2			4.00E–03
1H-2W, 56–58	2.07	–54.9	69.3			4.80E–03
1H-3W, 42–44	3.14	177.9	–40.7	5.7	20–40	2.04E–03
1H-4W, 42–44	4.13	7.8	76.1			2.55E–04
2H-1W, 116–118	5.87	–20.8	71.8			4.51E–03
2H-2W, 46–48	6.67	–48.6	79.7			2.74E–03
2H-3W, 54–56	7.70	204.1	–38.1	8.7	20–40	2.00E–03
2H-4W, 72–74	9.38	–0.9	71.3			5.27E–03
2H-5W, 72–74	10.88	197.8	–49.5			3.56E–03
2H-6W, 52–54	12.18	247.5	–67.0			9.24E–05
2H-7W, 64–66	13.39	227.5	3.2			1.25E–05
3H-1W, 111–113	15.32	147.0	–43.6			3.93E–05
3H-2W, 78–80	16.49	224.5	–19.9			4.50E–05
3H-3W, 64–66	17.85	151.2	44.9			7.06E–05
3H-4W, 76–78	19.47	34.6	70.8			5.98E–05
3H-5W, 55–57	20.76	193.6	–27.2			2.82E–05
3H-6W, 40–42	21.81	213.7	83.9			4.29E–05
5H-1W, 92–94	34.13	218.9	–56.0			7.06E–05
5H-2W, 74–76	35.45	187.5	–30.7			5.43E–05
5H-3W, 94–96	37.15	170.1	58.2			3.67E–05
5H-4W, 74–76	38.45	36.3	47.1			4.47E–05
5H-5W, 66–68	39.87	–3.4	65.5			7.48E–05
6H-1W, 74–76	43.45	13.2	57.1			1.02E–04
6H-2W, 74–76	44.95	50.8	75.4			7.70E–05
6H-3W, 74–76	46.45	80.8	42.9			6.31E–05
6H-4W, 54–56	47.75	231.6	–35.1			6.63E–05
6H-5W, 35–37	48.76	216.5	–43.6			7.75E–05
7H-1W, 75–77	52.96	–63.4	71.5			6.68E–05
7H-2W, 75–77	54.46	–84.1	–8.6			3.86E–05
7H-3W, 50–52	55.71	65.4	72.4			5.53E–05
7H-4W, 75–77	57.46	19.2	47.9			7.00E–05
7H-5W, 39–41	58.60	5.8	63.4			9.53E–05
8H-1W, 75–77	62.46	150.1	75.2			3.65E–05
8H-2W, 75–77	63.96	86.1	47.5			4.08E–05
8H-3W, 75–77	65.46	25.4	48.9			5.11E–05
8H-4W, 75–77	66.96	48.9	55.9			3.08E–05
8H-5W, 75–77	68.46	–17.6	58.8			4.48E–05
8H-6W, 60–62	69.81	18.9	75.2			5.71E–05
8H-7W, 29–31	70.80	–40.8	72.8			4.71E–05
9H-1W, 75–77	71.96	4.2	33.7			5.78E–05
9H-2W, 75–77	73.46	48.4	25.1			2.36E–05
9H-3W, 75–77	74.96	92.3	–3.9			3.12E–05
9H-4W, 75–77	76.46	–66.8	4.6			1.01E–05
9H-5W, 75–77	77.96	76.3	–27.7			2.58E–05
9H-6W, 75–77	79.46	162.1	–29.9			3.21E–05
9H-7W, 32–34	80.53	169.3	–61.2			4.39E–05
10H-1W, 65–67	81.36	249.9	–20.7			6.60E–05
10H-2W, 75–77	82.96	227.5	–38.3			8.21E–05
10H-3W, 75–77	84.46	224.7	–25.5			8.28E–05
10H-4W, 75–77	85.96	194.7	–34.7			5.95E–05
10H-5W, 75–77	87.46	243.9	–26.1			7.19E–05
10H-6W, 75–77	88.96	236.3	–24.8			6.41E–05
10H-7W, 30–52	90.11	236.3	–34.6			7.00E–05
11H-1W, 60–62	90.81	–27.2	–42.9			1.78E–05
11H-2W, 81–83	92.35	241.7	39.3			2.46E–05
11H-3W, 75–77	93.82	–50.8	46.3	14.7	20–60	9.96E–05
11H-4W, 63–65	95.16	–15.5	58.0			6.16E–05
12H-1W, 63–65	96.84	–8.4	7.5			2.00E–05
12H-2W, 63–65	98.29	266.3	–37.0			2.63E–05
12H-3W, 63–65	99.74	233.6	–76.0			7.96E–05
12H-4W, 63–65	101.19	–27.4	10.2			1.58E–05
12H-5W, 63–65	102.64	53.5	50.9			6.27E–05
12H-6W, 60–62	104.11	–73.8	–27.2			4.43E–05
12H-7W, 29–31	105.30	230.1	–20.6			4.23E–05
13H-2W, 76–78	106.99	–23.2	–10.8			1.09E–04
13H-3W, 74–76	108.48	238.1	–62.1			5.60E–05

Table T12 (continued). (Continued on next page.)

Core, section, interval (cm)	Depth (mbsf)	Declination 20 mT or PCA (°)	Inclination 20 mT or PCA (°)	PCA MAD (°)	PCA range (mT)	NRM 20 mT (A/m)
13H-4W, 74–76	109.98	233.9	–30.1			7.67E–05
13H-5W, 74–76	111.48	248.6	–17.4			6.58E–05
13H-6W, 104–106	113.28	189.7	–46.5			8.49E–05
13H-7W, 48–50	114.22	48.1	–58.0			5.92E–05
14H-1W, 74–76	115.95	218.0	–20.7			2.55E–05
14H-2W, 74–76	117.45	169.9	–45.5			4.01E–05
14H-3W, 74–76	118.95	7.6	56.9	4.6	30–60	1.73E–04
14H-4W, 74–76	120.45	–2.4	47.4			1.20E–04
14H-5W, 74–76	121.95	42.3	23.9			1.27E–04
14H-6W, 44–46	123.15	65.1	36.4			3.45E–05
14H-7W, 44–46	124.15	–66.5	46.0			1.15E–05
15H-1W, 74–76	125.45	229.8	–21.2			6.76E–05
15H-2W, 74–76	126.91	230.9	–43.1			7.75E–05
15H-3W, 80–82	128.44	191.0	–40.7	14.5	20–60	1.39E–04
15H-4W, 74–76	129.84	214.1	–16.7			7.15E–05
15H-5W, 74–76	131.30	–29.3	54.1			8.07E–05
15H-6W, 68–70	132.71	67.2	73.0			4.60E–05
15H-7W, 44–46	133.98	34.7	56.1			8.06E–05
16H-1W, 74–76	134.95	–16.1	27.0			7.02E–05
16H-2W, 74–76	136.45	3.3	64.8			5.59E–05
16H-3W, 74–76	137.95	–58.7	48.5			2.93E–05
16H-4W, 76–78	139.47	–51.3	48.9			2.63E–05
16H-5W, 74–76	140.95	22.9	29.2			3.74E–05
16H-6W, 65–67	142.36	154.0	–42.3			2.06E–05
16H-7W, 42–44	143.33	46.8	3.1			4.85E–05
17H-1W, 74–76	144.45	–14.5	20.9			8.44E–05
17H-2W, 74–76	145.96	–75.9	53.9			4.06E–05
17H-3W, 74–76	147.41	167.9	–17.0	11.0	20–60	1.19E–04
17H-4W, 74–76	148.87	169.8	–67.5			1.08E–04
17H-5W, 74–76	150.33	202.9	–46.6			3.28E–05
17H-6W, 74–76	151.79	265.5	33.2			1.99E–05
17H-7W, 46–48	152.97	–51.6	–10.8			2.47E–05
18H-1W, 75–77	153.96	–18.8	–50.9			4.07E–05
18H-2W, 75–77	155.47	99.6	–26.7			4.14E–05
18H-3W, 75–77	156.98	150.7	51.4			3.69E–05
18H-4W, 75–77	158.50	64.7	26.9			3.76E–06
18H-5W, 75–77	160.01	234.1	–33.4			2.62E–05
18H-6W, 55–57	161.32	74.6	45.4			9.53E–05
18H-7W, 40–42	162.38	78.7	38.1			9.18E–05
19H-1W, 75–77	163.46	141.9	50.4			2.65E–05
19H-2W, 75–77	164.96	163.7	21.6			9.46E–05
19H-3W, 75–77	166.46	153.2	37.2			9.74E–05
19H-4W, 75–77	167.97	188.5	27.6			6.31E–05
19H-5W, 75–77	169.48	157.0	23.1			9.42E–05
19H-6W, 75–77	171.00	–64.2	–25.3			1.01E–04
19H-7W, 45–47	171.92	–39.5	–15.6			8.31E–05
20H-1W, 75–77	172.96	84.0	–7.2			1.35E–05
20H-2W, 75–77	174.46	166.5	–71.5			2.68E–05
20H-3W, 75–77	175.96	200.0	–26.8	8.1	10–60	9.84E–05
20H-4W, 75–77	177.46	12.8	–30.8			3.83E–05
20H-5W, 75–77	178.96	191.2	–4.0			3.98E–05
20H-6W, 55–57	180.26	24.1	63.6			3.32E–05
20H-7W, 40–42	181.31	–40.5	18.1			7.97E–05
21H-1W, 85–87	182.56	25.9	28.6			7.26E–05
21H-2W, 75–77	183.96	4.5	58.4			1.70E–04
21H-3W, 62–64	185.33	40.5	61.2	6.7	10–60	1.58E–04
21H-4W, 75–77	186.96	–21.7	46.2			4.42E–05
21H-5W, 75–77	188.46	–43.2	52.4			1.60E–04
21H-6W, 50–52	189.71	12.3	42.3			1.82E–04
21H-7W, 32–34	191.03	18.9	51.5			2.01E–04
22H-1W, 90–92	192.11	32.7	11.5			1.33E–04
22H-2W, 55–57	193.26	8.6	69.1			6.52E–05
22H-3W, 26–28	194.07	163.0	8.4			4.58E–05
23H-1W, 75–77	195.66	57.4	11.4			6.08E–05
23H-2W, 75–77	197.16	67.9	–6.1			3.70E–05
23H-3W, 75–77	198.66	64.1	32.6	11.1	10–60	3.39E–03
23H-4W, 75–77	200.16	229.3	–26.4	3.7	20–60	1.12E–02
23H-5W, 75–77	201.66	66.0	31.0			6.48E–03

Table T12 (continued).

Core, section, interval (cm)	Depth (mbsf)	Declination 20 mT or PCA (°)	Inclination 20 mT or PCA (°)	PCA MAD (°)	PCA range (mT)	NRM 20 mT (A/m)
23H-6W, 42–44	202.83	65.5	50.8			5.59E–03
23H-7W, 27–29	203.68	98.7	55.7			9.20E–05
24H-1W, 70–72	205.01	12.3	–17.0			2.60E–03
24H-2W, 74–76	206.55	–78.6	4.5			3.86E–03
24H-3W, 74–76	208.05	228.7	33.2	7.2	10–80	7.05E–03
24H-4W, 74–76	209.55	218.5	46.5			3.10E–04
24H-5W, 64–66	210.95	204.5	51.8			1.94E–03
24H-6W, 47–49	212.28	230.1	34.2			5.58E–03
25H-1W, 74–76	213.55	219.9	–54.6			1.80E–03
25H-2W, 74–76	215.05	37.6	59.7			4.03E–04
25H-3W, 74–76	216.55	–27.3	56.7			7.98E–04
25H-4W, 66–68	217.97	45.2	51.9			4.00E–03
25H-5W, 21–23	219.02	17.8	54.5			4.40E–03
26H-1W, 67–69	221.18	–61.5	–20.5	8.1	20–40	3.64E–03
26H-1W, 120–122	221.71	–52.6	11.9			3.01E–05
26H-2W, 74–76	222.75	110.1	64.2			3.67E–03
26H-3W, 74–76	224.25	105.4	49.2			1.28E–03
26H-4W, 74–76	225.75	99.3	51.2			3.46E–03
26H-5W, 54–56	227.05	116.6	48.5			2.19E–03
26H-6W, 29–31	228.00	114.7	55.8			2.68E–04
27H-1W, 74–76	229.35	136.0	43.1	10.9	20–80	1.07E–04
27H-2W, 74–76	230.85	133.3	51.2			4.14E–04
27H-3W, 74–76	232.35	127.0	53.6			2.24E–04
27H-4W, 68–70	233.79	146.2	58.0			6.05E–04
27H-5W, 72–74	235.33	114.8	65.3			5.48E–04
28H-1W, 72–74	237.23	–22.8	41.7			1.65E–04
28H-2W, 72–74	238.73	–36.7	16.5			5.29E–05
28H-3W, 72–74	240.23	165.2	–63.2			1.06E–04
28H-4W, 68–70	241.69	–44.8	45.2			1.64E–04
28H-5W, 61–63	243.12	–53.8	26.9			1.08E–04
29H-1W, 74–76	244.85	213.1	21.6			3.39E–04
29H-2W, 74–76	246.35	211.2	34.7			1.27E–04
29H-3W, 74–76	247.85	207.2	9.8	7.4	10–60	3.26E–04
29H-4W, 74–76	249.35	–3.5	–3.1			1.09E–03
29H-5W, 66–68	250.77	266.4	4.8			1.43E–05
30H-1W, 60–62	253.61	–46.7	–18.2			2.72E–04
30H-2W, 46–48	254.72	–51.6	–23.1			1.78E–04
30H-3W, 43–45	255.58	–32.3	–9.6	12.5	20–60	1.51E–04
30H-4W, 75–77	257.40	–76.8	–11.9			9.23E–05
30H-5W, 25–27	258.40	234.8	–4.2			7.71E–05
31H-1W, 75–77	260.46	160.2	–11.9			1.75E–04
31H-2W, 75–77	261.96	144.6	–36.7			2.22E–03
31H-3W, 60–62	263.31	124.4	–34.7			2.25E–04
31H-4W, 30–32	264.51	137.8	30.7			1.18E–05
32H-2W, 53–55	266.20	242.3	30.7			4.83E–05
32H-3W, 75–77	267.74	198.9	42.3			4.50E–05
32H-4W, 60–62	269.09	–47.0	15.5			3.30E–04
33X-1W, 33–35	271.34	–83.2	–36.2			2.10E–04
33X-2W, 42–44	272.93	107.0	–59.0			1.28E–04
33X-3W, 80–82	274.81	213.1	–25.6			2.85E–04
33X-4W, 134–136	276.85	88.3	–13.9			5.54E–05
33X-5W, 99–101	278.00	129.8	–64.0			4.63E–05
33X-6W, 33–35	278.84	256.1	11.5			7.75E–05
34X-2W, 105–107	283.26	229.5	31.3			1.05E–04
34X-3W, 44–46	284.15	–26.6	59.8			1.91E–04
34X-4W, 48–50	285.69	–24.5	46.5			8.12E–05
34X-5W, 89–91	287.60	240.3	37.7			2.40E–04
34X-6W, 51–53	288.72	9.9	68.5	20.9	20–60	1.04E–04
34X-7W, 29–31	289.50	248.0	37.9			1.17E–04
35X-1W, 95–97	290.36	211.1	38.5			7.36E–05
35X-2W, 80–82	291.71	47.4	50.3	22.1	10–60	1.35E–04
35X-3W, 57–59	292.85	158.7	31.1			6.32E–05
36X-1W, 66–68	299.77	–14.3	–51.1			8.00E–05
342-U1404B-						
24H-4W, 50–52	207.21	246.3	60.6			8.14E–04

Declinations for Cores 342-U1404A-1H through 23H and 342-U1404B-24H are corrected into geographical coordinates using FlexIT orientation data. PCA = principal component analysis, MAD = maximum angle of deviation, NRM = natural remanent magnetism.

Table T13. Magnetostratigraphic tie points, Site U1404.

Chron boundary	Age (Ma)	Hole U1404A					Hole U1404B				
		Top		Bottom			Top		Bottom		
		Core, section, interval (cm)	Depth (mbsf)	Core, section, interval (cm)	Depth (mbsf)	Mid-point (mbsf)	Core, section, interval (cm)	Depth (mbsf)	Core, section, interval (cm)	Depth (mbsf)	Mid-point (mbsf)
		342-U1404A-		342-U1404A-			342-U1404B-		342-U1404B-		
C12r/C13n	33.157	23H-4, 125.0	200.65	23H-4, 127.5	200.68	200.67	24H-1, 82.5	203.03	24H-1, 90.0	203.10	203.07
C13n/C13r	33.705	NI	NI	NI	NI	NI	24H-3, 110.0	206.30	24H-3, 120.0	206.40	206.35
C13r/C15n	34.999	24H-2, 10.0	205.90	24H-2, 112.5	206.93	206.42	25H-1, 112.5	209.83	25H-1, 135.0	210.05	209.94
C15n/C15r	35.294	NI	NI	NI	NI	NI	25H-2, 57.5	210.78	25H-2, 77.5	210.98	210.88
C15r/C16n.1n	35.706	NI	NI	NI	NI	NI	25H-3, 25.0	211.95	25H-3, 30.0	212.00	211.98
C16n.1n/C16n.1r	35.892	NI	NI	NI	NI	NI	25H-3, 92.5	212.63	25H-3, 97.5	212.68	212.66
C16n.1r/C16n.2n	36.051	25H-1, 82.5	213.63	25H-1, 90.0	213.70	213.67	25H-3, 122.5	212.93	25H-3, 127.5	212.98	212.96
C16n.2n/C16r	36.700	25H-3, 47.5	216.28	25H-3, 82.5	216.63	216.46	NI	NI	NI	NI	NI
C16r/C17n.1n	36.969	25H-3, 140.0	217.20	24H-4, 25	217.55	217.38	NI	NI	NI	NI	NI
C17n.1n/C17n.1r	37.753	NI	NI	NI	NI	NI	26H-1, 135.0	216.55	26H-2, 10.0	216.80	216.68
C17n.1r/C17n.2n	37.872	26H-2, 12.5	222.13	26H-2, 30.0	222.30	222.22	26H-4, 42.5	220.13	26H-4, 50.0	220.20	220.17
C17n.2n/C17n.2r	38.093	NI	NI	NI	NI	NI	NI	NI	NI	NI	NI
C17n.2r/C17n.3n	38.159	NI	NI	NI	NI	NI	NI	NI	NI	NI	NI
C17n.3n/C17r	38.333	NI	NI	NI	NI	NI	NI	NI	NI	NI	NI
C17r/C18n.1n	38.615	NI	NI	NI	NI	NI	NI	NI	NI	NI	NI
C18n.1n/C18n.1r	39.627	28H-2, 80.0	238.80	28H-2, 100.0	239.00	238.90	NI	NI	NI	NI	NI
C18n.1r/C18n.2n	39.698	28H-3, 117.5	240.68	28H-3, 125.0	240.75	240.72	NI	NI	NI	NI	NI
C18n.2n/C18r	40.145	29H-4, 25.0	248.85	29H-4, 32.5	248.93	248.89	NI	NI	NI	NI	NI
C18r/C19n	41.154	32H-2, 27.5	265.94	32H-2, 47.5	266.14	266.04	NI	NI	NI	NI	NI
C19n/C19r	41.390	32H-3, 137.5	268.36	32H-4, 12.5	268.61	268.49	NI	NI	NI	NI	NI

Ages from Gradstein et al. (2012). NI = not identified.

Table T14. Summary of anisotropy of magnetic susceptibility of discrete samples, Hole U1404A. (Continued on next three pages.)

Core, section, interval (cm)	Depth (mbsf)	τ_3	V_3 (°)		τ_2	V_2 (°)		τ_1	V_1 (°)		Bulk susceptibility (SI)	Anisotropy (%)	*P*	L	F
			Declination	Inclination		Declination	Inclination		Declination	Inclination					
342-U1404A-															
1H-1W, 72–74	0.73	0.3327	243.9	73.2	0.3334	57.1	16.7	0.3338	147.7	1.9	4.81E–04	0.1	1.003	1.001	1.002
1H-2W, 56–58	2.07	0.3324	111.2	73.4	0.3334	259.1	14.2	0.3342	351.3	8.5	6.16E–04	0.2	1.005	1.002	1.003
1H-3W, 42–44	3.14	0.3317	97.8	81.9	0.3332	5.0	0.4	0.3351	275.0	8.1	5.28E–04	0.3	1.011	1.006	1.005
1H-4W, 42–44	4.13	0.3299	267.3	83.5	0.3344	1.2	0.4	0.3357	91.2	6.5	1.44E–04	0.6	1.018	1.004	1.014
2H-1W, 116–118	5.87	0.3317	149.6	80.7	0.3335	38.6	3.3	0.3348	308.1	8.6	3.17E–04	0.3	1.009	1.004	1.005
2H-2W, 46–48	6.67	0.3316	184.3	65.9	0.3329	84.4	4.4	0.3355	352.5	23.6	2.48E–04	0.4	1.012	1.008	1.004
2H-3W, 54–56	7.70	0.3314	183.2	66.6	0.3337	312.2	15.2	0.3349	47.0	17.3	2.39E–04	0.4	1.011	1.004	1.007
2H-4W, 72–74	9.38	0.3308	239.2	83.4	0.3337	94.3	5.4	0.3354	3.9	3.8	3.21E–04	0.5	1.014	1.005	1.009
2H-5W, 72–74	10.88	0.3307	268.6	58.2	0.3329	135.5	23.0	0.3363	36.2	20.7	2.32E–04	0.6	1.017	1.010	1.007
2H-6W, 52–54	12.18	0.3286	272.6	67.5	0.3337	118.3	20.5	0.3377	24.9	9.0	7.44E–05	0.9	1.028	1.012	1.015
2H-7W, 64–66	13.39	0.3295	135.6	19.9	0.3342	241.0	36.3	0.3363	22.8	47.0	5.95E–05	0.7	1.021	1.006	1.014
3H-1W, 111–113	15.32	0.3287	131.3	37.1	0.3305	23.5	22.0	0.3408	269.8	44.8	5.95E–05	1.2	1.037	1.031	1.005
3H-2W, 78–80	16.49	0.3306	194.3	38.5	0.3341	16.8	51.4	0.3353	285.3	1.2	6.38E–05	0.5	1.014	1.003	1.011
3H-3W, 64–66	17.85	0.3300	283.1	49.9	0.3329	152.3	28.9	0.3371	47.2	25.3	6.73E–05	0.7	1.022	1.013	1.009
3H-4W, 76–78	19.47	0.3285	119.0	25.0	0.3315	209.0	0.1	0.3400	299.2	65.0	6.91E–05	1.2	1.035	1.026	1.009
3H-5W, 55–57	20.76	0.3294	47.4	30.6	0.3332	286.5	41.0	0.3374	160.7	33.9	6.52E–05	0.8	1.024	1.013	1.011
3H-6W, 40–42	21.81	0.3309	246.1	21.9	0.3333	341.9	14.2	0.3358	102.5	63.5	7.15E–05	0.5	1.015	1.008	1.007
5H-1W, 92–94	34.13	0.3272	330.0	13.2	0.3313	144.6	76.7	0.3415	239.7	1.2	2.98E–05	1.4	1.044	1.031	1.013
5H-2W, 74–76	35.45	0.3278	275.2	56.2	0.3350	138.3	26.0	0.3372	38.1	20.0	3.05E–05	0.9	1.029	1.007	1.022
5H-3W, 94–96	37.15	0.3226	339.9	45.9	0.3325	232.8	15.9	0.3449	129.1	39.8	2.90E–05	2.2	1.069	1.037	1.031
5H-4W, 74–76	38.45	0.3303	168.9	3.9	0.3319	77.5	20.4	0.3378	269.3	69.2	4.11E–05	0.7	1.023	1.018	1.005
5H-5W, 66–68	39.87	0.3281	85.9	35.8	0.3326	194.7	24.0	0.3393	310.7	44.5	3.08E–05	1.1	1.034	1.020	1.014
6H-1W, 74–76	43.45	0.3275	247.3	32.5	0.3337	30.4	51.4	0.3388	145.0	18.4	3.00E–05	1.1	1.035	1.015	1.019
6H-2W, 74–76	44.95	0.3275	125.8	19.7	0.3332	246.6	55.0	0.3393	24.9	27.6	3.31E–05	1.2	1.036	1.018	1.017
6H-3W, 74–76	46.45	0.3255	325.5	6.1	0.3351	227.9	51.1	0.3395	60.3	38.2	3.60E–05	1.4	1.043	1.013	1.029
6H-4W, 54–56	47.75	0.3248	254.4	28.3	0.3354	72.7	61.7	0.3398	164.0	0.7	3.27E–05	1.5	1.046	1.013	1.033
6H-5W, 35–37	48.76	0.3283	175.1	3.9	0.3306	278.1	73.0	0.3412	83.9	16.5	3.05E–05	1.3	1.039	1.032	1.007
7H-1W, 75–77	52.96	0.3177	65.9	41.8	0.3350	265.5	46.5	0.3473	164.9	9.9	2.93E–05	3.0	1.093	1.037	1.054
7H-2W, 75–77	54.46	0.3176	312.9	54.3	0.3348	209.6	9.4	0.3475	113.2	34.1	3.18E–05	3.0	1.094	1.038	1.054
7H-3W, 50–52	55.71	0.3145	213.7	53.9	0.3356	61.0	32.9	0.3499	322.3	13.1	2.97E–05	3.5	1.113	1.043	1.067
7H-4W, 75–77	57.46	0.3244	32.4	15.1	0.3319	288.8	41.1	0.3437	138.1	45.0	3.11E–05	1.9	1.060	1.036	1.023
7H-5W, 39–41	58.60	0.3242	18.4	16.2	0.3323	126.5	47.1	0.3435	275.1	38.5	2.61E–05	1.9	1.060	1.034	1.025
8H-1W, 75–77	62.46	0.3279	93.3	12.0	0.3308	196.1	46.2	0.3413	352.5	41.3	3.06E–05	1.3	1.041	1.032	1.009
8H-2W, 75–77	63.96	0.3230	77.7	73.0	0.3305	245.7	16.7	0.3465	336.7	3.3	2.52E–05	2.4	1.073	1.048	1.023
8H-3W, 75–77	65.46	0.3200	324.7	12.7	0.3355	224.6	38.0	0.3445	69.8	49.2	2.73E–05	2.4	1.077	1.027	1.049
8H-4W, 75–77	66.96	0.3272	183.0	34.8	0.3323	10.9	54.9	0.3405	275.6	3.7	3.25E–05	1.3	1.041	1.024	1.016
8H-5W, 75–77	68.46	0.3282	142.0	12.2	0.3345	266.0	68.9	0.3374	48.2	17.0	3.61E–05	0.9	1.028	1.009	1.019
8H-6W, 60–62	69.81	0.3296	255.7	31.6	0.3329	356.3	16.7	0.3375	110.1	53.3	3.36E–05	0.8	1.024	1.014	1.010
8H-7W, 29–31	70.80	0.3252	157.8	59.4	0.3313	282.1	18.5	0.3435	20.4	23.5	3.38E–05	1.8	1.056	1.037	1.019
9H-1W, 75–77	71.96	0.3247	353.9	59.9	0.3292	221.4	21.4	0.3461	123.1	20.2	2.86E–05	2.1	1.066	1.052	1.014
9H-2W, 75–77	73.46	0.3183	334.7	73.0	0.3353	198.0	12.5	0.3464	105.4	11.3	2.86E–05	2.8	1.088	1.033	1.053
9H-3W, 75–77	74.96	0.3171	319.9	24.1	0.3343	218.9	23.2	0.3485	90.4	55.4	2.50E–05	3.1	1.099	1.042	1.054
9H-4W, 75–77	76.46	0.3257	43.3	41.5	0.3330	150.8	18.7	0.3413	258.9	42.6	3.32E–05	1.6	1.048	1.025	1.023
9H-5W, 75–77	77.96	0.3295	291.6	40.9	0.3332	76.2	43.3	0.3373	184.7	18.6	3.04E–05	0.8	1.024	1.012	1.011
9H-6W, 75–77	79.46	0.3294	57.8	33.5	0.3318	314.2	19.6	0.3388	199.3	49.8	4.03E–05	0.9	1.028	1.021	1.007
9H-7W, 32–34	80.53	0.3263	302.0	18.5	0.3321	73.5	63.2	0.3416	205.5	18.7	4.75E–05	1.5	1.047	1.028	1.018
10H-1W, 65–67	81.36	0.3268	326.4	27.3	0.3305	70.8	25.7	0.3428	197.0	50.9	3.32E–05	1.6	1.049	1.037	1.011
10H-2W, 75–77	82.96	0.3237	14.3	77.1	0.3300	180.3	12.5	0.3463	271.0	3.0	4.18E–05	2.3	1.070	1.049	1.019
10H-3W, 75–77	84.46	0.3247	305.4	12.8	0.3287	51.6	51.0	0.3467	205.9	36.1	4.11E–05	2.2	1.068	1.055	1.012

Table T14 (continued). (Continued on next page.)

Core, section, interval (cm)	Depth (mbsf)	τ_3	V_3 (°)		τ_2	V_2 (°)		τ_1	V_1 (°)		Bulk susceptibility (SI)	Anisotropy (%)	*P*	L	F
			Declination	Inclination		Declination	Inclination		Declination	Inclination					
10H-4W, 75–77	85.96	0.3273	86.1	9.7	0.3316	338.7	60.2	0.3411	181.3	27.9	3.30E–05	1.4	1.042	1.029	1.013
10H-5W, 75–77	87.46	0.3279	291.6	6.3	0.3302	47.5	76.0	0.3418	200.2	12.5	3.81E–05	1.4	1.042	1.035	1.007
10H-6W, 75–77	88.96	0.3283	180.7	32.4	0.3327	66.7	32.6	0.3390	303.6	40.5	3.69E–05	1.1	1.032	1.019	1.013
10H-7W, 30–52	90.11	0.3259	209.9	9.1	0.3342	335.4	74.6	0.3398	117.9	12.4	3.21E–05	1.4	1.043	1.017	1.025
11H-1W, 60–62	90.81	0.3247	107.4	32.7	0.3340	203.0	8.8	0.3413	306.2	55.9	4.37E–05	1.7	1.051	1.022	1.029
11H-2W, 81–83	92.35	0.3238	239.7	45.7	0.3320	147.7	1.9	0.3442	55.8	44.2	3.32E–05	2.0	1.063	1.037	1.025
11H-3W, 75–77	93.82	0.3258	102.6	12.1	0.3360	202.1	37.7	0.3382	358.0	49.7	3.38E–05	1.2	1.038	1.006	1.031
11H-4W, 63–65	95.16	0.3194	121.1	80.1	0.3365	234.8	4.0	0.3442	325.5	9.1	3.24E–05	2.5	1.078	1.023	1.054
12H-1W, 63–65	96.84	0.3263	242.8	13.0	0.3310	144.2	32.9	0.3426	351.3	54.0	3.80E–05	1.6	1.050	1.035	1.014
12H-2W, 63–65	98.29	0.3280	258.9	38.0	0.3323	118.0	44.8	0.3397	6.0	20.6	4.00E–05	1.2	1.036	1.022	1.013
12H-3W, 63–65	99.74	0.3277	46.5	2.3	0.3298	314.1	47.0	0.3425	138.7	42.9	4.36E–05	1.5	1.045	1.038	1.007
12H-4W, 63–65	101.19	0.3271	243.8	4.9	0.3306	134.4	75.6	0.3423	335.0	13.5	4.20E–05	1.5	1.047	1.035	1.011
12H-5W, 63–65	102.64	0.3268	89.3	60.7	0.3356	252.6	28.3	0.3376	346.4	7.1	4.89E–05	1.1	1.033	1.006	1.027
12H-6W, 60–62	104.11	0.3294	14.7	77.8	0.3336	175.8	11.6	0.3369	266.6	3.9	4.90E–05	0.8	1.023	1.010	1.013
12H-7W, 29–31	105.30	0.3300	145.1	9.1	0.3313	47.7	38.8	0.3387	245.9	49.7	5.29E–05	0.9	1.026	1.022	1.004
13H-2W, 76–78	106.99	0.3257	12.4	58.4	0.3321	131.1	16.5	0.3422	229.4	26.1	4.08E–05	1.7	1.051	1.031	1.020
13H-3W, 74–76	108.48	0.3288	167.0	15.7	0.3320	314.2	71.5	0.3392	74.3	9.5	4.82E–05	1.0	1.032	1.022	1.010
13H-4W, 74–76	109.98	0.3230	296.0	28.1	0.3349	37.5	20.4	0.3420	158.4	54.1	4.14E–05	1.9	1.059	1.021	1.037
13H-5W, 74–76	111.48	0.3270	347.5	11.9	0.3317	250.5	29.9	0.3414	96.7	57.4	4.79E–05	1.4	1.044	1.029	1.014
13H-6W, 104–106	113.28	0.3242	216.9	38.6	0.3344	6.3	47.2	0.3414	113.9	15.7	4.27E–05	1.7	1.053	1.021	1.031
13H-7W, 48–50	114.22	0.3232	57.1	61.0	0.3330	295.8	16.1	0.3438	198.6	23.5	4.13E–05	2.1	1.064	1.032	1.030
14H-1W, 74–76	115.95	0.3277	244.1	2.2	0.3341	154.0	2.6	0.3383	14.7	86.6	6.52E–05	1.1	1.032	1.013	1.020
14H-2W, 74–76	117.45	0.3293	64.7	57.3	0.3325	265.9	31.0	0.3382	170.0	9.7	4.51E–05	0.9	1.027	1.017	1.010
14H-3W, 74–76	118.95	0.3288	282.8	30.6	0.3345	140.2	53.3	0.3367	24.0	18.2	4.61E–05	0.8	1.024	1.007	1.017
14H-4W, 74–76	120.45	0.3259	128.8	25.6	0.3342	354.9	55.4	0.3399	229.8	21.7	4.40E–05	1.4	1.043	1.017	1.026
14H-5W, 74–76	121.95	0.3269	73.5	72.3	0.3334	274.8	16.5	0.3396	183.0	6.1	5.03E–05	1.3	1.039	1.019	1.020
14H-6W, 44–46	123.15	0.3276	169.3	61.6	0.3357	352.3	28.4	0.3368	261.6	1.3	4.64E–05	0.9	1.028	1.003	1.025
14H-7W, 44–46	124.15	0.3282	239.5	4.4	0.3336	333.4	41.3	0.3382	144.6	48.4	5.28E–05	1.0	1.031	1.014	1.017
15H-1W, 74–76	125.45	0.3296	94.3	21.3	0.3334	196.7	28.8	0.3371	333.3	52.8	4.43E–05	0.8	1.023	1.011	1.012
15H-2W, 74–76	126.91	0.3310	231.2	56.4	0.3336	95.8	25.3	0.3354	355.5	20.6	5.04E–05	0.4	1.013	1.005	1.008
15H-3W, 80–82	128.44	0.3303	205.0	33.9	0.3328	68.2	47.4	0.3369	311.3	22.6	5.30E–05	0.7	1.020	1.012	1.008
15H-4W, 74–76	129.84	0.3297	58.9	16.3	0.3328	170.9	52.1	0.3375	317.9	33.2	4.76E–05	0.8	1.024	1.014	1.010
15H-5W, 74–76	131.30	0.3297	215.0	22.8	0.3334	3.5	63.8	0.3369	119.7	12.3	4.87E–05	0.7	1.022	1.010	1.011
15H-6W, 68–70	132.71	0.3286	310.2	32.5	0.3347	213.4	10.5	0.3367	107.8	55.5	5.61E–05	0.8	1.025	1.006	1.019
15H-7W, 44–46	133.98	0.3293	191.0	67.3	0.3321	70.4	12.0	0.3387	336.2	19.0	5.24E–05	0.9	1.029	1.020	1.009
16H-1W, 74–76	134.95	0.3293	115.4	60.4	0.3324	327.9	25.6	0.3383	231.1	13.8	5.16E–05	0.9	1.027	1.018	1.009
16H-2W, 74–76	136.45	0.3286	215.2	29.5	0.3345	88.2	46.7	0.3369	323.1	28.4	4.91E–05	0.8	1.025	1.007	1.018
16H-3W, 74–76	137.95	0.3269	199.7	45.6	0.3333	77.8	27.4	0.3398	329.1	31.8	4.89E–05	1.3	1.039	1.020	1.019
16H-4W, 76–78	139.47	0.3272	23.3	16.7	0.3324	282.7	31.5	0.3403	137.2	53.3	4.11E–05	1.3	1.040	1.024	1.016
16H-5W, 74–76	140.95	0.3277	99.9	17.6	0.3309	223.2	60.0	0.3414	2.0	23.5	5.33E–05	1.4	1.042	1.032	1.010
16H-6W, 65–67	142.36	0.3270	210.2	74.3	0.3328	330.0	8.0	0.3402	61.9	13.5	5.13E–05	1.3	1.040	1.022	1.018
16H-7W, 42–44	143.33	0.3266	270.6	44.0	0.3344	42.8	34.8	0.3390	152.6	26.0	4.41E–05	1.2	1.038	1.014	1.024
17H-1W, 74–76	144.45	0.3298	72.2	34.2	0.3348	335.1	10.4	0.3354	230.6	53.9	5.70E–05	0.6	1.017	1.002	1.015
17H-2W, 74–76	145.96	0.3289	61.3	60.5	0.3324	325.8	3.1	0.3387	234.0	29.3	4.86E–05	1.0	1.030	1.019	1.010
17H-3W, 74–76	147.41	0.3282	119.2	38.0	0.3333	5.0	27.7	0.3385	249.3	39.5	5.45E–05	1.0	1.031	1.016	1.015
17H-4W, 74–76	148.87	0.3306	55.8	9.0	0.3345	316.1	46.9	0.3349	153.9	41.7	5.48E–05	0.4	1.013	1.001	1.012
17H-5W, 74–76	150.33	0.3307	282.3	21.5	0.3331	177.4	33.2	0.3362	39.1	48.8	5.49E–05	0.5	1.017	1.009	1.007
17H-6W, 74–76	151.79	0.3279	125.3	54.8	0.3314	323.0	33.9	0.3407	227.3	8.3	5.28E–05	1.3	1.039	1.028	1.011
17H-7W, 46–48	152.97	0.3285	58.1	18.8	0.3351	157.4	25.5	0.3365	295.8	57.5	5.24E–05	0.8	1.024	1.004	1.020
18H-1W, 75–77	153.96	0.3284	204.9	9.5	0.3317	327.5	72.8	0.3399	112.5	14.2	6.07E–05	1.1	1.035	1.025	1.010

Table T14 (continued). (Continued on next page.)

Core, section, interval (cm)	Depth (mbsf)	τ_3	V_3 (°)		τ_2	V_2 (°)		τ_1	V_1 (°)		Bulk susceptibility (SI)	Anisotropy (%)	*P*	L	F
			Declination	Inclination		Declination	Inclination		Declination	Inclination					
18H-2W, 75–77	155.47	0.3287	210.7	21.0	0.3302	98.1	45.0	0.3411	317.9	37.5	5.15E–05	1.2	1.037	1.033	1.004
18H-3W, 75–77	156.98	0.3258	45.4	66.6	0.3351	301.9	5.8	0.3391	209.4	22.6	5.88E–05	1.3	1.041	1.012	1.028
18H-4W, 75–77	158.50	0.3317	212.5	46.4	0.3335	338.0	28.9	0.3348	86.2	29.4	5.65E–05	0.3	1.010	1.004	1.006
18H-5W, 75–77	160.01	0.3288	68.8	87.3	0.3326	255.3	2.7	0.3386	165.3	0.3	5.62E–05	1.0	1.030	1.018	1.012
18H-6W, 55–57	161.32	0.3291	134.5	63.9	0.3323	308.2	26.0	0.3386	39.4	2.5	5.78E–05	1.0	1.029	1.019	1.010
18H-7W, 40–42	162.38	0.3292	29.2	86.5	0.3321	284.8	0.9	0.3387	194.8	3.4	5.93E–05	0.9	1.029	1.020	1.009
19H-1W, 75–77	163.46	0.3291	37.5	35.5	0.3333	301.5	8.3	0.3376	200.2	53.2	6.49E–05	0.9	1.026	1.013	1.013
19H-2W, 75–77	164.96	0.3304	122.1	70.1	0.3328	296.8	19.8	0.3368	27.4	1.7	6.16E–05	0.6	1.019	1.012	1.007
19H-3W, 75–77	166.46	0.3305	31.5	89.9	0.3335	219.7	0.1	0.3360	129.7	0.0	6.47E–05	0.6	1.017	1.007	1.009
19H-4W, 75–77	167.97	0.3306	259.1	32.1	0.3334	75.2	57.9	0.3360	168.0	1.8	6.86E–05	0.5	1.016	1.008	1.009
19H-5W, 75–77	169.48	0.3280	342.8	67.8	0.3351	238.7	5.7	0.3370	146.5	21.4	6.99E–05	0.9	1.027	1.006	1.022
19H-6W, 75–77	171.00	0.3291	348.5	34.9	0.3331	149.7	53.6	0.3378	252.1	9.0	7.24E–05	0.9	1.026	1.014	1.012
19H-7W, 45–47	171.92	0.3307	298.5	38.1	0.3332	118.1	51.9	0.3361	208.4	0.2	7.42E–05	0.5	1.016	1.009	1.008
20H-1W, 75–77	172.96	0.3258	172.3	75.1	0.3337	42.9	9.6	0.3404	310.9	11.3	7.57E–05	1.5	1.045	1.020	1.024
20H-2W, 75–77	174.46	0.3295	13.0	52.3	0.3336	227.1	32.7	0.3369	125.9	16.8	8.41E–05	0.7	1.022	1.010	1.012
20H-3W, 75–77	175.96	0.3298	297.0	35.3	0.3322	165.1	43.4	0.3380	47.4	26.2	7.69E–05	0.8	1.025	1.017	1.007
20H-4W, 75–77	177.46	0.3300	212.2	65.6	0.3335	329.6	11.8	0.3366	64.2	21.1	7.21E–05	0.7	1.020	1.009	1.011
20H-5W, 75–77	178.96	0.3305	350.9	71.1	0.3325	135.3	15.6	0.3370	228.3	10.5	9.47E–05	0.7	1.020	1.014	1.006
20H-6W, 55–57	180.26	0.3286	209.2	84.0	0.3343	59.4	5.2	0.3371	329.1	3.0	8.48E–05	0.9	1.026	1.008	1.017
20H-7W, 40–42	181.31	0.3316	349.4	62.6	0.3332	125.3	20.4	0.3352	222.0	17.5	7.99E–05	0.4	1.011	1.006	1.005
21H-1W, 85–87	182.56	0.3297	277.6	57.8	0.3335	139.8	25.0	0.3369	40.6	19.0	1.13E–04	0.7	1.022	1.010	1.011
21H-2W, 75–77	183.96	0.3303	127.8	68.3	0.3336	299.1	21.5	0.3362	30.3	3.0	9.75E–05	0.6	1.018	1.008	1.010
21H-3W, 62–64	185.33	0.3290	147.2	58.3	0.3334	301.9	29.2	0.3376	38.3	11.3	9.19E–05	0.9	1.026	1.013	1.013
21H-4W, 75–77	186.96	0.3310	156.9	72.2	0.3330	37.2	9.1	0.3360	304.7	15.2	1.08E–04	0.5	1.015	1.009	1.006
21H-5W, 75–77	188.46	0.3307	55.5	48.7	0.3331	315.9	8.4	0.3362	218.8	40.0	1.00E–04	0.6	1.017	1.009	1.007
21H-6W, 50–52	189.71	0.3270	73.7	61.9	0.3311	209.3	20.9	0.3419	306.4	17.9	9.13E–05	1.5	1.046	1.032	1.013
21H-7W, 32–34	191.03	0.3280	43.9	76.0	0.3325	193.8	12.2	0.3394	285.3	6.8	9.97E–05	1.1	1.035	1.021	1.014
22H-1W, 90–92	192.11	0.3294	140.3	39.0	0.3312	310.7	50.7	0.3394	46.4	4.7	9.87E–05	1.0	1.031	1.025	1.006
22H-2W, 55–57	193.26	0.3298	273.0	68.0	0.3336	56.3	18.0	0.3366	150.4	12.3	1.04E–04	0.7	1.021	1.009	1.012
22H-3W, 26–28	194.07	0.3306	257.5	59.2	0.3336	95.5	29.6	0.3357	1.0	7.9	1.09E–04	0.5	1.015	1.006	1.009
23H-1W, 75–77	195.66	0.3324	75.8	59.2	0.3328	200.3	18.6	0.3347	298.7	23.6	1.12E–04	0.2	1.007	1.006	1.001
23H-2W, 75–77	197.16	0.3301	64.1	72.2	0.3346	237.7	17.7	0.3354	328.3	1.9	1.20E–04	0.5	1.016	1.002	1.014
23H-3W, 75–77	198.66	0.3305	16.3	63.0	0.3338	114.0	3.9	0.3358	206.0	26.7	2.62E–04	0.5	1.016	1.006	1.010
23H-4W, 75–77	200.16	0.3318	356.6	54.7	0.3332	124.8	23.7	0.3350	226.4	24.6	3.43E–04	0.3	1.010	1.005	1.004
23H-5W, 75–77	201.66	0.3315	88.5	53.2	0.3330	305.0	31.0	0.3355	203.9	17.8	1.83E–04	0.4	1.012	1.007	1.005
23H-6W, 42–44	202.83	0.3308	350.5	65.8	0.3337	238.3	9.7	0.3356	144.3	22.0	2.12E–04	0.5	1.014	1.006	1.009
23H-7W, 27–29	203.68	0.3272	97.8	42.3	0.3329	234.4	38.6	0.3399	344.6	23.4	8.00E–05	1.3	1.039	1.021	1.017
24H-1W, 70–72	205.01	0.3307	332.0	70.6	0.3344	87.7	8.7	0.3349	180.4	17.2	3.34E–04	0.4	1.013	1.002	1.011
24H-2W, 74–76	206.55	0.3323	228.9	49.1	0.3330	15.1	35.7	0.3348	118.0	17.2	3.38E–04	0.2	1.007	1.005	1.002
24H-3W, 74–76	208.05	0.3312	328.2	47.4	0.3332	142.7	42.5	0.3356	235.2	2.7	2.93E–04	0.4	1.013	1.007	1.006
24H-4W, 74–76	209.55	0.3311	306.2	49.7	0.3335	128.0	40.3	0.3354	37.2	0.9	1.20E–04	0.4	1.013	1.006	1.007
24H-5W, 64–66	210.95	0.3319	267.0	86.3	0.3339	141.3	2.2	0.3342	51.2	3.1	1.65E–04	0.2	1.007	1.001	1.006
24H-6W, 47–49	212.28	0.3318	300.2	78.9	0.3338	144.4	10.2	0.3344	53.6	4.5	2.79E–04	0.3	1.008	1.002	1.006
25H-1W, 74–76	213.55	0.3303	174.2	74.6	0.3340	76.9	2.0	0.3356	346.4	15.2	2.44E–04	0.5	1.016	1.005	1.011
25H-2W, 74–76	215.05	0.3314	161.7	73.6	0.3329	65.1	1.9	0.3358	334.6	16.3	1.43E–04	0.4	1.013	1.009	1.005
25H-3W, 74–76	216.55	0.3296	197.4	79.6	0.3339	88.1	3.5	0.3365	357.5	9.8	2.10E–04	0.7	1.021	1.008	1.013
25H-4W, 66–68	217.97	0.3318	152.5	71.4	0.3339	46.0	5.4	0.3344	314.3	17.7	2.42E–04	0.3	1.008	1.001	1.006
25H-5W, 21–23	219.02	0.3325	215.2	60.6	0.3332	96.8	15.0	0.3343	359.7	24.7	2.95E–04	0.2	1.005	1.003	1.002
26H-1W, 67–69	221.18	0.3318	188.3	55.8	0.3334	88.3	6.7	0.3348	353.9	33.3	2.43E–04	0.3	1.009	1.004	1.005
26H-1W, 120–122	221.71	0.3317	299.4	9.1	0.3330	201.1	42.0	0.3353	39.1	46.5	1.32E–04	0.4	1.011	1.007	1.004

Table T14 (continued).

Core, section, interval (cm)	Depth (mbsf)	τ_3	V_3 (°)		τ_2	V_2 (°)		τ_1	V_1 (°)		Bulk susceptibility (SI)	Anisotropy (%)	*P*	L	F
			Declination	Inclination		Declination	Inclination		Declination	Inclination					
26H-2W, 74–76	222.75	0.3306	279.8	72.6	0.3340	115.3	16.8	0.3354	24.0	4.4	2.20E–04	0.5	1.014	1.004	1.010
26H-3W, 74–76	224.25	0.3302	206.6	73.0	0.3342	109.7	2.1	0.3356	19.1	16.9	1.73E–04	0.5	1.016	1.004	1.012
26H-4W, 74–76	225.75	0.3308	234.0	64.5	0.3340	62.2	25.3	0.3352	330.7	3.2	2.48E–04	0.4	1.013	1.003	1.010
26H-5W, 54–56	227.05	0.3289	237.3	60.4	0.3349	123.6	12.9	0.3361	27.2	26.2	2.01E–04	0.7	1.022	1.004	1.018
26H-6W, 29–31	228.00	0.3292	185.2	55.5	0.3340	295.5	13.4	0.3368	33.8	31.1	1.28E–04	0.8	1.023	1.008	1.014
27H-1W, 74–76	229.35	0.3317	248.3	72.5	0.3325	29.9	13.9	0.3358	122.5	10.4	1.21E–04	0.4	1.012	1.010	1.002
27H-2W, 74–76	230.85	0.3285	240.2	50.0	0.3336	41.8	38.6	0.3379	139.2	9.1	1.39E–04	0.9	1.029	1.013	1.016
27H-3W, 74–76	232.35	0.3319	60.1	53.3	0.3331	273.5	31.9	0.3350	173.0	16.2	1.40E–04	0.3	1.009	1.006	1.004
27H-4W, 68–70	233.79	0.3300	258.3	60.1	0.3340	115.7	24.6	0.3360	18.2	16.0	1.57E–04	0.6	1.018	1.006	1.012
27H-5W, 72–74	235.33	0.3304	239.7	71.8	0.3333	61.3	18.2	0.3363	331.2	0.5	1.92E–04	0.6	1.018	1.009	1.009
28H-1W, 72–74	237.23	0.3292	191.3	78.7	0.3331	30.6	10.7	0.3377	299.9	3.7	1.24E–04	0.9	1.026	1.014	1.012
28H-2W, 72–74	238.73	0.3308	189.9	77.4	0.3341	359.8	12.4	0.3350	90.2	2.1	1.44E–04	0.4	1.013	1.003	1.010
28H-3W, 72–74	240.23	0.3312	107.2	51.1	0.3328	212.0	11.7	0.3360	310.8	36.5	1.20E–04	0.5	1.015	1.010	1.005
28H-4W, 68–70	241.69	0.3302	179.0	71.4	0.3334	296.9	8.9	0.3364	29.5	16.1	1.23E–04	0.6	1.019	1.009	1.010
28H-5W, 61–63	243.12	0.3296	293.6	77.3	0.3346	186.8	3.7	0.3358	96.0	12.1	1.06E–04	0.6	1.019	1.003	1.015
29H-1W, 74–76	244.85	0.3291	327.9	71.1	0.3341	139.3	18.7	0.3368	230.2	2.6	1.21E–04	0.8	1.023	1.008	1.015
29H-2W, 74–76	246.35	0.3316	268.6	11.9	0.3328	30.8	68.3	0.3355	174.7	17.8	1.10E–04	0.4	1.012	1.008	1.004
29H-3W, 74–76	247.85	0.3310	3.6	61.2	0.3343	97.7	2.3	0.3347	188.9	28.7	1.34E–04	0.4	1.011	1.001	1.010
29H-4W, 74–76	249.35	0.3311	257.5	81.7	0.3337	98.5	7.8	0.3353	8.1	3.0	1.54E–04	0.4	1.013	1.005	1.008
29H-5W, 66–68	250.77	0.3289	254.7	73.6	0.3345	139.4	7.2	0.3366	47.5	14.7	1.05E–04	0.8	1.023	1.006	1.017
30H-1W, 60–62	253.61	0.3309	150.1	69.1	0.3339	8.2	16.8	0.3352	274.4	12.2	1.46E–04	0.4	1.013	1.004	1.009
30H-2W, 46–48	254.72	0.3306	148.3	84.5	0.3337	14.8	3.8	0.3357	284.6	4.0	1.28E–04	0.5	1.015	1.006	1.010
30H-3W, 43–45	255.58	0.3309	163.0	80.1	0.3333	259.3	1.1	0.3358	349.5	9.9	1.16E–04	0.5	1.015	1.008	1.007
30H-4W, 75–77	257.40	0.3314	132.9	65.7	0.3339	255.9	13.8	0.3346	350.9	19.6	1.58E–04	0.3	1.010	1.002	1.008
30H-5W, 25–27	258.40	0.3319	116.7	82.7	0.3333	303.3	7.3	0.3348	213.2	0.8	1.46E–04	0.3	1.009	1.004	1.004
31H-1W, 75–77	260.46	0.3322	102.3	80.5	0.3325	310.6	8.4	0.3352	220.0	4.5	1.99E–04	0.3	1.009	1.008	1.001
31H-2W, 75–77	261.96	0.3314	94.5	64.0	0.3340	340.4	11.3	0.3345	245.5	23.2	2.32E–04	0.3	1.009	1.002	1.008
31H-3W, 60–62	263.31	0.3292	355.0	84.5	0.3335	193.3	5.2	0.3372	103.2	1.7	1.48E–04	0.8	1.024	1.011	1.013
31H-4W, 30–32	264.51	0.3305	82.4	60.6	0.3339	307.7	21.7	0.3356	209.9	19.0	9.97E–05	0.5	1.016	1.005	1.010
32H-2W, 53–55	266.20	0.3304	280.6	68.0	0.3336	31.3	8.2	0.3360	124.4	20.3	1.38E–04	0.6	1.017	1.007	1.010
32H-3W, 75–77	267.74	0.3288	264.2	77.1	0.3337	158.8	3.5	0.3375	68.0	12.4	1.42E–04	0.9	1.027	1.011	1.015
32H-4W, 60–62	269.09	0.3307	254.7	21.1	0.3339	359.7	33.7	0.3354	138.8	48.6	1.27E–04	0.5	1.014	1.005	1.010
33X-1W, 33–35	271.34	0.3307	16.4	72.1	0.3344	232.0	14.7	0.3348	139.4	10.0	1.21E–04	0.4	1.012	1.001	1.011
33X-2W, 42–44	272.93	0.3313	103.9	58.2	0.3331	223.3	16.9	0.3356	321.8	26.1	1.42E–04	0.4	1.013	1.007	1.005
33X-3W, 80–82	274.81	0.3295	324.5	60.1	0.3346	138.1	29.7	0.3359	229.7	2.8	1.31E–04	0.6	1.019	1.004	1.015
33X-4W, 134–136	276.85	0.3298	108.0	47.9	0.3335	326.3	35.4	0.3367	221.4	19.8	7.81E–05	0.7	1.021	1.009	1.011
33X-5W, 99–101	278.00	0.3292	154.1	53.9	0.3340	327.9	36.0	0.3368	60.1	3.0	1.04E–04	0.8	1.023	1.008	1.014
33X-6W, 33–35	278.84	0.3288	70.6	63.3	0.3326	218.9	23.2	0.3386	314.4	12.5	8.17E–05	1.0	1.030	1.018	1.012
34X-2W, 105–107	283.26	0.3299	359.9	57.2	0.3343	232.6	21.3	0.3358	132.8	23.6	1.18E–04	0.6	1.018	1.004	1.013
34X-3W, 44–46	284.15	0.3302	206.1	64.8	0.3343	101.5	6.7	0.3356	8.5	24.1	1.21E–04	0.5	1.016	1.004	1.012
34X-4W, 48–50	285.69	0.3283	111.9	43.1	0.3338	353.5	26.9	0.3379	242.7	35.0	7.83E–05	1.0	1.029	1.013	1.017
34X-5W, 89–91	287.60	0.3304	21.8	40.1	0.3346	131.2	21.5	0.3350	242.1	42.2	1.29E–04	0.5	1.014	1.001	1.013
34X-6W, 51–53	288.72	0.3294	155.5	62.4	0.3338	63.8	0.9	0.3367	333.3	27.6	1.13E–04	0.7	1.022	1.009	1.013
34X-7W, 29–31	289.50	0.3283	52.3	47.1	0.3330	311.1	10.3	0.3387	212.0	41.1	9.90E–05	1.0	1.032	1.017	1.015
35X-1W, 95–97	290.36	0.3301	296.2	45.7	0.3331	202.8	3.3	0.3368	109.6	44.1	1.05E–04	0.7	1.020	1.011	1.009
35X-2W, 80–82	291.71	0.3297	121.9	61.1	0.3349	342.1	22.9	0.3355	244.8	16.7	1.07E–04	0.6	1.018	1.002	1.016
35X-3W, 57–59	292.85	0.3296	293.2	43.7	0.3327	114.5	46.3	0.3377	23.8	0.7	9.35E–05	0.8	1.025	1.015	1.010
36X-1W, 66–68	299.77	0.3306	294.3	43.4	0.3341	185.9	18.5	0.3353	79.1	40.8	1.03E–04	0.5	1.014	1.004	1.011

τ_1, τ_2, and τ_3 are eigenvalues, and V_3, V_2, and V_1 are eigenvectors associated with minimum, intermediate, and maximum susceptibility, respectively. Measurement field = 300 A/m, sample volume = 7 cm^3. *P* = ansiotropy degree, L = lineation, F = foliation.

Table T15. Biostratigraphic and magnetostratigraphic datums, Hole U1404A.

Datum tie point	Datum	Datum type	Zone/Subzone	Age (Ma)	Depth (mbsf)		
					Top	Bottom	Mid-point
	B *Gephyrocapsa* (>5.5 µm)	Calcareous nannofossil		1.62	0.41	1.35	0.88
D01	T *Discoaster tamalis*	Calcareous nannofossil		2.80	0.41	1.35	0.88
	T *Sphenolithus* spp.	Calcareous nannofossil		3.54	1.96	2.46	2.21
	T *Reticulofenestra pseudoumbilicus*	Calcareous nannofossil	NN16	3.70	1.96	2.46	2.21
D02	Tc *Discoaster deflandrei*	Calcareous nannofossil		15.80	40.59	49.36	44.97
	T *Triquetrorhabdulus carinatus*	Calcareous nannofossil		18.28	59.11	65.86	62.48
	B? *Sphenolithus disbelemnos*	Calcareous nannofossil		22.76	106.06	107.23	106.64
	B *Discoaster druggii*	Calcareous nannofossil		22.82	133.03	134.71	133.87
D05	T *Reticulofenestra bisecta* (>10 µm)	Calcareous nannofossil		23.13	144.00	145.76	144.88
D06	T *Sphenolithus ciperoensis*	Calcareous nannofossil	NP25	24.43	145.76	153.72	149.74
	T *Sphenolithus distentus*	Calcareous nannofossil		26.44	175.05	184.17	179.61
D07	Bc *Triquetrorhabdulus carinatus*	Calcareous nannofossil		26.57	181.99	185.63	183.81
	B *Sphenolithus ciperoensis*	Calcareous nannofossil	NP24	29.62	185.63	191.73	188.68
D08	T *Reticulofenestra umbilicus* (>14 µm)	Calcareous nannofossil	NP23	32.02	200.60	200.63	200.62
	T *Isthmolithus recurvus*	Calcareous nannofossil		32.49	200.60	200.63	200.62
	T *Coccolithus formosus*	Calcareous nannofossil	NP22	32.92	200.60	200.63	200.62
	Ta *Clausicoccus subdistichus*	Calcareous nannofossil		33.43	201.20	201.50	201.35
	T *Discoaster saipanensis*	Calcareous nannofossil	NP21	34.44	206.71	207.61	207.61
	T *Discoaster barbadiensis*	Calcareous nannofossil		34.76	206.71	207.61	207.61
	T *Reticulofenestra reticulata*	Calcareous nannofossil		35.40	209.26	210.61	209.93
	B *Isthmolithus recurvus*	Calcareous nannofossil	NP19/NP20	36.97	212.76	219.80	216.28
	T *Chiasmolithus grandis*	Calcareous nannofossil		37.98	219.80	220.56	220.18
	B *Dictyococcites bisectus* (>10 µm)	Calcareous nannofossil		40.36	244.03	245.01	244.52
	T *Chiasmolithus solitus*	Calcareous nannofossil	NP17	40.40	272.21	279.56	275.88
	T *Nannotetrina* spp.	Calcareous nannofossil		41.85	279.56	281.27	280.41
	B? *Reticulofenestra umbilicus* (>14 µm)	Calcareous nannofossil		41.94	281.27	281.27	281.27
	T *Dorcadospyris ateuchis*	Radiolarian		18.64	59.13	71.30	66.21
	B *Stichocory delmontensis*	Radiolarian		19.35	81.06	90.57	85.82
	B *Calocycletta virginis*	Radiolarian		21.82	124.87	134.71	129.79
	B *Cyrtocapsella tetrapera*	Radiolarian		21.82	124.87	134.71	129.79
	B *Eucyrtidium diaphanes*	Radiolarian		23.00	115.07	124.87	119.97
	B *Lychnocanoma elongata*	Radiolarian		24.18	144.00	153.72	148.86
	B *Calocycletta robusta*	Radiolarian		25.97	163.20	172.77	167.99
	B *Dorcadospyris ateuchus*	Radiolarian		28.64	172.77	244.03	208.40
	T *Sethochytris triconiscus*	Radiolarian		39.35	244.03	244.63	244.33
	B *Podocyrtis goetheana*	Radiolarian		40.14	244.63	253.05	248.84
	T *Lophocyrtis biaurita*	Radiolarian		40.14	244.63	253.05	248.84
	X *Podocyrtis mitra – P. chalara*	Radiolarian		40.65	270.63	289.83	280.23
D10	X *Podocyrtis sinuosa – P. mitra*	Radiolarian		43.38	299.80		299.80
D03	T *Paragloborotalia kugleri*	Planktonic foraminifer	M1b/M2	21.12	73.85	75.35	74.60
D04	B *Globoquadrina dehiscens*	Planktonic foraminifer	M1a/M1b	22.44	89.35	90.54	89.95
	B *Paragloborotalia kugleri*	Planktonic foraminifer	OE7/M1a	22.96	92.53	94.06	93.30
	C12r/C13n	Chron boundary		33.16			200.67
	C13r/C15n	Chron boundary		35.00			206.42
D09	C17n.1r/C17n.2n	Chron boundary		37.87			222.22
	C18n.1n/C18n.1r	Chron boundary		39.63			238.90
	C18n.1r/C18n.2n	Chron boundary		39.70			240.72
	C18n.2n/C18r	Chron boundary		40.15			248.89
	C18r/C19n	Chron boundary		41.15			266.04
	C19n/C19r	Chron boundary		41.39			268.49

T = top, Tc = top common, B = base, Bc = base common, X = faunal crossover.

Table T16. Age-depth datum tie points, Hole U1404A.

Datum tie point	Datum	Datum type	Zone/ Subzone	Age (Ma)	Mid-point depth (mbsf)	Distance (m)	Duration (Ma)	LSR (cm/k.y.)	Notes
D01	T *Discoaster tamalis*	Calcareous nannofossil		2.80	0.88				
D02	Tc *Discoaster deflandrei*	Calcareous nannofossil		15.80	44.97	44.09	13.00	0.34	
D03	T *Paragloborotalia kugleri*	Planktonic foraminifer	M1b/M2	21.12	74.60	29.63	5.32	0.56	
D04	B *Globoquadrina dehiscens*	Planktonic foraminifer	M1a/M1b	22.44	89.95	15.35	1.32	1.16	
D05	T *Reticulofenestra bisecta* (>10 µm)	Calcareous nannofossil		23.13	144.88	54.94	0.69	7.96	
D06	T *Sphenolithus ciperoensis*	Calcareous nannofossil	NP25	24.43	149.74	4.86	1.30	0.37	
D07	Bc *Triquetrorhabdulus carinatus*	Calcareous nannofossil		26.57	183.81	34.07	2.14	1.59	
D08	T *Reticulofenestra umbilicus* (>14 µm)	Calcareous nannofossil	NP23	32.02	200.62	16.81	5.45	0.31	Average rate = 0.27 cm/k.y.
D09	C17n.1r/C17n.2n	Chron boundary		37.87	222.22	13.05	5.85	0.22	
D10	X *Podocyrtis sinuosa – P. mitra*	Radiolarian		43.38	299.80	86.14	5.51	1.56	

LSR = linear sedimentation rate. T = top, Tc = top common, B = base, Bc = base common, X = faunal crossover.

Table T17. Carbonate content and accumulation rates, Site U1404. (Continued on next three pages.)

Age (Ma)	LSR (cm/k.y.)	Dry density (g/cm^3)	$CaCO_3$ (wt%)	MAR (g/cm^2/k.y.)	CAR (g/cm^2/k.y.)	nCAR (g/cm^2/k.y.)
3.2	0.34	0.74	0.48	0.25	0.00	0.25
3.4	0.34	0.78	0.53	0.27	0.00	0.26
3.6	0.34	0.78	0.48	0.27	0.00	0.26
3.8	0.34	0.76	0.42	0.26	0.00	0.26
4.0	0.34	0.72	0.36	0.24	0.00	0.24
4.2	0.34	0.68	0.31	0.23	0.00	0.23
4.4	0.34	0.65	0.40	0.22	0.00	0.22
4.6	0.34	0.62	0.41	0.21	0.00	0.21
4.8	0.34	0.61	0.40	0.21	0.00	0.21
5.0	0.34	0.64	0.42	0.22	0.00	0.21
5.2	0.34	0.66	0.44	0.22	0.00	0.22
5.4	0.34	0.67	0.43	0.23	0.00	0.23
5.6	0.34	0.68	0.40	0.23	0.00	0.23
5.8	0.34	0.64	0.39	0.22	0.00	0.22
6.0	0.34	0.59	0.37	0.20	0.00	0.20
6.2	0.34	0.59	0.40	0.20	0.00	0.20
6.4	0.34	0.60	0.43	0.20	0.00	0.20
6.6	0.34	0.56	0.43	0.19	0.00	0.19
6.8	0.34	0.52	0.44	0.18	0.00	0.17
7.0	0.34	0.48	0.44	0.16	0.00	0.16
7.2	0.34	0.50	0.43	0.17	0.00	0.17
7.4	0.34	0.53	0.52	0.18	0.00	0.18
7.6	0.34	0.59	0.68	0.20	0.00	0.20
7.8	0.34	0.63	0.72	0.21	0.00	0.21
8.0	0.34	0.64	0.56	0.22	0.00	0.22
8.2	0.34	0.64	0.45	0.22	0.00	0.22
8.4	0.34	0.62	0.47	0.21	0.00	0.21
8.6	0.34	0.59	0.49	0.20	0.00	0.20
8.8	0.34	0.57	0.44	0.19	0.00	0.19
9.0	0.34	0.55	0.41	0.19	0.00	0.19
9.2	0.34	0.54	0.41	0.18	0.00	0.18
9.4	0.34	0.53	0.41	0.18	0.00	0.18
9.6	0.34	0.51	0.41	0.17	0.00	0.17
9.8	0.34	0.50	0.41	0.17	0.00	0.17
10.0	0.34	0.49	0.41	0.17	0.00	0.17
10.2	0.34	0.48	0.41	0.16	0.00	0.16
10.4	0.34	0.46	0.41	0.16	0.00	0.16
10.6	0.34	0.45	0.41	0.15	0.00	0.15
10.8	0.34	0.44	0.41	0.15	0.00	0.15
11.0	0.34	0.42	0.41	0.14	0.00	0.14
11.2	0.34	0.41	0.40	0.14	0.00	0.14
11.4	0.34	0.40	0.40	0.14	0.00	0.13
11.6	0.34	0.39	0.40	0.13	0.00	0.13
11.8	0.34	0.37	0.40	0.13	0.00	0.13
12.0	0.34	0.36	0.40	0.12	0.00	0.12
12.2	0.34	0.35	0.40	0.12	0.00	0.12
12.4	0.34	0.34	0.40	0.11	0.00	0.11

Table T17 (continued). (Continued on next page.)

Age (Ma)	LSR (cm/k.y.)	Dry density (g/cm^3)	$CaCO_3$ (wt%)	MAR (g/cm^2/k.y.)	CAR (g/cm^2/k.y.)	nCAR (g/cm^2/k.y.)
12.6	0.34	0.35	0.38	0.12	0.00	0.12
12.8	0.34	0.38	0.35	0.13	0.00	0.13
13.0	0.34	0.38	0.37	0.13	0.00	0.13
13.2	0.34	0.36	0.41	0.12	0.00	0.12
13.4	0.34	0.35	0.43	0.12	0.00	0.12
13.6	0.34	0.36	0.41	0.12	0.00	0.12
13.8	0.34	0.36	0.41	0.12	0.00	0.12
14.0	0.34	0.35	0.45	0.12	0.00	0.12
14.2	0.34	0.34	0.48	0.12	0.00	0.12
14.4	0.34	0.34	0.44	0.12	0.00	0.11
14.6	0.34	0.34	0.38	0.12	0.00	0.12
14.8	0.34	0.34	0.32	0.12	0.00	0.12
15.0	0.34	0.34	0.26	0.12	0.00	0.12
15.2	0.34	0.34	0.20	0.12	0.00	0.12
15.4	0.34	0.36	0.19	0.12	0.00	0.12
15.6	0.34	0.39	0.19	0.13	0.00	0.13
15.8	0.56	0.40	0.20	0.22	0.00	0.22
16.0	0.56	0.40	0.21	0.22	0.00	0.22
16.2	0.56	0.40	0.22	0.22	0.00	0.22
16.4	0.56	0.38	0.41	0.21	0.00	0.21
16.6	0.56	0.38	1.11	0.21	0.00	0.21
16.8	0.56	0.40	2.11	0.22	0.00	0.22
17.0	0.56	0.41	3.12	0.23	0.01	0.22
17.2	0.56	0.43	3.83	0.24	0.01	0.23
17.4	0.56	0.42	3.23	0.23	0.01	0.23
17.6	0.56	0.41	2.47	0.23	0.01	0.22
17.8	0.56	0.40	2.19	0.23	0.00	0.22
18.0	0.56	0.41	2.26	0.23	0.01	0.22
18.2	0.56	0.40	0.85	0.22	0.00	0.22
18.4	0.56	0.40	0.57	0.22	0.00	0.22
18.6	0.56	0.40	0.66	0.22	0.00	0.22
18.8	0.56	0.40	0.77	0.22	0.00	0.22
19.0	0.56	0.43	2.00	0.24	0.00	0.24
19.2	0.56	0.47	4.22	0.26	0.01	0.25
19.4	0.56	0.44	6.28	0.25	0.02	0.23
19.6	0.56	0.44	2.31	0.24	0.01	0.24
19.8	0.56	0.43	0.21	0.24	0.00	0.24
20.0	0.56	0.43	0.74	0.24	0.00	0.24
20.2	0.56	0.46	2.45	0.26	0.01	0.25
20.4	0.56	0.45	3.92	0.25	0.01	0.24
20.6	0.56	0.44	4.51	0.24	0.01	0.23
20.8	0.56	0.43	3.91	0.24	0.01	0.23
21.0	0.56	0.43	4.64	0.24	0.01	0.23
21.2	1.16	0.44	7.42	0.51	0.04	0.48
21.4	1.16	0.46	6.88	0.53	0.04	0.50
21.6	1.16	0.44	0.30	0.52	0.00	0.52
21.8	1.16	0.43	0.50	0.50	0.00	0.50
22.0	1.16	0.44	0.66	0.51	0.00	0.51
22.2	1.16	0.46	1.93	0.53	0.01	0.52
22.4	1.16	0.46	3.06	0.54	0.02	0.52
22.6	7.96	0.47	2.70	3.76	0.10	3.65
22.8	7.96	0.52	1.81	4.12	0.07	4.04
23.0	7.96	0.55	1.02	4.40	0.05	4.36
23.2	0.37	0.57	0.35	0.21	0.00	0.21
23.4	0.37	0.57	0.73	0.21	0.00	0.21
23.6	0.37	0.58	1.38	0.22	0.00	0.22
23.8	0.37	0.59	1.52	0.22	0.00	0.22
24.0	0.37	0.59	1.07	0.22	0.00	0.22
24.2	0.37	0.59	0.78	0.22	0.00	0.22
24.4	0.37	0.57	0.68	0.21	0.00	0.21
24.6	1.59	0.58	1.85	0.93	0.02	0.91
24.8	1.59	0.63	1.87	1.01	0.02	0.99
25.0	1.59	0.64	1.62	1.01	0.02	1.00
25.2	1.59	0.65	1.27	1.04	0.01	1.02
25.4	1.59	0.67	2.62	1.07	0.03	1.04
25.6	1.59	0.69	5.26	1.09	0.06	1.03
25.8	1.59	0.70	0.61	1.12	0.01	1.11
26.0	1.59	0.74	0.72	1.19	0.01	1.18
26.2	1.59	0.76	1.28	1.21	0.02	1.19

Table T17 (continued). (Continued on next page.)

Age (Ma)	LSR (cm/k.y.)	Dry density (g/cm^3)	$CaCO_3$ (wt%)	MAR (g/cm^2/k.y.)	CAR (g/cm^2/k.y.)	nCAR (g/cm^2/k.y.)
26.4	1.59	0.80	0.31	1.27	0.00	1.27
26.6	0.31	0.84	0.40	0.26	0.00	0.26
26.8	0.31	0.84	0.84	0.26	0.00	0.26
27.0	0.31	0.83	1.12	0.26	0.00	0.25
27.2	0.31	0.83	0.83	0.26	0.00	0.25
27.4	0.31	0.83	0.49	0.26	0.00	0.25
27.6	0.31	0.83	0.35	0.26	0.00	0.26
27.8	0.31	0.84	0.31	0.26	0.00	0.26
28.0	0.31	0.85	0.41	0.26	0.00	0.26
28.2	0.31	0.87	0.91	0.27	0.00	0.27
28.4	0.31	0.90	1.29	0.28	0.00	0.27
28.6	0.31	0.91	0.81	0.28	0.00	0.28
28.8	0.31	0.92	0.21	0.28	0.00	0.28
29.0	0.31	0.91	0.19	0.28	0.00	0.28
29.2	0.31	0.90	0.37	0.28	0.00	0.28
29.4	0.31	0.93	0.42	0.29	0.00	0.29
29.6	0.31	0.96	0.44	0.30	0.00	0.29
29.8	0.31	0.98	0.34	0.30	0.00	0.30
30.0	0.31	1.00	0.28	0.31	0.00	0.31
30.2	0.31	1.02	0.24	0.31	0.00	0.31
30.4	0.31	1.04	0.20	0.32	0.00	0.32
30.6	0.31	1.06	0.20	0.33	0.00	0.33
30.8	0.31	1.08	0.16	0.33	0.00	0.33
31.0	0.31	1.09	0.21	0.34	0.00	0.34
31.2	0.31	1.11	0.16	0.34	0.00	0.34
31.4	0.31	1.11	0.19	0.34	0.00	0.34
31.6	0.31	1.12	0.18	0.34	0.00	0.34
31.8	0.31	1.12	1.36	0.35	0.00	0.34
32.0	0.31	1.12	14.44	0.35	0.05	0.30
32.2	0.22	1.12	35.31	0.25	0.09	0.16
32.4	0.22	1.12	33.38	0.25	0.08	0.17
32.6	0.22	1.11	40.14	0.25	0.10	0.15
32.8	0.22	1.11	46.49	0.25	0.11	0.13
33.0	0.22	1.11	50.28	0.25	0.12	0.12
33.2	0.22	1.13	46.42	0.25	0.12	0.13
33.4	0.22	1.13	48.04	0.25	0.12	0.13
33.6	0.22	1.12	33.61	0.25	0.08	0.17
33.8	0.22	1.10	12.73	0.25	0.03	0.22
34.0	0.22	1.12	4.76	0.25	0.01	0.24
34.2	0.22	1.14	1.74	0.25	0.00	0.25
34.4	0.22	1.16	0.25	0.26	0.00	0.26
34.6	0.22	1.17	0.19	0.26	0.00	0.26
34.8	0.22	1.16	3.72	0.26	0.01	0.25
35.0	0.22	1.15	6.04	0.26	0.02	0.24
35.2	0.22	1.15	4.32	0.26	0.01	0.25
35.4	0.22	1.18	4.76	0.26	0.01	0.25
35.6	0.22	1.22	10.56	0.27	0.03	0.24
35.8	0.22	1.25	26.00	0.28	0.07	0.21
36.0	0.22	1.25	32.87	0.28	0.09	0.19
36.2	0.22	1.23	21.13	0.27	0.06	0.22
36.4	0.22	1.21	18.63	0.27	0.05	0.22
36.6	0.22	1.19	20.52	0.27	0.05	0.21
36.8	0.22	1.18	22.27	0.26	0.06	0.20
37.0	0.22	1.17	10.35	0.26	0.03	0.23
37.2	0.22	1.16	4.27	0.26	0.01	0.25
37.4	0.22	1.13	8.12	0.25	0.02	0.23
37.6	0.22	1.10	3.19	0.25	0.01	0.24
37.8	0.22	1.12	5.00	0.25	0.01	0.24
38.0	1.56	1.16	2.92	1.81	0.05	1.76
38.2	1.56	1.15	2.23	1.80	0.04	1.76
38.4	1.56	1.11	6.51	1.73	0.11	1.62
38.6	1.56	1.12	5.82	1.75	0.10	1.65
38.8	1.56	1.10	0.37	1.72	0.01	1.71
39.0	1.56	1.09	0.72	1.71	0.01	1.70
39.2	1.56	1.07	0.25	1.68	0.00	1.67
39.4	1.56	1.02	1.02	1.60	0.02	1.59
39.6	1.56	1.06	6.67	1.66	0.11	1.55
39.8	1.56	1.00	7.58	1.57	0.12	1.45
40.0	1.56	0.90	0.28	1.40	0.00	1.40

Table T17 (continued).

Age (Ma)	LSR (cm/k.y.)	Dry density (g/cm^3)	$CaCO_3$ (wt%)	MAR (g/cm^2/k.y.)	CAR (g/cm^2/k.y.)	nCAR (g/cm^2/k.y.)
40.2	1.56	0.91	0.29	1.42	0.00	1.41
40.4	1.56	1.09	0.28	1.70	0.00	1.69
40.6	1.56	1.09	1.57	1.70	0.03	1.67
40.8	1.56	1.10	0.85	1.71	0.01	1.70
41.0	1.56	1.16	1.86	1.81	0.03	1.78
41.2	1.56	1.13	7.31	1.77	0.13	1.64
41.4	1.56	1.09	12.52	1.70	0.21	1.49
41.6	1.56	1.04	9.33	1.63	0.15	1.47
41.8	1.56	0.86	1.18	1.35	0.02	1.33
42.0	1.56	0.93	1.42	1.45	0.02	1.43
42.2	1.56	0.94	1.46	1.48	0.02	1.45
42.4	1.56	0.93	0.27	1.45	0.00	1.45
42.6	1.56	0.93	0.25	1.45	0.00	1.45
42.8	1.56	0.91	0.23	1.43	0.00	1.42
43.0	1.56	0.84	0.19	1.32	0.00	1.31
43.2	1.56	0.84	0.19			

LSR = linear sedimentation rate, MAR = mass accumulation rate, CAR = carbonate accumulation rate, nCAR = noncarbonate accumulation rate.

Table T18. Headspace gas sample geochemistry, Hole U1404A.

Core, section, interval (cm)	Depth (mbsf)	Methane (ppmv)	Ethane (ppmv)
342-U1404A-			
1H-2, 0–5	1.50	2.60	0.00
2H-7, 0–5	12.74	1.69	0.00
3H-6, 0–5	21.40	1.75	0.00
5H-5, 0–5	39.20	2.48	0.00
6H-5, 0–5	48.40	2.01	0.00
7H-5, 0–5	58.20	2.42	0.00
8H-7, 0–5	70.50	2.54	0.00
9H-7, 0–5	80.20	2.38	0.00
10H-7, 0–5	89.70	2.49	0.00
11H-4, 0–5	94.52	2.75	0.00
12H-7, 0–5	105.00	2.85	0.00
13H-6, 0–5	112.23	2.61	0.00
14H-7, 0–5	123.70	2.70	0.00
15H-7, 0–5	133.53	2.62	0.00
16H-7, 0–5	142.90	2.91	0.00
17H-7, 0–5	152.50	2.85	0.00
18H-7, 0–5	161.97	3.36	0.00
19H-7, 0–5	171.46	2.90	0.00
20H-7, 0–5	180.90	3.73	0.00
21H-7, 0–5	190.70	4.01	0.00
22H-CC, 0–5	194.32	3.98	0.00
23H-7, 0–5	203.40	4.96	0.00
24H-6, 0–5	211.80	4.24	0.00
25H-5, 0–5	218.80	7.36	0.61
26H-6, 0–5	227.70	9.56	0.72
27H-5, 0–5	234.60	15.20	0.98
28H-5, 0–5	242.50	14.08	0.80
29H-6, 0–5	251.60	13.71	0.95
31H-4, 0–5	264.20	26.28	1.73
32H-4, 0–5	268.48	28.76	1.79
33X-6, 0–5	278.50	26.23	1.67
34X-7, 0–5	289.20	28.08	1.72
35X-2, 0–5	290.90	25.33	1.18

Table T19. Interstitial water constituents, Hole U1404A.

Core, section, interval (cm)	Depth (mbsf)	pH	Alkalinity (mM)	Ammonium (μM)	Salinity	Cl^- (mM)*	Cl^- (mM)†	Na^+ (mM)	SO_4^{2-} (mM)	HPO_4^- (μM)	Mn^{2+} (μM)	Fe^{2+} (μM)	Ca^{2+} (mM)	Mg^{2+} (mM)	Sr^{2+} (μM)	K^+ (mM)	Sr/Ca	Mg/Ca
342-U1404A-																		
2H-6, 104–109	12.69	7.31	3.78	6	37	560	561	476	28.0	BDL	BDL	BDL	13.2	52.8	87.2	13.3	6.6	4.0
3H-5, 115–120	21.35	7.41	4.51	10	37	560	555	470	26.7	BDL	15.7	BDL	14.4	51.6	90.4	14.8	6.3	3.6
5H-4, 145–150	39.15	7.53	5.47	21	38	564	554	478	27.5	BDL	33.4	BDL	16.0	50.4	97.6	16.6	6.1	3.2
6H-4, 115–120	48.35	7.40	5.76	26	37	ND	553	469	27.1	BDL	44.9	2.9	16.6	49.4	102.5	16.2	6.2	3.0
7H-4, 145–150	58.15	7.31	5.96	36	38	ND	559	474	27.7	BDL	49.7	BDL	17.3	49.2	102.1	16.8	5.9	2.8
8H-6, 125–130	70.45	7.25	6.17	59	37	566	548	464	24.6	BDL	59.1	0.7	17.9	47.8	106.3	16.5	6.0	2.7
9H-6, 145–150	80.15	7.33	6.45	53	38	567	558	473	24.8	BDL	64.0	0.0	18.8	48.4	106.9	16.5	5.7	2.6
10H-6, 145–150	89.65	7.47	6.78	64	37	556	553	470	25.5	BDL	68.0	3.0	19.4	47.8	111.9	16.1	5.8	2.5
12H-6, 145–150	104.95	7.38	7.39	91	38	544	541	460	26.5	BDL	81.8	0.4	20.4	45.6	115.6	12.8	5.7	2.2
13H-5, 145–150	112.18	7.43	7.59	89	38	549	553	469	25.4	BDL	87.7	2.0	21.4	46.2	120.7	11.4	5.7	2.2
14H-6, 95–100	123.65	7.39	7.59	90	38	558	570	470	25.2	BDL	ND	ND	22.1	46.3	ND	13.4	ND	2.1
15H-6, 146–151	133.48	7.35	8.08	102	38	550	569	478	25.2	BDL	97.3	1.7	23.3	46.3	129.0	14.8	5.5	2.0
16H-6, 115–120	142.85	7.28	8.10	113	38	553	558	469	23.6	BDL	108.4	14.3	23.6	45.2	134.0	13.9	5.7	1.9
17H-6, 140–145	152.44	7.28	8.07	116	38	564	558	470	25.9	BDL	108.7	0.4	24.3	45.6	139.5	11.1	5.7	1.9
18H-6, 116–121	161.92	7.12	8.20	117	38	563	560	473	23.1	BDL	115.3	5.9	25.3	46.3	142.4	10.7	5.6	1.8
19H-6, 117–122	171.41	7.11	8.64	115	37	559	543	456	22.1	BDL	120.9	7.0	26.3	45.5	144.1	9.4	5.5	1.7
20H-6, 115–120	180.85	7.05	8.58	105	37	553	552	451	24.1	BDL	127.3	BDL	26.9	47.9	147.9	8.0	5.5	1.8
21H-6, 145–150	190.65	7.05	8.62	113	37	553	549	450	24.8	BDL	137.7	5.5	27.2	46.1	149.5	8.0	5.5	1.7
22H-1, 140–150	192.60	7.04	8.60	120	37	554	543	445	22.5	BDL	135.7	0.2	27.1	45.9	147.4	7.9	5.4	1.7
23H-6, 90–100	203.30	6.75	7.25	145	37	570	561	469	23.4	BDL	139.2	7.5	26.8	42.3	146.4	11.2	5.5	1.6
24H-5, 140–150	211.70	6.87	7.18	123	36	524	561	452	23.4	BDL	131.0	BDL	28.3	45.0	155.1	8.5	5.5	1.6
25H-4, 140–150	218.70	6.86	7.14	135	37	539	550	451	20.3	BDL	135.8	0.0	28.6	43.6	161.7	8.9	5.7	1.5
26H-5, 0–10	226.50	7.67	9.71	126	36	531	532	435	21.3	BDL	112.2	BDL	30.2	46.0	126.6	7.5	4.2	1.5
27H-4, 140–150	234.50	7.59	9.63	141	35	520	523	429	22.1	BDL	ND	ND	30.2	44.1	ND	7.9	ND	1.5
28H-4, 140–150	242.40	7.37	6.04	130	35	518	522	423	23.2	BDL	ND	ND	30.2	44.0	ND	6.2	ND	1.5
29H-5, 140–150	251.50	7.36	10.07	491	37	546	553	442	22.0	BDL	141.0	BDL	31.4	40.5	174.3	8.5	5.5	1.3
31H-3, 140–150	264.10	7.08	6.36	153	36	533	532	419	19.2	BDL	127.7	BDL	31.5	42.0	184.1	6.3	5.8	1.3
33X-5, 140–150	278.40	7.28	8.77	159	35	520	517	417	17.3	BDL	134.9	BDL	31.4	39.8	179.9	7.1	5.7	1.3
34X-6, 90–100	289.10	7.39	9.52	176	36	534	541	437	18.3	BDL	145.3	BDL	33.0	39.9	184.8	7.6	5.6	1.2
35X-1, 140–150	290.80	7.40	9.30	179	37	535	549	446	19.1	BDL	ND	ND	32.8	39.7	ND	7.8	ND	1.2

* = manual titration. † = ion chromatograph. BDL = below detection limit (HPO_4^- = 0.2 μM, Mn^{2+} = 0.1 μM, and Fe^{2+} = 0.6 μM) calculated as three times the standard deviation of multiple measures of a blank. ND = not determined.

Table T20. Interstitial water constituents, Holes U1404B and U1404C.

Core, section, interval (cm)	Depth (mbsf)	pH	Alkalinity (mM)	Salinity	Cl^- (mM)*
342-U1404B-					
4H-1, 44–46	21.84	ND	N D	ND	571
342-U1404C-					
2H-1, 145–150	17.45	7.59	5.21	37	539
2H-2, 145–150	18.95	ND	ND	38	ND
2H-3, 145–150	20.45	7.59	5.26	38	551
2H-4, 145–150	21.95	ND	ND	37	ND
2H-5, 145–150	23.45	7.73	5.39	37	542
2H-6, 145–150	24.95	ND	ND	38	ND
3H-1, 145–150	26.95	7.48	5.41	37	547
3H-2, 145–150	28.45	ND	ND	37	ND
3H-3, 145–150	29.95	7.62	5.61	38	551
3H-4, 145–150	31.45	7.55	5.62	38	549
4H-1, 145–150	36.45	7.45	5.44	38	544
4H-2, 145–150	37.95	ND	ND	37	ND
4H-3, 145–150	39.45	7.83	6.17	ND	538
4H-5, 145–150	42.45	7.35	5.81	ND	557
4H-6, 145–150	43.95	7.47	5.53	ND	556

* = manual titration. ND = not determined.

Table T21. Sedimentary sample and bulk elemental geochemistry, Hole U1404A. (Continued on next five pages.)

Core, section, interval (cm)	Depth (mbsf)	$CaCO_3$ (wt%)	IC (wt%)	TC (wt%)	TN (wt%)	TOC (wt%)	Corrected TOC (wt%)
342-U1404A-							
1H-1, 38–39	0.38	3.61	0.43	1.56	0.08	1.13	0.08
1H-2, 26–27	1.76	BDL	0.05	0.39	0.19	0.34	0.08
1H-3, 20–21	2.91	BDL	0.07	0.39	0.08	0.32	0.06
1H-4, 29–30	3.99	BDL	0.05	0.40	0.10	0.35	0.08
2H-1, 100–101	5.70	BDL	0.04	0.20	0.08	0.17	0.03
2H-2, 27–28	6.47	BDL	0.05	0.21	0.08	0.16	0.02
2H-3, 27–28	7.42	BDL	0.05	0.22	0.08	0.17	0.03
2H-4, 38–39	9.03	BDL	0.05	0.29	0.10	0.24	0.04
2H-5, 38–39	10.53	BDL	0.05	0.31	0.09	0.26	0.05
2H-6, 27–28	11.92	BDL	0.04	0.28	0.09	0.24	0.05
2H-7, 27–28	13.01	BDL	0.05	1.05	0.15	1.00	0.30
3H-1, 86–87	15.06	BDL	0.05	0.74	0.19	0.69	0.19
3H-2, 38–39	16.08	BDL	0.05	1.37	0.15	1.32	0.40
3H-3, 38–39	17.58	BDL	0.09	1.67	0.16	1.58	0.46
3H-4, 38–39	19.08	BDL	0.05	0.97	0.12	0.92	0.27
3H-5, 27–28	20.47	BDL	0.06	0.52	0.10	0.46	0.11
3H-6, 20–21	21.60	BDL	0.05	0.50	0.10	0.45	0.12
5H-1, 38–39	33.58	BDL	0.05	1.98	0.19	1.93	0.61
5H-2, 38–39	35.08	BDL	0.04	1.85	0.18	1.81	0.57
5H-3, 38–39	36.58	BDL	0.05	1.50	0.16	1.45	0.44
5H-4, 38–39	38.08	BDL	0.05	0.84	0.13	0.79	0.23
5H-5, 38–39	39.58	BDL	0.06	1.54	0.17	1.48	0.45
6H-1, 39–40	43.09	BDL	0.02	1.61	BDL	1.59	0.51
6H-2, 39–40	44.59	BDL	0.02	1.42	0.09	1.40	0.45
6H-3, 39–40	46.09	BDL	0.03	0.89	0.10	0.86	0.27
6H-4, 39–40	47.59	BDL	0.03	0.87	0.04	0.84	0.26
6H-5, 39–40	48.79	BDL	0.06	1.38	0.08	1.32	0.39
7H-1, 48–49	52.68	BDL	0.49	3.44	0.16	2.96	0.65
7H-2, 53–54	54.23	ND	ND	2.50	0.15	ND	0.54
7H-3, 45–46	55.65	2.03	0.24	2.21	0.15	1.97	0.49
7H-4, 49–50	57.19	2.55	0.31	2.05	0.07	1.74	0.37
7H-5, 29–30	58.49	0.49	0.06	1.33	0.13	1.27	0.38
8H-1, 38–39	62.08	0.79	0.10	1.46	0.07	1.37	0.39
8H-2, 38–39	63.58	3.34	0.40	2.51	0.07	2.11	0.43
8H-3, 38–39	65.08	7.25	0.87	4.20	0.17	3.33	0.52
8H-4, 38–39	66.58	0.19	0.02	1.49	0.12	1.47	0.47
8H-5, 38–39	68.08	0.24	0.03	1.45	0.09	1.42	0.45

Table T21 (continued). (Continued on next page.)

Core, section, interval (cm)	Depth (mbsf)	$CaCO_3$ (wt%)	IC (wt%)	TC (wt%)	TN (wt%)	TOC (wt%)	Corrected TOC (wt%)
8H-6, 38–39	69.58	2.65	ND	2.71	0.19	ND	0.58
8H-7, 29–30	70.79	4.22	0.51	2.94	0.08	2.43	0.47
9H-1, 38–39	71.58	4.72	0.57	3.17	0.12	2.60	0.49
9H-2, 38–39	73.08	3.65	0.44	3.56	0.17	3.12	0.74
9H-3, 38–39	74.58	5.38	0.65	3.89	0.21	3.24	0.64
9H-4, 38–39	76.08	8.73	1.05	4.95	0.13	3.90	0.59
9H-5, 38–39	77.58	9.86	1.18	4.93	0.14	3.75	0.45
9H-6, 38–39	79.08	0.23	0.03	0.72	0.05	0.69	0.21
9H-7, 17–18	80.37	0.22	0.03	1.45	0.11	1.42	0.45
10H-1, 38–39	81.08	0.50	0.06	1.80	0.14	1.74	0.54
10H-2, 39–40	82.59	0.46	0.06	1.73	0.15	1.68	0.52
10H-3, 39–40	84.09	0.64	0.08	1.48	0.13	1.40	0.41
10H-4, 39–40	85.59	0.60	0.07	0.98	0.11	0.91	0.25
10H-5, 39–40	87.09	2.47	0.30	1.76	0.11	1.46	0.29
10H-6, 39–40	88.59	1.48	0.18	1.64	0.10	1.46	0.37
10H-7, 16–17	89.86	4.84	0.58	3.42	0.14	2.84	0.55
11H-1, 20–21	90.40	0.32	0.04	1.00	0.05	0.96	0.29
11H-2, 38–39	91.91	0.23	0.03	1.13	0.14	1.10	0.35
11H-3, 38–39	93.44	7.12	0.85	3.79	0.15	2.94	0.40
11H-4, 31–32	94.83	7.81	0.94	3.82	0.10	2.88	0.33
12H-1, 38–39	96.58	4.53	0.54	2.34	0.12	1.80	0.23
12H-2, 38–39	98.03	10.58	1.27	5.10	0.13	3.83	0.42
12H-3, 38–39	99.48	0.24	0.03	1.22	0.14	1.19	0.38
12H-4, 38–39	100.93	4.50	0.54	3.45	0.17	2.91	0.60
12H-5, 38–39	102.38	0.26	0.03	1.01	0.11	0.98	0.30
12H-6, 38–39	103.88	0.22	0.03	0.97	0.13	0.94	0.30
12H-7, 29–30	105.29	0.20	0.02	0.56	0.13	0.54	0.16
13H-1, 51–52	106.21	0.62	0.07	0.69	0.08	0.62	0.15
13H-2, 51–52	106.73	2.91	0.35	2.69	0.16	2.34	0.54
13H-3, 38–39	108.11	0.92	0.11	1.56	0.12	1.45	0.41
13H-4, 38–39	109.61	0.26	0.03	1.36	0.13	1.33	0.42
13H-5, 38–39	111.11	0.20	0.02	1.40	0.15	1.38	0.44
13H-6, 75–76	112.98	0.24	0.03	1.04	0.12	1.01	0.32
13H-7, 22–23	113.95	0.21	0.03	1.34	0.22	1.32	0.42
14H-1, 38–39	115.58	0.34	0.04	0.76	0.10	0.72	0.21
14H-2, 38–39	117.08	3.47	0.42	3.29	0.16	2.87	0.67
14H-3, 38–39	118.58	3.44	0.41	2.46	0.18	2.05	0.40
14H-4, 38–39	120.08	1.91	0.23	2.06	0.18	1.83	0.45
14H-5, 38–39	121.58	0.21	0.03	1.43	0.15	1.40	0.45
14H-6, 22–23	122.92	2.44	0.29	1.49	0.60	1.20	0.20
14H-7, 22–23	123.92	2.39	0.29	1.99	0.13	1.70	0.37
15H-1, 38–39	125.08	4.79	0.58	3.77	0.19	3.20	0.67
15H-2, 38–39	126.54	2.77	0.33	2.61	0.18	2.28	0.53
15H-3, 38–39	128.01	0.42	0.05	1.50	0.14	1.45	0.45
15H-4, 38–39	129.47	3.63	0.44	2.64	0.15	2.20	0.44
15H-5, 38–39	130.93	0.21	0.03	1.25	0.14	1.22	0.39
15H-6, 38–39	132.40	0.30	0.04	1.41	0.17	1.37	0.43
15H-7, 20–21	133.73	0.31	0.04	1.19	0.12	1.15	0.36
16H-1, 38–39	134.58	0.43	0.05	1.63	0.16	1.58	0.49
16H-2, 38–39	136.08	0.25	0.03	1.65	0.12	1.62	0.52
16H-3, 38–39	137.58	0.73	0.09	1.86	0.14	1.77	0.53
16H-4, 38–39	139.08	3.23	0.39	2.98	0.19	2.59	0.60
16H-5, 38–39	140.58	0.18	0.02	1.46	0.16	1.44	0.46
16H-6, 30–31	142.00	0.23	0.03	1.27	0.19	1.24	0.39
16H-7, 20–21	143.10	0.13	0.02	1.79	0.23	1.77	0.58
17H-1, 38–39	144.08	0.28	0.03	1.40	0.15	1.37	0.43
17H-2, 38–39	145.59	0.47	0.06	2.08	0.18	2.02	0.63
17H-3, 38–39	147.04	1.73	0.21	1.93	0.13	1.72	0.43
17H-4, 38–39	148.50	0.84	0.10	1.24	0.14	1.22	0.39
17H-5, 38–39	149.96	0.63	0.08	1.08	0.12	1.00	0.28
17H-6, 38–39	151.42	0.88	0.11	1.29	0.12	1.18	0.32
17H-7, 20–21	152.70	3.48	0.42	2.49	0.19	2.07	0.41
18H-1, 38–39	153.58	1.26	0.15	1.31	0.13	1.16	0.28
18H-2, 38–39	155.09	0.78	0.09	1.20	0.18	1.11	0.30
18H-3, 38–39	156.60	3.30	0.40	2.35	0.38	1.95	0.38
18H-4, 38–39	158.12	1.85	0.22	1.96	0.18	1.74	0.43
18H-5, 38–39	159.63	1.20	0.14	1.64	0.18	1.50	0.40
18H-6, 38–39	161.14	0.59	0.07	1.03	0.14	0.96	0.27

Table T21 (continued). (Continued on next page.)

Core, section, interval (cm)	Depth (mbsf)	$CaCO_3$ (wt%)	IC (wt%)	TC (wt%)	TN (wt%)	TOC (wt%)	Corrected TOC (wt%)
18H-7, 21–22	162.18	1.84	0.22	1.83	0.17	1.61	0.39
19H-1, 38–39	163.08	1.48	0.18	2.08	0.20	1.90	0.51
19H-2, 38–39	164.58	1.40	0.17	1.62	0.16	1.45	0.37
19H-3, 38–39	166.08	3.50	0.42	2.24	0.19	1.82	0.32
19H-4, 38–39	167.59	8.60	1.03	4.00	0.13	2.97	0.29
19H-5, 38–39	169.10	3.11	0.37	2.02	0.12	1.65	0.30
19H-6, 38–39	170.62	0.39	0.05	0.64	0.12	0.59	0.16
20H-1, 38–39	172.58	0.62	0.08	1.25	0.16	1.18	0.34
20H-2, 38–39	174.08	0.22	0.03	0.97	0.15	0.94	0.29
20H-3, 38–39	175.58	1.00	0.12	1.02	0.12	0.90	0.22
20H-4, 38–39	177.08	2.55	0.31	1.89	0.14	1.58	0.32
20H-5, 38–39	178.58	0.30	0.04	0.60	0.28	0.56	0.16
20H-6, 28–29	179.98	0.37	0.05	1.02	0.16	0.98	0.29
20H-7, 20–21	181.10	0.26	0.03	0.89	0.13	0.86	0.26
21H-1, 43–44	182.13	0.30	0.04	0.72	0.13	0.68	0.20
21H-2, 38–39	183.58	0.28	0.03	1.38	0.20	1.35	0.42
21H-3, 32–33	185.02	1.22	0.15	1.18	0.14	1.03	0.24
21H-4, 38–39	186.58	0.38	0.05	1.11	0.11	1.06	0.32
21H-5, 38–39	188.08	0.28	0.03	0.51	0.12	0.48	0.14
21H-6, 26–27	189.46	1.44	0.17	1.43	0.17	1.26	0.30
21H-7, 17–18	190.87	0.00	0.00	1.17	0.16	1.17	0.39
22H-1, 45–46	191.65	0.34	0.04	1.09	0.16	1.05	0.32
22H-2, 30–31	193.00	0.47	0.06	0.94	0.15	0.88	0.26
22H-3, 14–14	193.94	0.32	0.04	0.56	0.12	0.52	0.15
23H-1, 30–31	195.20	0.22	0.03	0.62	0.11	0.59	0.18
23H-1, 60–61	195.50	0.19	0.02	ND	ND	ND	ND
23H-1, 90–91	195.80	0.21	0.03	ND	ND	ND	ND
23H-1, 120–121	196.10	0.22	0.03	ND	ND	ND	ND
23H-1, 149–150	196.39	0.18	0.02	ND	ND	ND	ND
23H-2, 10–11	196.50	0.20	0.02	ND	ND	ND	ND
23H-2, 30–31	196.70	0.17	0.02	0.69	0.14	0.67	0.21
23H-2, 50–51	196.90	0.18	0.02	ND	ND	ND	ND
23H-2, 70–71	197.10	0.09	0.01				
23H-2, 90–91	197.30	0.23	0.03				
23H-2, 110–111	197.50	0.23	0.03				
23H-2, 130–131	197.70	0.22	0.03				
23H-2, 149–150	197.89	0.15	0.02				
23H-3, 110–111	199.00	0.20					
23H-4, 10–11	199.50	0.16	0.02				
23H-4, 30–31	199.70	0.20	0.02	0.23	0.11	0.21	0.05
23H-4, 50–51	199.90	0.26	0.03				
23H-4, 70–71	200.10	3.44	0.41				
23H-4, 90–91	200.30	1.52	0.18				
23H-4, 110–111	200.50	1.24	0.15				
23H-4, 130–131	200.70	32.17	3.86				
23H-4, 148–149	200.88	40.51	4.86				
23H-5, 10–11	201.00	33.72	4.04				
23H-5, 30–31	201.20	32.88	3.94	12.13	0.08	8.19	0.08
23H-5, 45–46	201.35	36.77	4.41				
23H-5, 60–61	201.50	30.96	3.71				
23H-5, 70–71	201.60	30.28	3.63				
23H-5, 90–91	201.80	43.56	5.22				
23H-5, 110–111	202.00	38.10	4.57				
23H-5, 130–131	202.20	41.63	4.99				
23H-5, 148–149	202.38	47.85	5.74				
23H-6, 10–11	202.50	49.66	5.95				
23H-6, 30–31	202.70	56.98	6.83	20.76	0.07	13.93	0.05
23H-6, 50–51	202.90	45.03	5.40				
23H-6, 70–71	203.10	44.98	5.39				
23H-7, 10–11	203.50	48.63	5.83				
23H-7, 30–31	203.70	47.80	5.73	17.47	0.07	11.74	0.06
23H-7, 50–51	203.90	47.94	5.75				
24H-1, 20–21	204.50	12.32	1.48				
24H-1, 51–52	204.81	9.81	1.18				
24H-1, 71–72	205.01	4.15	0.50				
24H-1, 90–91	205.20	2.02	0.24				
24H-1, 110–111	205.40	3.04	0.36				
24H-1, 130–131	205.60	0.44	0.05	0.48	0.11	0.43	0.11
24H-2, 10–11	205.90	0.21	0.03				

Table T21 (continued). (Continued on next page.)

Core, section, interval (cm)	Depth (mbsf)	$CaCO_3$ (wt%)	IC (wt%)	TC (wt%)	TN (wt%)	TOC (wt%)	Corrected TOC (wt%)
24H-2, 30–31	206.10	0.24	0.03	0.22	0.11	0.19	0.04
24H-2, 50–51	206.30	0.15	0.02				
24H-2, 70–71	206.50	0.20					
24H-2, 90–91	206.70	0.23	0.03				
24H-2, 110–111	206.90	6.93	0.83				
24H-2, 130–131	207.10	6.24	0.75				
24H-3, 10–11	207.40	5.87	0.70				
24H-3, 30–31	207.60	5.20	0.62	1.96	0.10	1.34	0.03
24H-3, 50–51	207.80	3.17	0.38				
24H-3, 70–71	208.00	4.34	0.52				
24H-3, 90–91	208.20	4.78	0.57				
24H-3, 110–111	208.40	5.81	0.70				
24H-3, 130–131	208.60	12.44	1.49				
24H-4, 10–10.5	208.90	12.31	1.48				
24H-4, 30–30.5	209.10	31.95	3.83				
24H-4, 38–39	209.18	37.15	4.45	13.36	0.07	8.91	0.00
24H-4, 50–50.5	209.30	42.99	5.16				
24H-4, 70–70.5	209.50	25.94	3.11				
24H-4, 90–90.5	209.70	33.54	4.02				
24H-4, 110–110.5	209.90	22.48	2.70				
24H-4, 130–130.5	210.10	12.59	1.51				
24H-4, 149–149.5	210.29	14.35	1.72				
24H-5, 10–10.5	210.40	19.81	2.38				
24H-5, 30–30.5	210.60	25.18	3.02				
24H-5, 32–33	210.62	23.31	2.80	8.23	0.09	5.43	0.00
24H-5, 50–50.5	210.80	21.97	2.63				
24H-5, 70–70.5	211.00	16.18	1.94				
24H-5, 90–90.5	211.20	28.19	3.38				
24H-5, 110–110.5	211.40	18.98	2.28				
24H-5, 130–130.5	211.60	12.27	1.47				
24H-6, 10–10.5	211.90	7.05	0.85				
24H-6, 22–23	212.02	3.94	0.47	1.90	0.10	1.43	0.16
24H-6, 30–30.5	212.10	3.48	0.42				
24H-6, 50–50.5	212.30	4.10	0.49				
24H-6, 70–70.5	212.50	9.43	1.13				
24H-6, 90–90.5	212.70	9.31	1.12				
25H-1, 10–10.5	212.90	0.80	0.10				
25H-1, 30–30.5	213.10	6.53	0.78				
25H-1, 38–39	213.18	0.97		0.74	0.13		0.13
25H-1, 50–50.5	213.30	4.46	0.54				
25H-1, 70–70.5	213.50	4.26	0.51				
25H-1, 90–90.5	213.70	5.85	0.70				
25H-1, 110–110.5	213.90	9.85	1.18				
25H-1, 130–130.5	214.10	3.84	0.46				
25H-1, 149–149.5	214.29	13.98	1.68				
25H-2, 10–10.5	214.40	5.88	0.71				
25H-2, 30–30.5	214.60	11.28	1.35				
25H-2, 38–39	214.68	8.87	1.06	3.53	0.12	2.47	0.11
25H-2, 50–50.5	214.80	2.74	0.33				
25H-2, 70–70.5	215.00	5.46	0.66				
25H-2, 90–90.5	215.20	0.20	0.02				
25H-2, 110–110.5	215.40	0.17	0.02				
25H-2, 130–130.5	215.60	0.05	0.01				
25H-2, 149–149.5	215.79	0.18	0.02				
25H-3, 10–11	215.90	0.23	0.03				
25H-3, 30–31	216.10	0.20	0.02				
25H-3, 38–39	216.18	0.16	0.02	0.23	0.09	0.21	0.06
25H-3, 50–51	216.30	0.16	0.02				
25H-3, 70–71	216.50	0.20	0.02				
25H-3, 90–91	216.70	0.25	0.03				
25H-3, 110–111	216.90	4.05	0.49				
25H-3, 130–131	217.10	2.64	0.32				
25H-3, 149–150	217.29	3.97	0.48				
25H-4, 10–11	217.40	2.65	0.32				
25H-4, 29–30	217.59	1.67	0.20	0.87	0.05	0.67	0.09
25H-4, 30–31	217.60	1.49	0.18				
25H-4, 50–51	217.80	3.84	0.46				
25H-4, 70–71	218.00	6.27	0.75				
25H-4, 90–91	218.20	0.33	0.04				

Table T21 (continued). (Continued on next page.)

Core, section, interval (cm)	Depth (mbsf)	$CaCO_3$ (wt%)	IC (wt%)	TC (wt%)	TN (wt%)	TOC (wt%)	Corrected TOC (wt%)
25H-4, 110–111	218.40	3.36	0.40				
25H-4, 130–131	218.60	5.13	0.62				
25H-5, 9–10	218.89	3.04	0.36	1.53	0.10	1.17	0.14
25H-5, 10–11	218.90	2.29	0.28				
25H-5, 30–31	219.10	0.22	0.03				
25H-5, 50–51	219.30	0.94	0.11				
25H-5, 70–71	219.50	0.80	0.10				
25H-5, 90–91	219.70	1.72	0.21				
25H-CC, 10–11	219.91	0.32	0.04				
25H-CC, 30–31	220.11	0.73	0.09				
25H-CC, 50–51	220.31	0.91	0.11				
26H-1, 38–39	220.88	7.47	0.90	2.77	0.09	1.87	0.02
26H-1, 80–81	221.30	5.61	0.67				
26H-1, 120–121	221.70	10.62	1.27				
26H-2, 38–39	222.38	8.80	1.06	3.22	0.10	2.17	0.01
26H-2, 80–81	222.80	6.57	0.79				
26H-2, 120–121	223.20	0.12	0.01				
26H-2, 120–121	223.20	0.44	0.05				
26H-3, 38–39	223.88	12.77	1.53	4.72	0.10	3.19	0.03
26H-3, 80–81	224.30	8.42	1.01				
26H-3, 120–121	224.70	9.28	1.11				
26H-4, 38–39	225.38	4.51	0.54	1.67	0.10	1.13	0.01
26H-4, 80–81	225.80	1.70	0.20				
26H-4, 120–121	226.20	0.30	0.04				
26H-5, 25–26	226.75	0.81	0.10	0.55	0.11	0.45	0.08
26H-5, 80–81	227.30	0.11	0.01				
26H-6, 15–16	227.85	0.34	0.04	0.36	0.12	0.32	0.08
26H-6, 55–56	228.25	0.30	0.04				
26H-CC, 17–18	228.47	0.44	0.05				
27H-1, 38–39	228.98	0.12	0.01	0.33	0.12	0.32	0.10
27H-2, 38–39	230.48	1.40	0.17	1.02	0.10	0.85	0.17
27H-3, 38–39	231.98	0.24	0.03	0.32	0.12	0.29	0.08
27H-4, 31–32	233.41	0.26	0.03	0.40	0.11	0.37	0.10
27H-5, 39–40	234.99	0.26	0.03	0.32	0.11	0.29	0.07
28H-1, 38–39	236.88	0.22	0.03	0.48	0.11	0.45	0.13
28H-1, 120–121	237.70	0.27	0.03				0.01
28H-2, 38–39	238.38	1.70	0.20	0.73	0.10	0.53	0.04
28H-2, 80–81	238.80	4.25	0.51				
28H-2, 120–121	239.20	0.43	0.05				
28H-3, 38–39	239.88	5.56	0.67	1.98	0.13	1.31	0.00
28H-3, 80–81	240.30	7.10	0.85				
28H-3, 120–121	240.70	11.05	1.33				
28H-4, 33–34	241.33	0.29	0.03	0.38	0.11	0.35	0.09
28H-4, 80–81	241.80	10.37	1.24				
28H-4, 120–121	242.20	17.21	2.06				
28H-5, 30–31	242.80	14.45	1.73	5.40	0.09	3.67	0.06
28H-5, 80–81	243.30	12.35	1.48				
28H-5, 120–121	243.70	8.28	0.99				
28H-CC, 13–14	243.87	7.78	0.93				
29H-1, 38–39	244.48	0.46	0.06	0.50	0.29	0.45	0.11
29H-1, 80–81	244.90	0.47	0.06				
29H-1, 120–121	245.30	0.39	0.05				
29H-2, 38–39	245.98	0.23	0.03	0.37	0.12	0.34	0.10
29H-3, 38–39	247.48	0.29	0.04	0.54	0.14	0.50	0.14
29H-4, 38–39	248.98	0.27	0.03	0.24	0.23	0.21	0.05
29H-5, 38–39	250.48	0.31	0.04	0.35	0.85	0.31	0.08
29H-6, 27–28	251.87	0.28	0.03	0.68	0.15	0.65	0.19
30H-1, 30–31	253.30	0.29	0.03	0.33	0.11	0.30	0.08
30H-2, 21–22	254.46	0.26	0.03	0.44	0.14	0.41	0.11
30H-3, 36–37	255.50	0.27	0.03	0.46	1.03	0.43	0.12
30H-4, 38–39	257.02	3.34	0.40	2.17	0.12	1.77	0.32
30H-5, 13–14	258.27	0.23	0.03	0.40	0.70	0.37	0.10
31H-1, 38–39	260.08	1.17	0.14	0.63	0.11	0.49	0.07
31H-2, 38–39	261.58	1.30	0.16	0.73	0.11	0.57	0.09
31H-3, 30–31	263.00	1.63	0.20	0.78	0.12	0.58	0.06
31H-3, 80–81	263.50	4.47	0.54				
31H-3, 120–121	263.90	0.39	0.05				
31H-3, 120–121	263.90	0.49	0.06				
31H-4, 11–12	264.31	5.99	0.72	2.32	0.11	1.60	0.05

Table T21 (continued).

Core, section, interval (cm)	Depth (mbsf)	$CaCO_3$ (wt%)	IC (wt%)	TC (wt%)	TN (wt%)	TOC (wt%)	Corrected TOC (wt%)
31H-4, 40–41	264.60	6.20	0.74				
31H-CC, 5–6	264.92	0.52	0.06				
31H-CC, 32–33	265.19	10.35	1.24				
32H-1, 20–21	265.50	3.33	0.40				
32H-2, 26–27	265.92	15.31	1.84	5.87	0.10	4.03	0.11
32H-2, 79–80	266.45	4.18	0.50				
32H-2, 120–121	266.86	7.49	0.90				
32H-3, 38–39	267.36	13.81	1.66	4.98	0.09	3.32	0.00
32H-3, 80–81	267.78	15.32	1.84				
32H-3, 120–121	268.18	12.45	1.49				
32H-4, 31–32	268.79	17.40	2.09	7.16	0.11	5.07	0.29
32H-4, 80–81	269.28	3.93	0.47				
32H-4, 120–121	269.68	23.33	2.80				
32H-5, 15–16	269.89	2.44	0.29				
32H-5, 45–46	270.19	11.32	1.36				
32H-CC, 20–21	270.58	0.52	0.06				
32H-CC, 50–51	270.88	21.69	2.60				
33X-1, 80–81	271.80	0.45	0.05				
33X-1, 112–113	272.12	23.70	2.84	8.60	0.07	5.76	0.01
33X-1, 120–121	272.20	25.21	3.02				
33X-2, 22–23	272.72	4.69	0.56	2.02	0.10	1.46	0.11
33X-2, 80–81	273.30	0.38	0.05				
33X-2, 120–121	273.70	0.23	0.03				
33X-3, 36–37	274.36	0.13	0.02	0.34	0.61	0.32	0.10
33X-3, 80–81	274.80	0.37	0.04				
33X-3, 120–121	275.20	3.60	0.43				
33X-4, 77–78	276.27	0.32	0.04	0.50	0.13	0.46	0.13
33X-4, 80–81	276.30	0.76	0.09				
33X-4, 120–121	276.70	2.24	0.27				
33X-5, 30–31	277.30	4.66	0.56				
33X-5, 57–58	277.57	0.21	0.03	0.76	0.29	0.74	0.23
33X-5, 80–81	277.80	2.10	0.25				
33X-5, 120–121	278.20	0.32	0.04				
33X-6, 10–11	278.60	0.29	0.03	0.63	0.20	0.60	0.17
33X-6, 35–36	278.85	1.28	0.15				
33X-6, 65–66	279.15	0.39	0.05				
33X-CC, 24–25	279.49	0.34	0.04				
34X-1, 50–51	281.20	2.96	0.35				
34X-1, 101–102	281.71	1.19	0.14	0.75	0.11	0.61	0.11
34X-2, 58–59	282.78	0.32	0.04	0.40	0.11	0.36	0.09
34X-3, 31–32	284.01	ND	ND	0.41	0.24		0.10
34X-4, 87–88	286.07	0.22	0.03	0.63	0.14	0.60	0.18
34X-5, 55–56	287.25	0.28	0.03	0.48	0.22	0.45	0.12
34X-6, 29–30	288.49	0.20	0.02	0.55	0.48	0.53	0.16
34X-7, 8–9	289.28	0.34	0.04	0.60	0.11	0.56	0.16
35X-1, 82–83	290.22	0.21	0.03	0.73	0.33	0.71	0.22
35X-2, 36–37	291.26	0.22	0.03	0.63	0.54	0.60	0.18
35X-3, 29–30	292.56	0.19	0.02	0.40	0.28	0.38	0.11
36X-1, 65–66	299.75	0.18	0.02	0.49	0.21	0.47	0.14

IC = inorganic carbon, TC = total carbon, TN = total nitrogen, TOC = total organic carbon. ND = not determined, BDL = below detection limit ($CaCO_3$ = <1 wt%, TOC = <0.03 wt%) as determined by three times the standard deviation of replicable measures of a low concentration sample.

Table T22. Core top and composite depth, Site U1404. (Continued on next page.)

Core	Depth (mbsf)	Depth (m CCSF)	Offset (m)	Cumulative offset (m)	Comment	Data sets used
342-U1404A-						
1H	0.00	0.00	0.00	0.00		Physical properties
2H	4.70	5.30	0.60	0.60	Tentative	Physical properties
3H	14.20	14.84	0.04	0.64	Tentative	Physical properties
4H	23.70	24.35	0.01	0.65	No recovery	
5H	33.20	33.85	0.00	0.65	Tentative	Physical properties
6H	42.70	45.35	2.00	2.65	Tentative	Physical properties
7H	52.20	54.86	0.01	2.66	Tentative	Physical properties
8H	61.70	64.37	0.01	2.67	Tentative	Physical properties
9H	71.20	74.07	0.20	2.87	Tentative	Physical properties
10H	80.70	83.67	0.10	2.97	Tentative	Physical properties
11H	90.20	93.18	0.01	2.98	Tentative	Physical properties
12H	96.20	99.78	0.60	3.58	Tentative	Physical properties
13H	105.70	109.73	0.45	4.03	Tentative	Physical properties
14H	115.20	119.24	0.01	4.04	Tentative	Physical properties
15H	124.70	128.75	0.01	4.05	Tentative	Physical properties
16H	134.20	139.00	0.75	4.80	Tentative	Physical properties
17H	143.70	148.83	0.33	5.13	Tentative	Physical properties
18H	153.20	158.83	0.50	5.63	Tentative	Physical properties
19H	162.70	168.86	0.53	6.16	Tentative	Physical properties
20H	172.20	178.51	0.15	6.31		XRF core scanning
21H	181.70	188.16	0.15	6.46		XRF core scanning
22H	191.20	197.67	0.01	6.47		XRF core scanning
23H	194.90	202.77	1.40	7.87		XRF core scanning
24H	204.30	212.92	0.75	8.62	Flow-in bottom 20 cm	XRF core scanning
25H	212.80	223.97	2.55	11.17	Flow-in bottom sections	XRF core scanning
26H	220.50	231.81	0.14	11.31		XRF core scanning
27H	228.60	240.13	0.22	11.53	Tentative	XRF core scanning
28H	236.50	248.13	0.10	11.63		XRF core scanning
29H	244.10	255.87	0.14	11.77		XRF core scanning
30H	253.00	264.96	0.19	11.96		XRF core scanning
31H	259.70	271.82	0.16	12.12		XRF core scanning
32H	265.30	277.54	0.12	12.24		XRF core scanning
33X	271.00	283.36	0.12	12.36		XRF core scanning
34X	280.70	293.16	0.10	12.46		XRF core scanning
35X	289.40	302.42	0.56	13.02		XRF core scanning
36X	299.10	312.22	0.10	13.12		XRF core scanning
342-U1404B-						
1H	0.00	0.60	0.60	0.60	Tentative	Physical properties
2H	2.40	4.00	1.00	1.60	Tentative	Physical properties
3H	11.90	15.10	1.60	3.20	Tentative	Physical properties
4H	21.40	21.63	–2.97	0.23	Pulled up 3 m	Physical properties
5H	27.40	30.18	2.55	2.78	Tentative	Physical properties
6H	36.90	39.83	0.15	2.93	Tentative	Physical properties
7H	46.40	49.52	0.19	3.12	Tentative	Physical properties
8H	55.90	59.22	0.20	3.32	Tentative	Physical properties
9H	65.40	68.73	0.01	3.33	Tentative	Physical properties
10H	74.90	77.68	–0.55	2.78	Tentative	Physical properties
11H	84.40	87.19	0.01	2.79	Tentative	Physical properties
12H	93.90	96.70	0.01	2.80	Tentative	Physical properties
13H	103.40	106.45	0.25	3.05	Tentative	Physical properties
14H	112.90	116.15	0.20	3.25	Tentative	Physical properties
15H	122.40	125.66	0.01	3.26	Tentative	Physical properties
16H	131.90	134.96	–0.20	3.06	Tentative	Physical properties
17H	141.40	145.56	1.10	4.16	Tentative	Physical properties
18H	150.90	152.06	–3.00	1.16	Pulled up 4 m	Physical properties
19H	156.40	161.86	4.30	5.46	Tentative	Physical properties
20H	165.90	171.86	0.50	5.96	Tentative	Physical properties
21H	175.40	181.37	0.01	5.97		XRF core scanning
22H	184.10	189.82	–0.25	5.72		XRF core scanning
23H	193.60	199.87	0.55	6.27	Flow-in bottom sections	XRF core scanning
24H	202.20	207.77	–0.70	5.57		XRF core scanning
25H	208.70	212.58	–1.69	3.88	Tentative	XRF core scanning
26H	215.20	221.68	2.60	6.48	Flow-in bottom sections	XRF core scanning
27H	223.30	236.03	6.25	12.73		XRF core scanning

Table T22 (continued).

Core	Depth (mbsf)	Depth (m CCSF)	Offset (m)	Cumulative offset (m)	Comment	Data sets used
342-1404C-						
1H	0.00	0.00	0.00	0.00	Drilling advance	
2H	16.00	31.50	15.50	15.50	Tentative	Physical properties
3H	25.50	41.20	0.20	15.70	Tentative	Physical properties
4H	35.00	50.71	0.01	15.71	Tentative	Physical properties

XRF = X-ray fluorescence.

Table T23. Splice tie points, Site U1404.

Hole, core, section, interval (cm)	Depth (mbsf)	Depth (m CCSF)		Hole, core, section, interval (cm)	Depth (mbsf)	Depth (m CCSF)	Comment	Data sets used
342-				342-				
				U1404A-1H-1, 0	0.00	0.00		
U1404A-1H-4, 60	4.30	4.30	Tie to	U1404B-2H-1, 30	2.70	4.30	Tentative	Physical properties
U1404B-2H-3, 55	5.95	7.55	Tie to	U1404A-2H-2, 75	6.95	7.55	Tentative	Physical properties
U1404A-2H-CC, 20	14.14	14.74	Append to	U1404A-3H-1, 0	14.20	14.84	Tentative	Physical properties
U1404A-3H-2, 15	15.85	16.49	Tie to	U1404B-3H-1, 139	13.29	16.49	Tentative	Physical properties
U1404B-3H-CC, 18	21.88	25.08	Append to	U1404B-4H-3, 45	24.85	25.08	Pull-up	Physical properties
U1404B-4H-6, 101	29.67	29.90	Append to	U1404B-5H-1, 0	27.40	30.18	Tentative	Physical properties
U1404B-5H-4, 129	33.19	35.97	Tie to	U1404A-5H-2, 62	35.32	35.97	Tentative	Physical properties
U1404A-5H-5, 56	39.76	40.41	Tie to	U1404B-6H-1, 58	37.48	40.41	Tentative	Physical properties
U1404B-6H-5, 113	44.03	46.96	Tie to	U1404A-6H-2, 11	44.31	46.96	Tentative	Physical properties
U1404A-6H-5, 12	48.52	51.17	Tie to	U1404C-4H-1, 46	35.46	51.17	Tentative	Physical properties
U1404C-4H-7, 11	44.11	59.82	Tie to	U1404B-8H-1, 60	56.50	59.82	Tentative	Physical properties
U1404B-8H-4, 109	61.49	64.81	Tie to	U1404A-8H-1, 44	62.14	64.81	Tentative	Physical properties
U1404A-8H-6, 113	70.33	73.00	Tie to	U1404B-9H-3, 127	69.67	73.00	Tentative	Physical properties
U1404B-9H-5, 117	72.57	75.90	Tie to	U1404A-9H-2, 33	73.03	75.90	Tentative	Physical properties
U1404A-9H-5, 84	78.04	80.91	Tie to	U1404B-10H-3, 23	78.13	80.91	Tentative	Physical properties
U1404B-10H-6, 59	82.99	85.77	Tie to	U1404A-10H-2, 60	82.80	85.77	Tentative	Physical properties
U1404A-10H-4, 74	85.94	88.91	Tie to	U1404B-11H-2, 22	86.12	88.91	Tentative	Physical properties
U1404B-11H-6, 36	92.26	95.05	Tie to	U1404A-11H-2, 54	92.07	95.05	Tentative	Physical properties
U1404A-11H-4, 60	95.12	98.10	Tie to	U1404B-12H-1, 140	95.30	98.10	Tentative	Physical properties
U1404B-12H-4, 53	98.93	101.73	Tie to	U1404A-12H-2, 50	98.15	101.73	Tentative	Physical properties
U1404A-12H-7, 47	105.47	109.05	Tie to	U1404B-13H-2, 110	106.00	109.05	Tentative	Physical properties
U1404B-13H-5, 106	110.46	113.51	Tie to	U1404A-13H-4, 25	109.48	113.51	Tentative	Physical properties
U1404A-13H-7, 65	114.38	118.41	Tie to	U1404B-14H-2, 76	115.16	118.41	Tentative	Physical properties
U1404B-14H-5, 85	119.75	123.00	Tie to	U1404A-14H-3, 76	118.96	123.00	Tentative	Physical properties
U1404A-14H-6, 57	123.27	127.31	Tie to	U1404B-15H-2, 15	124.05	127.31	Tentative	Physical properties
U1404B-15H-4, 68	127.58	130.84	Tie to	U1404A-15H-2, 63	126.79	130.84	Tentative	Physical properties
U1404A-15H-6, 94	132.96	137.01	Tie to	U1404B-16H-3, 39	133.95	137.01	Tentative	Physical properties
U1404B-16H-5, 79	137.14	140.20	Tie to	U1404A-16H-1, 120	135.40	140.20	Tentative	Physical properties
U1404A-16H-5, 124	141.44	146.24	Tie to	U1404B-17H-1, 68	142.08	146.24	Tentative	Physical properties
U1404B-17H-4, 131	147.21	151.37	Tie to	U1404A-17H-2, 103	146.24	151.37	Tentative	Physical properties
U1404A-17H-7, 57	153.07	158.20	Tie to	U1404B-18H-5, 12	157.04	158.20	Tentative	Physical properties
U1404B-18H-6, 23	158.65	159.81	Tie to	U1404A-18H-1, 98	154.18	159.81	Tentative	Physical properties
U1404A-18H-5, 62	159.87	165.50	Tie to	U1404B-19H-3, 64	160.04	165.50	Tentative	Physical properties
U1404B-19H-6, 124	165.14	170.60	Tie to	U1404A-19H-2, 24	164.44	170.60		Physical properties
U1404A-19H-6, 59	170.83	176.99	Tie to	U1404B-20H-4, 63	171.03	176.99		XRF core scanning
U1404B-20H-6, 45	173.85	179.81	Tie to	U1404A-20H-1, 130	173.50	179.81		XRF core scanning
U1404A-20H-7, 56	181.46	187.77	Tie to	U1404B-21H-7, 19	181.80	187.77	Tentative	XRF core scanning
U1404B-21H-7, 141	183.02	188.99	Tie to	U1404A-21H-1, 83	182.53	188.99	Tentative	XRF core scanning
U1404A-21H-4, 131	187.51	193.97	Tie to	U1404B-22H-3, 115	188.25	193.97		XRF core scanning
U1404B-22H-6, 116	192.78	198.50	Tie to	U1404A-22H-1, 83	192.03	198.50		XRF core scanning
U1404A-22H-3, 34	194.14	200.61	Tie to	U1404B-23H-1, 74	194.34	200.61		XRF core scanning
U1404B-23H-3, 63	197.23	203.50	Tie to	U1404A-23H-1, 73	195.63	203.50		XRF core scanning
U1404A-23H-6, 74	203.14	211.01	Tie to	U1404B-24H-3, 24	205.44	211.01		XRF core scanning
U1404B-24H-4, 103	207.73	213.30	Tie to	U1404A-24H-1, 38	204.68	213.30	Tentative	XRF core scanning
U1404A-24H-6, 95	212.75	221.37	Append to	U1404B-26H-1, 0	215.20	221.68		XRF core scanning
U1404B-26H-2, 114	217.84	224.32	Tie to	U1404A-25H-1, 35	213.15	224.32		XRF core scanning
U1404A-25H-CC, 64	220.44	231.61	Append to	U1404A-26H-1, 0	220.50	231.81		XRF core scanning
U1404A-26H-5, 67	227.17	238.48	Tie to	U1404B-27H-3, 64	225.75	238.48		XRF core scanning
U1404B-27H-5, 80	227.81	240.54	Tie to	U1404A-27H-1, 41	229.01	240.54	Tentative	XRF core scanning
U1404A-27H-CC, 40	236.44	247.97	Append to	U1404A-28H-1, 0	236.50	248.13		XRF core scanning
U1404A-28H-CC, 24	243.94	255.57	Append to	U1404A-29H-1, 0	244.10	255.87		XRF core scanning
U1404A-29H-CC, 35	252.99	264.76	Append to	U1404A-30H-1, 0	253.00	264.96		XRF core scanning
U1404A-30H-CC, 72	260.07	271.63	Append to	U1404A-31H-1, 0	259.70	271.82		XRF core scanning
U1404A-31H-CC, 34	265.21	277.33	Append to	U1404A-32H-1, 0	265.30	277.54		XRF core scanning
U1404A-32H-CC, 48	270.86	283.10	Append to	U1404A-33X-1, 0	271.00	283.36		XRF core scanning
U1404A-33X-CC, 28	279.50	291.86	Append to	U1404A-34X-1, 0	280.70	293.16		XRF core scanning
U1404A-34X-7, 59	289.79	302.25	Append to	U1404A-35X-1, 0	289.40	302.42		XRF core scanning
U1404A-35X-CC, 15	293.93	306.95	Append to	U1404A-36X-1, 0	299.10	312.22		XRF core scanning
U1404A-36X-1, 68	299.78	312.90						

XRF = X-ray fluorescence.